Investigating sphingolipid metabolism in budding yeast using stable isotope-labeled and caged vacuole-specific probes

Girik, Vladimir

How to cite

GIRIK, Vladimir. Investigating sphingolipid metabolism in budding yeast using stable isotope-labeled and caged vacuole-specific probes. Doctoral Thesis, 2019. doi: 10.13097/archive-ouverte/unige:125912

This publication URL: https://archive-ouverte.unige.ch/unige:125912
Publication DOI: 10.13097/archive-ouverte/unige:125912

UNIVERSITÉ DE GENÈVE
Section de chimie et biochimie
Département de biochimie

FACULTÉ DES SCIENCES
Professeur Howard Riezman

Investigating Sphingolipid Metabolism in Budding Yeast using Stable Isotope-labeled and Caged Vacuole-specific Probes

THÈSE

présentée aux Facultés de médecine et des sciences de l'Université de Genève
pour obtenir le grade de Docteur ès sciences en sciences de la vie,
mention Biosciences moléculaires

par

Vladimir GIRIK

de

Almaty (Kazakhstan)

Thèse N° 30

GENÈVE
Atelier Repromail
2019

LIFE SCIENCES
PhD SCHOOL
GENEVA

THESE DE DOCTORAT ES SCIENCES EN SCIENCES DE LA VIE DES FACULTÉS DE MÉDECINE ET DES SCIENCES
MENTION BIOSCIENCES MOLECULAIRES

Thèse de Monsieur Vladimir GIRIK

intitulée :

«Investigation Sphingolipid Metabolism in Budding Yeast Using Stable Isotope-labeled and Caged Vacuole-specific Probes»

Les Facultés de médecine et des sciences, sur le préavis de Monsieur H. RIEZMAN, professeur ordinaire et directeur de thèse (Département de biochimie), Monsieur M. KAKSONEN, professeur ordinaire (Département de biochimie), Monsieur T. HORNEMANN, professeur (Institute for Clinical Chemistry, University Hospital Zurich, University of Zurich, Switzerland), autorisent l'impression de la présente thèse, sans exprimer d'opinion sur les propositions qui y sont énoncées.

Genève, le 25 septembre 2019

Thèse - 30 -

Le Doyen
Faculté de médecine

Le Doyen
Faculté des sciences

N.B. - La thèse doit porter la déclaration précédente et remplir les conditions énumérées dans les "Informations relatives aux thèses de doctorat à l'Université de Genève".

FACULTÉ DE MÉDECINE
FACULTÉ DES SCIENCES

UNIVERSITÉ DE GENÈVE

Table of Contents

Acknowledgements

I would first like to express my gratitude to my doctoral supervisor professor Howard Riezman for giving me the opportunity to join his lab and conduct cutting edge research. I am also thankful to Howard for his patience, guidance and many insightful remarks and suggestions which had great scientific and educational value for me.

I would like to thank all the lab members who helped and supported me throughout my stay in the lab. I am thankful to Maria Auxiliadora Aguilera-Romero for support especially during my first months in the lab, showing me the basic techniques used in the lab. I thank Isabelle Riezman for assistance with mass spectrometry and lab routines. I am grateful to Suihan Feng for the synthesis of all chemical probes described in this study as well as for many helpful scientific discussions and advice. Also, many thanks to Kyohei Umebayashi from whom I learned a lot of practical tips and who gave me many helpful remarks and suggestions. I thank Thomas Hannich for useful scientific tips and tricks I learned from him. I would also like to thank Takeshi Harayama and Miwa Umebayashi for critical remarks and helpful suggestions for my research. I also say *merci* to the former technicians in the lab Brigitte Bernadets and Gisèle Dewhurst for their help with my daily lab struggles and for friendly chats during lunchtime. I would like to say thank you to Galih Haribowo for assistance with some experiments and in day-to-day lab tasks. I am thankful to all present a past lab members with whom I had a chance to work together for creating a nice and friendly working environment. I also thank our secretary Cécile Heymans for her helping me with numerous administrative issues. Last, but not least I thank my good friend Vaibhav Wasnik for friendly chats which provided great relief from inevitable work-related stress.

Besides that, I would like to thank people who made my research possible: Fabrice David from EPFL for creating and maintaining lipid analysis software platform, Bioimaging platform for microscopy service, ACCESS Geneva. I am also grateful to the Swiss National Science Foundation for supporting this research.

Finally, I am thankful to my parents for their endless love and psychological support during all these years I spent in the lab.

Résumé

Les sphingolipides constituent une classe de composés lipidiques qui exercent des fonctions structurelles et de signalisation importante dans les cellules. La levure de boulanger, *Saccharomyces cerevisiae*, a été utilisée dans les études fondamentales du métabolisme des sphingolipides en raison de la tractibilité génétique et du degré élevé de conservation évolutive entre cet organisme eucaryote unicellulaire et les mammifères. La sérine palmitoyltransférase (SPT) et la céramide synthase (CS) catalysent les étapes initiales de la biosynthèse des sphingolipides et sont enrichies dans différents compartiments du réticulum endoplasmique. En utilisant la levure de boulanger comme système modèle, nous montrons dans cette étude que la fusion de sous-unités catalytiques de la sérine palmitoyltransférase et de la céramide synthase n'augmente pas la biosynthèse des sphingolipides, ce qui suggère que la distance entre les deux complexes enzymatiques ne représente pas un facteur qui limite l'anabolisme des sphingolipides. Cependant, nous montrons également que le flux à travers les sphingolipides est augmenté lorsque la SPT est localisé dans la membrane nucléaire interne. Ces résultats mettent en évidence un lien entre la localisation subcellulaire et l'homéostasie des sphingolipides.

Les connaissances sur le métabolisme et le transport des sphingolipides entre les organites intracellulaires sont incomplètes. Les sondes sphingolipides spécifiques aux organites nous permettent de déduire plus de détails sur le métabolisme et le transport des lipides. Dans cette étude, nous caractérisons des sondes en cage spécifiques aux vacuoles qui contiennent des sphingolipides pouvant être libérés par irradiation UV. Nous montrons que les sphingolipides libérés par irradiation UV sont métabolisés en espèces plus complexes. De plus, nous avons observé que l'épuisement des sites de contact entre le réticulum endoplasmique et la vacuole diminue la conversion métabolique et le transport des sphingolipides libérés par la vacuole. Nous avons également constaté que la surexpression de la protéine de site de contact Mdm1 qui élargit les contacts entre le réticulum endoplasmique et les vacuoles, augmente le transport et la conversion des bases sphingoïdes en céramides et en sphingolipides complexes. Dans cette étude, nous établissons une méthode pour étudier le transport des sphingolipides de la vacuole au réticulum endoplasmique *in vivo*.

Summary

Sphingolipids constitute a class of lipid compounds which carry out important structural and signaling functions in the cells. Baker's yeast, *Saccharomyces cerevisiae*, has been widely used in fundamental studies of sphingolipid metabolism due to genetic tractability and the high degree of evolutionary conservation between this unicellular eukaryotic organism and mammals. Serine palmitoyltransferase (SPT) and ceramide synthase (CS) catalyze initial steps of sphingolipid biosynthesis and are presumed to be enriched in different compartments of the endoplasmic reticulum. Using baker's yeast as a model system, we show in this study that fusing together catalytic subunits of serine palmitoyltransferase and ceramide synthase does not increase of sphingolipid biosynthesis suggesting that distance between the two enzyme complexes does not represent a limiting factor for sphingolipid anabolism. However, we also show that the flux through sphingolipids is increased when SPT is localized to the inner nuclear membrane. These results point out to a link between subcellular localization and sphingolipid homeostasis.

The knowledge on the metabolism and transport of sphingolipids between intracellular organelles is limited. Organelle specific sphingolipid probes allow us to infer more details about subcellular lipid metabolism and transport. In this study we characterize caged vacuole-targeted probes which contain sphingolipids that can be released by UV-irradiation. We show that UV-released sphingolipids are metabolized into more complex species. Furthermore, we observed that the depletion of contact sites between the endoplasmic reticulum and the vacuole decreases metabolic conversion and transport of sphingolipids released from the vacuole. We also found, that overexpression of contact site protein Mdm1 which expands the contacts between the endoplasmic reticulum and the vacuoles, increases transport and conversion of sphingoid bases into ceramides and complex sphingolipids. In this study we establish a method to investigate transport of sphingolipids from the vacuole to the ER *in vivo*.

Chapter 1: Introduction

Chapter 1.1: Regulation of sphingolipid metabolism in budding yeast

Cellular membranes play a vital role for the existence of cellular life as they form the border between the exterior and the interior of a cell and establish membrane-enclosed intracellular organelles. Most membranes are formed by a lipid bilayer, consisting of hydrophobic lipid tails opposing each other with their head groups located on the opposite sides facing the hydrophilic environments. Lipids make up about 40% of the dry mass of the membrane, while proteins comprise the remaining 50-60. Glycans, or polysaccharides attached to proteins or lipids may constitute 1-10% of the membrane's mass (1). Membranes proteins perform various functions: from selective passage of biomolecules and ions to molecular recognition and signal transduction. The bilayer-bases structural organization of membranes depend on lipids which are highly diverse biomolecules. This great diversity of lipid molecules is translated into a multitude of functions they perform at the subcellular, cellular and organismal levels (2). On the basis of their chemical composition lipids can be subdivided into three classes : glycerophospholipids, sphingolipids and sterols (3). Despite representing a minor fraction of total cellular lipids (~ 10%-20%) sphingolipids carry out important structural and signaling functions in the cell. Recent research progress in the field has identified roles for sphingolipids in the wide range of physiological processes such as apoptosis, autophagy, chemotaxis, inflammation, endocytosis (4–9).

The evolutionary importance of sphingolipids is supported by the conservation of many enzymes of sphingolipid metabolism between unicellular eukaryotic organisms such as the baker's yeast *Saccharomyces cerevisiae* and mammals (10). This feature of the yeast along with genetic tractability and the ease of handling make this unicellular fungus a model organism of choice for fundamental research in lipid biochemistry. Most enzymes and regulatory mechanisms of sphingolipid metabolism were first characterized in yeast and later described in mammalian cells, although there are some differences.

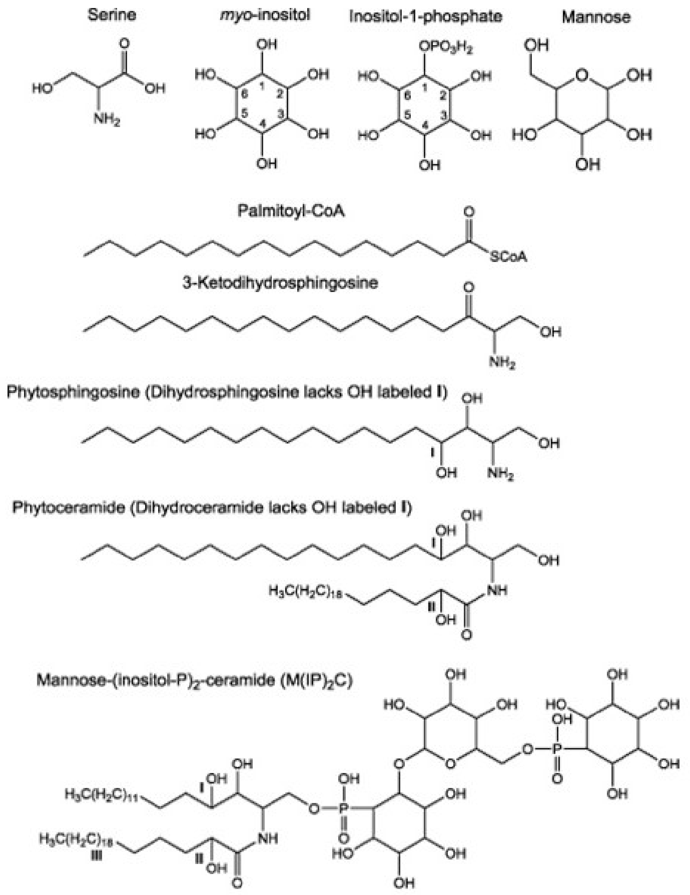

Figure 1. Chemical structures of selected yeast sphingolipid species and their precursors. Reproduced from http://lipidlibrary.aocs.org. The first committed step of sphingolipid biosynthesis begins with the condensation of serine and palmitoyl-CoA to form 3-ketodihydrosphingosine, which is subsequently reduced and hydroxylated into phytosphingosine. The latter is then acylated into phytoceramide. Ceramides are further glycosylated into complex sphingolipids by the addition of Inositol-1-phosphate and mannose molecules. The example of the most complex yeast sphingolipid - $M(IP)_2C$ (mannose di(inositolphosphoryl)ceramide is shown.

Overview of sphingolipid metabolism in *Saccharomyces cerevisiae*

Sphingolipid metabolic pathways in yeast have been well described with most enzymes having been identified and characterized. The schematic illustration of major metabolic routes and enzymes are depicted in Figure 2. The backbone of sphingolipids is formed by amino alcohols called sphingoid bases or long-chain bases (LCBs). Their formation is the rate-limiting step of sphingolipid biosynthesis and is accomplished by the condensation of a fatty acyl-CoA (preferentially palmitoyl-CoA) and an amino acid serine (Figure 1) by serine palmitoyltransferase (SPT) composed of 3 catalytic subunits Lcb1, Lcb2 and an auxiliary subunit Tsc3 in yeast (11–13). The reaction product, 3-ketosphinganine (Figure 1), is then reduced to C18-dihydrosphingosine (DHS) by 3-ketosphinganine reductase, Tsc10 (14). DHS can be hydroxylated by Sur2 into phytosphingosine (PHS) (Figure 1), the most abundant sphingoid base in yeast (15). Note, that the alternative widely used name for DHS is sphinganine (Sa). In order to be degraded, long-chain bases need to be phosphorylated at the C1 position, by lipid kinases Lcb4 or Lcb5 (16). Finally, LCB-1Ps are degraded by Dpl1 into ethanolamine phosphate and a fatty aldehyde (hexadecanal) (17).

The next major stage in sphingolipid biosynthesis is the N-acylation of long chain bases with a fatty acid to yield dihydroceramides. This enzymatic step is catalyzed by the enzyme complex Ceramide Synthase (CerS) consisting of two catalytic subunits Lac1, Lag1 and an auxiliary protein Lip1. Yeast CerS preferentially utilizes very long chain fatty acyl-CoA with 26 carbon atoms (18–20). N-acylation of dihydrosphingosine yields dihydroceramide (DHCs or Ceramides A), ceramides formed directly from PHS are called phytoceramides (PHCs or Ceramides B). Besides catalyzing hydroxylation of long-chain bases, Sur2 can also act on DHCs, converting them to PHCs (15). Both DHCs and PHCs can be further hydroxylated at the α(C2)-position of the fatty acyl forming α-hydroxyl-DHCs (Ceramides B' or DHC-B') or α-hydroxyl-PHCs (Ceramides C or PHC-C) (15). The letter classification of ceramide species – A,B,C,D – is based on the separation of species by thin layer chromatography (TLC) with the spots on top, or, in other words, having the highest retention factor Rf being assigned the letter A followed by species B,C and the lowermost spots being termed ceramides D. The D species have been identified as α-x-OH-PHCs where the fatty acyl chain is hydroxylated at an undefined position by a yet unknown enzyme which requires Cu^{+2}-transporting P-type ATPase Ccc2 for its function. It is still unclear whether Ccc2 performs a catalytic function, most likely enhancing hydroxylation as an auxiliary protein for a yet uncharacterized hydroxylase (21). A, B, C and D ceramides are then converted to complex sphingolipids that retain the letter designations of their precursors. Chemical structures of different classes of ceramides are shown in Figure 2.

The degradation of ceramides is catalyzed by two alkaline ceramidases Ypc1 and Ydc1, which have also been shown to possess an Acyl-CoA-independent ceramide synthase activity. Ceramidase have different substrate specificities so that PHC is a preferred substrate for Ypc1, DHC – for Ydc1 (21). Ceramides generated by the reverse activity of ceramidase in CerS-deficient yeast mutants have mostly C16 and C18 acyl chains (22).

Ceramides are further processed by Golgi-resident proteins Aur1 and Kei1, the former being the catalytic subunit, while the latter being required for the correct localization and proper functioning of the enzyme. Aur1 adds myoinositol phosphate onto the 1-hydroxyl group of ceramides forming Inositolphosphorylceramides (IPCs) (23). IPCs can then be mannosylated into mannosyl-inositolphosphorylceramides (MIPC) by the enzymatic complex consisting of 2 catalytic subunits Sur1, Csh1 and a regulatory subunit Csg2 (24). The terminal biosynthetic step in the yeast sphingolipid metabolism is the addition of one more myoinositol phosphate by the enzyme Ipt1, yielding mannosyl-diinositolphosphorylceramide (M(IP)2C) (Figure 1) (25). Complex sphingolipids make up about 10% of total lipids, whereas ceramides constitute a mere 0.1% (26, 27).

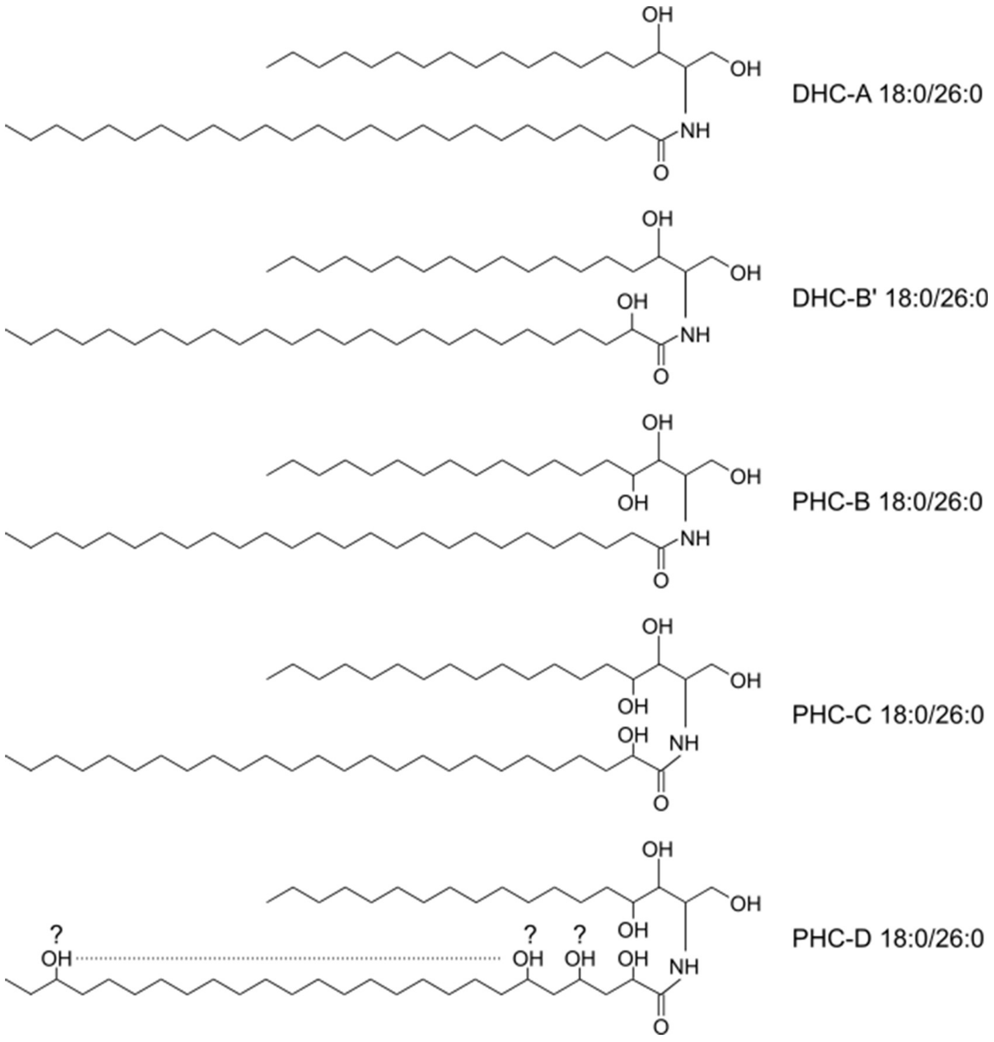

Figure 2. Chemical structures of different ceramide classes according to the ABC classification. The question mark denotes an undefined position at which the fatty acyl chain is hydroxylated in Class D ceramides.

Biosynthesis of long-chain bases and ceramides occurs in the endoplasmic reticulum (ER) while the subsequent enzymatic steps leading to the formation of complex sphingolipids take place in the Golgi (Figure 2). The movement of ceramide from the ER to the Golgi proceeds by both vesicular and non-vesicular mechanisms (22). Sphingolipid metabolism in *Saccharomyces cerevisiae* is schematically shown in Figure 3.

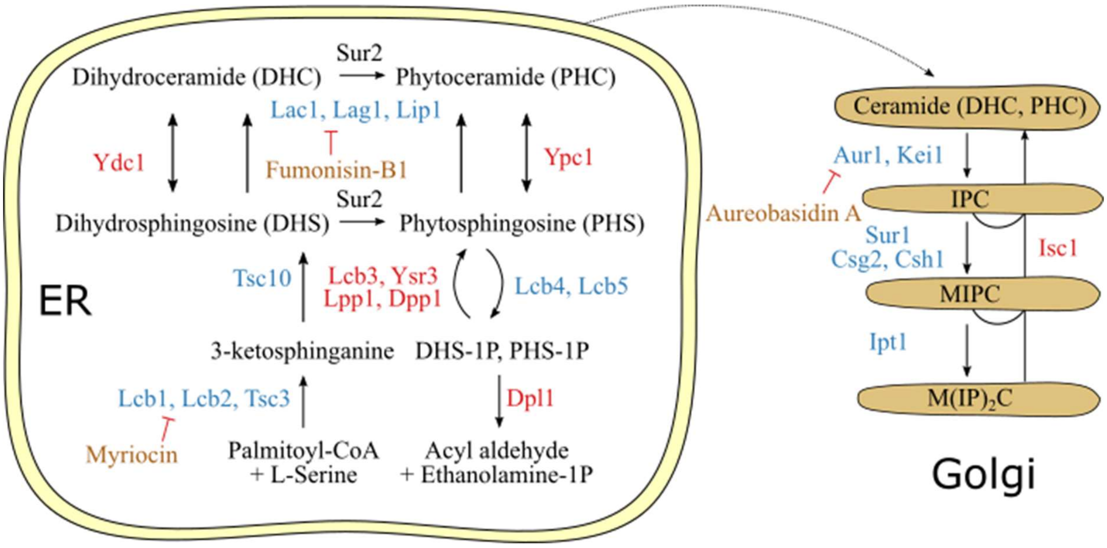

Figure 3. Schematic illustration of sphingolipid metabolism in *Saccharomyces cerevisiae*. Enzymes catalyzing biosynthetic reactions are shown in blue, those shown in red catalyze degradative steps, enzyme inhibitors are shown in brown.

Regulation of serine palmitoyltransferase activity

As free-living unicellular organisms, yeast cells are frequently challenged by environmental stresses such as extreme temperatures, pH, osmolarity or toxic compounds. Thus, yeast cells have been forced by evolution to develop multiple mechanisms aimed at adaptation to various conditions. Therefore, the composition of membrane lipids must be maintained in a precisely controlled manner.

Since the first committed step of *de novo* sphingolipid biosynthesis is catalyzed by SPT, this enzyme is subjected to rigorous regulation. Recent research has identified Orm proteins as major homeostatic regulators of SPT in yeast and mammalian cells. Yeast Orm family proteins Orm1 and Orm2 were found to form a complex with SPT subunits Lcb1, Lcb2 in co-immunoprecipitation experiments. Furthermore, *orm1Δorm2Δ* mutant cells had an almost 6-fold increase in long-chain base levels, pointing to an inhibitory role of the Orms. These transmembrane proteins have a cytosolically-exposed N terminus containing multiple serine residues serving as phosphorylation sites for multiple kinase regulators of Orm proteins (23).

Indeed, it was shown that treatment with a potent SPT inhibitor, myriocin, induced phosphorylation of the Orms. The extent of phosphorylation matched with the degree of SPT inhibition, highlighting that Orm proteins can fine-tune SPT activity. The seminal discovery of Orm-mediated regulation of SPT was followed up by several studies providing new details of how sphingolipid homeostasis is maintained in yeast cells. One of them showed that a kinase Ypk1 phosphorylated Orm1 and Orm2 on specific N-terminal phosphosites in response to sphingolipid depletion induced by the treatment with an SPT inhibitor myriocin (24). Ypk1 is a known substrate of TORC2, a multiprotein kinase complex that is involved in the organization of actin cytoskeleton, regulation of endocytosis. Moreover, the Ypk1-mediated homeostatic regulation of Orm proteins was dependent on Tor2, a core kinase of the TORC2 complex (25). Another study by Berchtold et al. characterized upstream regulators of TORC2-Ypk1 signaling cascade. In a series of elegant experiments, it was demonstrated that the re-localization of plasma membrane-bound proteins Slm1/2 from furrow-like sub-compartments called eisosomes into the TORC2-containing domain (MCT) led to TORC2-mediated by Ypk1 activation, subsequent Orm protein phosphorylation and the upregulation of sphingolipid biosynthesis. Furthermore, this signaling axis was not only activated by long-chain base depletion but was also triggered by stretching the plasma membrane either mechanically or by inducing hypo-osmotic shock (26). This research reveals a molecular mechanism of how sphingilipid metabolism is altered in response to environmental stimuli.

One of the most well-studied environmental stress is a rapid increase in temperature, commonly known as heat shock which entails global changes in gene transcription and protein translation. In addition, several studies showed that heat stress in yeast leads to a fast and pronounced upregulation of sphingoid base levels as early as 5 minutes after the switch from 24ºC to 39ºC (27–29). After the regulatory function of Orms was documented, Sun et al. showed that Orm2 was hyperphosphorylated as early as 90 seconds after switching culture temperature from 24ºC to 39ºC. As in the case of sphingolipid depletion, heat-triggered phosphorylation of Orm2 was

Ypk1-dependent. However, Ypk1 activation was dependent on kinases Pkh1/2 (30), which had previously been identified as upstream activators of Ypk1 (31). It was also shown that Orm2 phosphorylation gradually decreased over the course of heat shock returning to initial level after 10 min of heat stress. Members of the heterotrimeric phosphatase complex PP2A - Pph21, Pph22, Cdc55, Tpd3, were found responsible for Orm2 dephosphorylation. Therefore, the inhibition of SPT by Orm proteins can be reactivated, once the cells have adapted to the new environmental conditions (30). Orm proteins function as regulators of sphingolipid metabolism extends beyond responding to long-chain base levels, heat stress or membrane stretching. Orm2 mRNA and protein levels increase in response to ER stress in a calcineurin-dependent manner. Orm2 protein abundance has also shown to be upregulated upon induction of cell-wall stress. Under some conditions, like accumulation of complex sphingolipids in *isc1Δ* mutants, increased Orm2 might be needed to decrease the metabolic flux, reducing the amount of sphingoid precursors (32). Overall, Orm proteins appear to integrate multiple stress signals which affect membrane integrity and invoke a response from sphingolipid metabolic pathways.

Despite being paralogous proteins with a high degree of similarity, Orm1 and Orm2 appear to have some differences. Orm2 is considered to be a major protein in the couple due to higher abundance (30). Neither of the proteins is essential, the deletion of either of Orm1 or Orm2 does not significantly alter cell growth, while the double knockout *orm1Δorm2Δ* strain shows poor growth, ER stress, accumulation of long-chain bases (32, 33). This suggests that the Orms can functionally replace each other, which was demonstrated by almost complete dephosphorylation of Orm1 in *orm2Δ* cells and vice versa (34).

As has been mentioned, TORC2 regulates sphingolipid metabolism through Ypk1 and Orm proteins. However, in yeast there is another multiprotein complex termed TORC1, which has a different composition and, unlike TORC2, is sensitive to a macrolide antibiotic rapamycin. TORC1 has been extensively studied and appears to serve as a master regulator of cell growth, coordinating cell cycle according to the availability of nutrients. Nutrient depletion, or starvation inhibits TORC1 activity. Npr1 kinase is downstream substrate of TORC1 and is activated upon rapamycin treatment or nutrient limitation. Shimobayashi *et al* conducted a study where it was shown that Npr1 can directly phosphorylate both Orm1 and Orm2 on sites different from those used by Ypk1. Interestingly, TORC1-inhibition by rapamycin leading to the Npr1-dependent phosphorylation of the Orm proteins resulted in the upregulation of complex sphingolipids such as IPC and M(IP)$_2$C, but not long-chain bases. This mechanism was required for the sorting of general amino acid permease Gap1 to the plasma membrane stimulation of Gap1-mediated amino acid uptake. Therefore, starvation launched a homeostatic signaling cascade that led to the Orm-dependent increase in complex sphingolipid levels that in turn, resulted in the activation of nutrient uptake (35). Orm proteins ability to boost the production of complex sphingolipids without increasing long-chain base levels might arise due to the increased activity of ceramide synthase which has been shown to interact with Orm proteins (34). Although many molecular mechanisms of Orm protein regulation through phosphorylation have been characterized, it is still unclear how Orms exert their inhibitory action upon SPT. More details have been recently revealed underscoring the role of the first transmembrane domain of Lcb1 protein as a binding site for Orm proteins. Lcb1 without the first TM domain is functionally active but, unable to bind Orms, and is no longer regulated by them. Also, Orm proteins appear to induce SPT oligomerization and alter Lcb1 localization. Oligomer formation was shown to be induced by sphingoid bases which links SPT downregulation and oligomerization. The absence of TM domain caused Lcb1 to localize mostly to the nuclear ER (36) which is in line with an earlier observation that Orm2 re-localizes to the nuclear ER upon sphingolipid depletion with myriocin, when Orm2 activity is repressed (23). Another layer of Orm-dependent control of SPT activity has been very recently characterized. In both mammalian and yeast cells ceramide could inhibit SPT activity in isolated membranes (37). Taken together, Orm proteins serve as gatekeepers of sphingolipid metabolism, integrating multiple environmental signals and fine-tuning SPT activity to adapt to them.

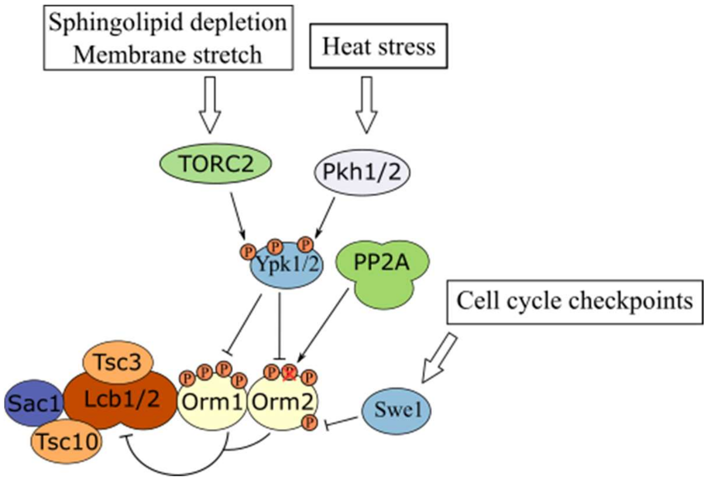

Figure 4. A scheme illustrating the regulation of yeast SPT complex via Orm proteins. Pointed arrows indicate activation, blunt-end arrows denote inhibition of Orm proteins.

SPT activity is not solely regulated by Orm1 and Orm2. Tsc3 is 80kD protein associated with Lcb1/2 catalytic subunits of SPT and, contrary to the Orms, is a positive regulator of SPT activity. *tsc3Δ* mutants exhibit decreased SPT activity and increased sensitivity to palmitoyl-CoA inhibition, which might be explained by the role of Tsc3 in mediating the interaction of substrates with SPT (13). A very recent study has identified a previously unappreciated role of Tsc3 in selecting amino acid substrate for long-chain base biosynthesis. Tsc3-deficient cells could not utilize alanine as a substrate to produce deoxy-sphingoid bases (38). In normal conditions deoxy-sphingolipids represent only a barely detectable minor fraction with their physiological function remaining enigmatic (39). Despite much progress achieved in the understanding of homeostatic regulation of SPT activity, the mechanistic details of Orm-mediated SPT inhibition are still missing.

Regulation of ceramide synthase activity

Ceramide synthase (CS) catalyzes the acylation of long-chain bases into ceramides. In yeast, Lac1 and its paralog Lag1 are catalytic subunits of CS. Lac1 and Lag1 yeast ceramide synthase subunits show different substrate specificity preferentially utilizing dihydrosphingosine or phytosphingosine, respectively (40). Most of yeast ceramides contain a very long fatty acyl chain C26, suggesting a substrate specificity towards elongated fatty acids (19). Both Lac1 and Lag1 proteins are integral membrane proteins having 8 membrane spanning domains and cytosolic N and C termini. The active site of CS is predicted to be embedded in the membrane (41). GFP-tagged Lac1 and Lag1 displayed localization in the ER, both nuclear and peripheral. However, GFP-tagging may significantly alter a protein's localization and the results should be taken with caution. Indirect immunofluorescence experiments suggest predominant localization in the nuclear ER (20).

There are a number of factors that can affect CS activity. CS catalytic subunits appear to be directly regulated by Lip1, a 28kD integral membrane protein associated with Lac1 and Lag1, which has been shown to be essential for CS activity in yeast. The deletion of *lip1* drastically downregulates ceramide biosynthesis and severely affects cell growth (20). Ceramide biosynthesis is dependent on substrate availability: long-chain bases and C26-fatty acyl-CoA. This means that ceramide production is influenced by a range of factors: fatty acid elongation, acyl-CoA synthesis and delivery.

Homeostatic maintenance of ceramide levels is crucial for the cell. Treatment of cells with an Aur1 inhibitor, Aureobasidin A, blocked IPC production and lead to ceramide upregulation, which was found to be toxic and cause cell growth arrest (42). Therefore, CS activity must be carefully regulated, analogous to SPT. So far 2 major mechanisms of CS regulation have been described. One of them involves the TORC2-Ypk1/2 signaling cascade. Lac1 and Lag1 were identified in a series of screens as Ypk1 substrates. It was further demonstrated that Ypk1 was capable of phosphorylating both CS subunits in their N-terminal cytosolic regions to elevate their activity. Ca^{2+}/calmodulin-dependent phosphatase calcineurin was found to dephosphorylate Lac1/Lag1. This mechanism was found to be stress-responsive, as Lac1/Lag1 were stimulated in response to heat stress. Finally, the Ypk1-triggered upregulation of CS activity was shown to be required for diverting metabolic flux from autophagy-inducing long-chain base phosphates (LCB-1Ps) to ceramides and complex sphingolipids. (43). Therefore, TORC2-Ypk1/2 kinases control sphingolipid metabolic flux in such a way, that there is no induction of autophagy in nutrient replete conditions and no toxic intermediates accumulate.

The other mechanism that impacts ceramide biosynthesis relies on a Cka2 casein kinase subunit. It was first noticed, that *cka2Δ* cells were hypersensitive to ceramide synthase inhibitors australifungin and fumonisin B_1 (44). Later, Cka2 was found to directly phosphorylate Lac1/Lag1 in the C-terminal parts, close to the dilysine ER-retrieval signal. Phosphorylation by Cka2 enhanced ceramide levels and was essential for Lac1/Lag1 function, since the mutant proteins lacking all 3 Cka2 phosphosites were unable to rescue *lac1Δlag1Δ* cells which could be explained by the aberrant localization as well as decreased stability (45). The results revealed the connection between Cka2-dependent phosphorylation and correct ER localization. While Ypk1-dependent regulation of Lac1/Lag1 is a homeostatic stimulation of ceramide production as a result of stress or sphingolipid depletion, Cka2 might be essential for basal activity of ceramide synthase. Detailed molecular mechanisms governing ceramide synthase regulation are still not well characterized and await further studies.

Sphingolipids as signaling molecules in yeast

The role of long-chain base sphingosine 1-phosphate as a signaling molecule in mammalian cells has been investigated in many cell types and physiological processes (46). In yeast sphingolipids, especially long-chain bases, have been linked to heat shock response. The amounts of yeast long-chain bases C18-DHS and C18-PHS increase 5-10 fold within 2-5 minutes of heat shock, while the minor species, C20-PHS, is elevated almost 100 fold (47, 48).

Interestingly, ceramide levels peak only after 20-30 minutes of heat shock (49). Heat-induced upregulation suggests a thermoprotective role for sphingolipids. This is consistent with the observation that the cells deficient for *de novo* sphingolipid biosynthesis are hypersensitive to heat stress (9, 50). Indeed, long-chain bases are required for the transcriptional induction of *TPS2*, a gene required for the biosynthesis of a thermoprotective sugar trehalose (49). Although sphingolipids are not necessary for the induction of major heat-shock genes, they are required for the re-initiation of protein translation, which is stalled upon heat shock (51). Sphingoid bases are also needed for the formation of p-bodies – stress-induced cytoplasmic granules sequestering mRNAs and RNA-interacting proteins (52, 53). It is assumed, that sphingolipids promote the return of mRNA associated with p-bodies back to translation to resume cell growth after initial adaptation to elevated temperatures. The major yeast long-chain base, phytosphingosine (PHS), is shown to facilitate heat-induced ubiquitin-dependent proteolysis of damaged proteins (50). All the evidence points out to the sphingolipids' exceptional role in the adaptation to heat stress, yet the exact molecular mechanisms are still unclear.

Chapter 1.2: Membrane contact sites in budding yeast

Maintaining distinctive lipid composition of eukaryotic organelles is of utmost importance for cell survival. The majority of thousands of lipid species are synthesized in the endoplasmic reticulum (ER) and have to be transported to various intracellular organelles. Movement of lipids can be mediated either by vesicular trafficking or non-vesicular transport. Serving as carriers for organelle-specific delivery of selected protein cargoes, vesicle membranes differ in lipid composition from the donor compartment thus carrying out a transport function. Secretory vesicles at the Trans Golgi Network (TGN) were found enriched in sterols and sphingolipids (54). A recent study also demonstrates that secretory COPII vesicles have a different lipid composition showing enrichment in lyso-phosphatidylinositol levels (55). Yet, the extent of intracellular transport and the lack of known vesicular carriers between certain organelles suggest alternative mechanisms. For example, the transport of sterols from the ER to the plasma membrane and vice versa was shown to be independent of vesicular trafficking (56, 57).

Early electron microscopy studies have revealed zones of close contacts between organelles (58–60). Despite discovery of inter-organelle contacts, their extent and physiological importance were not fully acknowledged until recently. The first hint of organelle contact site importance came from the finding that the membrane fraction from the crude rat liver mitochondrial preparation was required for phospholipid biosynthesis (61). In yeast, it was found that one of the ER subfractions established extensive contact area with the plasma membrane and the had a higher activity of particular phospholipid biosynthetic enzymes (62).

Membrane contact sites (MCSs) are defined as sites where the membranes of two organelles are found in close proximity to each other at the distance of 10 to 80 nm. MCS are formed by protein tethers that establish physical interaction bringing two opposing membranes closer to each other. Specific proteins populate the contact site, recruiting various effectors or carrying out specific functions (63). First contacts sites were mainly identified between the ER and other organelles since endoplasmic reticulum represents a branched extensive network of sheets and tubules. Presently, a range of various contact sites between organelles have been characterized, casting light onto an underestimated complexity of cellular architecture. Many of such contact sites were first described in yeast and later characterized in mammalian cells (64).

Nucleus-vacuole junctions (NVJs)

One of the most studied types of MCSs in *S. cerevisiae* are the nucleus-vacuole junctions between the nuclear ER and the vacuole - an acidic, membrane-delimited organelle with functions in storage and degradation. NVJs can be formed by the physical interaction between an outer nuclear ER membrane protein Nvj1 and a vacuole-resident protein Vac8 (65, 66). Vac8 is anchored in the vacuole membrane due to N-terminal myristoylation and palmitoylation (67). A hydrophobic sequence close to the N-terminus of Nvj1 sequesters the protein to the perinuclear ER (68). Crystal structures of the 2 bound proteins show that an extended loop of Nvj1 specifically binds a conserved groove formed from 12 armadillo repeats of Vac8 (66). Aside from Vac8, two other proteins have been found to be localized at the NVJs: Osh1 and Tsc13 (69, 70). Osh1 is a member of the oxysterol-binding protein (OSBP) family and implicated in non-vesicular lipid transport. Tsc13 is an enoyl-CoA reductase, an enzyme required for fatty acid elongation and biosynthesis of very-long-chain fatty acids. Both Osh1 and Tsc13 interact with Nvj1 (71, 72). What is the function of this assembly of proteins that make up the contact zone between the ER and the vacuole? It was noticed that at the stationary growth phase when the amount of nutrients is insufficient, some parts of the nuclear envelope were engulfed by the vacuole and subsequently degraded. The non-essential parts of the nucleus formed characteristic teardrop-like blebs. This organelle-specific degradative process was found to be independent of general autophagy and was termed the piecemeal microautophagy of the nucleus (PMN). PMN can be induced by the depletion of nitrogen or carbon source in growth medium or treatment with rapamycin. The PMN structures colocalize with NVJs and Nvj1 itself is degraded by the PMN (73). PMN depends on NVJ-resident proteins - Nvj1, Osh1, as well as VLCFA biosynthesis (71). NVJ are found in distinct microdomains in the vacuole membrane defined by a specific lipid microenvironment. Therefore, downregulation of VLCFA or sphingolipid biosynthesis disrupts the domain formation and likely affects NVJ integrity (74).

Nvj1-Vac8 interaction is not the sole tether mediating NVJ biogenesis. Recently, two more proteins – a ER membrane Mdm1 and its soluble paralog Nvj3, were found at the NVJs. While the localization of both Mdm1 and Nvj3 does not depend on Nvj1, a soluble Nvj3 is no longer exclusively found at the contact site in the absence of Mdm1. Mdm1 overexpression alone could induce hypertethering between the ER and the vacuole. Mdm1 can bind the vacuole membrane due to the presence of the lipid-binding PX domain, which preferentially interacts with phosphatidylinositol 3-phosphate (PI3P), a vacuole specific lipid species (75).

Another important physiological function of the NVJs was supported by the finding that lipid droplet formation occurs at the edges of the NVJs (76). Lipid droplets (LD) are ER-derived structures enclosed by a single phospholipid monolayer with the hydrophobic core of storage lipids, mainly triacylglycerides and sterol esters. Their formation is induced when the major carbon source, i.e. glucose, becomes limiting, stimulating cells to produce energy-rich lipids and store them in LDs for further re-utilization. Biogenesis of LD is not fully understood, as the site from which they originate was not clearly identified (77). The NVJ protein Mdm1 is a major coordinator of LD formation, it also interacts with fatty acid biosynthesis enzymes and fatty acid-CoA ligase Faa1, promoting conversion of free fatty acids into storage lipids (76). The ability of Mdm1 to initiate LD biogenesis is independent of other NVJ proteins. Chimeric Mdm1 redirected to the cell periphery away from the ER-vacuole contact sites could still stimulate LD formation (76, 78). N-terminal PXA domain of Mdm1 can bind neutral lipids and alone is sufficient to drive lipid droplet biogenesis (78). Accumulation of free fatty acid induces apoptotic cell death in yeast (79). Mdm1 can alleviate free fatty acid-induced lipotoxicity by providing an escape route to the neutral lipids that can be deposited in lipid droplets (78).

Another protein, Lam6 (previously termed Ltc1) was found to be localized at the ER-vacuole and ER-mitochondria contact sites and possess sterol transport activity *in vitro* due to the presence of the lipid binding GRAM and VAST domains. Also, when Lam6 targeting to mitochondria was disrupted it was exclusively found at the NVJs and its overexpression could induce the formation of ergosterol-rich domains in the vacuolar membrane normally occurring in stress conditions (80). Moreover, overexpression of Lam6 caused the expansion of contact areas between several types of interorganelle junctions, including NVJs (81). New studies are required to clarify the enigmatic nature of this protein.

A mounting body of evidence reveal more details about NVJs' protein composition and physiological importance. Undoubtedly, these contact sites are of big importance for interogranelle communication and lipid transport, but there is still much uncertainty with regards to the mechanistic understanding of those processes.

ER-mitochondria contact sites (ERMES)

Although the first evidence pointing to the close association between the ER and mitochondrial membranes came from studies in mammalian cells, the tethering complex between these two organelles was identified in a synthetic screen in *Saccharomyces cerevisiae* and termed ERMES which stands for ER-mitochondria encounter structure (82). The notion of the ER-mitochondria contact zone was appreciated before since it had been known that the biosynthesis of phosphatidylcholine (PC) necessitates the decarboxylation of phosphatidylserine (PS) into phosphatidylethanolamine (PE) by the enzyme Psd1 located in mitochondria followed by the transport of PE back to the ER where it could finally be converted to PC (83) – the most abundant class of phospholipids in yeast (84, 85). The generation of cardiolipins occurs in mitochondria but the synthetic precursors are made in the ER which would require ER-to-mitochondria lipid transport (86). Of note, mitochondria are not connected through vesicular trafficking to the endomembrane network which implies that lipid exchange must proceed through direct contact.

The ERMES complex consists of the ER transmembrane proteins Mmm1, cytosolic proteins Mdm12 and Mdm34, the outer mitochondrial membrane protein Mdm10 and associated proteins Gem1 and Tom7 (82, 87, 88). Crystal structures of Mmm1 and Mdm12 predict their ability to bind phospholipids conferred by the Synaptotagmin-like mitochondrial lipid-binding (SMP) domain (89–91). In spite of all this evidence, the cells lacking ERMESs do not observe drastic alteration of their mitochondrial lipidome and remain viable (82). The loss of ERMES or Gem1 did not alter ER-to-mitochondria transport of PS (92). These observations might be explained by the existence of bypass routes through the different contact sites formed by the ER. Experimental support of this hypothesis comes from the observation that the depletion of ERMES and *VPS13* renders cells inviable (93). Vps13 protein resides on endosomes and at the NVJs and has been shown to form mitochondria-vacuole contact sites known as vCLAMPs

(94, 95). Vps13 interaction with Mcp1 protein can compensate for the loss of ERMES (95). While the loss of ERMES does not alter phospholipid levels, the mutants lacking both ERMES and vacuole-mitochondria contact site protein Vps39, cause marked phospholipid imbalance with reduced amounts of PC and increased levels of PS which is indicative of aberrant lipid transport (96). Theoretical estimates of the number and lipid transport capacity of ERMES fall far below the estimated amounts of lipid molecules that need to be transferred between the ER and mitochondria (97). This suggests that there must be other proteins or multiprotein complexes that facilitate the bulk movement of lipids between the organelle membranes. The energetically unfavorable extraction of lipids from their host membrane may constitute a limiting factor for efficient lipid transport (98). Many details of lipid exchange between the ER and mitochondria are missing and are the subjects of intense research.

Vacuole-mitochondria contact sites (vCLAMPs)

The contacts between the vacuole and mitochondria are functionally linked with ERMES and become crucial for cell viability when ERMES complexes are depleted (93, 95, 99). Vps39 – a HOPS tethering complex subunit was identified in two independent studies as the vacuole-mitochondria contact site protein (96, 100). The interorganellar junctions required the interaction between Vps39 and vacuole-resident Rab GTPase Ypt7 and were named vCLAMPs (*v*a*c*uo*l*e *a*nd *m*itochondria *p*atch) (100). The extent and number of such contacts respond to metabolic state and are decreased in respiratory conditions and appear to be regulated through Vps39 phosphorylation (100). Vps39 is a soluble effector of Ypt7 and it became more clear when Vps39 was shown to interact with Tom40, an outer mitochondrial protein responsible for much of protein import into mitochondria (101). Vps39-Ypt7-Tom40 is not the sole complex mediating the contact site formation, the interaction between Vps13 and a mitochondrial protein Mcp1 marked distinct regions of vacuole-mitochondria junctions. Moreover, the overexpression of Mcp1 rescues ERMES mutants expressing vCLAMP-formation deficient Vps39, indicating the Mcp1-Vps13-dependent contacts are sufficient for supporting cell growth (101). It is likely that the role of vCLAMPS extends beyond a bypass route for ER-mitochondria lipid exchange, yet it has still not been demonstrated and remains to be rosolved.

ER-plasma membrane junctions

In yeast, the endoplasmic reticulum is subdivided into two subdomains: the perinuclear ER and the peripheral (cortical ER) interconnected by just a few tubules (102). The cortical ER is composed of tubules and fenestrated flat cisternae as revealed by 3D EM tomography (103).

About 40% of the cortical ER was found in contact with the plasma membrane making it the biggest heterotypic organelle contact zone in the yeast cell (62). Over the last yeast most proteins participating in ER-PM junction formation have been characterized. First, the human (vesicle-associated membrane protein–associated protein) VAP protein orthologs, Scs2 and Scs22 were shown to form contact sites and be involved in ER inheritance (104). Quantitative mass spectrometry analysis of proteins interacting with Scs2 and Sac1 identified three tricalbin proteins Tcb1-3 and Ist2 all of them showing cortical ER localization pattern (105). Ist2 is a multi-pass ER-transmembrane protein that binds plasma membrane phosphatidylinositolphosphate species PI(4,5)P2$_2$ through its polybasic domain thereby tethering ER to the PM (106, 107). Tricalbins are embedded in the ER membrane through their N-terminal hydrophobic region and contain SMP and Ca^{2+}-binding C2 domain (105). It has been shown that SMP domains of yeast ERMES proteins can promiscuously bind phospholipids (108). The yeast mutant strain lacking all mentioned ER-PM junction proteins (Tcb1-3, Scs2, Scs22, Ist2), Δtether, has a drastic reduction in the percentage of the cortical ER adhering to the plasma membrane from 40% to 4.8-5% (105). This reduction of the contact area between the ER and PM was even more pronounced, when in *ICE2* gene was deleted in Δtether cells (109). Ice2 is a an integral ER-membrane known to be required for maintaining cortical ER structure and ER inheritance (110). Collectively, these 7 proteins contribute to the formation of much of the ER-PM contact sites.

The most important role of the ER-PM contact sites is non-vesicular lipid transfer. Before the widely acknowledged function of membrane contact sites in lipid transport it was shown that a subdomain of the ER called plasma membrane associated membrane (PAM) had a higher PE and PI biosynthetic capacity (62). Opi3, an enzyme catalyzing last steps of *de novo* PC biosynthesis, requires ER-PM junctions for its activity (111). Like the other phospholipids, PS molecules are synthesized in the ER but chiefly found in the inner leaflet of the plasma membrane (112). Oxysterol-binding homology (Osh) proteins Osh6 and Osh7 facilitate transfer of PS to the PM. (113). The transfer proceeds via the exchange of PS molecules for PI4P (a plasma membrane lipid) carried out by the Osh proteins and driven by Sac1, a PI4P-phosphatase which maintains PI4P gradient (114). Other Osh proteins such as Osh2 and Osh3 are also targeted to the cortical ER via their FFAT motifs binding to Scs2/Scs22 proteins (115). Osh3, for example, regulates the activity of Opi3 and thus PC biosynthesis (111). In addition to perturbations in phospholipid levels, the yeast Δtether mutant showed decreased level of long-chain base and ceramide biosynthesis (116). All these studies indicate that ER-PM contacts are crucial for lipid homeostasis.

Sterols in yeast constitute ~40 mol% of total plasma membrane lipids and ER-PM crosstalk is important for sterol homeostasis (56).Disruption of the cortical ER contacts with the PM was shown to affect the delivery of exogenously supplied sterols to the ER (retrograde transport), while at the same time not causing defects in anterograde ER-to-PM sterol transport (109). Osh proteins are not essential for the retrograde trafficking of sterols since depleting all Osh protein-encoding genes in yeast slow down the transport just by 50%, suggesting other transport mechanisms (117). More recently, yeast proteins belonging to the StART superfamily (Steroidogenic Acute Regulatory transfer) have been characterized. These proteins Ysp2, Lam4, Lam1 and Sip3 are localized to punctate structures at the ER-PM junctions and their depletion slows down the transport of exogenously provided sterols (118). Moreover, two of these proteins, paralogous Ysp2 and Lam4 are downregulated via phosphorylation by the TORC2-dependent kinase Ypk1 which results in the increase of sterol pool in the plasma membrane (24). This mechanisms explains the increased amounts of sterols in the PM (manifesting in the increased sensitivity to ergosterol-binding drug Amphotericin B) observed in sphingolipid-depleting conditions (119). Previously, it was shown that sterols and sphingolipids are co-regulated and function together (120). It is becoming evident, that TORC2-Ypk1 signaling controls plasma membrane lipid homeostasis and ER-PM contact sites are important in these processes. Although many studies have demonstrated the prominent role of ER-PM junctions in phospholipid and sterol transport, the experimental approaches for investigating lipid transfer have their limitations and disadvantages. The mounting body of evidence proposes membrane contacts sites as major hubs for lipid non-vesicular lipid transport. Figure 5 illustrates yeast contacts sites and the principal proteins participating in organelle tethering.

Experimental tools to investigate membrane contacts sites

A range of various experimental approaches have been utilized to identify and characterize MCSs in yeast. In budding yeast, big genetic screens have been extensively utilized to uncover functions of poorly characterized proteins. Genetic screens have also been useful for finding proteins involved in organelle contact site formation. Mutagenesis screen helped identify ERMES, while the use of entire genome deletion sets led to the characterization of mitochondria-vacuole contact sites (82, 96). ER-PM and vCLAMP proteins were revealed by protein mass spectrometry techniques (100, 105).

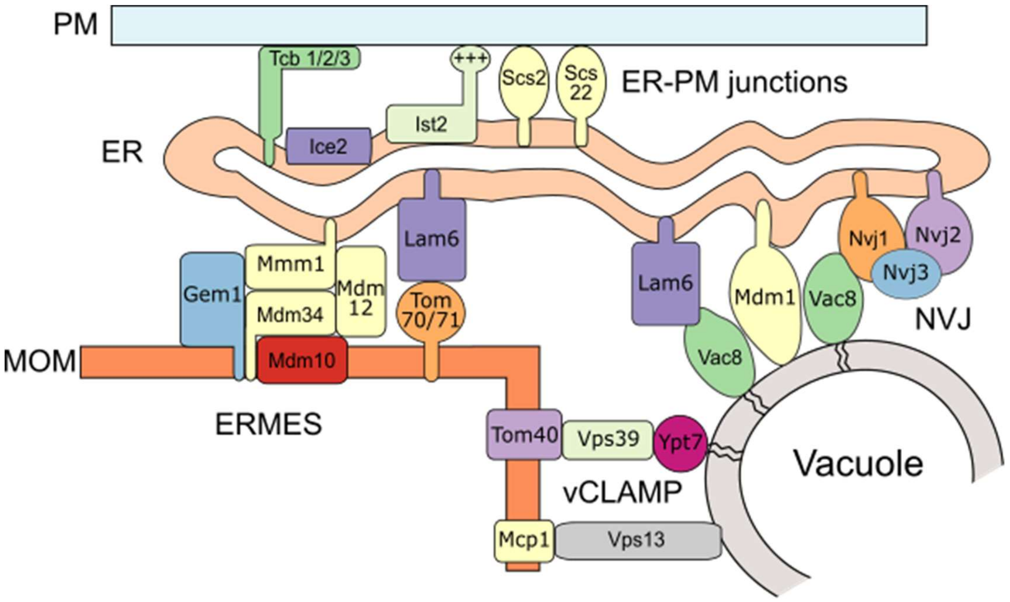

Figure 5. A scheme illustrating membrane contact sites in *Saccharomyces cerevisiae* and their membrane composition. PM – plasma membrane, ER – endoplasmic reticulum, MOM – mitochondrial outer membrane, ERMES – ER mitochondria encounter structure, vCLAMP -vacuole and mitochondria patch, NVJ – nucleus-vacuole junction.

Epifluorescence and confocal microscopy are routinely used to confirm the proximity of contact site-resident molecules, but the resolution is far too low to provide unbiased proof of organelle-contacts. Transmission electron microscopy provides an atomic resolution and is a preferred technique for the studies of organelle contact sites. Techniques such as proximity-labeling allow capturing proteins in vicinity to the contact zone which allows for a more detailed characterization of organelle junctions (121). Lipid transfer is thought to be the major function of organelle contacts. Hence, there is a need for experimental approaches that allow to track lipid metabolism across the membrane contact sites. In-vitro studies of lipid transport rely on purified proteins reconstituted into liposomes whose lipid composition is designed according to the experimental need. This, however, introduces a lot of biases such as non-native behavior of purified proteins, artificial lipid environment, the use of fluorescently labeled lipids with altered physico-chemical properties. Thus, *in vivo* studies help avoid these disadvantages, but conventional metabolic traces such as radioactive or heavy isotope-labeled lipids lack spatial and temporal resolution. That is where synthesized probes offer a great hope for lipid research in the context of organelle contact sites (122). One of the commonly used strategies relies on the chemical synthesis of a lipid biomolecule which is rendered inactive by its coupling to the so called “chemical cage”, such as coumarin, which can also serve as fluorophore. The active biomolecules are liberated from the “cage” by illumination with ultraviolet (UV) light and can be further metabolized or active signaling cascades (123). Further development led to the synthesis of organelle specific caged probes which could be efficiently targeted to the plasma membrane, mitochondria, or lysosomes (124–126). The chemical structure of one of the organelle-specific caged sphingolipid probes is illustrated in Figure 6.

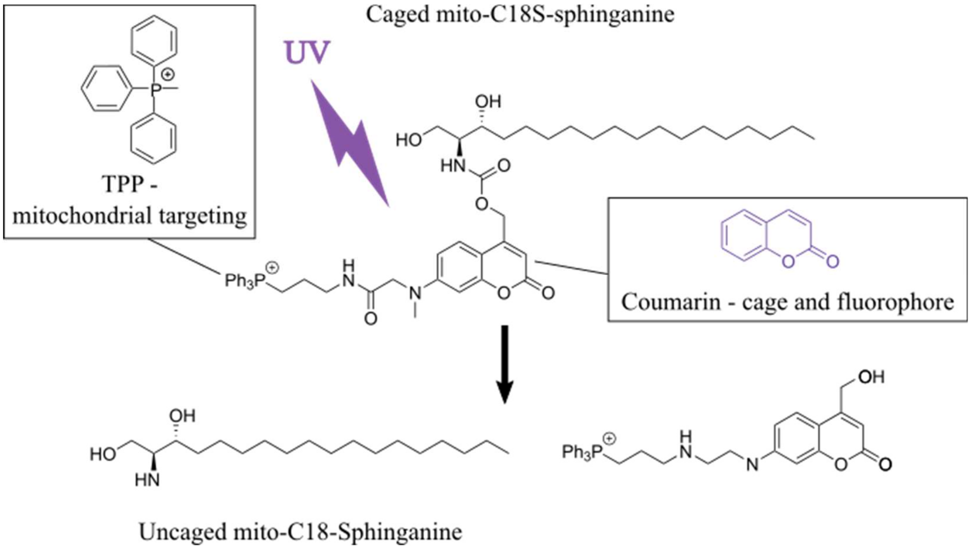

Figure 6. UV uncaging of C18-Sphinganine (partially adapted from (125). TPP - triphenylphosphonium.

Additional chemical modifications to lipid probes can endow them with more functions such as an ability to capture protein-lipid interaction or visualize the lipid’s localization by light or electron microscopy (127). So far, most of these chemical probes have been tested in mammalian cells in which they are efficiently internalized. The use of chemical probes may be limited in yeast cells, where ATP-binding cassette (ABC) transporter proteins pump out unwanted xenobiotics (128). Nevertheless, yeast cells can be genetically modified to reduce the activity of ABC transporters, which would allow to use the rapidly growing toolbox of functionalized lipid probes in this eukaryotic model organism (129)

Chapter 2: Materials and Methods

A list of yeast strains used in this study.

№	Name	Genotype	Source
	WT (BY4741)	*MATa his3Δ1leu2Δ0 met15Δ0 ura3Δ0*	EUROSCARF
	BY4741 lac1Δ	BY4741 *lac1::LEU2*	This study
	lac1Δ-Fus	BY4741 *lac1::KanMX6 LCB1pr-LCB1-LAC1-ADH1term::HIS3*	This study
	lac1Δpep4Δ-Fus	BY4741 *lac1::KanMX6 lag1::LEU2 pep4::URA3 LCB1pr-LCB1-LAC1-*	This study
	lac1Δlag1Δ	BY4741 *lag1::KanMX4 lac1::LEU2* + pRS416- *LAG1pr-LAG1-LAG1term*	This study
	Lcb1-Lag1-Fus	BY4741 *lag1::KanMX4 lac1::LEU2 LCB1pr-LCB1-LAG1-LAG1term::HIS3*	This study
	Lcb2-Lag1-Fus	BY4741 *lag1::KanMX4 lac1::LEU2 LCB2pr-LCB2-LAG1-LAG1term::HIS3*	This study
	lac1Δlag1Δ-GFP-LAC1	BY4741 *lac1::KanMX4 lag1::HphMX4 GFP-LAC1:: NATMX4*	This study
	lac1Δlag1Δ-GFP-LAC1-IST2	BY4741 *lac1::KanMX4 lag1::HphMX4 GFP-LAC1-IST2::NATMX4*	This study
	orm1Δorm2Δ	BY4741 *orm1::HphMX4 orm2::KanMX4*	This study
	orm1Δorm2ΔGFP-ORM2	BY4741 *orm1::HphMX4 rm2::KanMX4 GFP-ORM2::NATMX4*	This study
	orm1Δorm2ΔGFP-Heh2-ORM2	BY4741 *orm1::HphMX4 orm2::KanMX4 GFP-Heh2-*	This study
	LCB1-mCherry	BY4741 *LCB1-mCherry::HIS3*	This study
	orm1Δorm2ΔGFP-ORM2 LCB1-mcherry	BY4741 *orm1::HphMX4 Orm2::KanMX4 GFP-*	This study
	orm1Δorm2ΔGFP-Heh2-ORM2 LCB1-mCherry	BY4741 *orm1::HphMX4 orm2::KanMX4 GFP-Heh2-*	This study

	orm1Δorm2ΔGFP-ORM2 LCB2-mcherry	BY4741 *orm1::HphMX4 orm2::KanMX4 GFP-*	This study
	orm1Δorm2ΔGFP-Heh2-ORM2 LCB2-mCherry	BY4741 *orm1::HphMX4 orm2::KanMX4 GFP-Heh2-*	This study
	Sac1-mCherry GFP-ORM2	BY4741 *orm1::HphMX4 orm2::KanMX4 GFP-*	This study
	Sac1-mCherry GFP-Heh2-ORM2	BY4741 *orm1::HphMX4 orm2::KanMX4 GFP-Heh2-*	This study
	LCB1-mCherry LAC1-Ist2	*lac1::KanMX4 lag1::HphMX4 GFP-LAC1-Ist2::NATMX4 LCB1-*	This study
	LCB1-Heh2-mCherry LAC1-Ist2	*lac1::KanMX4 lag1::HphMX4 GFP-LAC1-Ist2::NATMX4 LCB1-Heh2-*	This study
	Vph1-mCherry	BY4741 *VPH1-mCherry::HIS3*	This study
	Mdh1-mCherry	BY4741 *MDH1-mCherry::KanMX4*	Howard Riezman lab
	Nup49-mCherry	BY4741 NUP49-*mCherry::HIS3*	This study
	rsb1Δpdr5Δ	BY4741 *rsb1:KanMX4 pdr5::NATMX4*	This study
	ypc1Δ	BY4741 *ypc1::NATMX4*	This study
	ypc1Δydc1Δ	BY4741 *ypc1::NATMX4 ydc1::KanMX4*	This study
	pep4Δ	BY4741 pep4*::URA3*	This study
	SEY6210 WT	*MATα leu2-3,112 ura3-52 his3Δ200 trp1- Δ901 lys2-801 suc2Δ9*	Scott D. Emr lab
	mdm1Δ	SEY6210 *mdm1::KanMX*	Scott D. Emr lab
	mdm1Δ nvj3Δ nvj1Δ nvj2Δ	SEY6210 *mdm1Δ::KanMX nvj3::NATMx nvj1::TRP1 nvj2::HIS3*	Scott D. Emr lab
	RH431 WT	*MATa his4 leu2 ura3 bar1*	Howard Riezman lab
	RH3334 end3Δ	*MATa his4 leu2 bar1 END3::URA3*	Howard Riezman lab
	fat1Δ	BY4741 *fat1::NATMX4*	This study

	faa1Δfaa4Δfat1Δ	BY4741 *fat1::NATMX4 faa1::KanMX4 faa4::HIS3*	This study

Bacteria strains:

DH5α (NEB® 5-alpha Competent E. coli, NewEnglandBiolabs)

Plasmids

Plasmid	Characteristics	Source
pRS305N	Vector for genome integration at the *LEU2* locus	Taxis, C., and Knop, M. (2006)
pAG25	Vector for a PCR-based gene deletion marker NATMX4	Goldstein, A. L., and McCusker, J. H. (1999)
pAG32	Vector for a PCR-based gene deletion marker HPHMX4	Goldstein, A. L., and McCusker, J. H. (1999)
pFA6a-HIS3MX6	Vector for a PCR-based gene deletion, *HIS3* marker	Longtine, M. S et al. (1998)
pRS305	Vector for a PCR-based gene deletion, *LEU2* marker	Sikorski, R. S., and Hieter, P. (1989)
pRS306	Vector for a PCR-based gene deletion,*URA3* marker	Sikorski, R. S., and Hieter, P. (1989)
pFA6a-link-mCherry-SpHis5	Vector for C-terminal mCherry tagging	Kurt Thorn lab
pFA6a-Lac1	Vector for tagging with *LAC1*	This study
pFA6a-Lag1	Vector for tagging with *LAG1*	This study
pBP73G-Mdm1-GFP	Overexpressed Mdm1-GFP	Henne et al. (2015)
pRS416-LAG1	*LAG1* (N-term., Myc-tagged), endogenous promoter and terminator	Kageyama-Yahara, N et al. (2006)
pRS416-ADH1-LAC1	*LAC1,* ADH1 promoter, CYC1 terminator	This study
pRS305N-sfGFP-LAC1	Integrative vector bearing sfGFP-Lac1, endogenous promoter and terminator	This study

pRS305N-sfGFP-LAC1-Ist2	Integrative vector bearing sfGFP-Lac1-Ist2(878-946), endogenous promoter and terminator	This study
pRS305N-sfGFP-ORM2	Integrative vector bearing sfGFP-ORM2, endogenous promoter and terminator	This study
pRS305N-sfGFP-heh2-ORM2	Integrative vector bearing sfGFP- Heh2(93-317)-Orm2, endogenous promoter and terminator	This study
pFA6a-Heh2-mCherry	Vector for tagging containing INM targeting signal of Heh2	This study

Antibodies

αLCB1, αLCB2 (rabbit, polyclonal) – from Teresa Dunn-Giroux lab.

Yeast media:

1. YPUAD: 2% glucose, 1% yeast extract, 2% Bacto™ Peptone 2%, 10 mM MES (2-ethanesulfonic acid), 2% agar, 40 mg/l adenine and uracil, pH = 6.0

2. SD: 2% glucose, 0.67% Yeast Nitrogen Base (without amino acids, with ammonium sulfate), 1.92 g/l amino acid supplements, 2% agar, Na_2HPO_4 10 mM, KH_2PO_4 40 mM, pH = 6.0

3. SD-5-FOA: 2% glucose, 0.67% Yeast Nitrogen Base (without amino acids, with ammonium sulfate), 1 g/l 5-Fluoroorotic acid, 60 mg/l uracil, pH = 3.5.

4. YPUAG: 2% glycerol, 1% yeast extract, 2% Bacto™ Peptone 2%, 10 mM MES (2-ethanesulfonic acid), 2% agar, 40 mg/l adenine and uracil, pH = 6.0

5. Low fluorescence medium (LFM): 2% glucose, 6.7 g/l Yeast Nitrogen Base (without riboflavin and folic acid: (5g/l$(NH_4)_2SO_4$, 1g/lKH_2PO_4, 0.5 g/l $MgSO_4$, 0.1 g/l NaCl, 0.1 g/l Ca_2Cl, 0.5 mg/l H_3BO_4, 0.04 mg/l $CuSO_4$, 0.1 mg/l KI, 0.2 mg/l $FeCl_3$, 0.4 mg/l $MnSO_4$, 0.2 mg/l Na_2MoO_4, 0.4 mg/l $ZnSO_4$, 2μg/l biotin, 0.4 mg/l calcium pantothenate, 2 mg/l inositol, 0.4 mg/l niacin, 0.2 mg/l PABA, 0.4 mg/l pyridoxine HCl, 0.4 mg/l thiamine), 1.92 g/l amino acid supplements, Na_2HPO_4 10 mM, KH_2PO_4, 40 mM, pH = 6.0

Chemicals and reagents

Yeast media were prepared from the following reagents: Glucose monohydrate, ammonium molybdate and ascorbic acid were from Merck (Darmstadt, Germany), Bacto Peptone, Bacto yeast extract, Bacto agar were purchased from BD Biosciences (Sparks, MD); Yeast synthetic drop-out amino acid supplements were from Sigma-Aldrich (St. Louis, MO); amino acids uracil, adenine were from Sigma-Aldrich, histidine, ammonium acetate were from Fluka (Steinheim, Germany), 5-Fluoroorotic acid was from USBiological (Salem, MA). Trichloroacetic acid, pyridine, monomethylamine were all from Sigma-Aldrich; ammonium hydroxide, n-Butanol, Diethyl ether, LC-MS-grade chloroform were all from Acros (Geel, Belgium); LC-MS-grade water, methanol were purchased from J.T. Baker (Loughborough, United Kingdom); analytical grade ethanol and methanol were from Fischer Chemical (Basel, Switzerland). All internal lipid standards used for sphingolipid and phospholipid analysis as well as sphingolipid metabolic tracers - C17Phytosphingosine and C17Sphinganine, were purchased from Avanti Polar Lipids (Alabaster, AL). Caged chemical probes were synthesized as described in (Feng, S., et al, 2018) and 10 mM stock solutions were dissolved in DMSO. Heavy isotope-labeled (2,3,3-D3) L-Serine was from Cambridge Isotope Laboratories Inc. (Tewksbury, MA).

Experimental procedures

Yeast strain construction

Yeast strains were constructed using standard techniques based on homologous recombination of PCR-generated linear fragments (Longtine et al. 1998). Gene deletions were verified by colony PCR, correct insertion of cassettes encoding fluorescent tags was checked by sequencing. All genetic modifications of yeast strains were carried out using a standard lithium acetate-ssDNA-PEG transformation protocol (Gietz, D. R., and Woods, R. A., 2002). For integration of sequences into the yeast genome, integrative plasmids were used (Taxis, C., and Knop, M., 2006).

Molecular cloning

Chimeric proteins were constructed using Gibbson Assembly kits (NEB, Ipswitch, MA) following the manufacturer's protocols. For fusion protein construction *LAC1* or *LAG1* sequences including ORF and terminator were PCR amplified using Q5 High Fidelity Polynerase (NEB, Ipswitch, MA) followed by the second PCR amplification with the primers containing 50 base-pair homology sequences flanking the desired insertion sites (immediately upstream of stop codons in *LCB1* or *LCB2*).

Yeast spot assay

Yeast cells were grown overnight to saturation in liquid YPUAD medium. Next day, 10-fold serial dilutions were prepared in double distilled water starting from OD_{600} of 1. Cells suspensions were then transferred onto agar plates using a 48-slot pin replicator. Droplets of transferred suspensions were completely dried at room temperature, plates were placed in an incubator and grown for 2 days at 30ºC.

Yeast growth recordings

Yeast cells grown overnight in liquid YPUAD or YPUAG were diluted to $OD_{600} = 0.1$ in the same medium, 200 µl of cells suspensions were put into flat-bottom 96-well plates. The plate was sealed with gas permeable moisture barrier seal (4titude) and absorbance at a wavelength of 600 nm (OD_{600}) was recorded every 10 minutes over the period of 17 or 25 hours at 30ºC, using a plate reader (Biotek™ Synergy™ H1, BioTec Instruments, Winooski, VT).

Western blotting

Yeast cells were grown in rich medium (YPUAD) to the log phase (OD_{600}~1). 10 OD_{600} units were collected. Cells were resuspended in 100 µl of TNE buffer (50 mM Tris-HCl pH7.5, 150 mM NaCl, 2 mM EDTA, 1 mM PMSF, 1X Protease Inhibitor Cocktail (Roche, Switzerland)), disrupted with glass beads by vortexing, resuspended in 2X Sample Buffer (100 mM Tris-HCl pH6.8, 4% w/v SDS, 0.2% bromphenol blue, 200 mM β-mercaptoethanol) and boiled at 50ºC for 10 minutes. Protein extracts were subjected to SDS-PAGE, transferred onto a nitrocellulose membrane, probed with rabbit polyclonal antibodies against yeast Lcb1 or Lcb2 and imaged with the Fusion FX system (Vilber Lourmat, Collegien, France).

Fluorescence microscopy

Cells were grown in YPUAD or selective SD medium to the exponential phase, washed and resuspended in low-fluorescence medium (LFM). 15 µl of cells suspension were applied onto Concanavalin-A pre-treated glass slides and incubated at room temperature for 5 min. The unattached cells were gently aspirated, the slides were covered with a coverslip and sealed with nail polish. The samples were imaged with LSM700 Zeiss confocal microscope using a X100 oil immersion objective.

Vacuole staining with FM™ 4-64

Cells grown to the early exponential phase were incubated with 8 µM FM™4-64 (Thermo Fisher) for 30 min at 30°C, washed twice in YPUAD, resuspended in fresh medium and further incubated for 30 minutes to allow the dye to be internalized.

Labeling with synthetic chemical probes

Yeast cells were grown in YPUAD or SD medium to the logarithmic phase, labeled with 10 µM caged mito-LCBs for 20 minutes at 30°C, centrifuged at 800g, resuspended in LFM medium and processed for imaging as described above.

In vivo D3-Serine labeling

Heat shock induction

Yeast cells were grown in SD medium without serine until the OD_{600}=1, cultures were labeled with 1 mM D3-L-Serine for 5 minutes. Then, heat-shock was induced by transferring yeast cultures to water bath (Adolf Kunher, Birsfelden, Switzerland) set at 40°C. After incubation for indicated time periods, samples were collected by adding TCA to 5% (vol/vol) and frozen at -80°C.

D3-Serine labeling

Yeast cells were grown in SD medium without serine until the OD_{600}=1, cultures were labeled with 1 mM D3-L-Serine for the indicated time period (30 min or 1 hour) followed by sample collection using a TCA protocol.

UV uncaging experiments

Uncaging experiments were carried out using a 1000-Watt Arc Lamp Source (NewPort) supplied with a 350-450 nm dichromic mirror. Cells were cultured in rich or selective medium to the exponential phase. Following the incubation with 10 µM caged probes at 30°C, cells were washed three times with ddH_2O at 4°C, resuspended in 2 ml cold culture medium and placed under the arc lamp source at a distance of 20 cm, on ice. The samples were irradiated for 2 min at 1000 Watt and were either resuspended in larger volume of medium for incubation at 30°C for 20, 40, 60 min, or immediately collected and processed for lipid extraction.

Lipid analysis

Sample collection

Yeast cell cultures were grown in YPUAD or SD medium to the logarithmic growth phase. Cell metabolism was stopped by transferring cell suspensions into a tube containing 100% TCA (trichloroacetic acid) to the 5% final. Samples placed on ice were incubated for at least 10 min, centrifuged at 800 g for 5 minutes, washed in 5% TCA, centrifuged again and re-suspended in 5 ml ice-cold ddH_2O. The amount corresponding to 25 OD_{600} units was transferred into glass tubes, centrifuged at 800 g, supernatant was completely removed and the pellets were frozen at -80°C for subsequent lipid extraction.

Lipid extraction

The extraction procedure was performed as described in (Guan, X et al. 2009) with minor modifications. First, a mix containing internal lipid standards (7.5 nmol 17:0/14:1 PC, 4.0 nmol 17:0/14:1 PS, 6.0 nmol 17:0/14:1 PI , 7.5 nmol 17:0/14:1 PE, 1.2 nmol C17 ceramide and 2.0 nmol C8 glucosylceramide (C8GC)) was added to the cell pellets together with 1.5 ml of extraction solvent (H_2O, ethanol, diethyl ether, pyridine, 4.2 N NH_4OH 15:15:5:1:0.018) and 500 μl glass beads. Cells were disrupted by vigorous vortexing on a multivortexer (Labtek International, Christchurch, New Zealand) for 6 minutes at room temperature, followed by the incubation at 60°C for 20 minutes. After centrifugation at 800 g, the supernatant was transferred to fresh 13 mm glass tubes. Then, the extraction procedure was repeated. Supernatants from the two rounds of extraction were combined and split into 2 equal aliquots: for glycerophospholipid and sphingolipid analysis. The extracts were dried either under the flow of N_2 at 80°C or vacuum in a CentriVap (Labconco, Kansas City, MO), flushed with nitrogen glow and stored at -80°C unless proceeded for further steps. The fractions for sphingolipid analysis were subjected to mild alkaline hydrolysis to deacylate glycerophospholipids that might cause ion suppression. For this the dried samples were re-suspended by sonication in 1 ml monomethylamine reagent (methanol, H_2O, *n*-butanol, methylamine 4:3:1:5 vol/vol/vol), incubated at 53°C for 1 hour, dried and frozen. Finally, sample desalting was accomplished by *n*-butanol extraction. Dried samples were re-suspended in 300 μl water-saturated *n*-butanol followed by addition of 150 μl of LC-MS-grade water. In order to induce phase separation, the samples were centrifuged at 3200 g for 10 minutes at 20°C, the upper phases were collected. The desalting procedure was repeated twice, the combined extracts were dried and frozen at -80°C.

Mass spectrometry

For the mass spectrometry analysis the dried samples were resuspended by sonication in 500 µl of LC-MS-grade chloroform:methanol (1:1, vol/vol) followed by dilution in chloroform:methanol:water (2:7:1, vol/vol/vol) or in chloroform:methanol (1:2, vol/vol) containing 5 mM ammonium acetate for positive or negative mode MS analysis, respectively. The samples containing sphingolipids were diluted 1:20 (vol/vol), samples for phospholipid analysis were diluted 1:100 (vol/vol). Using glass syringes (Hamilton Company, Bonaduz, Switzerland) lipid mixtures were transferred into wells of a 96-well plate which was sealed with an aluminum foil before MS analysis. Samples were injected into the TSQ Vantage Triple Quadrupole mass spectrometer (ThermoFisherScientific, Waltham, MA) equipped with the TriVersaNanomate - automated chip-based electrospray ionization platform (Advion Bioscience, Ithaca, NY). Samples were injected at a gas pressure of 30 psi with a spray voltage of 1.2 kV and run on the mass spectrometer operated with a spray voltage of 3.5 kV for positive mode and 3.0 kV for negative mode and a capillary temperature set at 190°C. Phospholipid and sphingolipid species were identified and quantified using multiple reaction monitoring (MRM). Each lipid species was quantified using standard curves created of for internal standards. Data analysis was performed using R language.

Phosphate measurement

Total lipid extracts were re-suspended in 500 µl of LC-MS-grade chloroform:methanol (1:1, vol/vol), 50 µl were transferred into Pyrex tubes and dried. Different amounts of standard solution of 5 mM KH_2PO_4 were prepared for the standard curve. 140 µl of perchloric acid (70%) and 20 µl of water were added to the dried lipids and standards and the tubes were incubated in a heating-block at 100°C for 1h in a fume hood. Tubes were cooled for 5 min at RT and a 800 µl of freshly-prepared reagent solution (water:1.25% ammonium molybdate:1.67% ascorbic acid, 5:2:1, vol/vol) was added and the samples were heated at 180°C for 5 min. After cooling at RT, 100 µl was used to measure absorbance at 820 nm.

Sphingoid base measurement (Metabolomics)

Sample collection

For the measurement of intracellular metabolites yeast cells were grown in rich or SD medium and collected at the exponential phase (OD_{600} ~ 1.2-1.5). Samples subjected to heat-shock treatment at 40°C or control samples incubated at 24°C were rapidly cooled to 10°C by placing the samples into dry ice-ethanol bath for 25 or 15 sec, respectively. After rapid cooling the cells were placed on ice. Sample subjected to UV uncaging were kept on ice throughout the whole procedure and immediately processed after UV irradiation. Cells were collected by centrifugation at 1000g for 2 min at 0°C, washed in 5 ml ice-cold water then re-suspended in 1 ml od water. The amount corresponding to 5 OD_{600} units was transferred to 2ml screw-cap tubes, cells were pelleted at max speed for 1 min and the supernatant was completely removed. The pellets were flash-frozen in liquid nitrogen and stored at -80°C.

Extraction and derivatization

To analyze yeast long-chain bases, 150 µl of extraction solvent (water, ethanol, diethyl ether, pyridine, 4.2 N ammonium hydroxide 15:15:5:1:0.018, vol/vol) together with a mix of internal standards (0.04 nmol of C17 sphinganine, 0.04 nmol of C17 Phytosphingosine, 0.4 nmol of C17 sphinganine-1-phosphate) and 100 µl of Zirconium oxide beads (Bertin Technologies, Montigny-le-Bretonneux, France) were added to cell pellets. Cells were disrupted in a cryolysis breaker (Bertin Technologies) at 0°C, incubated for 20 min on ice and centrifuged at 14000 rpm for 2 min at 0°C. Supernatants were collected and 150 µl of extraction solvent were added again followed by brief vortexing and centrifugation. The supernatants from the two extraction steps were combined and centrifuged at 14000 rpm for 2 min at 0°C to remove the residual debris. The extracts were then transferred into 250 µl glass inserts (Interchim, France) which were placed inside amber glass tubes. Finally, the samples were vacuum-dried in CentriVap. In the next step, a mixture consisting of 70 µl borate buffer (200 mM boric acid pH 8.8, 10 mM tris(2-carboxyethyl)-phosphine, 10 mM ascorbic acid and 33.7 mM $^{15}N^{13}C$-valine), and 10 ml of formic acid solution (0.1%in water) was derivatized by the reaction with 20 µl AQC (6-aminoquinolyl-N-hydroxysuccinimidyl carbamate) solution (2.85 mg/ml in acetonitrile) at 55°C for 15 min. After that the samples were incubated overnight at 24°C.

LC-MS/MS

AQC-derivatized samples were analyzed by LC-MS/MS using an Accela-HPLC system coupled with a TSQ Vantage Triple Quadrupole mass spectrometer (Thermo Fisher Scientific). Selected metabolites were detected in a multiple reaction monitoring setup. Signals were normalized by the corresponding internal standards.

Chapter 3: Results

Chapter 3.1: The role of serine palmitoyltransferase and ceramide synthase localization in controlling flux through sphingolipids

The endoplasmic reticulum is an interconnected network of tubules and cisternae with the shared lumen (130). One part of the ER network is the nuclear ER which surrounds the nucleus and is connected with the nuclear membrane forming the structure called the nuclear envelope (NE). The other part is the peripheral ER composed of tubules and cisternae which in yeast makes extensive contacts with the plasma membrane (131). In *S. cerevisiae,* both SPT and ceramide synthase (CS) localize to the endoplasmic reticulum. However, CS is enriched in the nuclear ER, while SPT complex is found in the cortical as well as in the nuclear ER (20, 132). We hypothesized that SPT and CS might be separated by a diffusion barrier, which may be crucial for homeostatic regulation, as both sphingoid base precursors and ceramides are toxic when accumulated. Bringing together the two enzymatic complexes may thus result in accelerated metabolic flux from sphingoid base precursors into ceramides.

Construction and characterization of SPT-CS fusion proteins

Lcb1-Lac1 fusion protein is partially degraded in the vacuole

To test this assumption, chimeric fusion proteins composed of SPT components Lcb1/Lcb2 and catalytic subunits of CS, Lac1/Lag1 were constructed. Linear PCR-amplified fragments containing *LAC1* or *LAG1* genes with their terminator sequences were integrated into the site just before the stop codon of *LCB1* or *LCB2* via homologous recombination (Figure 7, A). Lcb1-Lac1 fusion protein was not stable, additional bands indicate cleavage of the chimeric protein (Figure 7, B). Indeed, the fusion protein is partially degraded in the vacuole, since the protein was more stable when expressed in the strain with no vacuolar proteinase activity due to the deletion of *PEP4* gene (Figure 7, C). Ceramides and MIPC levels are reduced in the cells expressing the unstable chimeric protein (Figure 7, D) compared to the wild type yeast. Altogether, the evidence suggests that Lcb1-Lac1 protein is not sufficiently functional.

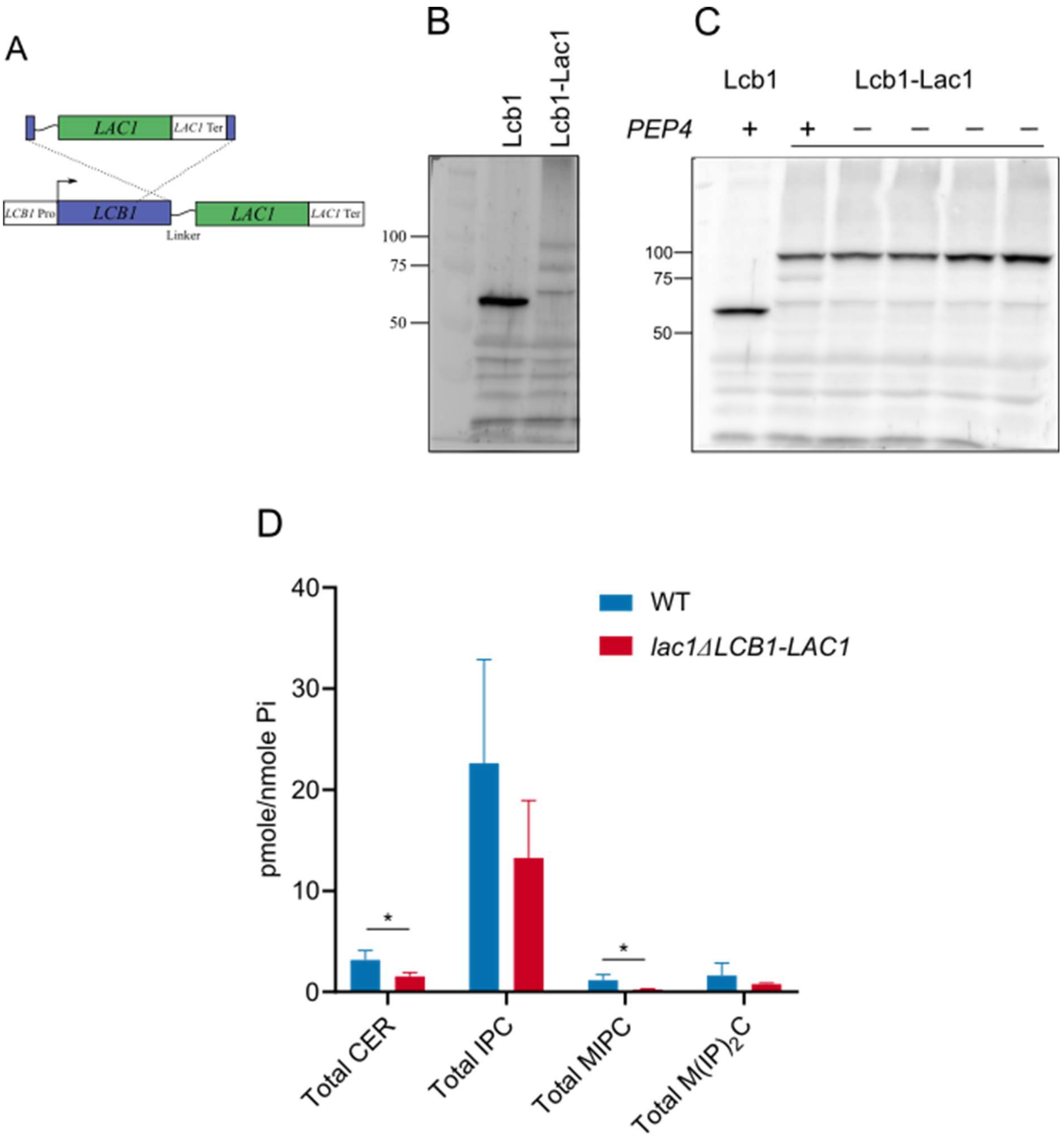

Figure 7. Lcb1-Lac1 fusion protein is partially degraded. A) The schematic illustration of fusion protein construction. Pro – promoter. Ter – terminator. Linker sequence encodes an 8 amino acid peptide GGGSGGGS. B) Western blots of wild type (LCB1) or chimeric (LCB1-LAC1) protein, yeast cells lysates were probed with anti-Lcb1 antibody. C) Western blots of Lcb1-Lac1 from WT or a *PEP4*-deficient strains. D) Sphingolipid profiles of indicated yeast strains. Cer -ceramides, IPC – inositolphosphorylceramides, MIPC - mannosyl-inositolphosphorylceramide, $M(IP)_2C$ – mannosyl-diinositolphosphorylceramide Date represent mean of three independent biological replicates, error bars show SD. * $p < 0.05$, two-tailed *t* test.

Lcb1-Lag1 fusion proteins is stable and functional

The deletion of both *LAC1* and *LAG1* genes, which is lethal for yeast cells, can be rescued by a centromeric plasmid bearing either *LAC1* or *LAG1*. The plasmids harboring a *URA3* gene encoding the enzyme orotidine-5'-phosphate decarboxylase, can be counter-selected by treating cells with 5-Fluoroorotic acid which is converted to a very toxic product by Ura3 (133). Hence, *lac1Δlag1Δ* will not grow without the rescue plasmid on a medium supplemented with 5-FoA. The *lac1Δlag1Δ* expressing fusion proteins Lcb1-Lag1 and Lcb2-Lag1 could grow (Figure 8, C) without the rescue plasmid on 5-FoA agar plates which indicates that Lag1 part of the fusion protein is functional.

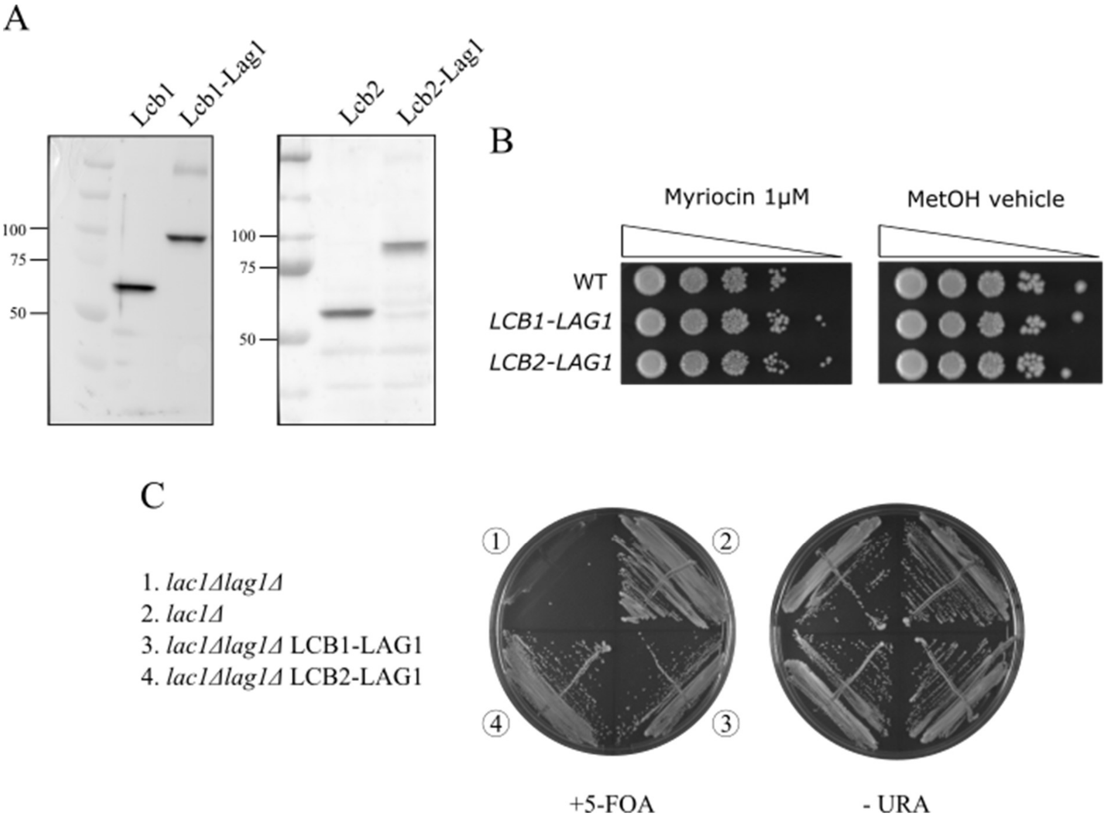

Figure 8. Fusion proteins with Lag1 are more stable and functionally active. A) Western blots of Lcb1-Lag1 (left) or Lcb2-Lag1 (right) fusion proteins. B) Serial dilution of yeast cells expressing fusion proteins were spotted onto YPD plates containing vehicle (methanol) or 1 µM myriocin. C) The indicated yeast strains were transformed with a plasmid expressing LAG1 under the control of endogenous promoter (pRS416-LAG1). The resulting strains were streaked onto SD minus uracil or 5-Fluoroorotic acid agar plates and incubated at 30°C for 2 days.

Lipid profile of cells expressing Lcb1-Lag1 chimeric fusion protein

In the next step we sought to characterize the effect of the chimeric protein Lcb1-Lag1 on lipid profile of the cells. To detect and quantify distinct lipid species from complex cellular extracts we used multiple-reaction monitoring mass spectrometry (MRM-MS) (134). First, molecular ions are generated by electrospray ionization (ESI), pre-selected molecular ions (precursor ions) undergo fragmentation and the corresponding fragment ions are also detected. Therefore, we can identify each lipid species by its precursor and fragment ions, which improves the robustness and accuracy of detection. Moreover, with MRM-MS many cellular lipid species can be detected and quantified at once. Later, distinct species can be grouped into various lipid categories based on the type, head-group, number of carbon atoms etc.

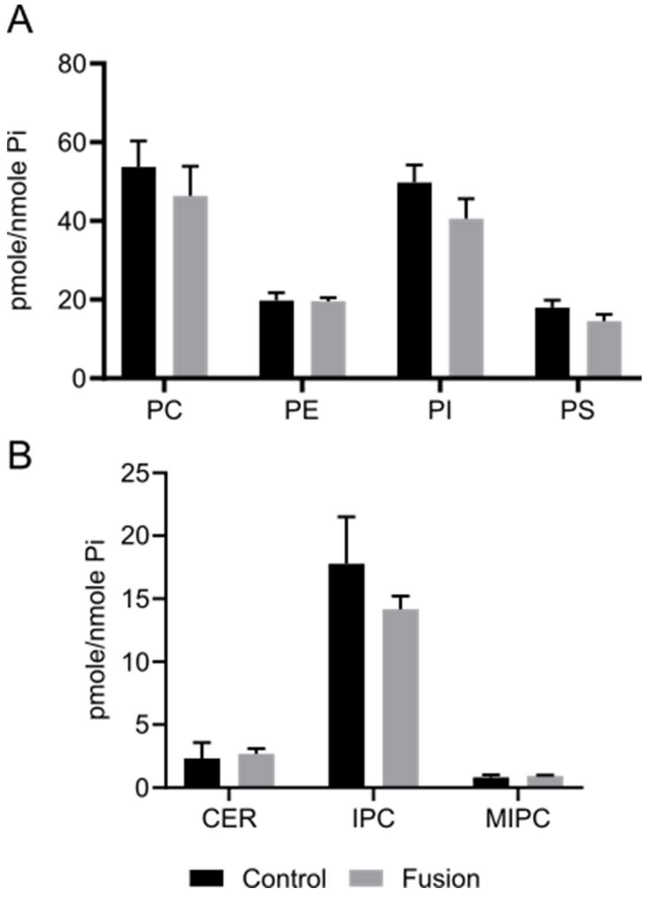

Figure 9. Lipid profile is not altered in cells expressing LCB1-LAG1 fusion protein. Mass spectrometry (MS) analysis of steady-state phospholipid (A) or sphingolipid (B) levels. Control (*lac1Δ)* or Fusion

(*lac1Δlag1ΔLCB1-LAG1*) yeast strains were grown in rich medium, lipids were extracted, desalted and measured by MS. The values are shown as pmole of lipids normalized to the amount of inorganic phosphate in the samples. A) Lipid profile of glycerophospholipids. PC – phosphatidylcholine; PE – phosphatidylethanolamine; PI – phosphatidylinositol; PS – phosphatidylserine B) Sphingolipid profile CER -ceramide, IPC – inositolphosphorylceramides; MIPC - mannosyl-inositolphosphorylceramides. Errors bars show standard deviation (SD).

We compared *lac1Δ* cells (control) with the fusion protein-expressing strain *lac1Δlag1ΔLCB1-LAG1* so that only Lag1 protein is expressed in both conditions. However, the expression of the chimera is driven by a stronger *LCB1* promoter which may lead to higher abundance of Lag1 than in the control strain. Major glycerophospholipid classes PC, PE, PI, PS were not altered by the expression of Lcb1-Lag1 (Figure 9, A) which is expected since sphingolipids are much less abundant than phospholipids in yeast cells making up about 10% of total lipids (84, 85, 135) and changes in sphingolipids are not likely to affect phospholipid levels. Despite possible difference in Lag1 protein amounts, the levels of ceramides and complex sphingolipids (IPCs, MIPCs, $M(IP)_2Cs$) were similar in control and fusion-expressing strains (Figure 9, B). The profile of individual sphingolipid species was also similar between control and chimera-expressing cell. The most prevalent ceramide species was PHC-C 18:0/26:0 which in all samples amounted to about 91-93% of all ceramides (Figure 4 and Table 1) which is consistent with previous observations (85, 135). In budding yeast, ceramides mostly incorporate a very long-chain fatty acid with 26 carbon atoms, with C26-Ceramides amounting to 95% of all ceramides (Figure 10). IPC-C 18:0/26:0 made about 80% of all IPC species (Figure 10). Consistent with ceramide and IPC profiles, MIPC and $M(IP)_2C$ species were mainly derived from 18:/26:0 C and B class ceramides (Figure 10).

Sphingolipid dynamics upon heat stress

Heat-shock induces a rapid upregulation in long-chain base levels

Unaltered levels of sphingolipid levels in the Lcb1-Lag1 expressing strain suggests that the activity of both enzymes is not severely compromised. It is though still possible that the chimeric protein has a reduced activity, but homeostatic regulation overrules the difference and the steady state levels remain unaltered. To address directly address whether the Lcb1-Lag1 chimeric protein can accelerate the metabolic flux towards ceramides, a heavy-labeled sphingolipid precursor, D3-L-serine was used. It is well documented, that the induction of heat-shock at 39-40^{o}C leads to rapid increase in long-chain base levels (48, 136).

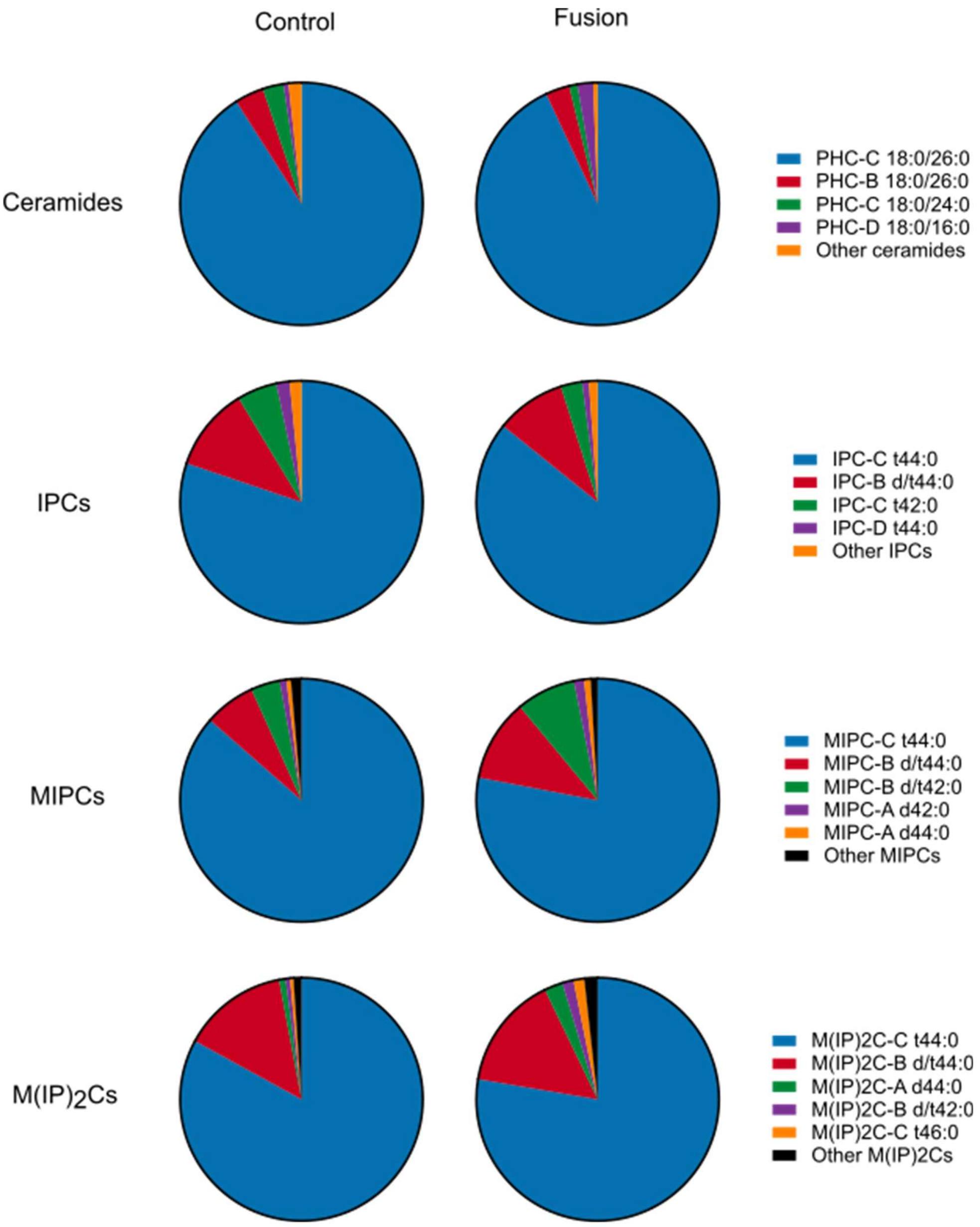

Figure 10. Analysis of sphingolipid species in Control (*lac1Δ)* or Fusion (*lac1Δlag1ΔLCB1-LAG1*) yeast strains. Pie charts show the average percentage of the most abundant sphingolipid species relative to the total amounts within each class. Data shows the average of three independent experiments.

First, we checked if heat-shock treatment upregulates long-chain base levels in our wild-type BY4741 cells. Sphingolipid regulation might differ considerably among different genetic backgrounds of yeast strains, as was shown for *lac1Δlag1Δ* mutants cells viable in W303 background and inviable in YPK9 strains (137, 138). Consistent with the previous reports, we observed fast upregulation of C18PHS and C18PHS-1P. The increase in LCB amounts was more pronounced than previously reported (47, 136), showing 21-fold elevation of C18PHS at 8 minutes of heat-stress (Figure 11, A). Levels of C20PHS, barely detectable at 40°C were increased almost 270-fold after 10 minutes of heat-shock (Figure 11, B), which also corresponds to the earlier reports (136). Interestingly, heat-shock treatment only induced PHS levels, while C18-Sphinganine (Figure 11, A) amounts did not change as drastically as PHS, contrary the previous report (136). This might be explained by the high activity of long-chain base hydroxylase Sur2 in our strains, which would result in efficient conversion of sphinganine into PHS.

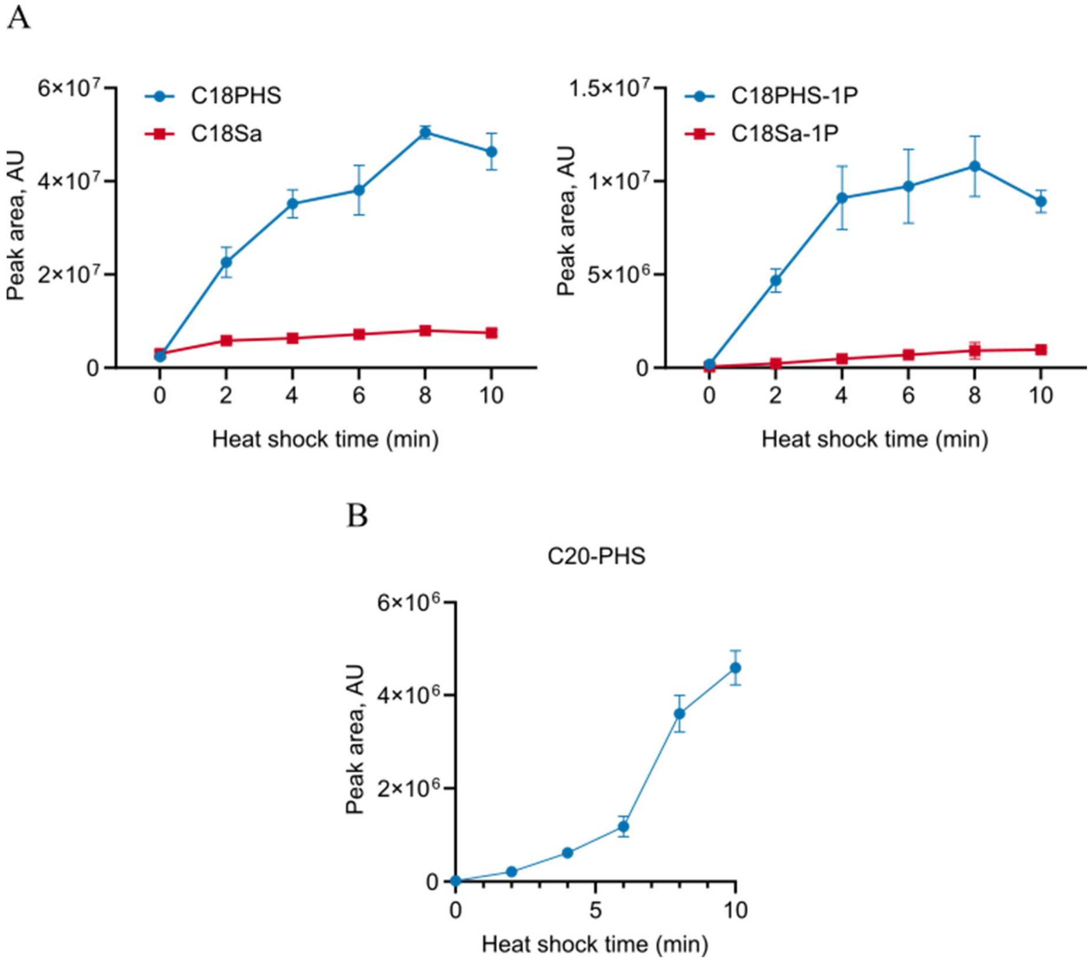

Figure 11. Heat stress induces rapid increase in long-chain base levels in BY4741 cells. WT cells were grown in YPUAD medium to OD_{600}=1 at 30ºC, the temperature was increased to 40ºC and samples were collected at the indicated time points. Extracted metabolites were derivatized with AQC, run on LC-MS and long-chain bases were detected and quantified by comparison to the internal standards. A) C18-bases and their phosphorylated derivatives. B) C20PHS. Error bars represent standard deviation (SD).

D3-Serine is efficiently incorporated into sphingoid bases upon heat stress

In the next step we investigated the incorporation of heavy isotope-labeled serine into sphingolipids shortly after heat shock. When cells were labeled with D3-L-Serine followed by heat stress, the "heavy" serine was rapidly incorporated into sphingoid-bases in both control and chimera-expressing cells (Figure 12, A). The degree of long-chain base elevation immediately after heat-shock was similar for C18PHS, in all samples we saw an 8-fold increase compared to basal levels. Interestingly, only D3-species were markedly upregulated upon heat stress, while the levels of unlabeled LCBs did not change drastically (Figure 12, B). This might indicate that the cells increase serine uptake in order to boost the sphingolipid biosynthesis, which is in agreement with the previous studies. (139) It also demonstrates that the increase in LCB amounts comes from *de novo* biosynthesis, not from the degradation of ceramides. D3-C18PHS increased 8-fold after 2 minutes of heat-stress, while D3-C18Sa showed a milder 3-fold upregulation. Amounts of D3-C18PHS-1P, D3-C18Sa, D3-Sa-1P were slightly higher in control cells at 2 min of heat-shock, but at 5 minutes there was no significant difference in all species between the control and the fusion-expressing cells (Figure 12, A). Altogether, the data suggests that Lcb1-Lag1 expression does not compromise *de novo* long-chain base biosynthesis.

Expression of Lcb1-Lag1 does not accelerate sphingolipid flux

Unlike long-chain bases that rapidly accumulate upon heat-shock, ceramides start to accrue much later, after 30-40 minutes (140). To test whether the expression of SPT-CS fusion protein would enhance the conversion of long-chain base to ceramides, we followed *de novo* biosynthesis of sphingolipids by tracing the incorporation of heavy-isotope-labeled serine following a heat-shock treatment to induce the accumulation of sphingolipid precursors. In this experiment the percentage of D3-labeled species to the total amount within each sphingolipid class was measured at 10 and 20 minutes of heat shock. The results show that Lcb1-Lag1 fusion protein does not increase conversion to ceramides and complex phospholipids (Figure 13, A, B, C).

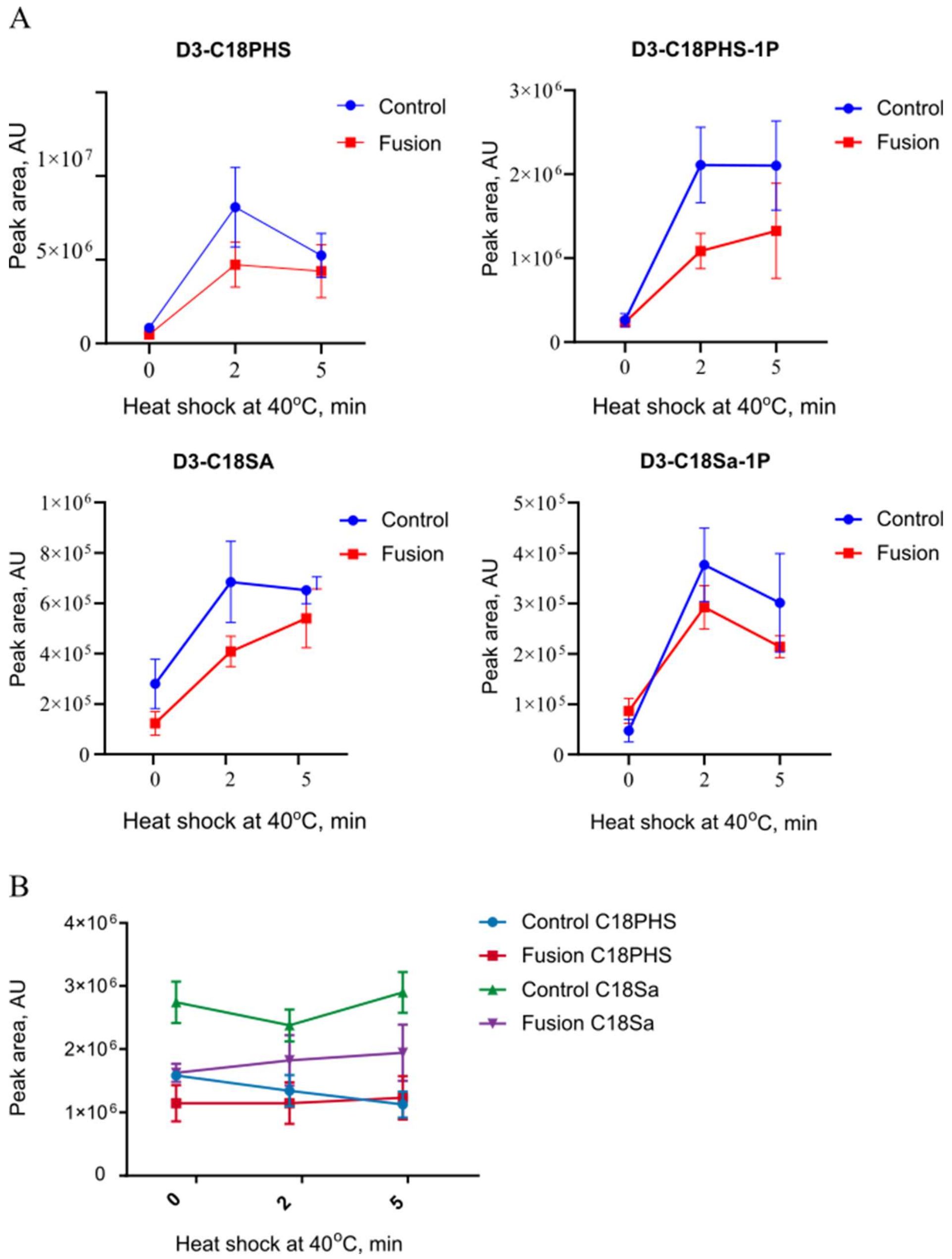

Figure 12. Upregulation of long-chain bases upon heat shock. Control (*lac1Δ)* or Fusion (*lac1Δlag1ΔLCB1-LAG1*) yeast strains were grown in SD medium without serine, labeled with 1mM D3-L-Serine for 5 min at 30°C, incubated at 40°C for 2 or 5 min. Long-chain bases were extracted, derivatized with AQC and analyzed using LC-MS/MS. PHS – Phytosphingosine; Sa – Sphinganine. A) Dynamics of indicated D3-labeled species B) Dynamics of unlabeled C18PHS and C18Sa. Errors bars represent standard deviation (SD).

After 10 minutes of heat-stress about 7% of all ceramides were labeled with D3-Serine (Figure 14, A). The most upregulated species upon heat shock are C20 long-chain bases. (136) Accordingly, C20:0/C26:0 ceramides were efficiently labeled by D3-Serine, making up more than 50% of all C46 cellular ceramides after 10 minutes of heat shock (Figure 13, B). The *de novo* biosynthesis of complex sphingolipids (IPC and MIPC) progressively increased from 10 to 20 minutes, while ceramide levels stabilized at 10 min. This indicates that a fraction of freshly synthesized ceramides leaves the ER and is glycosylated to form IPC and MIPC since the accumulation of ceramides might be toxic to the cells (141).

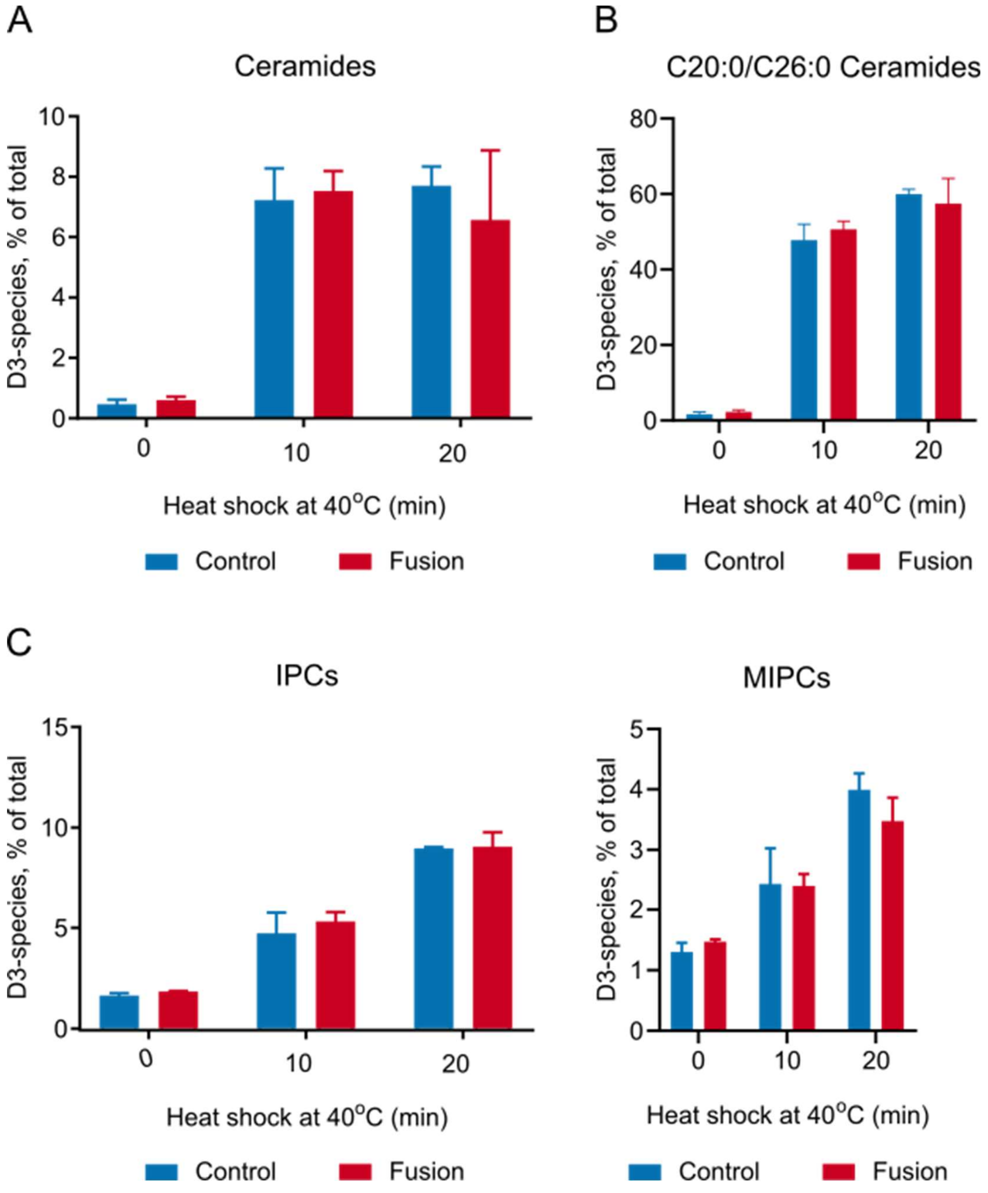

Figure 13. De novo sphingolipid biosynthesis upon heat shock is not accelerated by the expression of Lcb1-Lag1 fusion protein. Analysis of D3-Serine-labeled sphingolipids following heat-shock. Control (*lac1Δ)* or Fusion (*lac1Δlag1ΔLCB1-LAG1*) were cultured to OD_{600}=1 at 30ºC were labeled with 1mM D3-L-Serine for 5 min, followed by the heat-shock treatment at 40ºC for the indicated time periods. Extracted lipids were treated with methylamine, desalted with n-butanol, directly injected into triple-quadrupole mass spectrometer, quantified and normalized using the internal standards. The percentage of D3-labled species of total amount within each category is shown A) Total ceramides B) C46-Cermides (C20:0/C26:0) C) Complex sphingolipids IPC and MIPC Error bars represent standard deviation.

Tsc10 overexpression rescues slower sphingolipid flux in Lcb1-Lag1-expressing cells

The product of SPT, 3-ketosphinganine must first be reduced into sphinganine (dihydrosphingosine) before N-acylation to form ceramides. Tsc10, 3-ketosphinganine reductase catalyzes this step and could therefore be a limiting step that slows down the metabolic flux to ceramides. We transformed control or Lcb1-Lag1-expressing (fusion) strains with plasmids overexpressing Tsc10 and as in the previous experiment, followed sphingolipid biosynthesis after heat shock exposure for 10 or 20 minutes. Overexpressed Tsc10 preferentially localized to the nuclear ER in both control and fusion protein-expressing strains (Figure 14, A). Surprisingly, we found that metabolic flux was slower in Lcb1-Lag1 chimera-expressing cells than in control cells and Tsc10 overexpression accelerated the flux in the fusion-expressing cells, but not in the control strain. The percentage of D3-labeled ceramides was significantly lower in the fusion strain at 10 minutes of heat stress but Tsc10 overexpression partially restored biosynthesis rate to the control levels (Figure 14, B). Moreover, Tsc10 overexpression decreased ceramide biosynthesis in control cells (Figure 14, B) which may indicate excessive Tsc10 proteins rather interfered with the functioning of SPOTS complex. It is interesting to note that at 20 minutes of heat shock we could see no difference between chimera-expressing strains and controls or between empty vector or Tsc10-overexpressing samples. Lcb1-Lag1 expression also resulted in lower mean IPC biosynthesis rate (albeit not statistically significant), but MIPC biosynthesis was clearly faster at 20 minutes in control cells indicating slower flux in chimera-expressing cells. Again, Tsc10 expression sped up the flux only in the Lcb1-Lag1 strain (Figure 14, B). SPT and ceramide synthases form enzymatic complexes and the fusion of two catalytic subunits from these two complexes likely interfered with the architecture and stoichiometry of SPOTS complex. The results indicate that Tsc10 overexpression speeds up the metabolic flux in chimera-expressing cells and slows it down in control cells. This may indicate that Tsc10 does not function properly in the cells expressing Lcb1-Lag1 requiring extra amounts of the enzyme. Collectively, the results of the two experiments indicate that fusing SPT and CS catalytic subunits does not increase but rather slow down sphingolipid flux possibly by disrupting the integrity of the SPOTS complex. Also, the data suggests that the distance between SPT and CS complexed may not be as critical as we hypothesized.

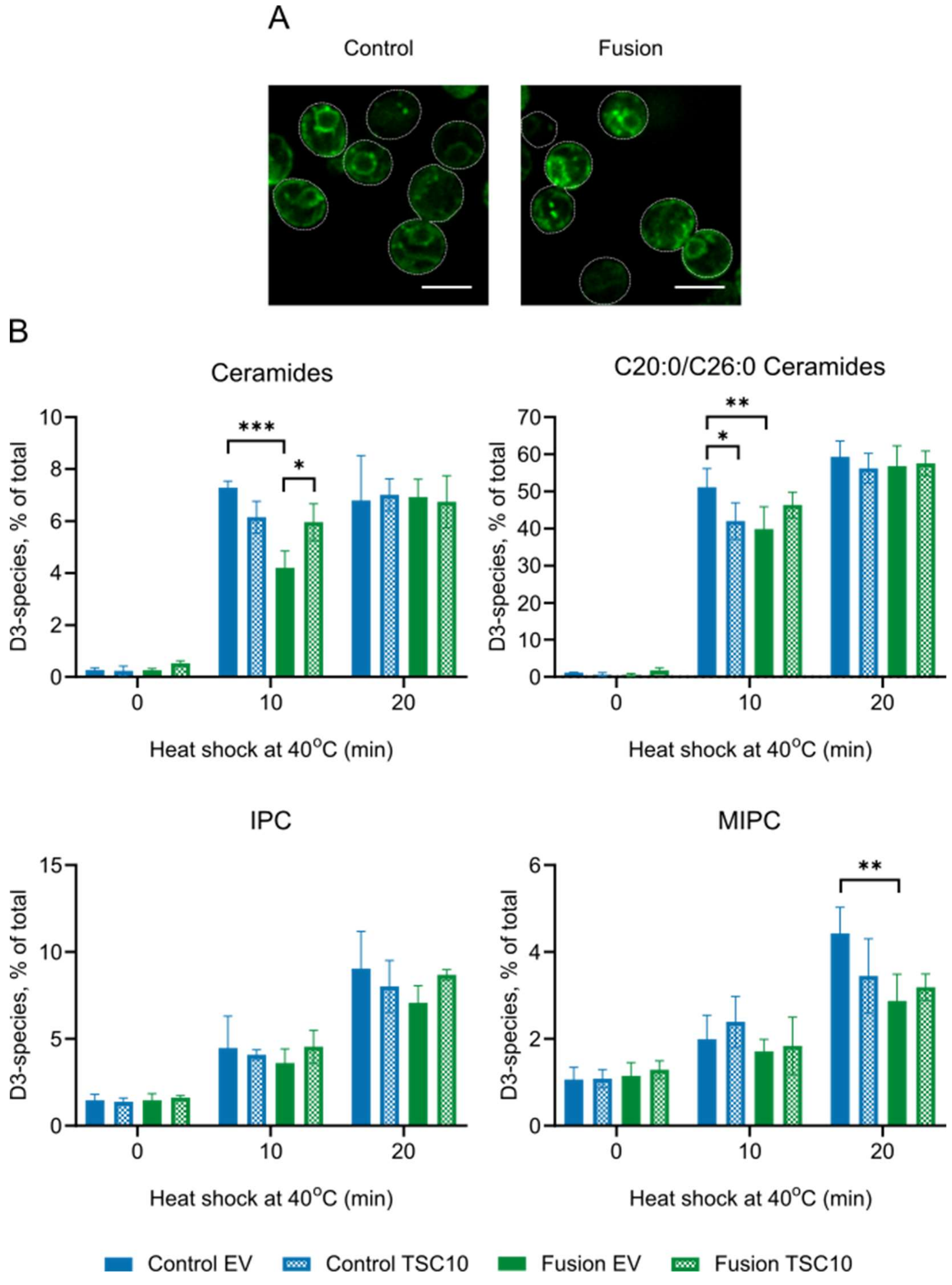

Figure 14. Tsc10 reductase accelerates sphingolipid metabolism in Lcb1-Lag1 expressing cells. A) Fluorescence microscopy images of control (*lac1Δ)* or fusion (*lac1Δlag1ΔLCB1-LAG1*) strains expressing GFP-Tsc10. Cells transformed with plasmid overexpressing *TSC10* (pRS416-GPD-GFP-TSC10) were grown in SD minus uracil selective medium to the exponential phase and imaged as described using a GFP filter. Bars, 5 µm. B) Analysis of D3-Serine-labeled sphingolipids following heat-shock. Control (*lac1Δ)* or Fusion (*lac1Δlag1ΔLCB1-LAG1*) stains transformed with a plasmid overexpressing *TSC10* (pRS416-GPD-GFP-TSC10) or an empty vector (EV, pRS416-GPD) were cultured to OD_{600}=1 at 30ºC and labeled with 1mM D3-L-Serine for 5 min, followed by the heat-shock treatment at 40ºC for the indicated time periods. Extracted lipids were treated with methylamine, desalted with n-butanol, directly injected into triple-quadrupole mass spectrometer, quantified and normalized using the internal standards. The percentage of D3-labled species of total amount within each category is shown. Values show means of three biological replicates. Statistical significance was determined using two-way ANOVA (*P<0.05, **P<0.01, ***P<0.001). Error bars represent standard deviation.

Ceramide synthase re-localization to the cell periphery does not affect ceramide biosynthesis

The cortical-targeting sequence from Ist2 re-localizes Lac1 to the cell periphery

In an alternative approach to investigate the role of enzyme localization on sphingolipid metabolic flux, we asked whether the localization of one of the enzyme complexes, ceramide synthase, affects sphingolipid biosynthesis and homeostasis. GFP-tagged catalytic subunits of ceramide synthase shows predominantly nuclear ER localization. However, the introduction of fluorescent tags frequently compromises the protein's localization, topology and activity (142, 143). Indirect immunofluorescence of the FLAG-tagged ceramide synthase subunit Lip1 shows a clear perinuclear localization (20). We decided to alter the localization of ceramide synthase by enriching it in the cortical ER where SPT-containing SPOTS complex is thought to localize. To specifically target ceramide synthase to the cortical ER, we constructed a chimeric Lac1 protein that contains C-terminal cortical sorting sequence (amino acids 879-946) from Ist2. This cortical targeting sequence directs Ist2 to the ER-PM junctions since it can bind a phosphatidylinositolphosphate species $PI(4,5)P_2$ which is enriched in the plasma membrane (106, 107). The schematic illustration of EGFP-tagged PM-targeted Lac1 ($Lac1^{ER\text{-}PM}$) shown in (Figure 15, A). Both chimeric $Lac1^{ER\text{-}PM}$ and control intact Lac1 proteins were EGFP-tagged at the N-terminus, have native promoter and terminator sequences and are stably expressed in yeast cells due to genomic integration in the LEU2 locus (144). Lac1$^{ER\text{-}PM}$ localizes to peripheral punctate structures while still being partially found in the perinuclear region (Figure 15, B right panel) while the wild type Lac1 resides mostly in the nuclear ER.

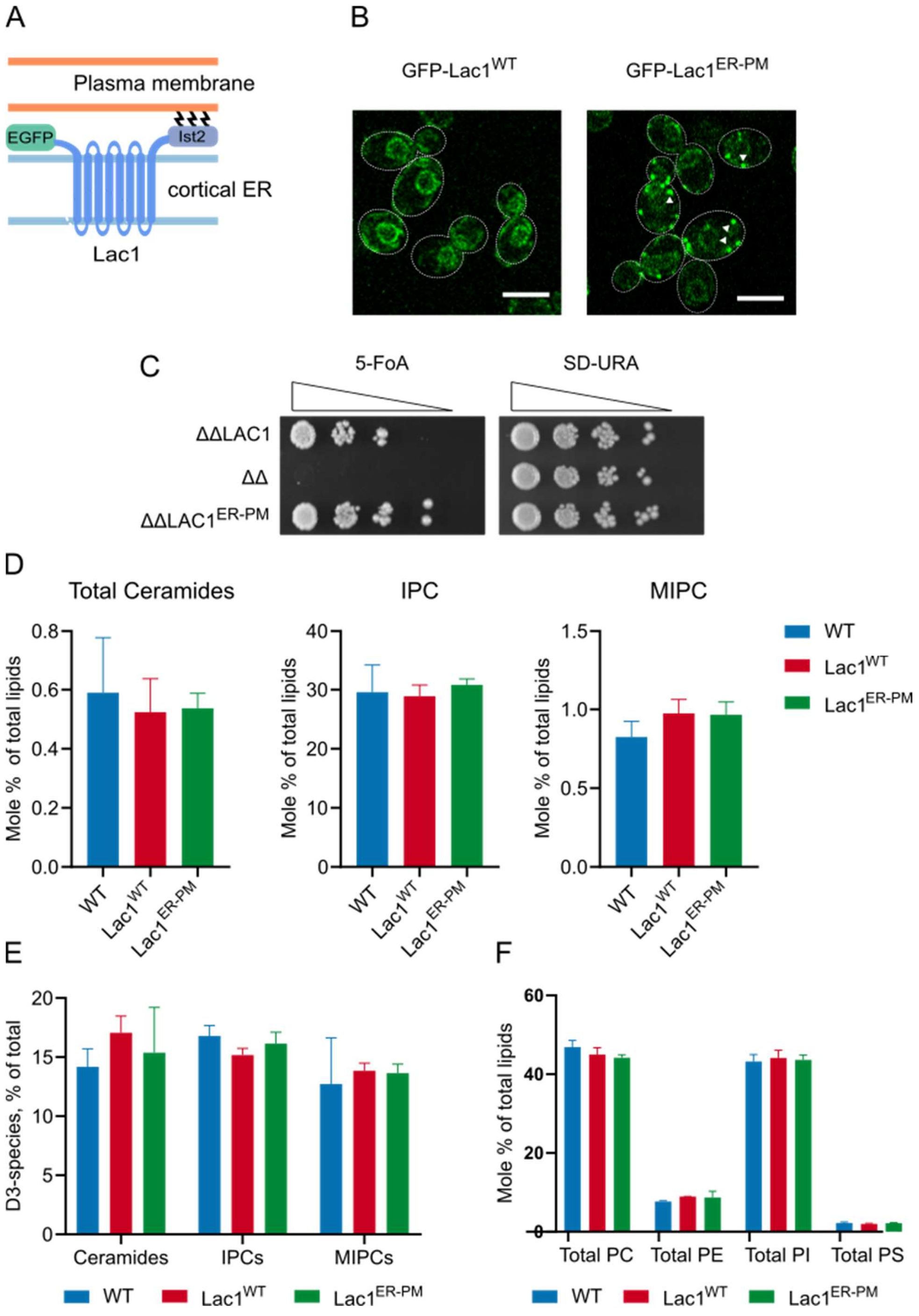

Figure 15. Targeting Lac1 to cortical ER does not affect sphingolipid biosynthesis. A) A diagram of GFP-tagged chimeric Lac1 $^{ER-PM}$ protein containing C-terminal cortical targeting domain of Ist2 . B) Lac1^{ER-PM} is predominantly targeted to the cell periphery. Confocal microscopy images of GFP-tagged wild-type (left) or cortical ER-targeted chimeric Lac1 (right). Cells were grown to mid-log phase and imaged as described in the methods. White arrowheads indicate dot-like punctate structures. Scale bar, 5 µm. C) Lac1^{ER-PM} can functionally replace the wild-type protein. Synthetic lethality assay. The indicated yeast strains (ΔΔLAC1 – *lac1Δlag1ΔGFP-LAC1*, ΔΔ - *lac1Δlag1Δ*, ΔΔLAC1^{ER-PM} - *lac1Δlag1ΔGFP-LAC1-IST2*(878-946)) were transformed with a plasmid expressing *LAG1* (pRS416-LAG1) and 10-fold serial dilutions were spotted onto SD minus uracil or 5-Fluoroorotic acid agar plates and incubated at 30ºC for 2 days. D-F) Lipid profile and *de novo* sphingolipid biosynthesis is not compromised in Lac1^{ER-PM}-expressing cells. WT(BY4741), Lac1^{WT} *(lac1Δlag1ΔGFP-LAC1)* or Lac1^{ER-PM} (*lac1Δlag1ΔGFP-LAC1-IST2*(878-946)) were grown in SD medium without serine to mid-log phase, labeled with 1mM D3-L-Serine for 30 min at 30ºC and processed for lipid extraction. Extracted lipids were analyzed by mass spectrometry. D) and F) The values show mole percentage to the sum of major phospholipids (PC, PE, PI, PS). E) Values represent the percentage of D3-labeled lipids of all lipids in the category. F) The amounts of major phospholipid classes. D-F) The values show the mean of three biological replicates. Error bars represent standard deviation (SD).

The expression of Lac1^{ER-PM} does not alter sphingolipid biosynthesis or homeostasis

Next, we tested whether the PM-targeted chimera could functionally substitute native proteins. Indeed, Lac1^{ER-PM} could support cell growth in the absence of both Lac1 and Lag1 proteins as shown by the synthetic lethality assay (Figure 15, C). The analysis of phospholipids and sphingolipids by mass-spectrometry showed that altered localization of Lac1^{ER-PM} does not affect lipid homeostasis (Figure 15, D and F). Cells stably expressing EGFP-tagged wild-type Lac1 or Lac1^{ER-PM} had endogenous *LAC1* and *LAG1* genes deleted but that did not alter total amounts of ceramides or complex sphingolipids when compared to the wild-type strain. It has been shown that cells lacking *LAG1* upregulate the expression of *LAC1* (145). Therefore, this might explain that yeast expressing only one ceramide synthase subunit have similar amounts of sphingolipids. Nevertheless, similar steady-state levels might conceal the difference in *de novo* biosynthesis rates. Yet, our data shows that altered localization of Lac1 does not change the rates of heavy-serine incorporation into ceramides, IPCs, MIPCs (Figure 15, E).

Inner nuclear membrane-targeted Orm2 and increases metabolic flux to ceramides

Orm2 fused with the INM-targeting sequence from Heh2 is localizes to the nuclear membrane and recruits SPT catalytic subunits

It was previously shown that treatment with myriocin caused an increase in perinuclear localization of Orm2 (23). Downregulation of sphingolipid biosynthesis by myriocin leads to the relief of Orm-mediated inhibition of SPT and stimulates sphingolipid production (146). Therefore, stimulation of SPT activity may be linked with its perinuclear localization. The nucleus is enclosed in the nuclear envelope (NE) composed by two lipid bilayer membranes separated by the perinuclear space and joined at the nuclear pores: the outer nuclear membrane (ONM) and the inner nuclear membrane (INM). The ONM is contiguous with the nuclear ER so that ER membrane protein can freely diffuse into the ONM and eventually INM (147). Many integral ER proteins have been found in the INM. Orm proteins and ceramide synthase subunits Lac1 and Lag1, but not SPT proteins Lcb1, Lcb2 were found to localize in the INM (132). We hypothesized that anchoring Orm2 in the INM might upregulate sphingolipid biosynthesis. To test this we made use of a nuclear localization sequence of a transmembrane protein Heh2 which directs it to the INM (148, 149). INM-targeting sequence oh Heh2 (aa 93-317) was placed after an EGFP-tag and before Orm2 ORF. Both GFP-Orm2 and GFP-NLS-Orm2 were expressed from constructs flanked by native promoter and terminator sequences and integrated into the genome of a strain lacking both endogenous Orm proteins. The diagram shows the expected localization of IMN-targeted Orm2 is shown in Figure 16, A. Orm2 is an integral ER protein, previously shown to localize to localized to both cortical and perinuclear ER (23), which is consistent with our observations (Figure 16, B and C). INM-tageted Orm2 showed a clear perinuclear localization with no fluorescence detected outside the nucleus suggesting efficient targeting and retention endowed by the NLS of Heh2 (Figure 16, B and C). Since Orm2 was found to be associated with SPT (23), we tested if SPT catalytic subunits Lcb1 and Lcb2 also changed their localization. Indeed, Lcb1 and Lcb2 localized in all ER sub-compartments in control cells, showed predominant perinuclear localization in cells when Orm2 was targeted to the INM (Figure 16, B and C).

SPT inhibition by INM-targeted Orm2 is diminished resulting in elevated LCB amounts

Next, the effect of Orm2 INM-targeting on long-chain base levels was investigated. Cells expressing chimeric NLS-Orm2 or control Orm2 had both endogenous *ORM* genes deleted.

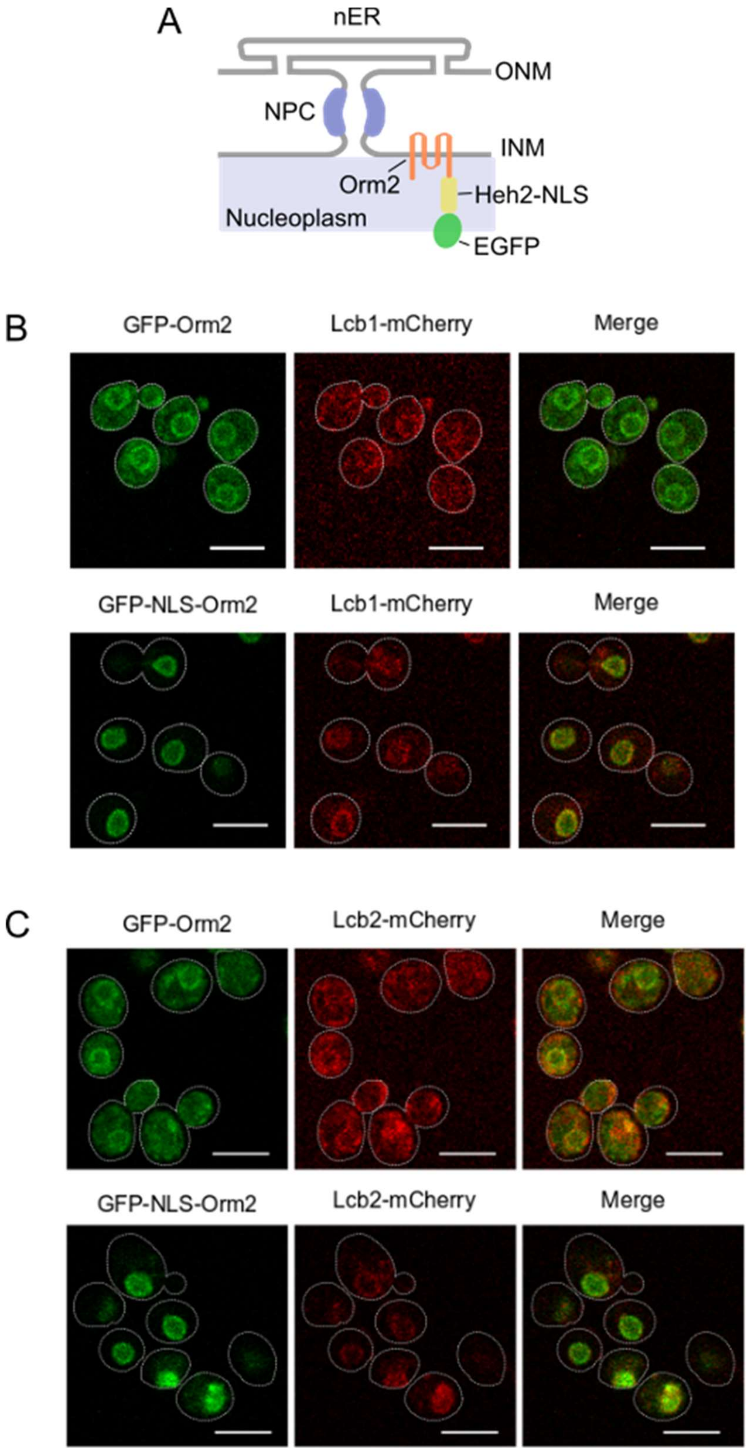

Figure 16. NLS-Orm2 is targeted to the nucleus. A) Diagram showing localization of GFP-tagged Orm2. nER – nuclear ER, ONM – outer nuclear membrane, INM – inner nuclear membrane, NPC- nuclear pore complex. B) and C) NLS-Orm2 recruits SPT subunits Lcb1 and Lcb2 to the nuclear membrane. Cells expressing mCherry tagged (red) Lcb1 (B) or Lcb2 (C) and GFP-tagged (green) Orm2

(top) or NLS-Orm2 (bottom) were grown in rich medium to log-phase and imaged according to the protocol described in methods. Bars, 5 µm.

Consistent with their role as SPT inhibitors, depletion of Orm proteins lead to a pronounced (increase in LCB and LCB-1P levels (Figure 17) which reproduces previously published observations (23, 33). Expression of GFP-Orm2 alone could restore C18 PHS and C18 Sa amounts to those of WT cells. Interestingly, GFP-Orm2 could not fully reduce the levels of phosphorylated sphingoid bases (Figure 17). The amounts of long-chain bases and their phosphorylated derivatives: C18 PHS, C18 Sa, C18 PHS-1P, C18 Sa-1P were significantly higher in NLS-Orm2 expressing cells compared to intact Orm2 (Figure x). Nevertheless, NLS-Orm2 could partially repress SPT as the levels of C18 PHS were about 2-fold lower than in the *orm1Δorm2Δ* mutants (Figure 17). These data suggest that INM-targeted Orm2 partially loses its ability to inhibit SPT. The results may also imply that the altered localization of SPT subunits does not affect its activity.

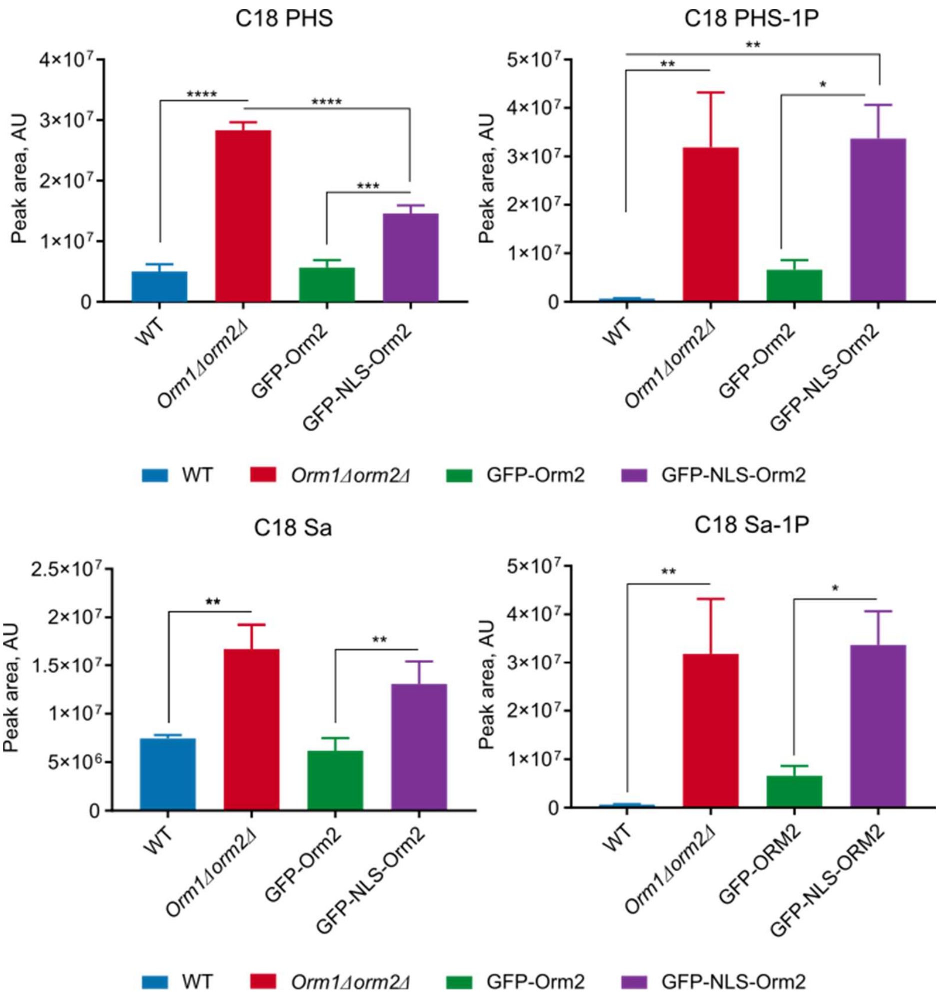

Figure 17. Cells expressing – INM-localized Orm2 have increased levels of long-chain bases. The indicated yeast strains (WT, GFP-Orm2 – *orm1Δorm2ΔGFP-ORM2*, *orm1Δorm2Δ,* GFP-NLS-Orm2 - *orm1Δorm2ΔGFP-NLS-ORM2*) were grown in rich medium YPUAD to OD_{600}=1 (mid-log phase), collected and subjected to metabolite extraction. Extracted metabolites were derivatized with AQC and analyzed by LC-MS. Values represent peak areas of the indicated long-chain bases normalized by internal standards. PHS – Phytosphingosine, Sa – Sphinganine. Statistical significance was determined using a one-way ANOVA test (*p<0.05, **p<0.01, ***p<0.001, ****p<0.0001). The values show the mean of three biological replicates. Error bars show standard deviation (SD).

INM-localized Orm2 expression stimulates ceramide *de novo* biosynthesis

To investigate the impact of NLS-Orm2 on de novo sphingolipid biosynthesis we labeled cells with heavy serine and measured sphingolipids by mass spectrometry. The amounts of non-labeled ceramides, IPCs, MIPCs reflect their steady-state levels and were similar in all strains except for *orm1Δorm2Δ* mutants, where ceramides were markedly upregulated (7-fold increase compared to WT) but complex sphingolipids (IPC, MIPC) amounts were lower (Figure 18, A). While we saw no difference in steady-state levels, the amounts of freshly made sphingolipids labeled with heavy D3-Serine differed considerably. Notably, *de novo* biosynthesis of ceramides, but not of complex sphingolipids, was increased in the strain expressing NLS-Orm2 (Figure 18, A and B). In contrast, *orm1Δorm2Δ* mutants demonstrated significantly lower rates of ceramides and complex sphingolipids (Figure 18, A and B). Overall the data show that the metabolic flux to ceramides is accelerated when SPOTS complex is enriched at the inner nuclear membrane.

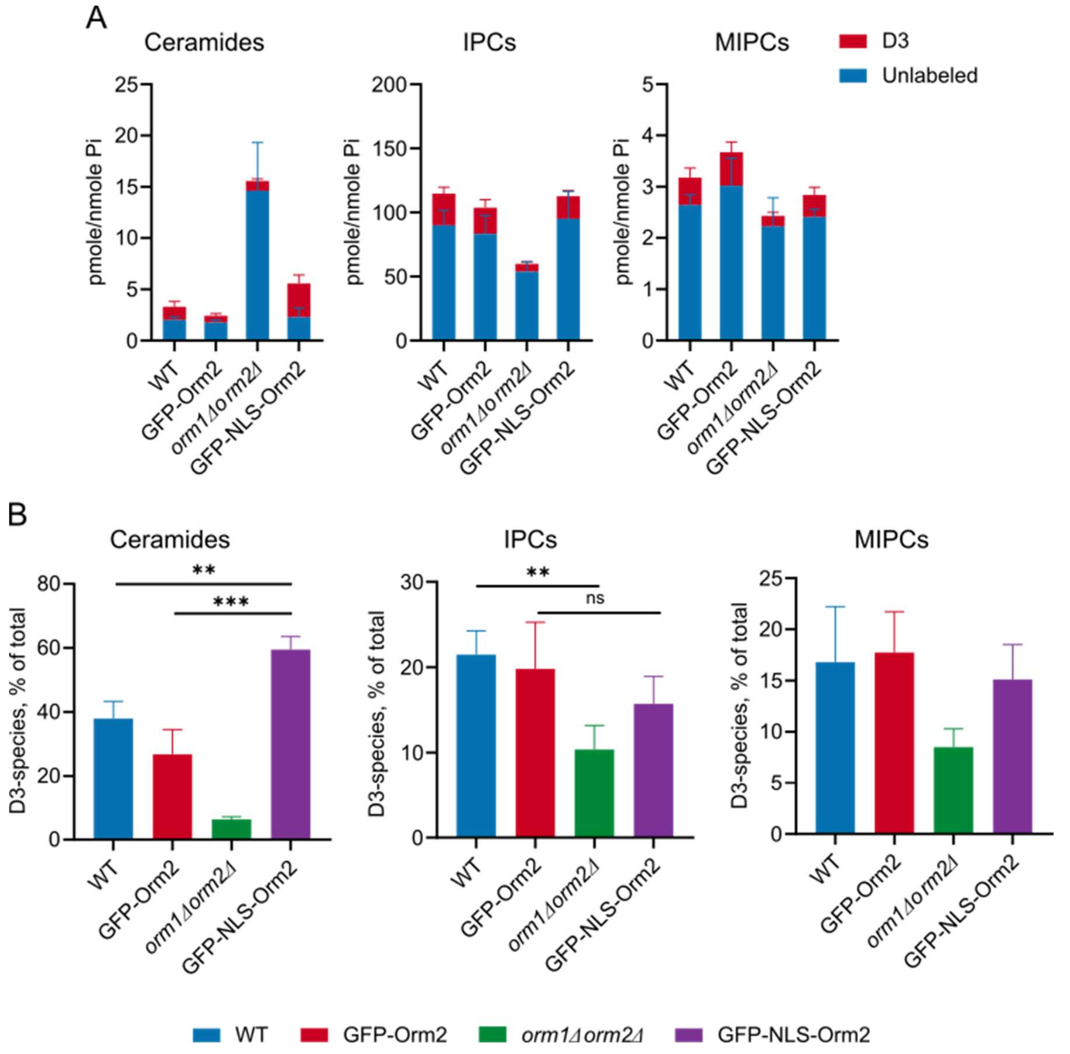

Figure 18. NLS-Orm2 upregulates *de novo* ceramide biosynthesis. The indicated yeast strains (WT, GFP-Orm2 – *orm1Δorm2ΔGFP-ORM2*, *orm1Δorm2Δ,* GFP-NLS-Orm2 - *orm1Δorm2ΔGFP-NLS-ORM2*) were cultured in SD medium without serine at 30ºC to OD_{600}=1 (mid-log phase) followed by labeling with 1mM D3-L-serine for 1 hour at 30ºC then processed for lipid extraction. Extracted lipids were analyzed by mass spectrometry. Lipid extraction and MS analyzed were performed as described in methods. A) The amounts of D3-labeled (red) and unlabeled (blue) sphingolipid classes. Values show lipid quantities in pmoles per nmole of inorganic phosphate. B) The percentage of D3-lableled species of total amount of lipids with the indicated sphingolipid class is shown. IPCs - Inositol phosphorylceramides, MIPCs – Mannosylinositol phosphorylceramides. Statistical significance was calculated using one-way ANOVA test (**p<0.01, ***p<0.001) The values show the mean of three biological replicates. Error bars represent standard deviation (SD).

Chapter 3.2: Characterization of vacuole-targeted caged sphingolipid probes in *Saccharomyces cerevisiae*

Localization of caged sphingolipid probes in budding yeast

Mistargeting of caged mito-sphingolipid probes to the vacuoles in yeast

Low spatial and temporal resolution of established techniques to study lipid metabolism and homeostasis has led to the development of artificial functionalized chemical probes (122). Recently, mitochondrially targeted caged sphingolipid probes have been developed and utilized in mammalian cells (125). The chemical cage allows for specific release of intact molecule triggered by ultraviolet (UV) irradiation ("UV-uncaging") while triphenylphosphonium moiety ensures efficient delivery to mitochondria. Moreover the protective cage represented by coumarin, allows to visualize probe localization before UV-triggered release (Figure 19, A) (125, 150, 151). Combining advantages of yeast as a well-studied, genetically tractable model organism with selective caged probes offers great opportunities for investigation of lipid transport and metabolism *in vivo*. Therefore, we decided to put these synthetic probes to test in budding yeast. To our surprise, one of the probes C18 mito-sphinganine did not colocalize with the mitochondria marked by Mdh1, but instead was found in the vacuoles marked by a subunit of vacuolar ATP-ase Vph1 (Figure 19, B and C).

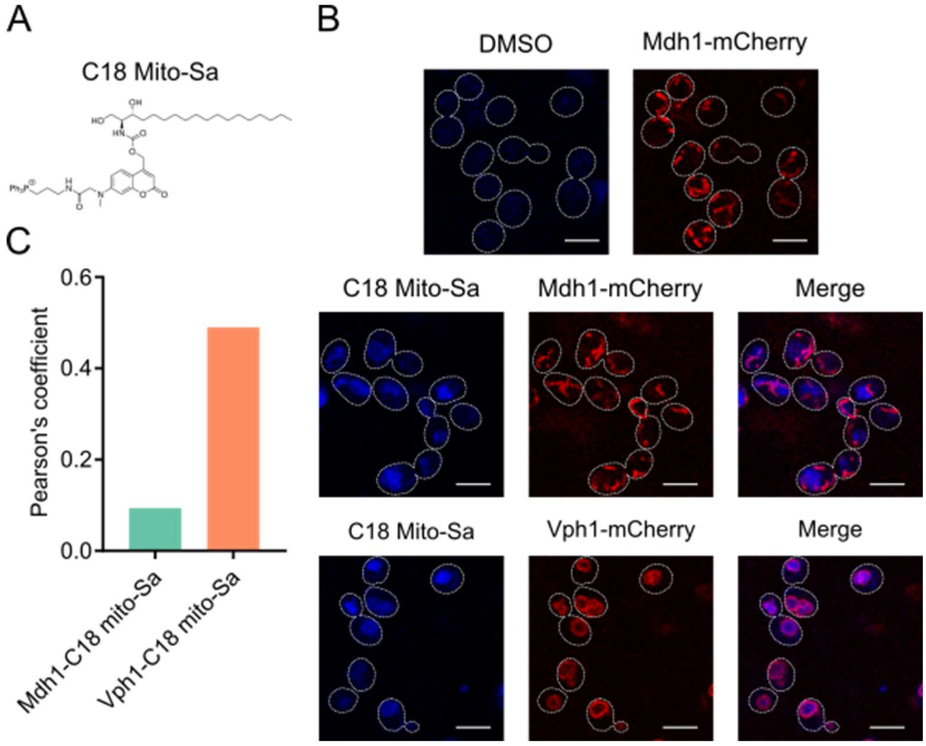

Figure 19. Mito-caged sphinganine probe is targeted to the vacuole instead of mitochondria. A) A chemical structure of C18 mito-Sa - mito-sphinganine (adapted from Feng, S. et al. *Elife*. 10.7554/eLife.34555). B) Localization of C18 mito-sphinganine in yeast cells. Yeast cells expressing mCherry-tagged mitochondrial marker Mdh1 (top) or vacuolar marker Vph1 (bottom) were grown in rich-medium to log-phase were incubated with 2 µM C18 mito-sphinganine or DMSO for 15 min, at 30ºC. Cells were washed, resuspended in low-fluorescence medium (LFM) and imaged as described. Cell outlines are shown by dashed lines. Bars, 5 µm. C) Co-localization coefficient of images in B (Pearson's coefficient) between mito-sphinaganine and Mdh1/Vph1. n = 55 cells.

Of note, the probe primarily stained the interior of the vacuoles. More similar sphingoid-base probes were tested - C17-C18 mito-PHS, mito-oleate all showing vacuolar localization (Figure 20, A). Though mito-Oleate probe showed a weaker signal which might indicate a difference in uptake mechanism(Figure 20, B).

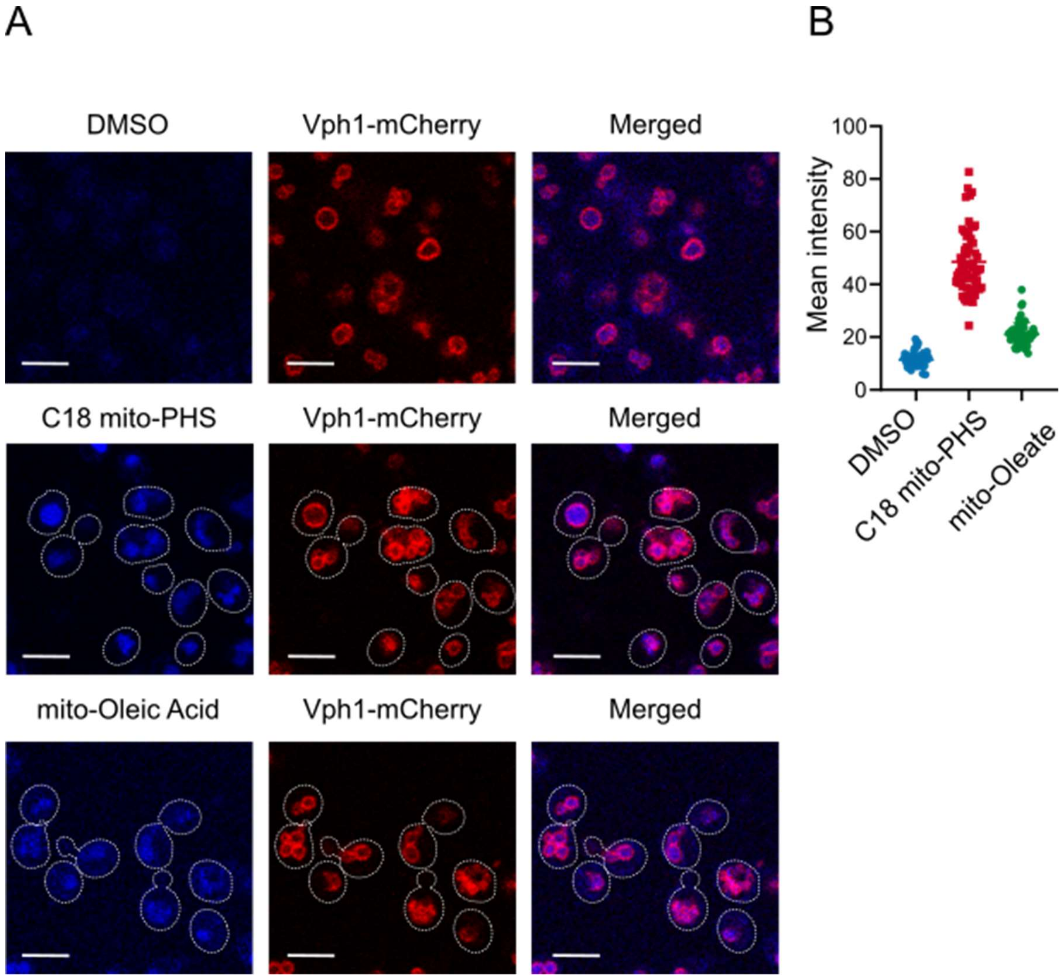

Figure 20. Mito-PHS and mito-Oleic acid are also targeted to the vacuole. A) Yeast cells expressing mCherry-tagged Vph1, which marks vacuoles were culture to mid-log phase in YPUAD, stained with 10 µM C17,C18 mito-Phytosphingosine (mito-PHS) or mito-Oleic acid or DMSO (control) for 15 min 30°C. Samples were imaged as described using the DAPI/mCherry channels. Cell shapes are outlined by dashed lines. Bars, 5 µm. B) Quantification of mean fluorescence intensity of coumarin in cells shown in panel A. n > 50 cells.

Factors affecting vacuolar localization of caged sphingolipid probes

TPP cation and long-chain base are both required for probe internalization

Surprisingly, yeast cells did not internalize C18 caged-PHS lacking the mitochondria-targeting group or the mito-cage (coumarin cage with the TPP targeting group) probes (Figure 21, A and B) even when caged C18PHS was supplied at a higher concentration, indicating that both long-chain base and TPP contribute to vacuolar targeting of mito-long-chain base probes. These results might indicate the activity of ABC-transporter pumps that efficiently clear yeast cells of potentially toxic xenobiotics (128). Another possibility is that a putative long-chain base exporter Rsb1 (152) is responsible for the efflux of caged C18PHS. To test the assumption that caged sphingolipid probes are pumped out by the yeast multidrug transporters, the uptake of caged C18PHS was observed in cells lacking one of the major yeast ABC-transporter, Pdr5 or Rsb1 (153). *PDR5* was selected because the deletion of this gene alone has been shown to slow down the xenobiotic efflux, increasing the sensitivity of yeast cells to a number of small molecules (154).

Caged C18PHS was not internalized in control cells, while in pdr5Δ and rsb1Δ mutants the caged PHS probe localized to the periphery in crescent-shaped patches (Figure 22, A). Interestingly only when both *PDR5* and *RSB1* genes were deleted, caged PHS could be detected inside the cells (Figure 22, A). The efficiency of uptake was still much lower compared to mito-caged probes, requiring higher concentration and longer incubation times. Yeast cells are equipped with several multidrug pumps, so the depletion of Pdr5 and Rsb1 is unlikely to completely block the probe efflux. The internalization was further confirmed by measuring C18PHS amounts in the double *pdr5Δrsb1Δ* mutants stained with caged PHS before and after UV-uncaging. Incubation with 100 µM caged PHS even in the absence of UV light increased C18PHS amounts by 6-fold compared to the control, suggesting probe degradation. Irradiation with UV further upregulated C18PHS, implying that the probe is not completely degraded inside the cells (Figure 22, B). Taken together, the data suggest that multidrug transporter Pdr5 and a long-chain base exporter Rsb1 are partially responsible for the efflux of caged sphingolipid probes.

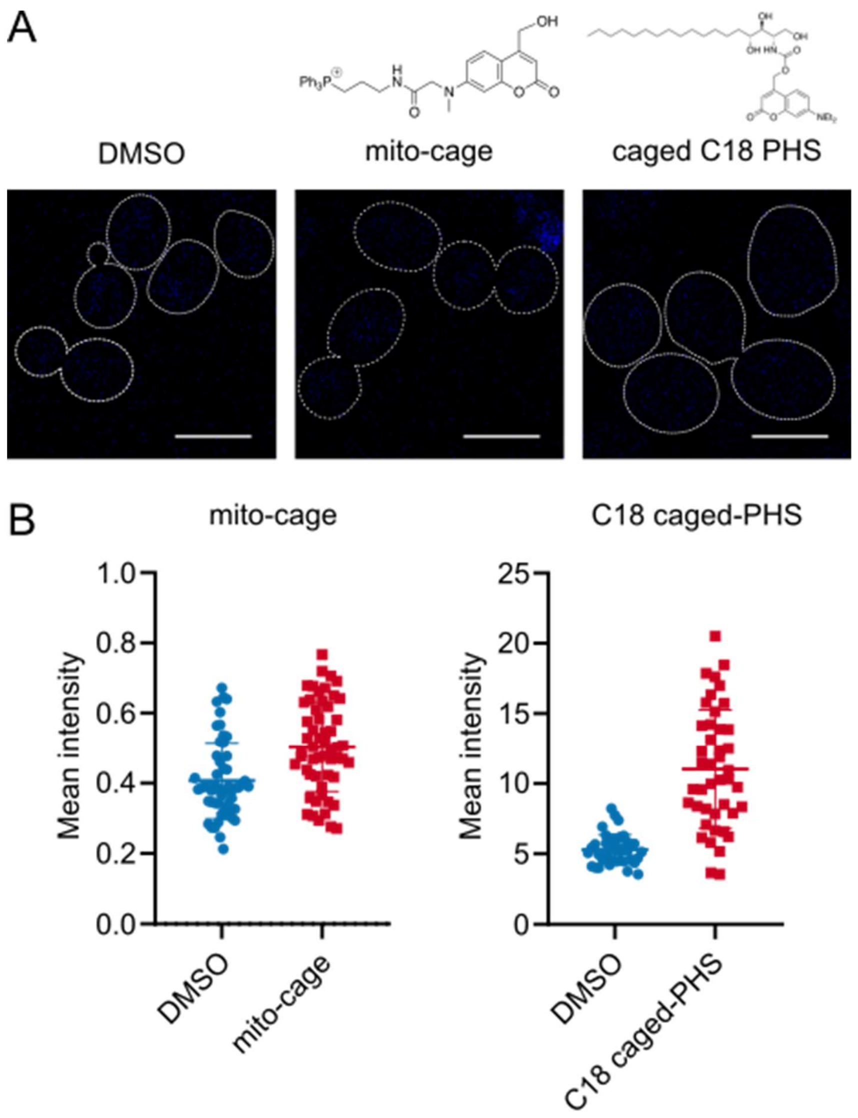

Figure 21. Caged PHS or mitochondrially-targeted cage alone are not internalized by the cells. A) WT cells grown in rich-medium were to exponential phase were incubated with 10 µM mito-cage or 50 µM C18-caged PHS (both dissolved in DMSO) for 15 min at 30ºC and imaged as described. Chemical structures of probes are shown above the images. Bars, 5 µm B) Quantification of mean fluorescent intensity of coumarin inside cells for samples shown in A. n > 50 cells, 3 biological replicates

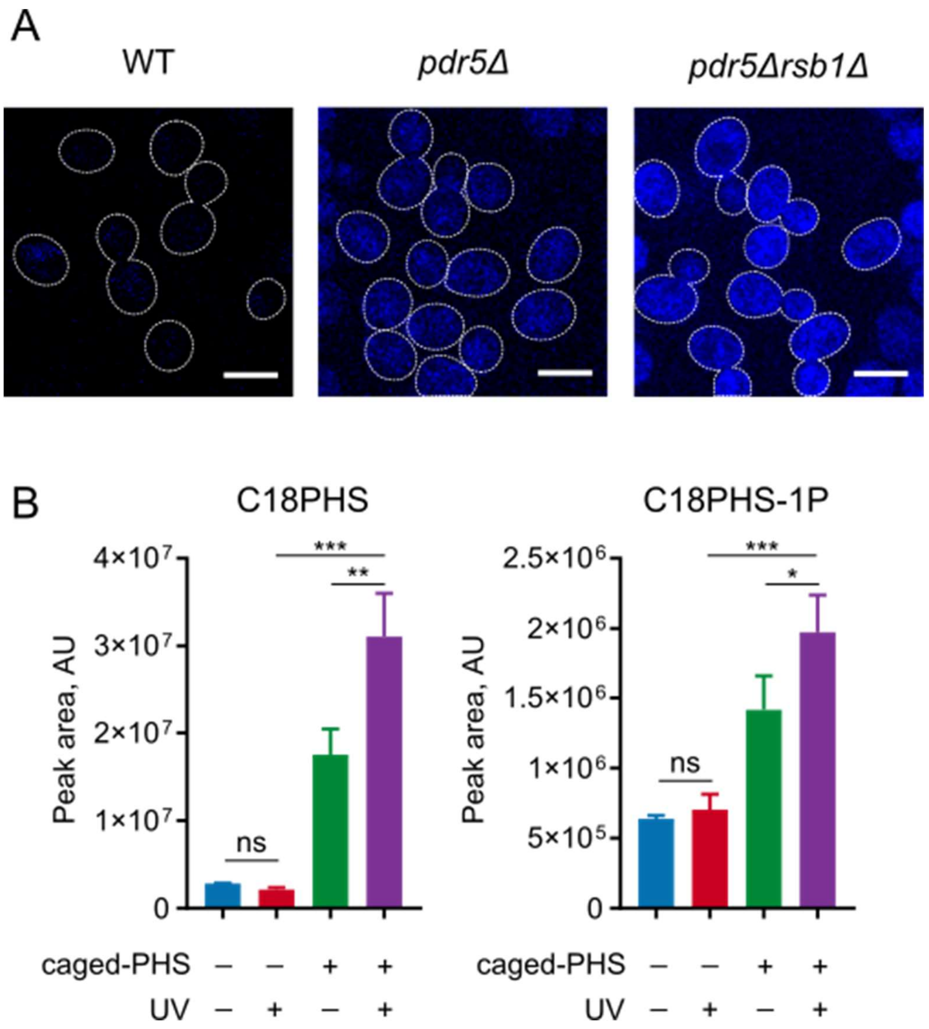

Figure 22. Multidrug transporter Pdr5 and putative long-chain base efflux transporter Rsb1 block the entry of caged C18PHS into the cells. A) Fluorescence microscopy images of the indicated yeast strains stained with caged C18PHS (shown in blue). WT, *pdr5Δ, pdr5Δrsb1Δ* cells grown to the early exponential phase were stained with 100 μM caged C18PHS and incubated for 60 minutes at 30ºC. Cells were washed and imaged as described using DAPI channel to observe caged PHS. Bars, 5 μm. B) Caged C18 PHS is internalized and can be released by UV irradiation *pdr5Δrsb1Δ* cells were cultured in rich medium to the exponential phase, labeled with 50 μM caged C18PHS or DMSO for 1 hour at 30ºC, washed and subjected to UV irradiation for 2 min on ice. Metabolites were extracted, derivatized with AQC and analyzed by LC-MS. Areas of the peaks corresponding to the indicated sphingolipid species were measured and normalized according to the internal standards. The values represent the means of three independent biological replicates. Statistical significance was determined using one-way ANOVA ($^*p<0.05$, $^{**}p<0.01$, $^{***}P<0.001$)

Growth on nonfermentable carbon source does not alter probe localization to the vacuoles

While the cage-only sphingolipid probes which are pumped out of the cells, the addition of TPP-targeting molecule promotes their fast and efficient vacuolar delivery. The targeting of TPP-containing compounds into mitochondria depends on mitochondrial membrane potential and TPP itself has been extensively employed for investigation of the electrochemical potential across the mitochondrial membrane (155). Since the mitochondrial membrane potential is generated as a result of electrochemical gradients formed by oxidative phosphorylation in mitochondria (156), the targeting of mito-probes might be altered in non-respiratory conditions with glucose as a carbon source. We hypothesized that the mito-probes may change their localization in respiratory conditions, when cells are grown on non-fermentable carbon sources such as glycerol. To test this assumption, yeast cells grown in YPG (containing 2% glycerol) were treated with C17 mito-PHS. However, the synthetic probe was still found mainly in the vacuoles and no association with mitochondria was observed (Figure 23).

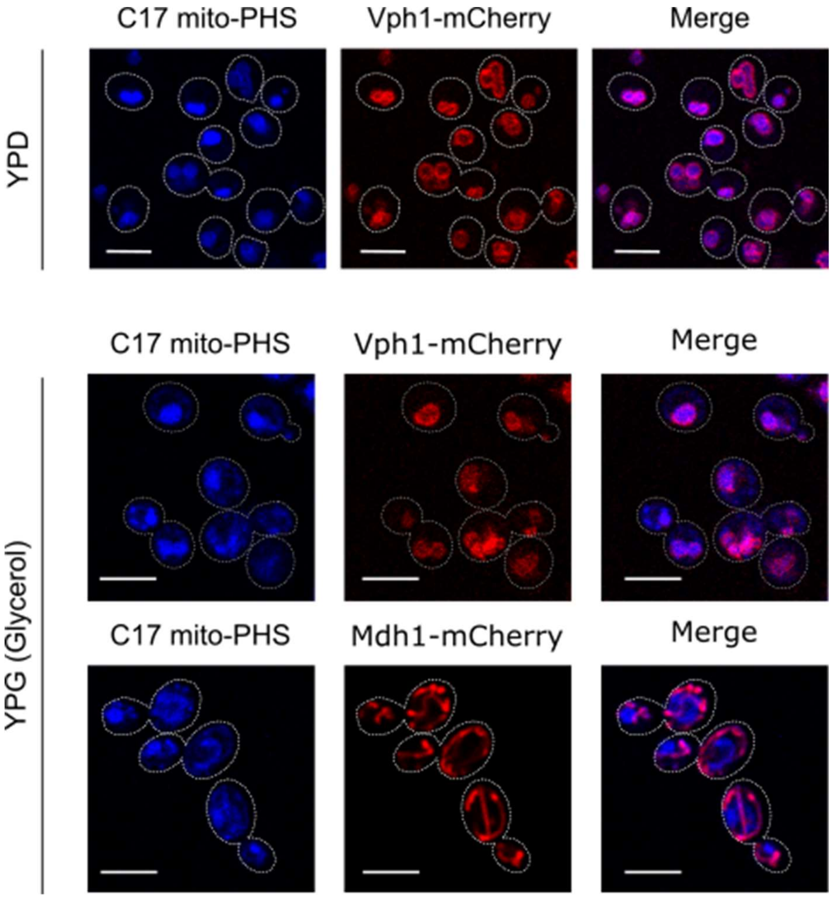

Figure 23. Growth on non-fermentable carbon source does not alter the localization of C17 mito-PHS. Representative fluorescent images of cells expressing mCherry-tagged mitochondrial (Mdh1) or vacuolar (Vph1) markers and stained with C17 mito-PHS (in DMSO). Cells were grown to the early exponential phase either in rich dextrose (YPD) or glycerol (YPG) medium, stained with 10 µM C17 mito-PHS for 20 min at 30ºC and imaged under the confocal microscope using the DAPI and mCherry channels. Bars, 5 µm

The abovementioned results show the vacuolar localization of mito-caged probes, yet throughout this work the prefix "mito" in relation to synthetic caged sphingolipids will be used, since the probes have been already published and characterized under this designation.

C17PHS Mito-caged sphingolipid probe is not toxic for the cells

Next, we addressed the toxicity of the probe. C17 mito-PHS did not affect cell growth even at higher concentration than those used for microscopy experiments (Figure 24), which suggests that the probe can be used in yeast cells.

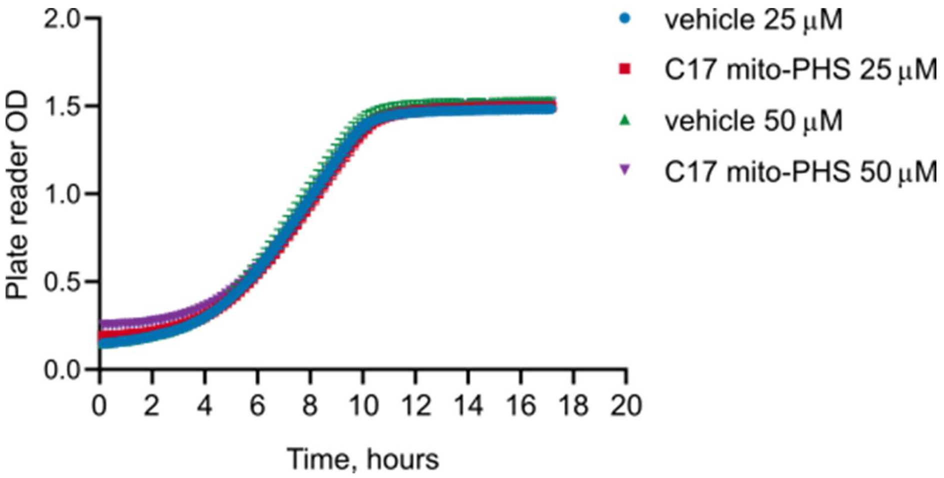

Figure 24. Growth of cells treated with C17 mito-PHS. WT cells grown overnight in YPD, diluted in YPD and the probe (C17 mito-PHS) at the indicated concentrations or vehicle (DMSO) was added to the cells. Cells were incubated in a plate reader and the growth was recorded by regular OD measurements over 18 hours at 30ºC. Individual values represent means of four biological replicates. Error bars show standard deviation (SD).

pH gradient is required for the vacuolar targeting of C17 mito-PHS

The vacuolar lumen has a lower pH compared to the cytosplasm due to the activity of vacuolar H^+-ATPases (V-ATPase) that couple ATP-hydrolysis with proton pumping (157). The difference in proton concentration generates potential across the vacuolae membrane akin to mitochondria. It was thus assumed that targeting of mito-probes to the vacuole might be abolished if the proton gradient is disrupted. To test this hypothesis the cells were treated with two compounds that affect proton gradient formation across intracellular organelles. The first is a potent protein uncoupler carbonyl cyanide m-chlorophenyl hydrazone (CCCP) that dissipates the proton gradient and therefore reduces the membrane potential in mitochondria and other organelles (158). Treatment with CCCP has been shown to abolish delivery of mito-sphingosine to mitochondria in mammalian cells (125). The second compound was Bafilomycin A1, a specific inhibitor of V-ATPase (159). Treatment with both CCCP and Bafilomycin A1 diminished the internalization of C17 mito-PHS as can be seen by the reduced fluorescent signal in the cells. (Figure 25, A and B). The effect of CCCP on probe uptake was stronger (Figure 25, B). It is known that CCCP can also affect vacuolar pH by increasing permeability of H^+ ions (157). Of note, the overall uptake of the probe is decreased not only in the vacuole which may suggest that the compound is efficiently pumped out unless delivered to the vacuole.

Fatty acyl-CoA synthetases mediate internalization of C17 mito-PHS

Since the chemical probes contain long-chain base protected by the cage, we speculated that the proteins involved in long-chain base uptake might affect probe internalization. It has been recently shown that yeast fatty acyl-CoA synthetases Faa1 and Faa4 are also involved in the uptake of long-chain bases (160). Fat1 is another acyl-CoA synthetase and fatty acid transporter (161). Indeed, the intracellular fluorescent signal corresponding to internalized C17 mito-PHS was significantly weaker in both *fat1Δ* and *faa1Δfaa4Δ* mutants. The signal was even lower in the triple mutant *fat1Δfaa1Δfaa4Δ* lacking all three proteins (Figure 26, A and C). In contrast no effect on the uptake was detected in the mutant lacking a putative long-chain base efflux protein, Rsb1 (Figure 26, B and D) (152). The data show that long-chain base importers might play a role in the uptake of mito-caged sphingolipid probes.

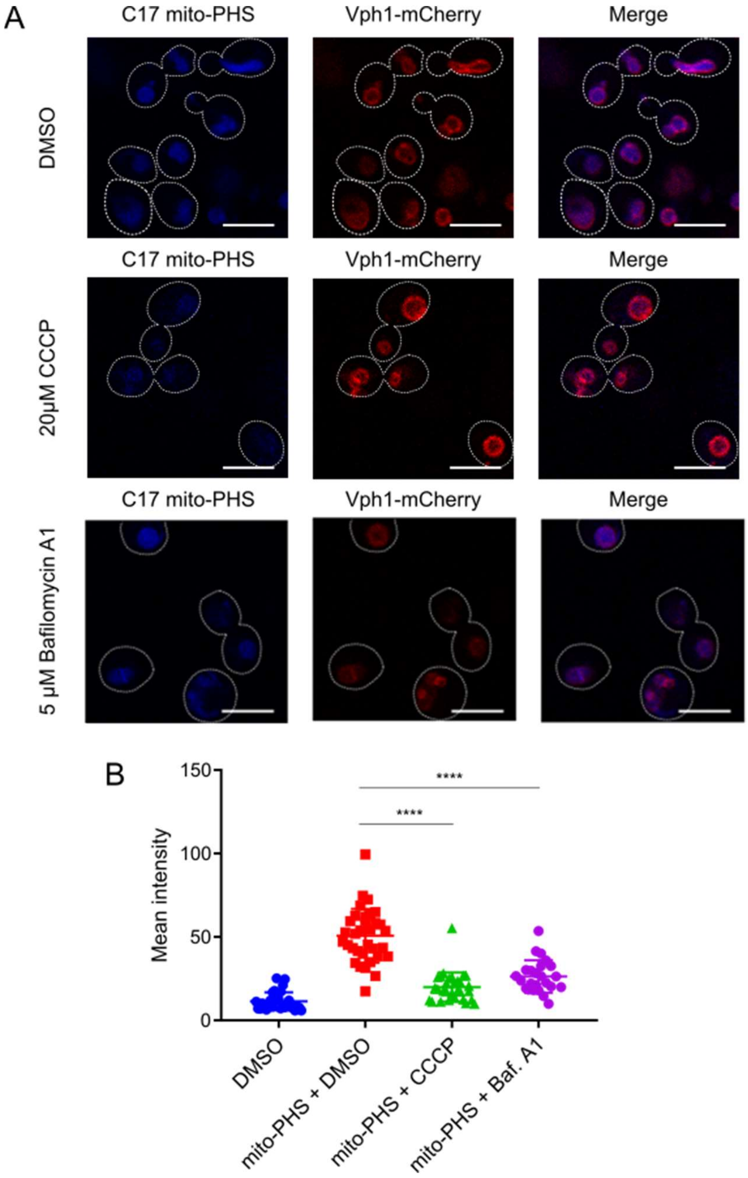

Figure 25. Disruption of proton gradient reduces internalization of C17 mito-PHS. A) Images of cells treated with CCCP and stained with C17 mito-PHS. Wild-type yeast cells expressing mCherry-tagged Vph1 were grown to mid-log phase in YPD, treated with 20 µM CCCP or 5 µM Bafilomycin A1 (both in DMSO) for 30 min at 30ºC followed by labeling with 20 µM C17 mito-PHS for 15 min. Samples were processed and imaged as described using the DAPI/mCherry channel. Bars, 5 µm. B) Quantification of mean fluorescence intensity inside cells of C17 mito-PHS from the images in A. n > 50 cells. Statistical significance was calculated using one-way ANOVA ****p<0.0001)

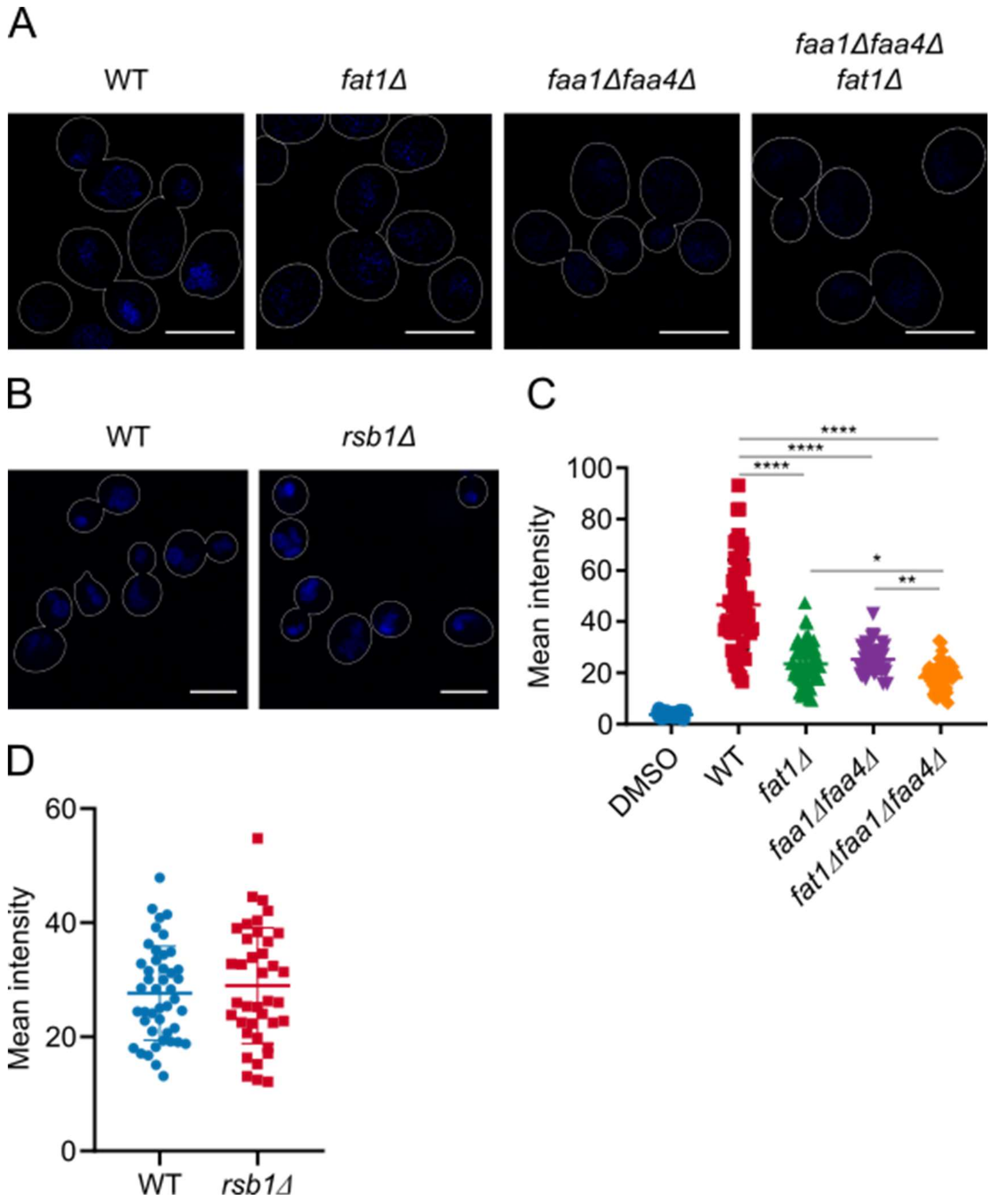

Figure 26. Deletion of fatty acyl-CoA synthetases downregulates the uptake of C17 mito-PHS. A) and B) Images of cell labeled with C17 mito-PHS (blue). The indicated yeast strains grown to mid-log phase in YPD were labeled with 10 µM C17 mito-PHS for 15 min at 30ºC and imaged as described using the DAPI channel. Bars, 5 µm. C) and D) Quantification of intracellular fluorescent signal of coumarin from images in A (C) or B (D). n = 60 cells. Statistical significance was calculated using a one-way ANOVA (*p<0.05, **p<0.01, ****p<0.0001)

Endocytosis is not responsible for internalization of mito-caged C17PHS

Endocytosis is the process of whereby cells internalize extracellular material or parts of the plasma membrane by confining them into vesicle that pinch off the cell surface and are eventually delivered into the vacuole for degradation (162).

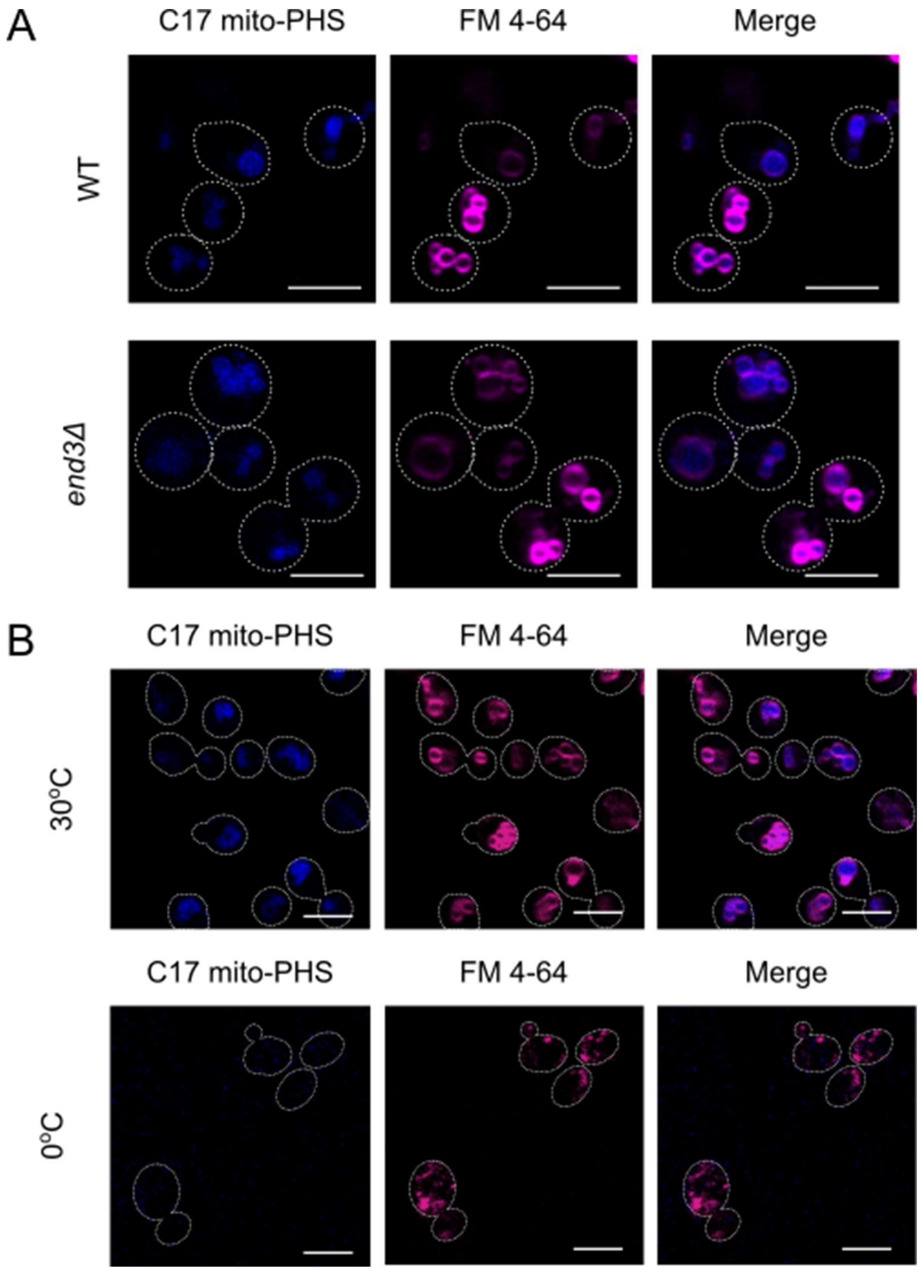

Figure 27. C17 mito-PHS entry into the cells is endocytosis independent. Fluorescent images of cells stained with FM 4-64 (magenta) and C17 mito-PHS (blue). A) WT and *end3Δ* cells were grown to the exponential phase, incubated with 6 μM FM 4-64 and 10 μM C17 mito-PHS for 20 min at 30°C prepared

for microscopy as described in methods and imaged using DAPI/mCherry channels. B) WT cells were culture to the exponential phase at 30ºC, stained as described in A. at 30ºC or 0ºC. mito-PHS and FM 4-64 were viewed using DAPI and mCherry channels, respectively. Bars, 5 µm.

We assumed that endocytic internalization may in part account for the delivery of mito-caged probes into the vacuole. To test this hypothesis cells lacking End3 protein were treated with C17 mito-PHS. End3 is protein involved in the internalization step of endocytosis (163, 164). However, the mitocage-compound was still internalized in *end3Δ* cells along with FM 4-64 (Figure 27, A), a styryl dye which marks the vacuolar membrane after internalization (165). FM 4-64 uptake is partially dependent of End3 and is a marker of bulk membrane endocytosis. Though, most endocytic events are blocked at low temperature (<4ºC) (166). When cells were incubated on ice, FM 4-64 uptake was blocked resulting in formation of FM 4-64 puncta at the cell periphery. Unlike FM 4-64, C17 mito-PHS did not enter the cells (Figure 27, B). The fact that C17 mito-PHS was not found in the same intermediate endocytic compartments as FM 4-64 argues that endocytosis does not account for the probe vacuolar targeting. Impaired uptake at low temperature might be due to the decreased activity of transporters and not the block in endocytosis.

Metabolism of sphingolipids uncaged from vacuole-targeted probes

UV uncaging of mito-caged sphingolipid probes in yeast cells

Vacuole-targeted probes are cleaved leading to the unspecific sphingolipid release

We observed the localization of synthetic mito-caged sphingolipid probes to the vacuoles in budding yeast cells. We further inquired whether the long-chain bases can be released from the caged-probe by UV irradiation in living cells. It has been shown before that mito-caged probes are stable and do not spontaneously decompose in solution and remain stable when delivered to mitochondria (125). The yeast vacuole is the degradative organelle, a confinement for active hydrolytic enzymes, therefore the stability of the chemical probes might be compromised in yeast. First, we tested if the exposure of yeast cells to powerful ultraviolet light pulses would affect cell viability. Fortunately, UV exposure did not significantly alter the number of colony-forming units indicating the absence of deleterious long-term effects (Figure 28, A and B). After that we analyzed sphingolipid levels in probe-treated cells after UV uncaging. In cells incubated with C18 mito-sphinganine and irradiated with UV light we saw a sharp specific

UV-triggered increase of “uncaged” C18 sphinganine (Sa). The exposure to UV alone did not cause any effect on C18Sa levels (Figure 28, C).

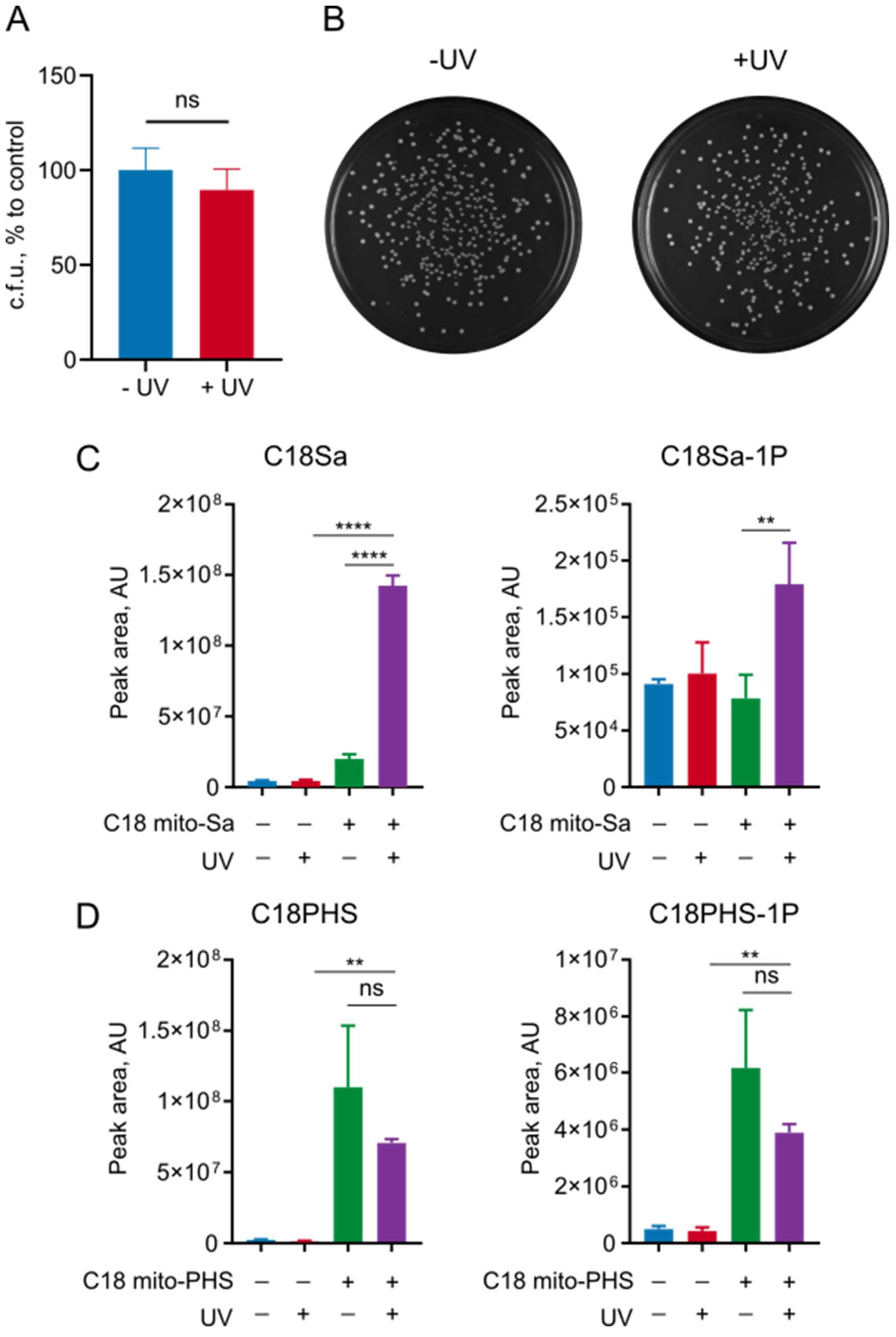

Figure 28. UV uncaging of sphingolipids in yeast cells. A, B) The effect of UV irradiation on cell viability. Wild-type yeasts (BY4741) grown to the exponential phase were irradiated with UV light for 2 min on ice, diluted in sterile distilled water, streaked onto YPUAD plates and incubated at 30ºC for 2 days. The resulting colonies (colony forming units, c.f.u.) were counted and the mean value for unirradiated control cells was set to 100%. B) Representative plate images of cells in (A) C, D) Sphingolipid analysis of mito-cage-labeled cells. Wilt-type yeast cells (BY4741) were grown to OD_{600} of 1, labeled with 10 µM C18 mito-Sa (C) or C18 mito-PHS (D) (both in DMSO) for 20 min at 30ºC, washed and irradiated with UV light (wavelength 350-450 nm) for 2 min on ice and collected immediately. Metabolites were extracted, derivatized with AQC and analyzed by LC-MS. Areas of the peaks corresponding to the indicated sphingolipid species were measured and normalized according to internal standards. The values represent the means of three independent biological replicates. Statistical significance was determined using one-way ANOVA for panels C and D and Student t test for panel A (**$p<0.01$, ****$p<0.0001$, ns – not significant). Error bars show standard deviation.

UV-uncaging also lead to an increase in the amounts of phosphorylated Sa and PHS, the upregulation of Sa-1P was rather moderate (Figure 28, C and D). Importantly, the unspecific release of sphingoid base in the absence of UV irradiation was detected for both mito-Sa and mito-PHS. The percentage of unspecific release for mito-Sa was about 15% while mito-PHS was efficiently cleaved and no difference was found between control and UV-irradiated samples (Figure 28, C and D). Difference in unspecific cleavage of mito-caged species suggests substrate specificity of hydrolytic enzymes. The UV-independent release of sphingoid-base was also detected for C17PHS and was less pronounced compared to C18 mito-PHS (Figure 29, A). Reducing the incubation time or temperature did not diminish unspecific cleavage of C17 mito-PHS (Figure 29, B and C).

Deletion of proteinase A or ceramidases does not reduce unspecific probe cleavage

UV-independent cleavage of mito-cage probes (“leaking”) might result from hydrolytic activity of vacuolar enzymes. The extensively studied aspartyl protease Pep4 in *S. cerevisiae* is known to be required for the maturation and activity of vacuolar hydrolases (167). Hence, the unspecific probe cleavage might hypothetically be decreased in *pep4Δ* mutants. However, the results refuted the assumption showing the same magnitude of unspecific “leaking” in the strain with deleted *PEP4* gene (Figure 29, D). Another assumption was that the caged probe distantly resembled ceramide molecules and could be recognized and cleaved by ceramidases, especially that GFP-tagged ceramidase Ydc1 shows a vacuolar localization (168, 169).Once more, the data argues that ceramidases do not play a role in mito-PHS cleavage, as the mutant lacking both yeast ceramidases Ypc1 and Ydc1 has the same rate of unspecific C18PHS release (Figure 29, E).

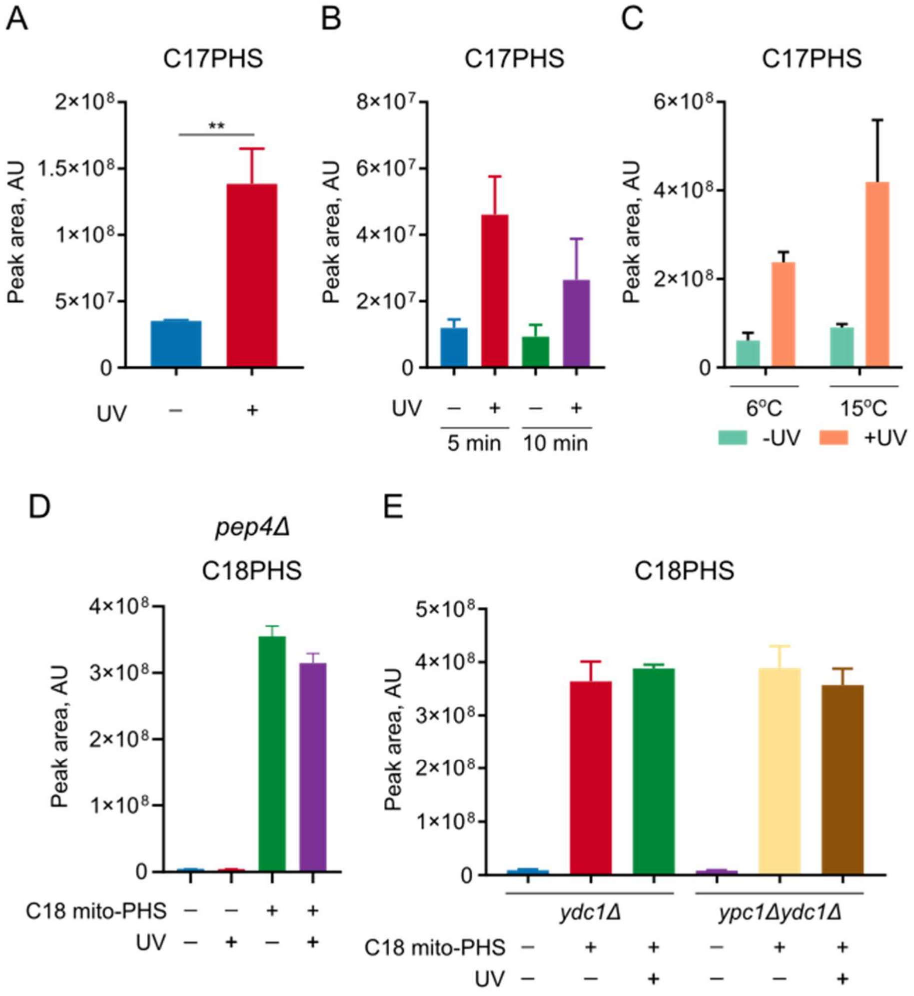

Figure 29. Testing different conditions to reduce unspecific cleavage of C18 mioto-PHS. A-C) Wild-type cells (BY4741) were grown to OD_{600} of 1 and labeled with 10 µM C17 mito-PHS for 20 min (A and C), 5 or 10 min (B) at 30ºC (A and B), 6 or 15ºC (C). D and E) *pep4Δ* (D), *ydc1Δ* , *ydc1Δypc1Δ* (E) mutants were grown to the exponential phase (OD_{600}=1) and incubated with 10 µM C18 mito-PHS for 20 min at 30ºC, washed and irradiated with UV light (wavelength 350-450 nm) for 2 min on ice and collected immediately. A-E) Metabolites were extracted, derivatized with AQC and analyzed by LC-MS. Areas of the peaks corresponding to C17PHS (A-C) or C18PHS (D-E) were measured and normalized according to the internal standards. The values show the means of three biological replicates, error bars represent standard deviation. Statistical significance in panel A was calculated using Student t test (**p <0.01)

Metabolism of UV-uncaged sphingoid bases

Uncaged sphingolipids are metabolized into C44 C-class ceramides

Once we could see that sphingoid bases can be efficiently released by UV irradiation, we next sought to investigate their conversion to ceramides and complex sphingolipids. Multiple-reaction monitoring mass spectrometry (MRM-MS) was used to detect and quantify different sphingolipid molecules from complex lipid mixtures (134).

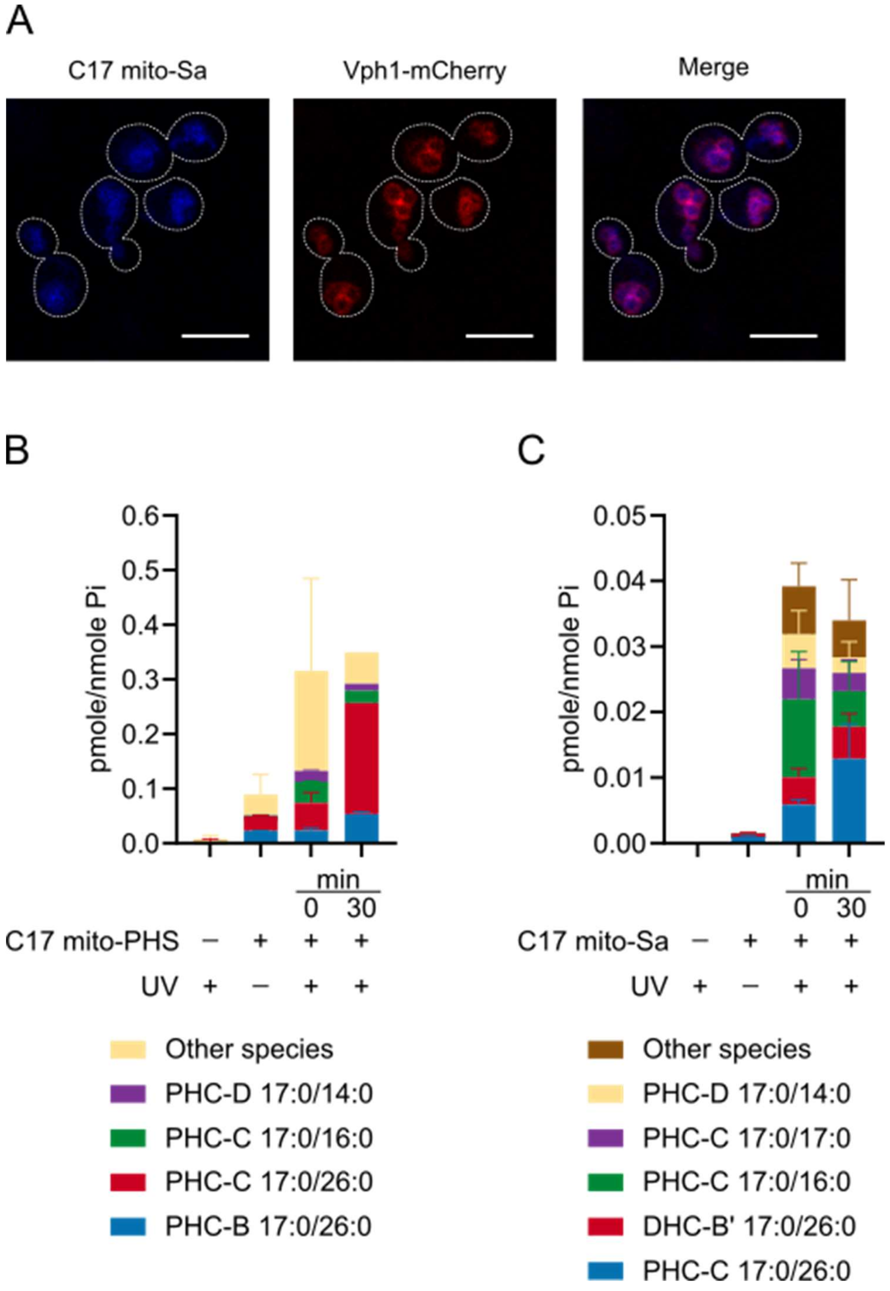

Figure 30. Stacked bar charts representing distinct ceramide species of cells labeled with C17 mito-PHS (B) or C17 mito-Sa (C). A) Fluorescent microscopy images of wild-type cells expressing mCherry-tagged vacuolar marker Vph1 and stained with 10 µM C17 mito-Sa 15 min at 30ºC. C17 mito-Sa was imaged with a DAPI channel. Bars, 5 µm. B and C) Wild-type yeast cells (BY4741) were grown in YPUAD to the exponential phase and labeled with C17 mito-PHS or C17 mito-Sa (20 µM final) or DMSO (vehicle) for 20 min at 30ºC. Mito-caged compounds were irradiated with UV light for 2 min on ice and collected immediately or after 30 min incubation at 30ºC in YPUAD. Lipids were extracted and processed as described and C17-sphingolipid species were analyzed by mass spectrometry. Internal standard-normalized values of C17 species were further refined by subtracting the background signals corresponding to DMSO-treated controls. The values represent the pmoles of lipids per nmole of inorganic phosphate, showing the means of three biological replicates. Errors bars represent standard deviation.

To investigate sphingolipid metabolism mito-cage probes containing non-natural odd-chain sphingoid bases were utilized: C17 Phytosphingosine (C17PHS) and C17 Sphinganine (C17 Sa). C17PHS has already been utilized in yeast to monitor sphingolipid biosynthesis (170). Similar to C17 mito-PHS, C17 mito-Sa probe localized to the vacuoles in yeast cells (Figure 30, A). Next, we characterized sphingolipid profiles of wild-type cells labeled with C17 mito-PHS or mito-Sa. DMSO-treated cells not subjected to UV irradiation were used as a control condition. First, we noticed that UV irradiation alone did not introduce artifact that could be detected as C17 ceramide species (Figure 30, A, B). Consistent with the above-mentioned partial cleavage of C17-mito PHS we could detect C17-ceramides before UV-uncaging. UV-irradiation induced the formation of C17-ceramides, which was more evident after 30 min of post-uncaging incubation (Figure 30, A) The most abundant ceramide species generated from UV-released C17PHS were PHC-C 17:0/26:0 and PHC-B 17:0/26:0 which represent the most abundant naturally-occurring yeast ceramides. The predominant ceramides derived from uncaged C17 sphinganine were PHC-C 17:0/26:0 and DHC-B’ 17:0/26:0 with PHC-C species increasing over time which indicates Sur2 hydroxylase activity converting sphinganine into PHS (15). The presence of DHC-B’ points to the activity of Scs7 hydroxylase (15) (Figure 30, B). In contrast to mito-PHS, C17 mito-Sa was more stable and there were barely detectable amounts of C17-ceramides before UV irradiation (Figure 30, A, B). Of note, the overall amounts of ceramides made from C17PHS was almost 10-fold higher (~0.3 versus ~0.03 pmole/nmole Pi) than those generated from C17Sa (Figure 30, A, B)

Vacuole-derived and exogenously added C17-PHS are similarly metabolized

Next, we compared the profiles of sphingolipids synthesized from UV-uncaged long-chain bases versus those made from exogenously added C17PHS or C17Sa. The results showed that most ceramides synthesized from both exogenously-added and uncaged C17PHS were represented by two ceramide species – 17:0/26:0 (C43) PHC-B and PHC-C. While the levels of C43 PHC-B were comparable the abundance of C43 PHC-C species was higher when C17PHS was exogenously supplied (Figure 31, A). Consistent with ceramide profile, the pool of complex sphingolipids consisted predominantly of species derived from C43(17:0/26:0) PHC-C ceramides no matter whether the C17 long-chain base was provided externally or was released from the vacuole (Figure 31, B and C).

Total amounts of C17Sa-derived sphingolipids were much lower compared to the C17PHS-generated pool. The profile of ceramides synthesized from C17Sa also differed considerably depending on whether the sphingoid bases were UV-released or supplied externally. C17Sa taken up from the medium was either acylated with C26 fatty acid forming DHC-A 17:0/26:0 species, or was acylated with C22 fatty acid and hydroxylated yielding DHC-B’ 17:0/22:0 ceramide, with the two species making up nearly 100% of C17-derived ceramides. When C17Sa was uncaged with UV light, it labeled a range of different ceramides most prominent of which were DHC-A, DHC-B’, PHC-C species with a C26-fatty acyl chain. The overall amount of ceramides made from externally-added C17Sa was higher compared to the ceramide pool generated by UV-uncaged C17Sa (Figure 31, A). The composition of C17-derived complex sphingolipids was also different: the majority of IPC and MIPC species were derived from C43 dihydroceramide (DHC-A C17:0/C26:0) in externally-labeled samples, while 17:0/26:0 B-class ceramides (both DHC and PHC species) composed most of the IPC and MIPC pools in mito-Sa treated cells (Figure 31, B and C). It is worthwhile to note, that as the signals corresponding to C17Sa-generated sphingolipids were low, there was much higher chance of detecting artifacts, signals not truly representing the detected species. The sphingolipids made from C17PHS, in contrast, show higher signals and consistent results, when the ceramide profiles match those of complex sphingolipids, which was not true for C17Sa tracer. Therefore, C17 mito-PHS was a probe of choice for subsequent experiments. M(IP)$_2$C species derived from C17 sphingolipids were not included in the analysis since many endogenous and C17-labeled species could not be distinguished due to the mass resolution limits of the mass spectrometer in the MRM mode.

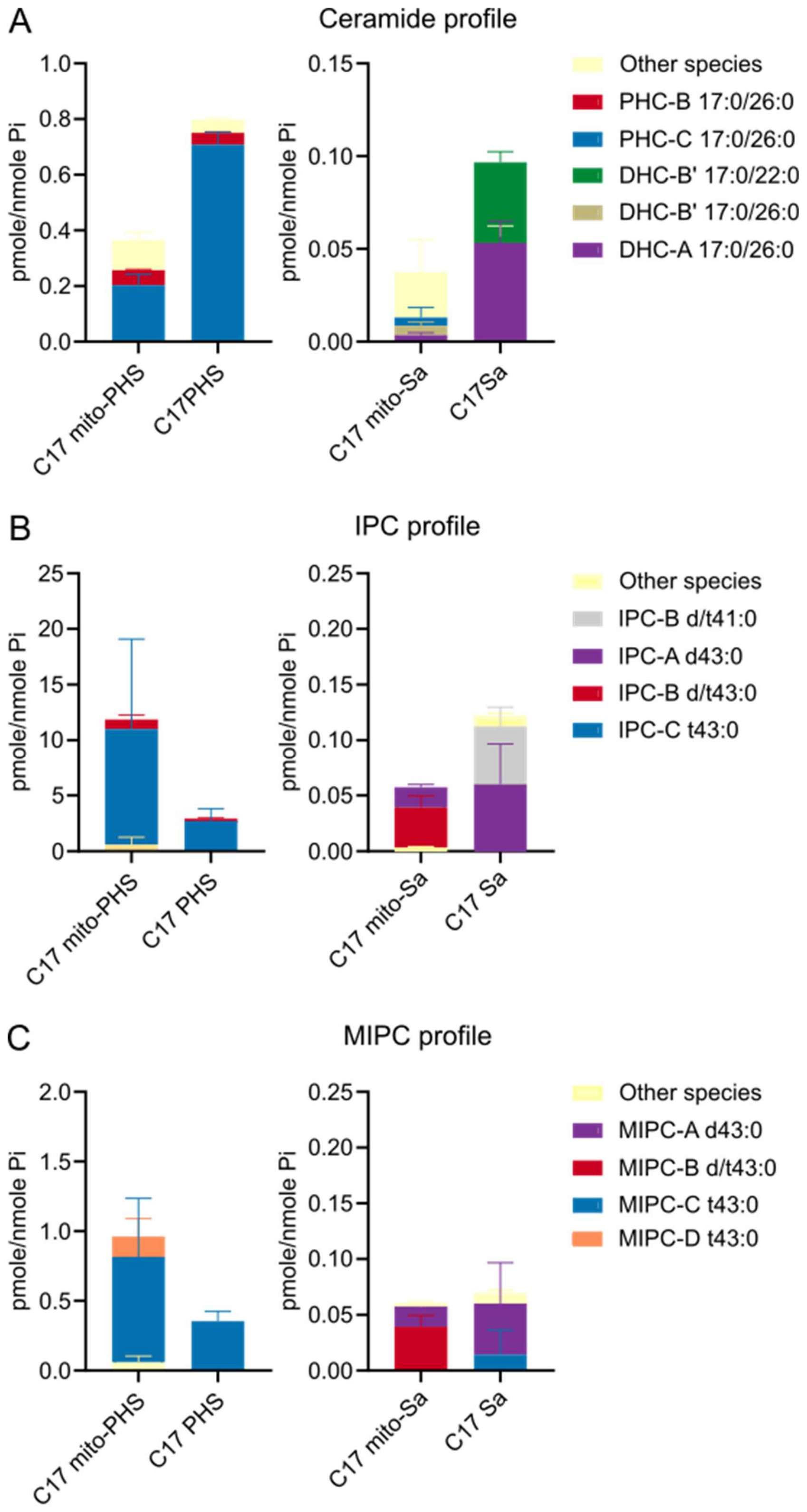
A
Ceramide profile
pmole/nmole Pi
1.0
0.8
0.6
0.4
0.2
0.0
C17 mito-PHS
C17PHS
0.15
0.10
0.05
0.00
C17 mito-Sa
C17Sa
Other species
PHC-B 17:0/26:0
PHC-C 17:0/26:0
DHC-B' 17:0/22:0
DHC-B' 17:0/26:0
DHC-A 17:0/26:0
B
IPC profile
25
20
15
10
5
0
C17 mito-PHS
C17 PHS
0.25
0.20
0.15
0.10
0.05
0.00
C17 mito-Sa
C17 Sa
Other species
IPC-B d/t41:0
IPC-A d43:0
IPC-B d/t43:0
IPC-C t43:0
C
MIPC profile
2.0
1.5
1.0
0.5
0.0
C17 mito-PHS
C17 PHS
0.25
0.20
0.15
0.10
0.05
0.00
C17 mito-Sa
C17 Sa
Other species
MIPC-A d43:0
MIPC-B d/t43:0
MIPC-C t43:0
MIPC-D t43:0

Figure 31. Stacked bar chart profile of ceramides and complex sphingolipids derived from C17 mito-PHS/Sa or C17 PHS/Sa. Wild-type yeast cells (BY4741) were grown in YPUAD to the exponential phase and labeled with C17 mito-PHS, C17 mito-Sa, C17PHS, C17Sa (20 µM final concentration, in DMSO) for 20 min at 30°C.Samples incubated with mito-caged compounds were irradiated with UV light for 2 min on ice, resuspended in fresh YPUAD and further incubated for 30 min at 30°C. C17PHS/Sa-labeled samples were treated similarly except no UV irradiation was applied. Lipids were extracted and the C17-sphingolipid species were analyzed by mass spectrometry. The data was normalized by internal standards and values corresponding to DMSO controls were subtracted from C17-derived species. The values show the means of three biological replicates. Error bars represent standard deviation.

Disruption of nucleus-vacuole junctions partially affects ER-to-vacuole transport of C17 PHS

Here it has been shown that vacuole-targeted caged sphingolipid probes can be released by UV-irradiation and their enzymatic conversion into more complex species can be studied *in vivo*. The vacuole and the nuclear ER form contacts known as nucleus-vacuole junctions (NVJs) (65, 72). It is still unclear if sphingolipids can be moved across NVJs and which proteins mediate the transport. Biosynthesis of ceramides and subsequent enzymatic modifications such as hydroxylation take place in the ER. (15, 171, 172). This means that sphingoid base released by UV-irradiation from the vacuole-targeted synthetic probe must be transported to the ER where it can be further converted into ceramides. To test if the conversion of UV-released C17PHS depends on contact sites we used a quadruple mutant (ΔNVJ) lacking all known NVJ proteins – Nvj1, Nvj2, Nvj3, Mdm1. Electron microscopy images have shown the lack of ER-vacuole contacts in this mutant (75).

First, we observed that the quadruple *nvj1Δnvj2Δnvj3Δmdm1Δ* mutant (ΔNVJ) mutant cells grew normally, like the wild-type cells (Figure 32, A). Next, we investigated the localization of C17 mito-PHS probe in the ΔNVJ strain. As can be seen on (Figure 32, B), C17 mito-PHS probe localized to the vacuoles. Finally, the incorporation of UV-released C17PHS into ceramide species was assessed over time after UV-uncaging in both strains. Consistent with the previous results, the most abundant background-subtracted C17PHS-dirived ceramides were PHC-B and PHC-C 17:0/26:0 species (Figure 33). Interestingly, the amount of class B ceramide species PHC-B 17:0/26:0 was lower after 20 and 40 minutes after UV-uncaging, reaching a statistically significant difference at 60 minutes. (Figure 33). Some difference in the levels of PHC-C ceramide could be seen at 40- and 60 minutes post-uncaging. Moreover, the mean amounts of all C17-ceramides and all C17-IPCs were lower at all time points. However, all these differences were not statistically significant due to high variability which may be explained by the low signal intensity of minor C17 sphingolipids (Figure 33).

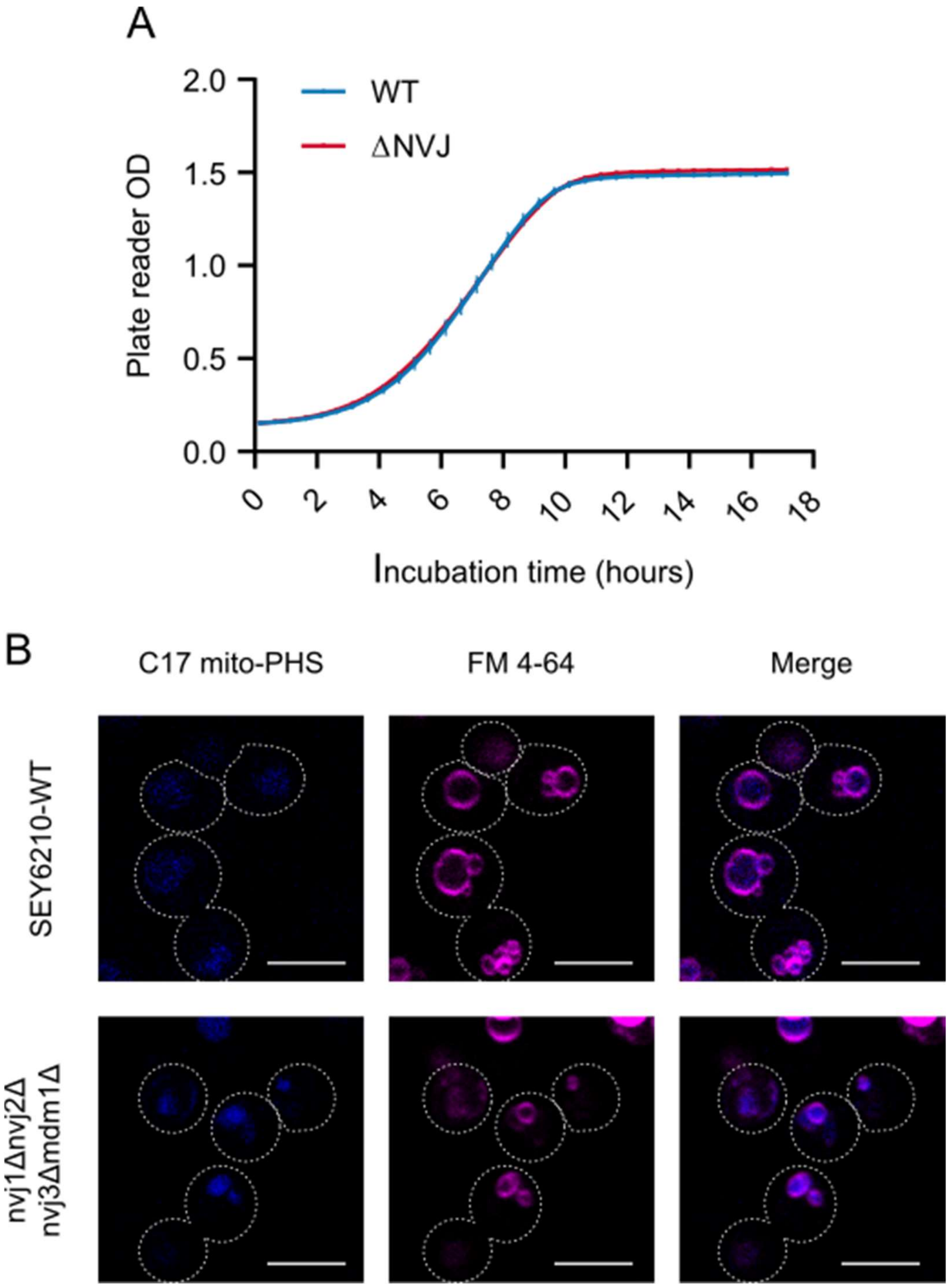

Figure 32. C17 mito-PHS is targeted to the vacuoles in cells NVJ-lacking cells. A) Growth curves of WT (SEY6210) or ΔNVJ (*nvj1Δnvj2Δnvj3Δmdm1Δ*) cells. Cells were grown overnight in YPUAD. Diluted cell suspensions were incubated in a plate reader and the growth was recorded by regular OD measurements over 18 hours at 30ºC. Individual values represent means of four biological replicates.

Error bars represent standard deviation B) Fluorescent images of WT or ΔNVJ cells stained with 10 µM C17 mito-PHS (blue). Vacuoles were visualized by staining with 6 µM FM 4-64 (magenta). Bars, 5 µm.

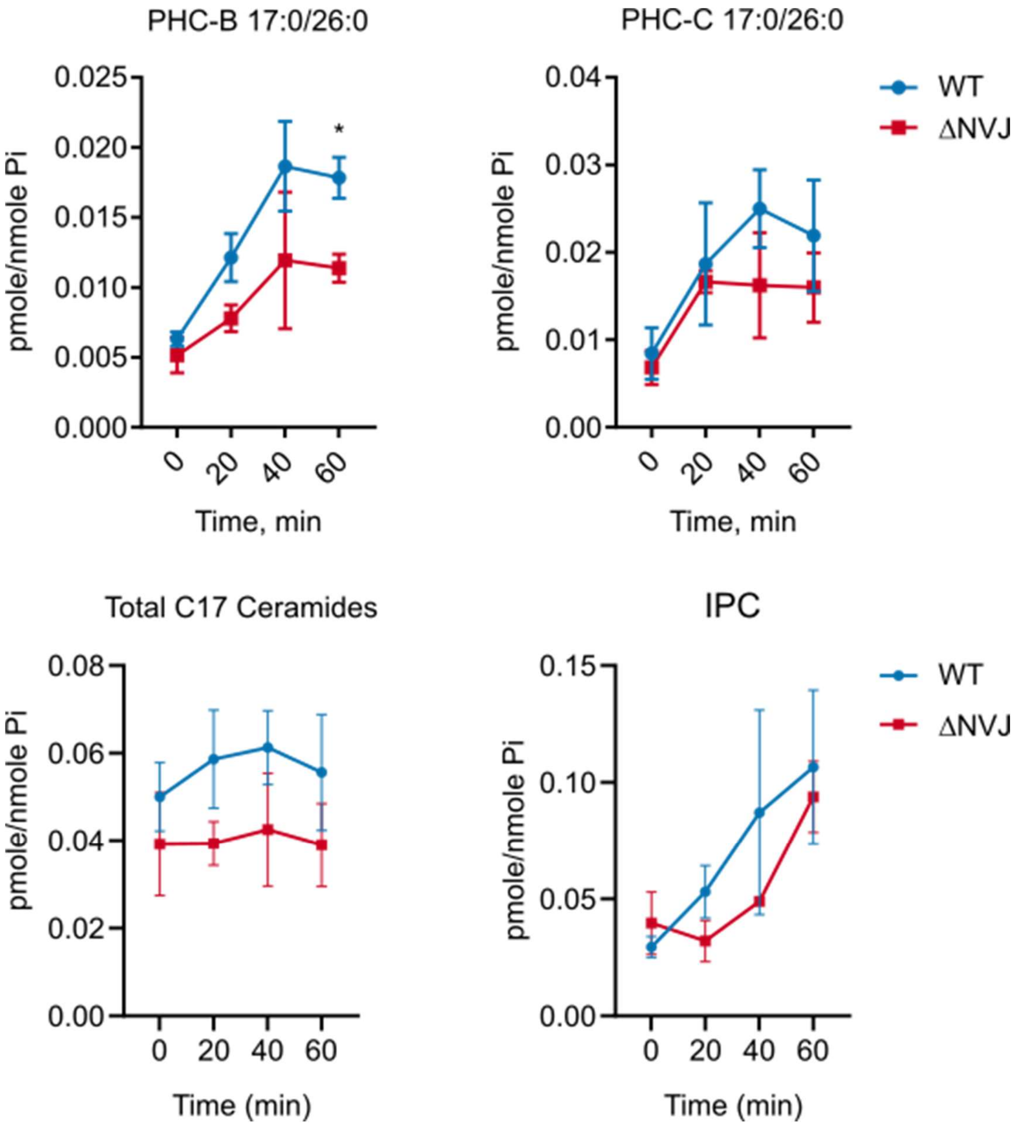

Figure 33. Time course lipidomics analysis of C17 ceramides after UV-uncaging in WT or ΔNVJ cells. Wild-type cells (SEY6210) or ΔNVJ ((*nvj1Δnvj2Δnvj3Δmdm1Δ*) were grown in YPUAD to the exponential phase and labeled with C17 mito-PHS (5 µM final) or DMSO for 20 min at 30°C. The cells were washed, irradiated with UV light for 2 min on ice, re-suspended in fresh YPUAD medium and further cultered at 30°C. Samples were collected after 20, 40, 60 minutes of incubation. Lipids were extracted and processed as described and C17-sphingolipid species were analyzed by mass spectrometry. Internal standard-normalized values of C17 species were further refined by subtracting

the background signals corresponding to DMSO-treated controls. The values represent the pmoles of lipids per nmole of inorganic phosphate, showing the means of three biological replicates. Statistical significance was inferred using Student t test (*p<0.05). Error bars represent standard deviation.

Overexpression of NVJ protein Mdm1 accelerated the metabolic conversion of the uncaged C17PHS into ceramides and complex sphingolipids.

Before we hypothesized that the contact sites between the ER and the vacuole might be important for sphingolipid transport. The overexpression of Mdm1, a NVJ-resident protein, has been shown to increase the area of contact between the organelles (75). Furthermore, it has been demonstrated that Mdm1 could bind free fatty acids and assist in their transport to lipid droplets in vicinity to the ER-vacuole contact sites (78). Therefore, we speculated that the enlarged contact area between the nuclear ER and the vacuoles may facilitate the conversion of long-chain bases released at the vacuole into ceramides in the ER. For this, yeast cells were transformed with a plasmid where GFP-tagged Mdm1 is expressed under a strong constitutive GPD promoter (75). As seen in (Figure 34, A), overexpressed Mdm1 was localized close to the vacuoles stained by FM4-64. Importantly, vacuolar targeting of C17 mito-PHS probe was not changed by Mdm1 overexpression (Figure 34, A). Next, the cells overexpressing Mdm1 and control cells transformed with an empty vector were labeled with C17PHS mito-cage probe, subjected to UV-irradiation and the levels of C17 ceramides and IPCs were measured over the course of 60 minute-incubation following the UV-uncaging. As early as at zero time point, the amounts of PHC-B 17:0/26:0 ceramides were already higher in the Mdm1-overexpressing cells. Moreover, although the levels of PHC-B steadily increased over time in control cells, Mdm1 overexpression notably accelerated PHC-B *de novo* biosynthesis, so that at all time points the differences were significant (Figure 34, B). The product of Scs7-mediated hydroxylation of PHC-B, PHC-C 17:0/26:0, showed a significant increase later, at 60 minutes after uncaging (Figure 34, B). Total levels of C17PHS-derived ceramides were upregulated at 0-, 20- and 60-minutes upon Mdm1 overexpression. The sudden drop in total levels at 40 minutes is due to the sharp decrease in other minor ceramides (PHC-B 17:0/24:0, PHC-D 17:0/18:0, PHC-D 17:0/26:0) (Figure 34, B). Importantly, the most noticeable boost in metabolic conversion by Mdm1 expression was evident for inositolphosphorylceramides (IPCs) (Figure 34, B).

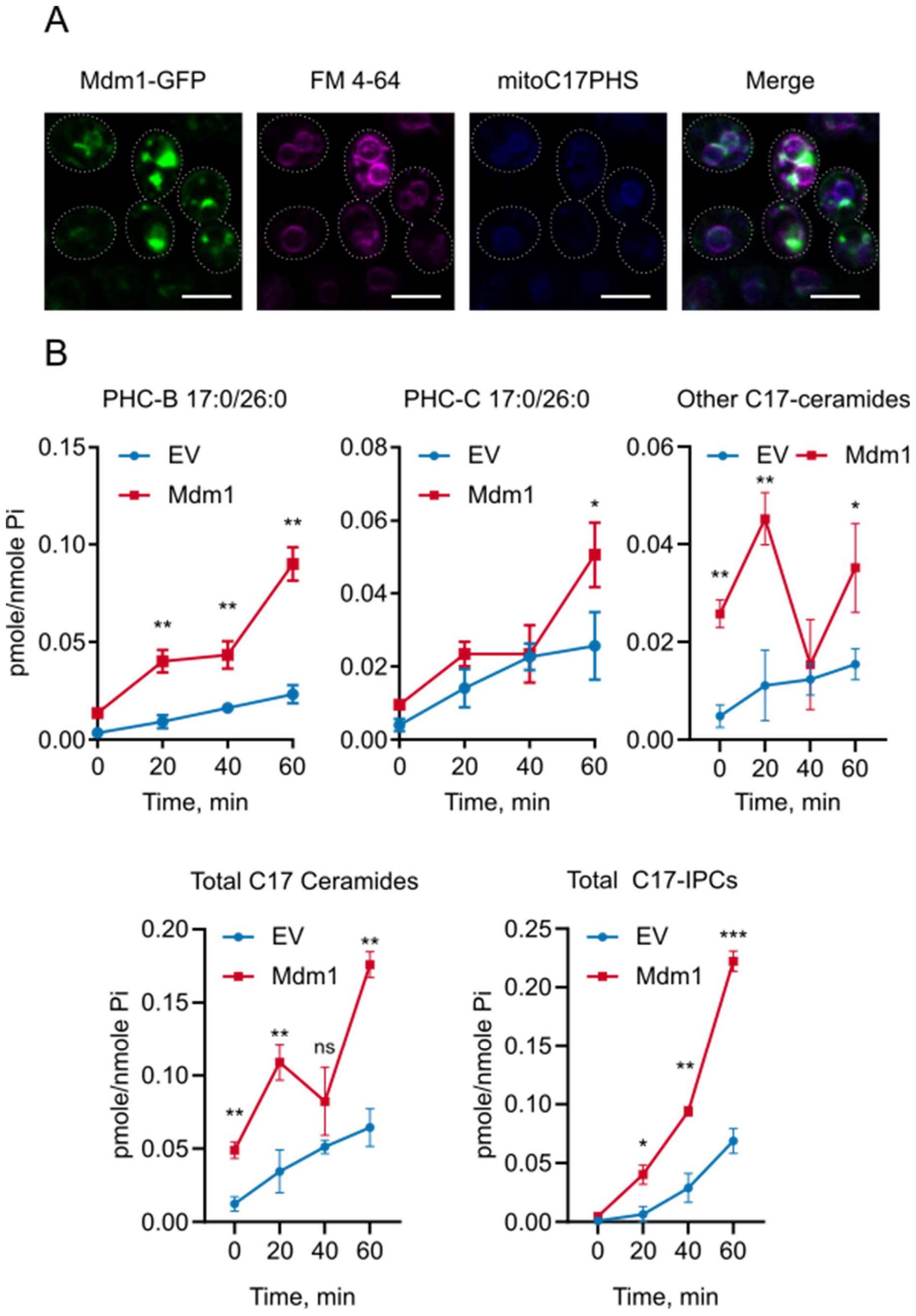

Figure 34. Mdm1 overexpression increases conversion of C17PHS into ceramides and complex sphingolipids. A) Fluorescence microscopy images of cells overexpressing GFP-tagged Mdm1 (green)

stained with C17 mito-PHS (blue). Wild-type cells transformed with Mdm1-GFP overexpressing plasmid (pBP73G-Mdm1-GFP) were grown to the exponential phase in the selective SD lacking uracil. Cells were first stained with 6 µM FM 4-64 (shown in magenta) for 30 min, at 30ºC, washed and stained with 10 µM C17 mito-PHS for 20 min at 30ºC. Cells were washed and imaged as described, using DAPI, GFP and mCherry channels. B) Time course lipidomics analysis of C17 sphingolipids after UV-uncaging in cells overexpressing Mdm1 protein. Wild-type cells transformed with Mdm1-GFP overexpressing plasmid (pBP73G-Mdm1-GFP) or empty vector (pBP73G) were cultured in SD minus Uracil medium to OD_{600}=1, incubated with 5 µM C17 mito-PHS or DMSO for 20 min at 30ºC, washed and subjected to UV-irradiation for 2 min on ice. Cells were resuspended in fresh SD medium and cultured at 30ºC and collected at the indicated time points. Lipids were extracted and processed as described and C17-sphingolipid species were analyzed by mass spectrometry. Internal standard-normalized values of C17 species were further refined by subtracting the background signals corresponding to DMSO-treated controls. The values represent the pmoles of lipids per nmole of inorganic phosphate, showing the means of three biological replicates. Statistical significance was inferred using Student t test (*$p<0.05$, **$P<0.01$, ***$p<0.001$). Error bars represent standard deviation.

Just after UV-induced released of C17PHS, the IPC levels were barely detectable in both strains, but starting from 20 minutes after uncaging the amounts of C17-IPCs were markedly higher in cells overexpressing Mdm1. Although IPCs gradually increased over time in control cells, Mdm1 expression further boosted IPC-biosynthesis. (Figure 34, B). Not surprisingly, the difference in IPC amounts was more pronounced compared to ceramides, since IPC biosynthesis requires two more steps: ceramide transport to the Golgi and glycosylation by Aur1/Kei1 (173). Altogether the results suggest that Mdm1 increases the ER-to-vacuole transport of long-chain bases. However, it is still unclear, whether the increased area of contact caused by Mdm1 overexpression *per se* account for this or Mdm1 activity mediates the movement of C17PHS to the ER.

Chapter 4: General discussion and conclusions

Chapter 4.1: The role of serine palmitoyltransferase and ceramide synthase localization in controlling flux through sphingolipids

The endoplasmic reticulum network is subdivided into the cortical ER, which is tightly associated with the plasma membrane and the perinuclear ER which envelops the nucleus and is continuous with the nuclear membrane (103). Catalytic subunits of the yeast SPT, Lcb1 and Lcb2 are presumed to predominantly localize to the peripheral (cortical) ER, whereas Lac1 and Lag1 – the catalytic subunits of the yeast ceramide synthase demonstrate predominantly perinuclear localization (20, 36, 172). It is well known that sphingoid base biosynthesis is rapidly upregulated upon heat stress, while ceramide upregulation follows suit later (136, 140, 174). We hypothesized that differential localization of enzymatic complexes (SPT and ceramide synthase) could explain this delay in metabolic flux from long-chain bases to ceramides. To test this this we constructed a chimeric fusion protein between an SPT subunits Lcb1 and a ceramide synthase subunit Lac1, assuming the proximity of catalytic centers would facilitate the transfer of the product of the first reaction to the catalytic site of the second enzyme promoting so called "metabolic channeling". Clustering of several enzymes together to promote metabolic channeling is a concept introduced several decades ago (175). Fusing different enzymes of the same pathway into a single fusion chimera to boost the production of desired biomolecules has been successfully used in yeast (176–178). The critical factor in the successful construct of fusion chimeras is the short stretch of amino acids separating the two parts of the fusion protein – linkers. We selected the glycine- and serine-rich GGGS-type linkers as they have previously been shown to improve the functions of yeast proteins when placed before epitope tags (179). The sequence encoding the fusion of *LCB1* and *LAC1* genes separated by the $(GGGS)_2$ linker sequence was integrated into the genome for stable expression. The expected molecular weight of the fusion protein was 110 kD. Using anti-Lcb1 antibody we could see a band corresponding to 100 kD, but also additional bands of smaller sizes could be seen which signaled degradation of the chimera. The expression of Lcb1-Lac1 was stabilized in a strain lacking vacuolar proteinase A (Pep4) clearly indicating degradation in the vacuole (Figure 7). Lipid profile of the chimera-expressing strain showed the reduced levels of ceramides even at steady-state levels indicating defective functioning of the Lcb1-

Lac1 protein (Figure 7). Therefore, we constructed new fusion proteins where Lag1 subunit was fused to Lcb1 or Lcb1 SPT subunits using the same linker sequence as before. Surprisingly, the new chimeras were more stable, although Lcb2-Lag1 protein was still partially degraded (Figure 8). Lcb1-Lag1 chimeric protein was stable, no smaller bands were detected. Curiously, though, we saw a band corresponding to 200 kD, twice the size of fusion (Figure 8, A, left). Both Lcb1 and Lac1 are integral ER proteins with multiple transmembrane domains (11 TM domains in total for Lcb1-Lac1). The presence of transmembrane domains may significantly alter protein mobility on SDS-PAGE gels due to increased detergent binding, for example (180). Also, membrane proteins are prone to precipitation when denatured by boiling with SDS. Despite heating the samples with SDS at lower temperature (50ºC, instead of 90ºC) aggregation may still have taken place. Thus, the apparent dimer likely represented an artifact. Next, Lcb1-Lac1 characterized. *LCB1* is an essential gene, so that abnormal functioning would result in the increased sensitivity to SPT inhibitor, myriocin. We found that 1µM myriocin did not alter the growth of the chimera-expressing cells (Figure 8, B). Moreover, Lag1 in the fusion could complement the loss of all ceramide synthase subunits, as shown by synthetic lethality test in Figure 8 (C). The results suggest that both parts of the fusion protein function normally. Next, we compared steady state lipid profiles of cells expressing only Lcb1-Lag1 and Lcb2 versus the strain expressing Lcb1, Lcb2, Lag1 proteins separately. No difference in the amounts of major glycerophospholipid classes was found (Figure 9). The levels of ceramides and complex sphingolipids (IPCs, MIPCs) were also similar (Figure 9). It should be noted, though, that Lag1 fused to Lcb1 is expressed under control of *LCB1* promoter, while intact Lag1 is expressed under a weaker endogenous promoter. Nevertheless, the difference in expression might be equalized by homeostatic regulation. It has been demonstrated by the observations that depleting a single ceramide synthase subunit does not alter total ceramide amounts (40). We took a closer look into the ceramide profiles in control and fusion-expressing cells. Ceramide and IPC profiles were very similar, and ceramides were largely composed of PHC-C 18:0/26:0 (~ 90%) and PHC-B 18:0/26:0 (~3.5%) species (Figure 10, Table 1). Consistently, the major IPC species were IPC-C 18:0/26:0 (~85%) and IPC-B 18:0/26:0 (~10%). The overwhelming prevalence of phytoceramides in sphingolipid profiles of cells expressing only Lag1 agrees with a very recent report demonstrating a substrate specificity of Lag1 towards PHS (40).

After the initial characterization of strains expressing Lcb1-Lag1 chimeric protein, we sought to investigate the metabolic flux to ceramides to put our hypothesis to test. First, we checked whether we could reproduce the well-known heat stress-induced rapid accumulation of long-chain bases in our yeast strain background. Indeed, we could see a pronounced increase in C18PHS and C18PHS1-P amounts as early as 2 minutes after switching cells to 40ºC. The most prominent upregulation was seen for C20PHS with its level increasing almost 1000-fold after 10-minute heat shock, which is consistent with previous observations (Figure 11) (136). Interestingly, while C18PHS levels sharply rose upon heat shock, the amounts of C18Sa and C18Sa-1P barely changed. This might be interpreted as a result of Sur2 hydroxylase activity. In order to follow *de novo* sphingolipid biosynthesis upon heat stress, we utilized a heavy isotope-labeled serine (D3-Serine) since this amino acid is incorporated into all sphingolipid species. We saw that only D3-labeled long-chain bases increase upon heat-shock indicating that the rise in sphingolipid levels chiefly comes from *de novo* biosynthesis (Figure 12). Comparison of sphingoid-base biosynthesis in control and Lcb1-Lag1-expressing cells showed similar dynamics, although C18PHS-1P and minor C18Sa species were lower at 2 minutes of heat stress in the fusion-expressing samples but reached control levels at 5 minutes. Next, we followed the incorporation of D3-Serine into ceramides 10 and 20 min after heat shock. The results showed that the expression of fusion chimera Lcb1-Lag1 did not accelerate the flux to ceramides and complex sphingolipids (Figure 13). We also checked if the overexpression of 3-ketosphinganine reductase Tsc10, an intermediate enzyme between SPT and CS, would facilitate sphingolipid flux. To our surprise, metabolic flux was slower in cells expressing chimeric fusion Lcb1-Lag1 but could be restored to control levels by Tsc10 overexpression. Excessive amount of Tsc10, in contrast, rather slowed down metabolic conversion in control cells (Figure 14). These findings may point out to the adverse effects of Lcb1-Lag1 fusion on the integrity and architecture of SPOTS, of which Tsc10 is a part. The fusion may have inhibited or displaced endogenous Tsc10, so that more enzymes were required for proper functioning. Direct fusion of Lcb1 and Lag1 likely affected stoichiometry of both complexes. An alternative way to bring SPT and CS together would be to employ chemically induced dimerization (CID). FRB-tagged Lcb1 would bind FKBP-tagged Lag1 upon treatment with rapamycin, since rapamycin-bound FKBP strongly binds to a TORC1 kinase subunit FRB (181). Nonetheless, the results argue that metabolic channeling induced by Lcb1-Lag1 fusion and Tsc10 overexpression does not accelerate metabolic flux, which may suggest that diffusion of reaction products might not be a limiting factor in sphingolipid metabolism in yeast.

Indirect evidence suggests that SPT complex might localize to the ER-PM junctions. PI4P phosphatase Sac1 has been shown to be involved in lipid transport at the ER-PM contacts sites (182). At the same time, Sac1 is associated with SPT in the SPOTS complex. We set to test if re-localization of ceramide synthase from the nuclear ER to the cortical ER-PM junctions would affect sphingolipid biosynthesis and homeostasis. For this Lac1 was fused with a short cortical ER targeting sequence from ER-PM junction protein Ist2. GFP-tagged cortical Lac1 was expressed from the endogenous promoter. The resulting GFP-Lac1$^{ER\text{-}PM}$ localized to the peripheral dot-like structures, although a fraction of the protein was still found in in the perinuclear ER (Figure 15). Lac1$^{ER\text{-}PM}$ was fully functional and could complement endogenous ceramide synthase subunits as demonstrated by a synthetic lethality test (Figure 15). Moreover, steady state profiles glycerophospholipid and sphingolipid profiles were unaltered in cells expressing Lac1$^{ER\text{-}PM}$. Importantly, *de novo* biosynthesis of ceramides and complex sphingolipids was not affected by the cortical localization of Lac1. It must be noted, that the data on Lac1 interaction with SPT subunits is lacking so co-immunoprecipitation experiments are required to clarify if cortically localized Lac1 is associated with SPT. Altogether, the data implies that ceramide synthase localization does not affect sphingolipid homeostasis and metabolic flux.

It has been shown that Orm proteins and ceramide synthase subunits are found in the inner nuclear membrane (INM), which is connected with the nuclear ER through nuclear pores (132). Furthermore, Orm2 was shown to re-localize to the nuclear ER upon SPT inhibition (23). We speculated that Orm2 may recruit SPT into the nuclear ER to upregulate sphingolipid biosynthesis. To test this, we fused GFP-tagged Orm2 with an INM-targeting sequence from Heh2 protein (Figure 16, A). INM-localized Orm2 (NLS-Orm2) was found in the nuclear ER. Moreover, both Lcb1 and Lcb2 SPT subunits predominantly localized to the nuclear ER in the strains expressing NLS-Orm2 (Figure 16, B). We found that the expression of INM-targeted Orm2 lead to a significant increase in long-chain bases compared to the control. Interestingly, *orm1Δorm2Δ* accumulated even higher levels of sphingoid bases, consistent with previous reports (Figure 17) (23, 33). These results suggest that NLS-Orm2 is partially active and SPT is not fully derepressed. When we followed the incorporation of heavy-isotope labeled serine into sphingolipids we found that although double *orm* mutants had elevated steady-state ceramide level, *de novo* biosynthesis of ceramides and complex sphingolipids rate was markedly lower compared to wild-type control (Figure 18). Interestingly, while steady state levels of sphingolipids were similar to the control in NLS-Orm2-expressing cells, biosynthesis of ceramides, but not IPC or MIPC was significantly upregulated (Figure 18). Thus, unlike in *orm1Δorm2Δ* strain, elevated levels of PHS and Sa translated into increased flux to ceramides in NLS-Orm2 expressing cells. These observations may be explained by Orm2 enhancing ceramide synthase activity. It has been previously described that both CS subunits can bind Orm proteins (183). Since Orm2 can bind ceramide synthase it could possibly serve as a linker bringing together SPT and CS in the inner nuclear membrane. Decreased inhibitory activity of NLS-Orm2 could be due to increased accessibility to Ypk kinases in the INM or the presence of bulk nucleus-targeting sequence interfering with Orm2-SPT interaction. More experiments are required to rule out or confirm these assumptions. Of note, we could only see increased sphingolipid flux in the inner nuclear membrane. This area was long considered to be metabolically silent but recent studies have disproved these speculations (184). Our results reveal a link connecting localization at the INM and sphingolipid homeostasis.

Chapter 4.2: Characterization of vacuole-targeted caged sphingolipid probes in *Saccharomyces cerevisiae*

The development of organelle-specific synthetic probes have opened new horizons for exploring intracellular lipid metabolism (122). A recently developed set of artificial sphingolipid probes includes a lipid molecule of interest, whose head group is protected by the chemical cage, and an organelle-targeting part mediating its delivery into mitochondria or lysosomes in mammalian cells (125, 126). Irradiation with UV light efficiently removes the protective cage, releasing bioactive sphingolipids in specific organelles. We sought to characterize mitochondria-targeted caged compounds in budding yeast, *Saccharomyces cerevisiae*. Mitochondrial targeting is achieved by the presence of a lipophilic cation TPP which is driven inside mitochondrial matrix due to the large membrane potential (150-180 mV) (150). The compound can be monitored under the microscope prior to UV uncaging, since the protective cage, coumarin, is a fluorophore. Here we show that synthetic sphingolipid probes designed to target mitochondria in mammalian cells were delivered to the vacuoles in budding yeast (Figures 18 and 19). The co-localization with vacuolar membrane marker protein Vph1 showed that the probe primarily stained the vacuolar lumen, although the probe might have also been associated with the limiting membrane. One possible explanation for this is that the probe delivered to mitochondria induces their degradation in the vacuole (mitophagy) where the probe is detected. However, the probe is observed in the vacuoles within 15-minute incubation period, while mitophagy is a slower process and can be observed within an hour after induction (185). Also, we performed staining with the probe in rich medium, while mitophagy has been shown to be efficient in respiratory conditions in media containing nonfermentable carbon source (186, 187). Moreover, staining with mito-cage probes does not alter the morphology of mitochondria visualized by a marker protein Mdh1 (Figure 20). Alternatively, the implication of mitophagy in the probe targeting to the vacuoles could be tested in mitophagy-deficient mutants, such as *atg32Δ*, *atg11Δ* or inspect the probe-stained cells using electron microscopy. The next important question we addressed was the toxicity of the vacuole-targeted compounds. Growth curves of cells treated with C17 mito-PHS indicate that even at 50 μM the probe does not inhibit yeast growth over a long time period and is therefore suitable for *in vivo* experiments. Next, we assumed that vacuolar targeting could be attributed to the low mitochondrial potential in non-respiratory conditions. Nonetheless, C17 mito-PHS was still found associated with the vacuoles but not with mitochondria in the cells grown on nonfermentable carbon source under respiratory conditions (Figure 22). Furthermore, vacuolar localization of the mito-caged probe appears to be background-independent. In this study several different strain backgrounds were used: BY4741 (Euroscarf™), SE6210 (mix of strains from different laboratories), RH431 (S288C origin) and in all of them the probe showed localization to the vacuoles.

We also considered a possibility that TPP-caged probe is internalized by endocytosis and as a result ends up in the vacuole. The probe, though, is still delivered to the vacuole in the strain lacking End3, a protein required for cargo internalization and actin cytoskeleton organization. Nonetheless, End3 depletion does not completely abrogate all endocytic events since the marker of bulk membrane internalization, a styryl dye FM 4-64 still targets the vacuoles in *end3Δ* cells (165) (Figure 27). Endocytosis is blocked at 4ºC and at this temperature FM 4-64 was found mainly in intermediate endocytic compartments and not in the vacuole, while the C17 mito-PHS did not enter the cells. If vacuolar localization of the caged compound depended on endocytosis it would be found in the same compartments as FM 4-64. Thus, the results argue against the endocytic mechanism of probe internalization.

The probe consists of three parts: a long-chain base, a coumarin cage and a TPP lipophilic cation. We addressed the issue of which part of the compound was essential for its targeting. No intracellular staining was observed when cells were incubated with a molecule containing a coumarin cage and the TPP-targeting group (Figure 21). In mammalian cells TPP-coupled compounds easily pass lipid bilayers in general and especially the plasma membrane due to its membrane potential (negative inside) (150). Budding yeast cells, though, are notorious for the efficient pumping of potentially toxic small molecules out of the cell due to the activity of a variety of transporters (128, 129). When the caged PHS probe lacked a TPP-cation part it also could not be internalized by the wild-type cells, but the entry was facilitated by the deletion of a multidrug transporter Pdr5 and a putative long-chain base exporter Rsb1 (Figure 22). These results argue in favor of the role of xenobiotic transporters in clearing cells of the probe lacking a lipophilic TPP cation. TPP-containing compounds are accumulated in mitochondrial matrix due to the negative charge, yet the opposite is true for the acidified positively charged vacuolar lumen (157). How do TPP-containing probes end up in the vacuole? It is known that vacuoles are able to accumulate high levels of basic amino acids through the action of proton gradient-dependent amino acid transporters (188). Moreover, some cations are also imported into the vacuolar lumen by the antiporter proteins pumping out protons and importing cations (189). Cation uptake is also dependent on pH gradient across the vacuolar membrane. The hypothesis that the caged-TPP probes are imported by the vacuole-resident transporter is supported by data showing a decrease in the probe uptake when vacuole pH gradient is disrupted either by the treatment with the proton uncoupling compound CCCP or the inhibition of the vacuolar proton pump H^+-V-ATPase by Bafilomycin A1 (Figure 25). Both CCCP and Bafilomycin A1 disrupt proton gradient across the vacuole membrane and would affect the activity of various transporters. Due to the big number of potential TPP-cation transporter candidates it is not easy to directly test this assumption by checking the probe uptake in deletion mutants.

We also tested the possibility that long-chain base part of the probe was essential for the internalization. Fatty acyl-CoA ligases Faa1 and Faa4 have been shown to mediate the uptake of sphingoid bases, while Fat1 ligase is involved in long-chain free fatty acid transport (160, 161). It must be noted, though, that the head group of a long-chain bases in the probe is blocked by the chemical cage altering its biological properties. Yet the aliphatic chain is unprotected and might be recognized by the transporters. We observed a noticeable decline in the probe uptake in a single *fat1Δ* and double *faa1Δfaa4Δ* mutants and the uptake defect was even stronger in the triple *fatΔfaa1Δfaa4Δ* mutant strain (Figure 26). This might suggest that the aliphatic part of the long-chain base is recognized by the ligases that facilitate the import into the cell. Alternatively, fatty acyl-CoA ligases might accelerate the probe degradation in the vacuole and the efflux of the fluorescent coumarin cage out of the cell resulting in the decrease of fluorescence intensity. To rule that out long-chain bases and their phosphorylated derivatives could be measured in the ligase mutant strains treated with the probe. Collectively the pieces of evidence suggest that the mito-caged sphingolipid compounds require an aliphatic carbon chain and the TPP lipophilic cation for the vacuolar delivery in yeast cells. The hypothetical model of the probe internalization includes import facilitated by fatty acyl-CoA ligases followed by the active import into the vacuole facilitated by transporters.

Furthermore, the stability of vacuole-targeted caged sphingolipid probes was characterized. Like their mammalian counterparts - lysosomes, yeast vacuoles are digestive organelles that host many hydrolytic enzymes that optimally function in the acidified environment in the lumen (157). Caged sphingosine probes targeted to mammalian lysosomes (lyso-So) were shown to be partially degraded while the mitochondria-targeted caged sphingosine proved more stable (126). Consistent with the mentioned observations we found that our vacuole-delivered probes released sphingoid base without UV treatment, indicating unspecific cleavage (Figure 28). More important, the stability of probes differed depending on a long-chain base, with C18 mito-PHS being the least stable probe showing complete degradation within 15-minute incubation period, while C18 mito-Sa was found to be more stable (15-20 % of unspecific release), arguing for a substrate specificity of an unidentified hydrolase. Chemical structure of the sphingolipid probes may resemble that of ceramides and the probe may be cleaved by the yeast ceramidases, given that one of them, Ydc1 is found in the vacuolar membrane (168, 172). The results, however, contradicted the assumption showing that the deletion of both yeast ceramidases did not reduce probe degradation (Figure 29). Depletion of Pep4 – Proteinase A that regulates the maturation and activity of several vacuolar hydrolases also showed no effect on unspecific release of C18PHS from the caged probe (Figure 29). Reducing incubation time or incubation temperature hardly altered the rate of C17 mito-PHS degradation, remaining 25-30% compared to UV-treated samples (Figure 29). Probe cleavage poses represents a significant drawback for our experimental approach. A potential solution of vacuole-targeted probe degradation may be the addition of an extra cage at the C3 or C4 (for PHS) hydroxyl group of the sphingoid base. This might, on the other hand affect probe uptake while increasing its stability. Aside from probe cleavage, another possible limitation of UV-induced uncaging might come from a toxic effect of UV *per se*, since it is a well-known mutagenic, DNA-damaging agent. We tested the impact of a 2-minute irradiation (same as in uncaging protocols) on yeast viability and found no effect on cell survival, ruling out severe toxic effect of UV illumination. Nonetheless, we cannot rule out short-term effect of UV on cell metabolism which are not explored in detail in this study.

Next, we characterized the metabolic conversion of long-chain bases released from the vacuoles into ceramides and complex sphingolipids. For this, we utilized mito-caged probes containing non-natural odd-chain sphingoid base analogs with 17 carbon atoms: C17PHS and C17Sa. These odd-chain length tracers have previously been characterized in yeast and shown to be efficiently incorporated into ceramides and complex sphingolipids (170). In agreement with results demonstrating unspecific release of C17PHS from the caged probe, we could detect C17PHS-derived ceramides before exposing the cells to UV light. Most of uncaged C17PHS molecules were converted over time into PHC-C 17:0/26:0 species, with the second most abundant species being PHC-B 17:0/26:0 ceramide (Figure 30). These observations agree well with the natural yeast ceramide profile where the most abundant ceramide is PHC-C 18:0/26:0 followed by PHC-C 20:0/26:0 (135). Furthermore, sphingolipid profiles generated from exogenously added C17PHS and those derived from UV-uncaged vacuolar C17PHS were similar, being predominantly derived from the PHC-C 17:0/26:0 ceramide with a minor fraction composed of the PHC-B 17:0/26:0 species (Figure 31). These results argue that ceramide synthase generates similar ceramides irrespective of the origin of C17PHS. Different results were obtained when C17Sa was used as a metabolic tracer. C17 mito-Sa probe was stable, showing virtually no ceramide signal before UV uncaging. The released C17Sa base was primarily incorporated into the PHC-C 17:0/26:0 ceramide. When C17Sa was exogenously supplied, it was mostly converted into DHC-A 17:0/26:0 ceramide which also labeled most of the complex sphingolipid pool. The difference in profiles might be due to the fact that exogenously supplied sphinganine has to be phosphorylated and dephosphorylated prior to conversion into ceramides (190). Interestingly, the overall abundance of C17Sa-generated sphingolipids was much lower compared to C17PHS, although the same concentration of C17 tracer were used in the experiments. Considering recently uncovered substrate specificity of different ceramide synthase subunits for PHS and Sa, this could be the result of a decreased Lac1 activity towards non-natural C17Sa (40). The overall low abundance of C17Sa-derived sphingolipids may explain the appearance of non-typical ceramide species such as DHC-B’ 17:0/22:0 seen in C17Sa-treated samples and undetected in complex sphingolipid pools. Such species may represent artifacts and more experiments need to be carried out to make an unbiased conclusion about their presence. Simply increasing the concentration of C17Sa-containing caged probe might solve the issue of low signal intensity. Despite partial cleavage of the probe in the vacuole most of C17PHS molecules were still released by UV irradiation and metabolic route of vacuole-derived C17PHS tracers closely resembles that of exogenously supplied odd-chain length PHS. As a result C17 mito-PHS was a probe of choice for subsequent experiments.

In this study we developed an assay in which we could target a chemically inert, caged C17PHS to the vacuoles, release the physiologically active sphingoid bases and track their incorporation into more complex sphingolipids. The degradation and sphingolipids in the yeast vacuole is not well understood. So far most of the enzymes participating in sphingolipid catabolism are presumed to localize to the ER or the Golgi (191). As has been recently shown, the loss of Golgi-associated retrograde protein complex (GARP) involved in vacuole-to-Golgi vesicular trafficking resulted in the accumulation of sphingolipid intermediate metabolites and reduction in complex sphingolipid biosynthesis (192). This implies the importance of the recycling of sphingolipids degraded in the vacuole for lipid homeostasis. Aside from vesicular trafficking, the vacuole can communicate with other organelles via direct contacts at the membrane contact sites (65, 96, 100). The extent, to which sphingolipid recycling depend on organelle contact sites is unknown and unappreciated. Hence, using the caged vacuole-targeted probe we sought to validate our assay, tracking the transport of long-chain bases from the vacuole to the ER, where ceramide biosynthesis is presumed to occur. For this we chose a quadruple mutant strain lacking all known nucleus-vacuole junction proteins, showing the lack of contacts between the two organelles (75). The lack of nucleus-vacuole contacts did not affect cell growth. We also observed no difference in localization of the caged C17PHS probe in the mutant strain. (Figure 32). Next, we conducted a time course experiment measuring the levels of C17PHS-generated sphingolipids over time in probe-treated cells after UV uncaging. We observed that mean values of the levels of ceramides and IPCs were lower in the quadruple mutant cells, although many of the observed differences were not statistically significant due to high variability. Nonetheless, we saw a significantly lower amounts of PHC-B 17:0/26:0 ceramide in ΔNVJ strain 60 minutes after UV uncaging. PHC-B species are generated from N-acylated PHS, while C species require further hydroxylation by Scs7. The results reveal higher levels of the B-class PHC species in control cells even at early time points, while the difference in PHC-C amount appear much later, at 40 minutes after UV uncaging. Altogether, the data might indicate that the transport of C17PHS was slower in the NVJ-deficient mutants. However, these results could also have originated from the reduced activity of ceramide synthase in the ΔNVJ strain. Labeling control and quadruple mutant cells with C17PHS from the medium would resolve this hypothesis. The published electron microscopy images, displaying lack of ER-vacuole contacts in ΔNVJ cells, were obtained from 70-nm-thick sections and could not fully explore all potential contact sites. Additionally, disruption of ER-vacuole contacts may force sphingolipids to take a bypass pathway through vacuole-mitochondria and mitochondria-ER contact sites. The existence of bypass routes, as demonstrated in ERMES-deficient cells rescued by Vps13 (93), might offer a clue on how cells remain viable, when organelle contact sites are disrupted. Therefore, multiple genes need to de deleted to observe pronounced defects in non-vesicular lipid transport between the organelles. It would also be interesting to track the metabolism of uncaged C17PHS in GARP-complex deficient mutants to estimate the contribution of retrograde vesicular trafficking in long-chain base transport from the vacuole.

Our data point to delayed metabolic conversion of uncaged C17PHS in NVJ-deficient strains. It was also tempting to test whether enhancing the area of contact between the ER and the vacuoles could boost the transport of C17PHS accelerating the metabolic flux towards ceramides and complex sphingolipids. It has been shown that overexpression of an NVJ-resident protein Mdm1 induced overtethering between the vacuoles and the ER (75). We observed the localization of overexpressed GFP-Mdm1 in vicinity to the vacuoles. Overexpression of Mdm1 did not affect the localization of caged C17PHS probe to the vacuoles (Figure 34). Similar to the experiment conducted with ΔNVJ mutants, we monitored the conversion of UV-released C17PHS into ceramides and complex sphingolipids over time in the wild-type strains overexpressing GFP-Mdm1 or bearing an empty vector. Surprisingly, we could see a statistically significant increase in C17-ceramides upon Mdm1 overexpression (Figure 34). Although the levels of PHC-B 17:0/26:0 in Mdm1-overexpressing cells were already higher at the beginning, the difference became even more pronounced over time. The increase in PHC-C 17:0/26:0 ceramide amounts became apparent later, after 60 minutes after the UV-mediated release. The dynamics of IPC biosynthesis, though, showed even more convincing results. At the start in both control and Mdm1-expressing cells C17PHS-derived IPC were barely detected, but Mdm1 overexpression boosted IPC levels and the difference became noticeable as early as within 20 minutes after UV-uncaging. Although IPC amounts kept increasing in controls cells, Mdm1 overexpression lead to a sustained 4-fold upregulation at 40- and 60 minutes following UV-uncaging (Figure 34).

The results discussed above, though, do not rule out the possibility that Mdm1 overexpression could have enhanced ceramide synthase activity but not the transport of C17PHS to the ER. Again, labeling with exogenous C17PHS would resolve this concern. Nonetheless, data from ΔNVJ mutants combined with the findings in the Mdm1-overexpressing strain argue in favor of the assumption, that the rate of long-chain base transport depends on the extent of direct contact between the vacuole and the ER. It is also important to understand if the boost in sphingolipid transport is a result of Mdm1 lipid transport activity is a consequence of the increased association between the ER and the vacuole membranes, which allow long-chain bases to reach ceramide synthase catalytic sites by diffusion. This assumption could be tested by expressing an artificial tether bridging the ER and the vacuole and checking the metabolism of an uncaged odd-chain length tracer. Here we demonstrate an assay enabling the investigation of the transport and metabolism of sphingolipids released in the yeast vacuoles. There are, however, several drawbacks which need to be improved in the future. One major drawback of our assay is high variability resulting from the low intensity of signals. Here we show that UV-released C17PHS and C17Sa are preferentially incorporated into PHC-C and PHC-B 17:0/26:0 species. Thus, focusing on these two species we could use more powerful liquid chromatography-coupled mass-spectrometers with higher resolution and sensitivity. This could partially circumvent the issue of high variability. It is also possible to increase the probe concentration, but it might result in undesired adverse toxic effects for the cells. Another issue is related to the partial degradation of caged probes in the vacuole. Although the C17Sa-containing probe was found to be more stable, its incorporation into ceramides was much less efficient compared to the odd-chain PHS. As has been previously mentioned, an additional coumarin cage could be added potentially increasing probe stability and fluorescence intensity. Collectively, our results demonstrate that vacuole-targeted caged sphingolipid probes can be used for *in vivo* studies of transport between the vacuole and the ER. We also show that probes containing other lipid biomolecules, such as oleic acid, also localized to the vacuoles. This implies that is also possible to study transport and metabolism of biomolecules other than sphingolipids from the vacuole. Yeast TORC1, a master coordinator of nutrient cues with cell growth, is constitutively localized on the vacuolar membrane (193, 194). Specific release of bioactive molecules at the vacuolar membrane could be used to study the impact of distinct lipids on the activity of TORC1 kinase complex and thus regulation of cell growth. Interestingly, it has been observed that vacuolar membrane formed micrometer-scale stable lipid raft-like domains upon nutrient starvation (195). Altogether, the yeast vacuole has emerged as a major hub, where multiple signaling, and metabolic pathways converge. The use of stable vacuole-specific lipid probes may provide insights into the mechanistic understanding of the complex interplay between the vacuole and other organelles.

References

1. Singer, S. J., and Nicolson, G. L. (1972) The Fluid Mosaic Model of the Structure of Cell Membranes. *Science (80-.).* **175**, 720–731

2. Harayama, T., and Riezman, H. (2018) Understanding the diversity of membrane lipid composition. *Nat. Rev. Mol. Cell Biol.* **19**, 281–296

3. van Meer, G., Voelker, D. R., and Feigenson, G. W. (2008) Membrane lipids: where they are and how they behave. *Nat. Rev. Mol. Cell Biol.* **9**, 112–124

4. Hannun, Y. A., and Obeid, L. M. (2017) Sphingolipids and their metabolism in physiology and disease. *Nat. Rev. Mol. Cell Biol.* **19**, 175–191

5. Harvald, E. B., Olsen, A. S. B., and Færgeman, N. J. (2015) Autophagy in the light of sphingolipid metabolism. *Apoptosis*. **20**, 658–670

6. Obeid, L., Linardic, C., Karolak, L., and Hannun, Y. (1993) Programmed cell death induced by ceramide. *Science (80-.).* **259**, 1769–1771

7. van der Weyden, L., Arends, M. J., Campbell, A. D., Bald, T., Wardle-Jones, H., Griggs, N., Velasco-Herrera, M. D. C., Tüting, T., Sansom, O. J., Karp, N. A., Clare, S., Gleeson, D., Ryder, E., Galli, A., Tuck, E., Cambridge, E. L., Voet, T., Macaulay, I. C., Wong, K., Spiegel, S., Speak, A. O., Adams, D. J., and Adams, D. J. (2017) Genome-wide in vivo screen identifies novel host regulators of metastatic colonization. *Nature*. **541**, 233–236

8. Maceyka, M., and Spiegel, S. (2014) Sphingolipid metabolites in inflammatory disease. *Nature*. **510**, 58–67

9. Zanolari, B., Friant, S., Funato, K., Sütterlin, C., Stevenson, B. J., and Riezman, H. (2000) Sphingoid base synthesis requirement for endocytosis in Saccharomyces cerevisiae. *EMBO J.* **19**, 2824–2833

10. Santos, A. X. S., and Riezman, H. (2012) Yeast as a model system for studying lipid homeostasis and function. *FEBS Lett.* **586**, 2858–2867

11. Buede, R., Rinker-Schaffer, C., Pinto, W. J., Lester, R. L., and Dickson, R. C. (1991) Cloning and characterization of LCB1, a Saccharomyces gene required for biosynthesis of the long-chain base component of sphingolipids. *J. Bacteriol.* **173**, 4325–32

12. Nagiec, M. M., Baltisberger, J. A., Wells, G. B., Lester, R. L., and Dickson, R. C. (1994) The LCB2 gene of Saccharomyces and the related LCB1 gene encode subunits of serine palmitoyltransferase, the initial enzyme in sphingolipid synthesis. *Proc. Natl. Acad. Sci. U. S. A.* **91**, 7899–902

13. Gable, K., Slife, H., Bacikova, D., Monaghan, E., and Dunn, T. M. (2000) Tsc3p is an 80-amino acid protein associated with serine palmitoyltransferase and required for optimal enzyme activity. *J. Biol. Chem.* **275**, 7597–7603

14. Beeler, T., Bacikova, D., Gable, K., Hopkins, L., Johnson, C., Slife, H., and Dunn, T. (1998) The Saccharomyces cerevisiae TSC10/YBR265w gene encoding 3-ketosphinganine reductase is identified in a screen for temperature-sensitive suppressors of the Ca2+-sensitive csg2Delta mutant. *J. Biol. Chem.* **273**, 30688–94

15. Haak, D., Gable, K., Beeler, T., and Dunn, T. (1997) Hydroxylation of Saccharomyces cerevisiae ceramides requires Sur2p and Scs7p. *J. Biol. Chem.* **272**, 29704–10

16. Nagiec, M. M., Skrzypek, M., Nagiec, E. E., Lester, R. L., and Dickson, R. C. (1998) The LCB4 (YOR171c) and LCB5 (YLR260w) genes of Saccharomyces encode sphingoid long chain base kinases. *J. Biol. Chem.* **273**, 19437–42

17. Saba, J. D., Nara, F., Bielawska, A., Garrett, S., and Hannun, Y. A. (1997) The BST1 gene of Saccharomyces cerevisiae is the sphingosine-1-phosphate lyase. *J. Biol. Chem.* **272**, 26087–90

18. Schorling, S., Vallée, B., Barz, W. P., Riezman, H., and Oesterhelt, D. (2001) Lag1p and Lac1p are essential for the Acyl-CoA-dependent ceramide synthase reaction in Saccharomyces cerevisae. *Mol. Biol. Cell.* **12**, 3417–27

19. Guillas, I., Kirchman, P. A., Chuard, R., Pfefferli, M., Jiang, J. C., Jazwinski, S. M., and Conzelmann, A. (2001) C26-CoA-dependent ceramide synthesis of Saccharomyces cerevisiae is operated by Lag1p and Lac1p. *EMBO J.* **20**, 2655–65

20. Vallee, B., and Riezman, H. (2005) Lip1p: a novel subunit of acyl-CoA ceramide synthase. *Embo J.* **24**, 730–741

21. Beeler, T. J., Fu, D., Rivera, J., Monaghan, E., Gable, K., and Dunn, T. M. (1997) SUR1 (CSG1/BCL21), a gene necessary for growth of Saccharomyces cerevisiae in the presence of high Ca 2+ concentrations at 37°C, is required for mannosylation of inositolphosphorylceramide. *Mol. Gen. Genet. MGG*. **255**, 570–579

22. Funato, K., and Riezman, H. (2001) Vesicular and nonvesicular transport of ceramide from ER to the Golgi apparatus in yeast. *J. Cell Biol.* **155**, 949–960

23. Breslow, D. K., Collins, S. R., Bodenmiller, B., Aebersold, R., Simons, K., Shevchenko, A., Ejsing, C. S., and Weissman, J. S. (2010) Orm family proteins mediate sphingolipid homeostasis. *Nature*. **463**, 1048-U65

24. Roelants, F. M., Chauhan, N., Muir, A., Davis, J. C., Menon, A. K., Levine, T. P., and Thorner, J. (2018) TOR complex 2–regulated protein kinase Ypk1 controls sterol distribution by inhibiting StARkin domain–containing proteins located at plasma membrane–endoplasmic reticulum contact sites. *Mol. Biol. Cell*. **29**, 2128–2136

25. Loewith, R., and Hall, M. N. (2011) Target of rapamycin (TOR) in nutrient signaling and growth control. *Genetics*. **189**, 1177–201

26. Berchtold, D., Piccolis, M., Chiaruttini, N., Riezman, I., Riezman, H., Roux, A., Walther, T. C., and Loewith, R. (2012) Plasma membrane stress induces relocalization of Slm proteins and activation of TORC2 to promote sphingolipid synthesis. *Nat. Cell Biol.* **14**, 542-U200

27. Nagiec, M. M., Nagiec, E. E., Baltisberger, J. A., Wells, G. B., Lester, R. L., and Dickson, R. C. (1997) Sphingolipid synthesis as a target for antifungal drugs. Complementation of the inositol phosphorylceramide synthase defect in a mutant strain of Saccharomyces cerevisiae by the AUR1 gene. *J. Biol. Chem.* **272**, 9809–17

28. Jenkins, G. M., Ashley Cowart, L., Signorelli, P., Pettus, B. J., Chalfant, C. E., and Hannun, Y. A. (2002) Acute activation of de novo sphingolipid biosynthesis upon heat shock causes an accumulation of ceramide and subsequent dephosphorylation of SR proteins. *J. Biol. Chem.* **277**, 42572–42578

29. Zhang, X., Skrzypek, M., Lester, R., and Dickson, R. (2001) Elevation of endogenous sphingolipid long-chain base phosphates kills Saccharomyces cerevisiae cells. *Curr. Genet.* **40**, 221–233

30. Sun, Y., Miao, Y., Yamane, Y., Zhang, C., Shokat, K. M., Takematsu, H., Kozutsumi, Y., and Drubin, D. G. (2012) Orm protein phosphoregulation mediates transient sphingolipid biosynthesis response to heat stress via the Pkh-Ypk and Cdc55-PP2A pathways. *Mol. Biol. Cell*. **23**, 2388–2398

31. Casamayor, A., Torrance, P. D., Kobayashi, T., Thorner, J., and Alessi, D. R. (1999) Functional counterparts of mammalian protein kinases PDK1 and SGK in budding yeast. *Curr. Biol.* **9**, 186-S4

32. Gururaj, C., Federman, R. S., Federman, R., and Chang, A. (2013) Orm proteins integrate multiple signals to maintain sphingolipid homeostasis. *J. Biol. Chem.* **288**, 20453–63

33. Han, S., Lone, M. A., Schneiter, R., and Chang, A. (2010) Orm1 and Orm2 are conserved endoplasmic reticulum membrane proteins regulating lipid homeostasis and protein quality control. *Proc. Natl. Acad. Sci. U. S. A.* **107**, 5851–6

34. Liu, M., Huang, C. J., Polu, S. R., Schneiter, R., and Chang, A. (2012) Regulation of sphingolipid synthesis through Orm1 and Orm2 in yeast. *J. Cell Sci.* **125**, 2428–2435

35. Shimobayashi, M., Oppliger, W., Moes, S., Jenö, P., and Hall, M. N. (2013) TORC1-regulated protein kinase Npr1 phosphorylates Orm to stimulate complex sphingolipid synthesis. *Mol. Biol. Cell*. **24**, 870–881

36. Han, G., Gupta, S. D., Gable, K., Bacikova, D., Sengupta, N., Somashekarappa, N., Proia, R. L., Harmon, J. M., and Dunn, T. M. (2019) The ORMs interact with transmembrane domain 1 of Lcb1 and regulate serine palmitoyltransferase oligomerization, activity and localization. *Biochim. Biophys. Acta - Mol. Cell Biol. Lipids*. **1864**, 245–259

37. Davis, D. L., Gable, K., Suemitsu, J., Dunn, T. M., and Wattenberg, B. W. (2019) The ORMDL/Orm-serine palmitoyltransferase (SPT) complex is directly regulated by ceramide: Reconstitution of SPT regulation in isolated membranes. *J. Biol. Chem.* **294**,

5146–5156

38. Ren, J., Saied, E. M., Zhong, A., Snider, J., Ruiz, C., Arenz, C., Obeid, L. M., Girnun, G. D., and Hannun, Y. A. (2018) Tsc3 regulates SPT amino acid choice in Saccharomyces cerevisiae by promoting alanine in the sphingolipid pathway. *J. Lipid Res.* **59**, 2126–2139

39. Duan, J., and Merrill, A. H. (2015) -Deoxysphingolipids: mysteries in an enigma 1-Deoxysphingolipids Encountered Exogenously and Made De Novo: Dangerous Mysteries Inside an Enigma* *Running Title: 1-Deoxysphingolipids: mysteries in an enigma. 10.1074/jbc.R115.658823

40. Megyeri, M., Prasad, R., Volpert, G., Sliwa-Gonzalez, A., Haribowo, A. G., Aguilera-Romero, A., Riezman, H., Barral, Y., Futerman, A. H., and Schuldiner, M. (2019) Yeast ceramide synthases, Lag1 and Lac1, have distinct substrate specificity. *J. Cell Sci.* **132**, jcs228411

41. Kageyama-Yahara, N., and Riezman, H. (2006) Transmembrane topology of ceramide synthase in yeast. *Biochem. J.* **398**, 585–593

42. Cerantola, V., Guillas, I., Roubaty, C., Vionnet, C., Uldry, D., Knudsen, J., and Conzelmann, A. (2009) Aureobasidin A arrests growth of yeast cells through both ceramide intoxication and deprivation of essential inositolphosphorylceramides. *Mol. Microbiol.* **71**, 1523–1537

43. Muir, A., Ramachandran, S., Roelants, F. M., Timmons, G., and Thorner, J. (2014) TORC2-dependent protein kinase Ypk1 phosphorylates ceramide synthase to stimulate synthesis of complex sphingolipids. *Elife*. ARTN e0377910.7554/eLife.03779

44. Kobayashi, S. D., and Nagiec, M. M. (2003) Ceramide/Long-Chain Base Phosphate Rheostat in Saccharomyces cerevisiae: Regulation of Ceramide Synthesis by Elo3p and Cka2p. *Eukaryot. Cell.* **2**, 284–294

45. Fresques, T., Niles, B., Aronova, S., Mogri, H., Rakhshandehroo, T., and Powers, T. (2015) Regulation of Ceramide Synthase by Casein Kinase 2-dependent Phosphorylation in Saccharomyces cerevisiae. *J. Biol. Chem.* **290**, 1395–1403

46. Proia, R. L., and Hla, T. (2015) Emerging biology of sphingosine-1-phosphate: its role in pathogenesis and therapy. *J. Clin. Invest.* **125**, 1379–1387

47. Dickson, R. C., Nagiec, E. E., Skrzypek, M., Tillman, P., Wells, G. B., and Lester, R. L. (1997) Sphingolipids are potential heat stress signals in Saccharomyces. *J. Biol. Chem.* **272**, 30196–30200

48. Jenkins, G. M., Cowart, L. A., Signorelli, P., Pettus, B. J., Chalfant, C. E., and Hannun, Y. A. (2002) Acute activation of de novo sphingolipid biosynthesis upon heat shock causes an accumulation of ceramide and subsequent dephosphorylation of SR proteins. *J. Biol. Chem.* **277**, 42572–42578

49. Jenkins, G. M., Richards, A., Wahl, T., Mao, C., Obeid, L., and Hannun, Y. (1997) Involvement of yeast sphingolipids in the heat stress response of Saccharomyces cerevisiae. *J. Biol. Chem.* **272**, 32566–32572

50. Chung, N., Jenkins, G., Hannun, Y. A., Heitman, J., and Obeid, L. M. (2000) Sphingolipids signal heat stress-induced ubiquitin-dependent proteolysis. *J. Biol. Chem.* **275**, 17229–32

51. Meier, K. D., Deloche, O., Kajiwara, K., Funato, K., and Riezman, H. (2006) Sphingoid Base Is Required for Translation Initiation during Heat Stress in *Saccharomyces cerevisiae*. *Mol. Biol. Cell*. **17**, 1164–1175

52. Cowart, L. A., Gandy, J. L., Tholanikunnel, B., and Hannun, Y. A. (2010) Sphingolipids mediate formation of mRNA processing bodies during the heat-stress response of *Saccharomyces cerevisiae*. *Biochem. J.* **431**, 31–38

53. Balagopal, V., and Parker, R. (2009) Polysomes, P bodies and stress granules: states and fates of eukaryotic mRNAs. *Curr. Opin. Cell Biol.* **21**, 403–408

54. Klemm, R. W., Ejsing, C. S., Surma, M. A., Kaiser, H.-J., Gerl, M. J., Sampaio, J. L., Robillard, Q. de, Ferguson, C., Proszynski, T. J., Shevchenko, A., and Simons, K. (2009) Segregation of sphingolipids and sterols during formation of secretory vesicles at the trans-Golgi network. *J. Cell Biol.* **185**, 601–612

55. Melero, A., Chiaruttini, N., Karashima, T., Riezman, I., Funato, K., Barlowe, C.,

Riezman, H., and Roux, A. (2018) Lysophospholipids Facilitate COPII Vesicle Formation. *Curr. Biol.* **28**, 1950-1958.e6

56. Nikola A. Baumann, ‡,§, David P. Sullivan, ‡, Henna Ohvo-Rekilä, ‡, Cedric Simonot, ‡,∥, Anita Pottekat, ‡, Zachary Klaassen, ⊥, Christopher T. Beh, ⊥ and, and Anant K. Menon*, ‡ (2005) Transport of Newly Synthesized Sterol to the Sterol-Enriched Plasma Membrane Occurs via Nonvesicular Equilibration†. 10.1021/BI048296Z

57. Li, Y., and Prinz, W. A. (2004) ATP-binding cassette (ABC) transporters mediate nonvesicular, raft-modulated sterol movement from the plasma membrane to the endoplasmic reticulum. *J. Biol. Chem.* **279**, 45226–34

58. COPELAND, D. E., and DALTON, A. J. (1959) An association between mitochondria and the endoplasmic reticulum in cells of the pseudobranch gland of a teleost. *J. Biophys. Biochem. Cytol.* **5**, 393–6

59. PORTER, K. R., and PALADE, G. E. (1957) Studies on the endoplasmic reticulum. III. Its form and distribution in striated muscle cells. *J. Biophys. Biochem. Cytol.* **3**, 269–300

60. PORTER, K. R., and MACHADO, R. D. (1960) Studies on the endoplasmic reticulum. IV. Its form and distribution during mitosis in cells of onion root tip. *J. Biophys. Biochem. Cytol.* **7**, 167–80

61. Vance, E. (1990) Phospholipid Mitochondria * Synthesis in a Membrane Fraction Associated identified. *J. Biol. Chem.* **265**, 7248–7257

62. Pichler, H., Gaigg, B., Hrastnik, C., Achleitner, G., Kohlwein, S. D., Zellnig, G., Perktold, A., and Daum, G. (2001) A subfraction of the yeast endoplasmic reticulum associates with the plasma membrane and has a high capacity to synthesize lipids. *Eur. J. Biochem.* **268**, 2351–2361

63. Scorrano, L., De Matteis, M. A., Emr, S., Giordano, F., Hajnóczky, G., Kornmann, B., Lackner, L. L., Levine, T. P., Pellegrini, L., Reinisch, K., Rizzuto, R., Simmen, T., Stenmark, H., Ungermann, C., and Schuldiner, M. (2019) Coming together to define membrane contact sites. *Nat. Commun.* **10**, 1287

64. Eisenberg-Bord, M., Shai, N., Schuldiner, M., and Bohnert, M. (2016) A Tether Is a Tether Is a Tether: Tethering at Membrane Contact Sites. *Dev. Cell*. **39**, 395–409

65. Pan, X., Roberts, P., Chen, Y., Kvam, E., Shulga, N., Huang, K., Lemmon, S., and Goldfarb, D. S. (2000) Nucleus–Vacuole Junctions in *Saccharomyces cerevisiae* Are Formed Through the Direct Interaction of Vac8p with Nvj1p. *Mol. Biol. Cell*. **11**, 2445–2457

66. Jeong, H., Park, J., Kim, H.-I., Lee, M., Ko, Y.-J., Lee, S., Jun, Y., Lee, C., and Hurley, J. H. (2017) Mechanistic insight into the nucleus–vacuole junction based on the Vac8p–Nvj1p crystal structure. 10.1073/pnas.1701030114

67. Subramanian, K. (2006) Palmitoylation determines the function of Vac8 at the yeast vacuole. *J. Cell Sci.* **119**, 2477–2485

68. Millen, J. I., Pierson, J., Kvam, E., Olsen, L. J., and Goldfarb, D. S. (2008) The luminal N-terminus of yeast Nvj1 is an inner nuclear membrane anchor. *Traffic*. **9**, 1653–1664

69. Levine, T. P., and Munro, S. (2001) Dual Targeting of Osh1p, a Yeast Homologue of Oxysterol-binding Protein, to both the Golgi and the Nucleus-Vacuole Junction. *Mol. Biol. Cell*. **12**, 1633–1644

70. Kohlwein, S. D., Eder, S., Oh, C. S., Martin, C. E., Gable, K., Bacikova, D., and Dunn, T. (2001) Tsc13p is required for fatty acid elongation and localizes to a novel structure at the nuclear-vacuolar interface in Saccharomyces cerevisiae. *Mol. Cell. Biol.* **21**, 109–25

71. Kvam, E., and Goldfarb, D. S. (2004) Nvj1p is the outer-nuclear-membrane receptor for oxysterol-binding protein homolog Osh1p in Saccharomyces cerevisiae. *J. Cell Sci.* **117**, 4959–68

72. Kvam, E., and Goldfarb, D. S. (2006) Structure and function of nucleus-vacuole junctions: outer-nuclear-membrane targeting of Nvj1p and a role in tryptophan uptake. *J. Cell Sci.* **119**, 3622–33

73. Roberts, P., Moshitch-Moshkovitz, S., Kvam, E., O'Toole, E., Winey, M., and Goldfarb, D. S. (2003) Piecemeal Microautophagy of Nucleus in *Saccharomyces cerevisiae*. *Mol.*

Biol. Cell. **14**, 129–141

74. Dawaliby, R., and Mayer, A. (2010) Microautophagy of the Nucleus Coincides with a Vacuolar Diffusion Barrier at Nuclear–Vacuolar Junctions. *Mol. Biol. Cell*. **21**, 4173–4183

75. Henne, W. M., Zhu, L., Balogi, Z., Stefan, C., Pleiss, J. A., and Emr, S. D. (2015) Mdm l/Snx 13 is a novel ER-endolysosomal interorganelle tethering protein. *J. Cell Biol.* **210**, 541–551

76. Hariri, H., Rogers, S., Ugrankar, R., Liu, Y. L., Feathers, J. R., and Henne, W. M. (2018) Lipid droplet biogenesis is spatially coordinated at ER–vacuole contacts under nutritional stress. *EMBO Rep.* **19**, 57–72

77. Walther, T. C., Farese, R. V, and Jr. (2009) The life of lipid droplets. *Biochim. Biophys. Acta*. **1791**, 459–66

78. Hariri, H., Speer, N., Bowerman, J., Rogers, S., Fu, G., Reetz, E., Datta, S., Feathers, J. R., Ugrankar, R., Nicastro, D., and Henne, W. M. (2019) Mdm1 maintains endoplasmic reticulum homeostasis by spatially regulating lipid droplet biogenesis. *J. Cell Biol.* 10.1083/jcb.201808119

79. Garbarino, J., Padamsee, M., Wilcox, L., Oelkers, P. M., D'Ambrosio, D., Ruggles, K. V, Ramsey, N., Jabado, O., Turkish, A., and Sturley, S. L. (2009) Sterol and diacylglycerol acyltransferase deficiency triggers fatty acid-mediated cell death. *J. Biol. Chem.* **284**, 30994–1005

80. Murley, A., Sarsam, R. D., Toulmay, A., Yamada, J., Prinz, W. A., and Nunnari, J. (2015) Ltc1 is an ER-localized sterol transporter and a component of ER-mitochondria and ER-vacuole contacts. *J. Cell Biol.* **209**, 539–548

81. Elbaz-Alon, Y., Eisenberg-Bord, M., Shinder, V., Stiller, S. B., Shimoni, E., Wiedemann, N., Geiger, T., and Schuldiner, M. (2015) Lam6 Regulates the Extent of Contacts between Organelles. *Cell Rep.* **12**, 7–14

82. Kornmann, B., Currie, E., Collins, S. R., Schuldiner, M., Nunnari, J., Weissman, J. S., and Walter, P. (2009) An ER-mitochondria tethering complex revealed by a synthetic

biology screen. *Science (80-.).* **325**, 477–481

83. Birner, R., Bürgermeister, M., Schneiter, R., and Daum, G. (2001) Roles of Phosphatidylethanolamine and of Its Several Biosynthetic Pathways in *Saccharomyces cerevisiae*. *Mol. Biol. Cell*. **12**, 997–1007

84. Klose, C., Surma, M. A., Gerl, M. J., Meyenhofer, F., Shevchenko, A., and Simons, K. (2012) Flexibility of a Eukaryotic Lipidome - Insights from Yeast Lipidomics. *PLoS One*. ARTN e3506310.1371/journal.pone.0035063

85. Ejsing, C. S., Sampaio, J. L., Surendranath, V., Duchoslav, E., Ekroos, K., Klemm, R. W., Simons, K., and Shevchenko, A. (2009) Global analysis of the yeast lipidome by quantitative shotgun mass spectrometry. *Proc. Natl. Acad. Sci. U. S. A.* **106**, 2136–41

86. Joshi, A. S., Zhou, J., Gohil, V. M., Chen, S., and Greenberg, M. L. (2009) Cellular functions of cardiolipin in yeast. *Biochim. Biophys. Acta*. **1793**, 212–8

87. Kornmann, B., Osman, C., and Walter, P. (2011) The conserved GTPase Gem1 regulates endoplasmic reticulum-mitochondria connections. *Proc. Natl. Acad. Sci.* **108**, 14151–14156

88. Yamano, K., Tanaka-Yamano, S., and Endo, T. (2010) Tom7 Regulates Mdm10-mediated Assembly of the Mitochondrial Import Channel Protein Tom40. *J. Biol. Chem.* **285**, 41222–41231

89. Jeong, H., Park, J., and Lee, C. (2016) Crystal structure of Mdm12 reveals the architecture and dynamic organization of the ERMES complex. *EMBO Rep.* **17**, 1857–1871

90. Jeong, H., Park, J., Jun, Y., and Lee, C. (2017) Crystal structures of Mmm1 and Mdm12-Mmm1 reveal mechanistic insight into phospholipid trafficking at ER-mitochondria contact sites. *Proc. Natl. Acad. Sci. U. S. A.* **114**, E9502–E9511

91. Kawano, S., Tamura, Y., Kojima, R., Bala, S., Asai, E., Michel, A. H., Kornmann, B., Riezman, I., Riezman, H., Sakae, Y., Okamoto, Y., and Endo, T. (2018) Structure–function insights into direct lipid transfer between membranes by Mmm1–Mdm12 of ERMES. *J. Cell Biol.* **217**, 959–974

92. Nguyen, T. T., Lewandowska, A., Choi, J.-Y., Markgraf, D. F., Junker, M., Bilgin, M., Ejsing, C. S., Voelker, D. R., Rapoport, T. A., and Shaw, J. M. (2012) Gem1 and ERMES Do Not Directly Affect Phosphatidylserine Transport from ER to Mitochondria or Mitochondrial Inheritance. *Traffic*. **13**, 880–890

93. Lang, A. B., John Peter, A. T., Walter, P., and Kornmann, B. (2015) ER-mitochondrial junctions can be bypassed by dominant mutations in the endosomal protein Vps13. *J. Cell Biol.* **210**, 883–90

94. Bean, B. D. M., Dziurdzik, S. K., Kolehmainen, K. L., Fowler, C. M. S., Kwong, W. K., and Grad, L. I. (2018) Competitive organelle-specific adaptors recruit Vps13 to membrane contact sites

95. Peter, A. T. J., Herrmann, B., Antunes, D., Rapaport, D., Dimmer, K. S., and Kornmann, B. (2017) Vps13-Mcp1 interact at vacuole-mitochondria interfaces and bypass ER-mitochondria contact sites. *J. Cell Biol.* **216**, 3219–3229

96. Elbaz-Alon, Y., Rosenfeld-Gur, E., Shinder, V., Futerman, A. H., Geiger, T., and Schuldiner, M. (2014) A Dynamic Interface between Vacuoles and Mitochondria in Yeast. *Dev. Cell*. **30**, 95–102

97. Petrungaro, C., and Kornmann, B. (2019) Lipid exchange at ER-mitochondria contact sites: a puzzle falling into place with quite a few pieces missing. *Curr. Opin. Cell Biol.* **57**, 71–76

98. Dittman, J. S., and Menon, A. K. (2017) Speed Limits for Nonvesicular Intracellular Sterol Transport. *Trends Biochem. Sci.* **42**, 90–97

99. Hönscher, C., Mari, M., Auffarth, K., Bohnert, M., Griffith, J., Geerts, W., van der Laan, M., Cabrera, M., Reggiori, F., and Ungermann, C. (2014) Cellular metabolism regulates contact sites between vacuoles and mitochondria. *Dev. Cell*. **30**, 86–94

100. Hönscher, C., Mari, M., Auffarth, K., Bohnert, M., Griffith, J., Geerts, W., van der Laan, M., Cabrera, M., Reggiori, F., and Ungermann, C. (2014) Cellular Metabolism Regulates Contact Sites between Vacuoles and Mitochondria. *Dev. Cell*. **30**, 86–94

101. González Montoro, A., Auffarth, K., Hönscher, C., Bohnert, M., Becker, T., Warscheid,

B., Reggiori, F., van der Laan, M., Fröhlich, F., and Ungermann, C. (2018) Vps39 Interacts with Tom40 to Establish One of Two Functionally Distinct Vacuole-Mitochondria Contact Sites. *Dev. Cell*. **45**, 621-636.e7

102. Preuss, D., Mulholland, J., Kaiser, C. A., Orlean, P., Albright, C., Rose, M. D., Robbins, P. W., and Botstein, D. (1991) Structure of the yeast endoplasmic reticulum: Localization of ER proteins using immunofluorescence and immunoelectron microscopy. *Yeast*. **7**, 891–911

103. West, M., Zurek, N., Hoenger, A., and Voeltz, G. K. (2011) A 3D analysis of yeast ER structure reveals how ER domains are organized by membrane curvature. *J. Cell Biol.* **193**, 333–46

104. Loewen, C. J. R., Young, B. P., Tavassoli, S., and Levine, T. P. (2007) Inheritance of cortical ER in yeast is required for normal septin organization. *J. Cell Biol.* **179**, 467–83

105. Manford, A. G., Stefan, C. J., Yuan, H. L., MacGurn, J. A., and Emr, S. D. (2012) ER-to-Plasma Membrane Tethering Proteins Regulate Cell Signaling and ER Morphology. *Dev. Cell*. **23**, 1129–1140

106. Fischer, M. A., Temmerman, K., Ercan, E., Nickel, W., and Seedorf, M. (2009) Binding of plasma membrane lipids recruits the yeast integral membrane protein Ist2 to the cortical ER. *Traffic*. **10**, 1084–1097

107. Maass, K., Fischer, M. A., Seiler, M., Temmerman, K., Nickel, W., and Seedorf, M. (2009) A signal comprising a basic cluster and an amphipathic -helix interacts with lipids and is required for the transport of Ist2 to the yeast cortical ER. *J. Cell Sci.* **122**, 625–635

108. AhYoung, A. P., Jiang, J., Zhang, J., Khoi Dang, X., Loo, J. A., Zhou, Z. H., and Egea, P. F. (2015) Conserved SMP domains of the ERMES complex bind phospholipids and mediate tether assembly. *Proc. Natl. Acad. Sci. U. S. A.* **112**, E3179-88

109. Quon, E., Sere, Y. Y., Chauhan, N., Johansen, J., Sullivan, D. P., Dittman, J. S., Rice, W. J., Chan, R. B., Paolo, G. Di, Beh, C. T., and Menon, A. K. (2018) Endoplasmic reticulum-plasma membrane contact sites integrate sterol and phospholipid regulation. *PLoS Biol.* **16**, e2003864

110. Estrada de Martin, P., Du, Y., Novick, P., and Ferro-Novick, S. (2005) Ice2p is important for the distribution and structure of the cortical ER network in Saccharomyces cerevisiae. *J. Cell Sci.* **118**, 65–77

111. Tavassoli, S., Chao, J. T., Young, B. P., Cox, R. C., Prinz, W. a, de Kroon, A. I. P. M., and Loewen, C. J. R. (2013) Plasma membrane--endoplasmic reticulum contact sites regulate phosphatidylcholine synthesis. *EMBO Rep.* **14**, 434–40

112. Cerbón, J., and Calderón, V. (1995) Generation, modulation and maintenance of the plasma membrane asymmetric phospholipid composition in yeast cells during growth: their relation to surface potential and membrane protein activity. *Biochim. Biophys. Acta*. **1235**, 100–6

113. Maeda, K., Anand, K., Chiapparino, A., Kumar, A., Poletto, M., Kaksonen, M., and Gavin, A.-C. (2013) Interactome map uncovers phosphatidylserine transport by oxysterol-binding proteins. *Nature*. **501**, 257–261

114. Filseck, J. M. von, Čopič, A., Delfosse, V., Vanni, S., Jackson, C. L., Bourguet, W., and Drin, G. (2015) Phosphatidylserine transport by ORP/Osh proteins is driven by phosphatidylinositol 4-phosphate. *Science (80-.).* **349**, 432–436

115. Loewen, C. J. R., Roy, A., and Levine, T. P. (2003) A conserved ER targeting motif in three families of lipid binding proteins and in Opi1p binds VAP. *EMBO J.* **22**, 2025–2035

116. Omnus, D. J., Manford, A. G., Bader, J. M., Emr, S. D., and Stefan, C. J. (2016) Phosphoinositide kinase signaling controls ER-PM cross-talk. *Mol. Biol. Cell*. **27**, 1170–1180

117. Georgiev, A. G., Sullivan, D. P., Kersting, M. C., Dittman, J. S., Beh, C. T., and Menon, A. K. (2011) Osh Proteins Regulate Membrane Sterol Organization but Are Not Required for Sterol Movement Between the ER and PM. *Traffic*. **12**, 1341–1355

118. Gatta, A. T., Wong, L. H., Sere, Y. Y., Calderon-Norena, D. M., Cockcroft, S., Menon, A. K., and Levine, T. P. (2015) A new family of StART domain proteins at membrane contact sites has a role in ER-PM sterol transport. *Elife*. ARTN e0725310.7554/eLife.07253

119. Sharma, S., Alfatah, , Bari, V. K., Rawal, Y., Paul, S., and Ganesan, K. (2014) Sphingolipid Biosynthetic Pathway Genes *FEN1* and *SUR4* Modulate Amphotericin B Resistance. *Antimicrob. Agents Chemother.* **58**, 2409–2414

120. Guan, X. L., Souza, C. M., Pichler, H., Dewhurst, G., Schaad, O., Kajiwara, K., Wakabayashi, H., Ivanova, T., Castillon, G. A., Piccolis, M., Abe, F., Loewith, R., Funato, K., Wenk, M. R., and Riezman, H. (2009) Functional interactions between sphingolipids and sterols in biological membranes regulating cell physiology. *Mol. Biol. Cell*. **20**, 2083–95

121. Lam, S. S., Martell, J. D., Kamer, K. J., Deerinck, T. J., Ellisman, M. H., Mootha, V. K., and Ting, A. Y. (2015) Directed evolution of APEX2 for electron microscopy and proximity labeling. *Nat. Methods*. **12**, 51–54

122. Bumpus, T. W., and Baskin, J. M. (2018) Greasing the Wheels of Lipid Biology with Chemical Tools. *Trends Biochem. Sci.* **43**, 970–983

123. Nadler, A., Reither, G., Feng, S., Stein, F., Reither, S., Müller, R., and Schultz, C. (2013) The fatty acid composition of diacylglycerols determines local signaling patterns. *Angew. Chemie - Int. Ed.* **52**, 6330–6334

124. Nadler, A., Yushchenko, D. A., Müller, R., Stein, F., Feng, S., Mulle, C., Carta, M., and Schultz, C. (2015) Exclusive photorelease of signalling lipids at the plasma membrane. *Nat. Commun.* **6**, 10056

125. Feng, S., Harayama, T., Montessuit, S., David, F. P., Winssinger, N., Martinou, J.-C., and Riezman, H. (2018) Mitochondria-specific photoactivation to monitor local sphingosine metabolism and function. *Elife*. 10.7554/eLife.34555

126. Feng, S., Harayama, T., Chang, D., Hannich, J. T., Winssinger, N., and Riezman, H. (2019) Lysosome-targeted photoactivation reveals local sphingosine metabolism signatures. *Chem. Sci.* **10**, 2253–2258

127. Höglinger, D., Nadler, A., Haberkant, P., Kirkpatrick, J., Schifferer, M., Stein, F., Hauke, S., Porter, F. D., and Schultz, C. (2017) Trifunctional lipid probes for comprehensive studies of single lipid species in living cells. *Proc. Natl. Acad. Sci. U. S. A.* **114**, 1566–1571

128. Ernst, R., Klemm, R., Schmitt, L., and Kuchler, K. (2005) Yeast ATP-Binding Cassette Transporters: Cellular Cleaning Pumps. in *Methods in enzymology*, pp. 460–484, **400**, 460–484

129. Stepanov, A., Nitiss, K. C., Neale, G., and Nitiss, J. L. (2008) Enhancing drug accumulation in Saccharomyces cerevisiae by repression of pleiotropic drug resistance genes with chimeric transcription repressors. *Mol. Pharmacol.* **74**, 423–31

130. de Martin, P. E., Novick, P., and Ferro-Novick, S. (2005) The organization, structure, and inheritance of the ER in higher and lower eukaryotes. *Biochem. Cell Biol.* **83**, 752–761

131. English, A. R., Zurek, N., and Voeltz, G. K. (2009) Peripheral ER structure and function. *Curr. Opin. Cell Biol.* **21**, 596–602

132. Smoyer, C. J., Katta, S. S., Gardner, J. M., Stoltz, L., McCroskey, S., Bradford, W. D., McClain, M., Smith, S. E., Slaughter, B. D., Unruh, J. R., and Jaspersen, S. L. (2016) Analysis of membrane proteins localizing to the inner nuclear envelope in living cells. *J. Cell Biol.* **215**, 575–590

133. Boeke, J. D., La Croute, F., and Fink, G. R. (1984) A positive selection for mutants lacking orotidine-5′-phosphate decarboxylase activity in yeast: 5-fluoro-orotic acid resistance. *Mol. Gen. Genet. MGG*. **197**, 345–346

134. Guan, X. L., Riezman, I., Wenk, M. R., and Riezman, H. (2010) Yeast Lipid Analysis and Quantification by Mass Spectrometry. in *Methods in enzymology*, pp. 369–391, **470**, 369–391

135. Lindberg, L., Santos, A. X., Riezman, H., Olsson, L., and Bettiga, M. (2013) Lipidomic Profiling of Saccharomyces cerevisiae and Zygosaccharomyces bailii Reveals Critical Changes in Lipid Composition in Response to Acetic Acid Stress. *PLoS One*. **8**, e73936

136. Ferguson-Yankey, S. R., Skrzypek, M. S., Lester, R. L., and Dickson, R. C. (2002) Mutant analysis reveals complex regulation of sphingolipid long chain base phosphates and long chain bases during heat stress in yeast. *Yeast*. **19**, 573–586

137. Jiang, J. C., Kirchman, P. A., Zagulski, M., Hunt, J., and Jazwinski, S. M. (1998)

Homologs of the Yeast Longevity Gene *LAG1* in *Caenorhabditis elegans* and Human. *Genome Res.* **8**, 1259–1272

138. Barz, W. P., and Walter, P. (1999) Two Endoplasmic Reticulum (ER) Membrane Proteins That Facilitate ER-to-Golgi Transport of Glycosylphosphatidylinositol-anchored Proteins. **10**, 1043–1059

139. Cowart, L. A., and Hannun, Y. A. (2007) Selective substrate supply in the regulation of yeast de novo sphingolipid synthesis. *J. Biol. Chem.* **282**, 12330–40

140. Wells, G. B., Dickson, R. C., and Lester, R. L. (1998) Heat-induced elevation of ceramide in Saccharomyces cerevisiae via de Novo synthesis. *J. Biol. Chem.* **273**, 7235–7243

141. Eisenberg, T., and Büttner, S. (2014) Lipids and cell death in yeast. *FEMS Yeast Res.* **14**, 179–197

142. Terpe, K. (2003) Overview of tag protein fusions: from molecular and biochemical fundamentals to commercial systems. *Appl. Microbiol. Biotechnol.* **60**, 523–533

143. Weill, U., Krieger, G., Avihou, Z., Milo, R., Schuldiner, M., and Davidi, D. (2019) Assessment of GFP Tag Position on Protein Localization and Growth Fitness in Yeast. *J. Mol. Biol.* **431**, 636–641

144. Taxis, C., and Knop, M. (2006) System of centromeric, episomal, and integrative vectors based on drug resistance markers for Saccharomyces cerevisiae. *Biotechniques*. **40**, 73–78

145. Kolaczkowski, M., Kolaczkowska, A., Gaigg, B., Schneiter, R., and Moye-Rowley, W. S. (2004) Differential regulation of ceramide synthase components LAC1 and LAG1 in Saccharomyces cerevisiae. *Eukaryot. Cell.* **3**, 880–92

146. Breslow, D. K. (2013) Sphingolipid homeostasis in the endoplasmic reticulum and beyond. *Cold Spring Harb. Perspect. Biol.* **5**, 1–16

147. Ungricht, R., and Kutay, U. (2017) Mechanisms and functions of nuclear envelope remodelling. *Nat. Rev. Mol. Cell Biol.* **18**, 229–245

148. King, M. C., Lusk, C., and Blobel, G. (2006) Karyopherin-mediated import of integral inner nuclear membrane proteins. *Nature*. **442**, 1003–1007

149. Lokareddy, R. K., Hapsari, R. A., van Rheenen, M., Pumroy, R. A., Bhardwaj, A., Steen, A., Veenhoff, L. M., and Cingolani, G. (2015) Distinctive Properties of the Nuclear Localization Signals of Inner Nuclear Membrane Proteins Heh1 and Heh2. *Structure*. **23**, 1305–1316

150. Murphy, M. P. (2008) Targeting lipophilic cations to mitochondria. *Biochim. Biophys. Acta - Bioenerg.* **1777**, 1028–1031

151. Murphy, M. P. (1997) Selective targeting of bioactive compounds to mitochondria. *Trends Biotechnol.* **15**, 326–330

152. Kihara, A., and Igarashi, Y. (2002) Identification and characterization of a Saccharomyces cerevisiae gene, RSB1, involved in sphingoid long-chain base release. *J. Biol. Chem.* **277**, 30048–54

153. Balzi, E., Wang, M., Leterme, S., Van Dyck, L., and Goffeau, A. (1994) PDR5, a novel yeast multidrug resistance conferring transporter controlled by the transcription regulator PDR1. *J. Biol. Chem.* **269**, 2206–14

154. Golin, J., Ambudkar, S. V., Gottesman, M. M., Habib, A. D., Sczepanski, J., Ziccardi, W., and May, L. (2003) Studies with Novel Pdr5p Substrates Demonstrate a Strong Size Dependence for Xenobiotic Efflux. *J. Biol. Chem.* **278**, 5963–5969

155. Battogtokh, G., Choi, Y. S., Kang, D. S., Park, S. J., Shim, M. S., Huh, K. M., Cho, Y.-Y., Lee, J. Y., Lee, H. S., and Kang, H. C. (2018) Mitochondria-targeting drug conjugates for cytotoxic, anti-oxidizing and sensing purposes: current strategies and future perspectives. *Acta Pharm. Sin. B*. **8**, 862–880

156. Mitchell, P. (1966) Chemiosmotic coupling in oxidative and photosynthetic phosphorylation. *Biol. Rev. Camb. Philos. Soc.* **41**, 445–502

157. Li, S. C., and Kane, P. M. (2009) The yeast lysosome-like vacuole: endpoint and crossroads. *Biochim. Biophys. Acta*. **1793**, 650–63

158. Hirose, S., Yaginuma, N., and Inada, Y. (1974) Disruption of charge separation followed

by that of the proton gradient in the mitochondrial membrane by CCCP. *J. Biochem.* **76**, 213–6

159. Droese, S., Bindseil, K. U., Bowman, E. J., Siebers, A., Zeeck, A., and Altendorf, K. (1993) Inhibitory effect of modified bafilomycins and concanamycins on P- and V-type adenosinetriphosphatases. *Biochemistry.* **32**, 3902–3906

160. Narita, T., Naganuma, T., Sase, Y., and Kihara, A. (2016) Long-chain bases of sphingolipids are transported into cells via the acyl-CoA synthetases. *Sci. Rep.* Artn 2546910.1038/Srep25469

161. Watkins, P. A., Lu, J. F., Steinberg, S. J., Gould, S. J., Smith, K. D., and Braiterman, L. T. (1998) Disruption of the Saccharomyces cerevisiae FAT1 gene decreases very long-chain fatty acyl-CoA synthetase activity and elevates intracellular very long-chain fatty acid concentrations. *J. Biol. Chem.* **273**, 18210–9

162. Lu, R., Drubin, D. G., and Sun, Y. (2016) Clathrin-mediated endocytosis in budding yeast at a glance. *J. Cell Sci.* **129**, 1531–6

163. Chvatchko, Y., Howald, I., and Riezman, H. (1986) Two yeast mutants defective in endocytosis are defective in pheromone response. *Cell.* **46**, 355–364

164. Bénédetti, H., Raths, S., Crausaz, F., and Riezman, H. (1994) The END3 gene encodes a protein that is required for the internalization step of endocytosis and for actin cytoskeleton organization in yeast. *Mol. Biol. Cell.* **5**, 1023–1037

165. Vida, T. A., and Emr, S. D. (1995) A new vital stain for visualizing vacuolar membrane dynamics and endocytosis in yeast. *J. Cell Biol.* **128**, 779–792

166. Munn, A. L. (2001) Molecular requirements for the internalisation step of endocytosis: insights from yeast. *Biochim. Biophys. Acta - Mol. Basis Dis.* **1535**, 236–257

167. Woolford, C. A., Daniels, L. B., Park, F. J., Jones, E. W., Van Arsdell, J. N., and Innis, M. A. (1986) The PEP4 gene encodes an aspartyl protease implicated in the posttranslational regulation of Saccharomyces cerevisiae vacuolar hydrolases. *Mol. Cell. Biol.* **6**, 2500–10

168. Mao, C., Xu, R., Bielawska, A., and Obeid, L. M. (2000) Cloning of an alkaline

ceramidase from Saccharomyces cerevisiae. An enzyme with reverse (CoA-independent) ceramide synthase activity. *J. Biol. Chem.* **275**, 6876–84

169. Yofe, I., Weill, U., Meurer, M., Chuartzman, S., Zalckvar, E., Goldman, O., Ben-Dora, S., Schutze, C., Wiedemann, N., Knop, M., Khmelinskii, A., and Schuldiner, M. (2016) One library to make them all: streamlining the creation of yeast libraries via a SWAp-Tag strategy. *Nat. Methods*. **13**, 371–378

170. Martínez-Montañés, F., and Schneiter, R. (2016) Following the flux of long-chain bases through the sphingolipid pathway in vivo using mass spectrometry. *J. Lipid Res.* **57**, 906–915

171. Schorling, S., Vallée, B., Barz, W. P., Riezman, H., and Oesterhelt, D. (2001) Lag1p and Lac1p Are Essential for the Acyl-CoA–dependent Ceramide Synthase Reaction in *Saccharomyces cerevisae*. *Mol. Biol. Cell*. **12**, 3417–3427

172. Dubreuil, B., Sass, E., Nadav, Y., Heidenreich, M., Georgeson, J. M., Weill, U., Duan, Y., Meurer, M., Schuldiner, M., Knop, M., and Levy, E. D. (2019) YeastRGB: comparing the abundance and localization of yeast proteins across cells and libraries. *Nucleic Acids Res.* **47**, D1245–D1249

173. Uemura, S., Kihara, A., Iwaki, S., Inokuchi, J. I., and Igarashi, Y. (2007) Regulation of the transport and protein levels of the inositol phosphorylceramide mannosyltransferases Csg1 and Csh1 by the Ca2+ binding protein Csg2. *J. Biol. Chem.* **282**, 8613–8621

174. Nagiec, M. M., Nagiec, E. E., Baltisberger, J. A., Wells, G. B., Lester, R. L., and Dickson, R. C. (1997) Sphingolipid synthesis as a target for antifungal drugs. Complementation of the inositol phosphorylceramide synthase defect in a mutant strain of Saccharomyces cerevisiae by the AUR1 gene. *J. Biol. Chem.* **272**, 9809–17

175. Srere, P. A. (1987) Complexes of Sequential Metabolic Enzymes. *Annu. Rev. Biochem.* **56**, 89–124

176. Guo, H., Yang, Y., Xue, F., Zhang, H., Huang, T., Liu, W., Liu, H., Zhang, F., Yang, M., Liu, C., Lu, H., Zhang, Y., and Ma, L. (2017) Effect of flexible linker length on the activity of fusion protein 4-coumaroyl-CoA ligase::stilbene synthase. *Mol. Biosyst.* **13**, 598–606

177. Yansheng Zhang, †, Song-Zhe Li, ‡, Jia Li, †, Xiangqing Pan, †, Rebecca E. Cahoon, †, Jan G. Jaworski, †, Xuemin Wang, †,§, Joseph M. Jez, †, Feng Chen, ‡ and, and Oliver Yu†, * (2006) Using Unnatural Protein Fusions to Engineer Resveratrol Biosynthesis in Yeast and Mammalian Cells. 10.1021/JA0622094

178. Albertsen, L., Chen, Y., Bach, L. S., Rattleff, S., Maury, J., Brix, S., Nielsen, J., and Mortensen, U. H. (2011) Diversion of flux toward sesquiterpene production in Saccharomyces cerevisiae by fusion of host and heterologous enzymes. *Appl. Environ. Microbiol.* **77**, 1033–40

179. Sabourin, M., Tuzon, C. T., Fisher, T. S., and Zakian, V. A. (2007) A flexible protein linker improves the function of epitope-tagged proteins inSaccharomyces cerevisiae. *Yeast*. **24**, 39–45

180. Rath, A., Glibowicka, M., Nadeau, V. G., Chen, G., and Deber, C. M. (2009) Detergent binding explains anomalous SDS-PAGE migration of membrane proteins. *Proc. Natl. Acad. Sci. U. S. A.* **106**, 1760–5

181. Belshaw, P. J., Ho, S. N., Crabtree, G. R., and Schreiber, S. L. (1996) Controlling protein association and subcellular localization with a synthetic ligand that induces heterodimerization of proteins. *Proc. Natl. Acad. Sci. U. S. A.* **93**, 4604–7

182. Stefan, C. J., Manford, A. G., Baird, D., Yamada-Hanff, J., Mao, Y., and Emr, S. D. (2011) Osh Proteins Regulate Phosphoinositide Metabolism at ER-Plasma Membrane Contact Sites. *Cell*. **144**, 389–401

183. Liu, M., Huang, C., Polu, S. R., Schneiter, R., and Chang, A. (2012) Regulation of sphingolipid synthesis through Orm1 and Orm2 in yeast. *J. Cell Sci.* **125**, 2428–35

184. Romanauska, A., and Köhler, A. (2018) The Inner Nuclear Membrane Is a Metabolically Active Territory that Generates Nuclear Lipid Droplets. *Cell*. **174**, 700-715.e18

185. Kiššová, I. B., Salin, B., Schaeffer, J., Bhatia, S., Manon, S., and Camougrand, N. (2007) Selective and Non-Selective Autophagic Degradation of Mitochondria in Yeast. *Autophagy*. **3**, 329–336

186. Okamoto, K., Kondo-Okamoto, N., and Ohsumi, Y. (2009) Mitochondria-Anchored

Receptor Atg32 Mediates Degradation of Mitochondria via Selective Autophagy. *Dev. Cell*. **17**, 87–97

187. Kanki, T., and Klionsky, D. J. (2008) Mitophagy in Yeast Occurs through a Selective Mechanism. *J. Biol. Chem.* **283**, 32386–32393

188. Shimazu, M., Sekito, T., Akiyama, K., Ohsumi, Y., and Kakinuma, Y. (2005) A family of basic amino acid transporters of the vacuolar membrane from Saccharomyces cerevisiae. *J. Biol. Chem.* **280**, 4851–7

189. Cagnac, O., Aranda-Sicilia, M. N., Leterrier, M., Rodriguez-Rosales, M.-P., and Venema, K. (2010) Vacuolar Cation/H $^+$ Antiporters of *Saccharomyces cerevisiae*. *J. Biol. Chem.* **285**, 33914–33922

190. Funato, K., Lombardi, R., Vallee, B., and Riezman, H. (2003) Lcb4p is a key regulator of ceramide synthesis from exogenous long chain sphingoid base in Saccharomyces cerevisiae. *J. Biol. Chem.* **278**, 7325–34

191. Megyeri, M., Riezman, H., Schuldiner, M., and Futerman, A. H. (2016) Making Sense of the Yeast Sphingolipid Pathway. *J. Mol. Biol.* **428**, 4765–4775

192. Frohlich, F., Petit, C., Kory, N., Christiano, R., Hannibal-Bach, H. K., Graham, M., Liu, X. R., Ejsing, C. S., Farese, R. V, and Walther, T. C. (2015) The GARP complex is required for cellular sphingolipid homeostasis. *Elife*. ARTN e0871210.7554/eLife.08712

193. Wedaman, K. P., Reinke, A., Anderson, S., Yates, J., McCaffery, J. M., and Powers, T. (2003) Tor Kinases Are in Distinct Membrane-associated Protein Complexes in *Saccharomyces cerevisiae*. *Mol. Biol. Cell*. **14**, 1204–1220

194. Kira, S., Tabata, K., Shirahama-Noda, K., Nozoe, A., Yoshimori, T., and Noda, T. (2014) Reciprocal conversion of Gtr1 and Gtr2 nucleotidebinding states by Npr2-Npr3 inactivates TORC1 and induces autophagy. *Autophagy*. **10**, 1565–1578

195. Toulmay, A., and Prinz, W. A. (2013) Direct imaging reveals stable, micrometer-scale lipid domains that segregate proteins in live cells. *J. Cell Biol.* **202**, 35–44

Appendix

Abbreviations

ABC - ATP-binding cassette

ANOVA – analysis of variance

AQC - 6-aminoquinolyl-N-hydrosysuccinimidyl carbamate

C8GC - C8-glucosylceramide

CCCP - carbonyl cyanide m-chlorophenyl hydrazine

CerS, CS – ceramide synthase

CoA – coenzyme A

DHC – dihydroceramide

DHS – dihydrosphingosine

DMSO - dimethyl sulfoxide

EM – electron microscopy

ER – endoplasmic reticulum

ERMES – ER-mitochondria encounter structures

ESI - electrospray ionization

FFAT - two phenylalanines (FF) in an Acidic Tract

FM™4-64 - (*N*-(3-Triethylammoniumpropyl)-4-(6-(4-(Diethylamino) Phenyl) Hexatrienyl) Pyridinium Dibromide)

HPLC – high performance liquid chromatography

INM – inner nuclear membrane

IPC – inositolphosphorylceramide

LCB – long-chain base

LC-MS – liquid chromatography mass spectrometry

LD – lipid droplet

LFM – low fluorescence medium

M(IP)$_2$C - mannosyl-diinositolphosphorylceramide

MCS – membrane contact sites

MCT - membrane compartment containing Tor2

MIPC – mannosyl- inositolphosphorylceramide

MRM - multiple reaction monitoring

MS – mass spectrometry

NE – nuclear envelope

NLS – nuclear localization sequence

NVJ – nucleus-vacuole junctions

OD - optical density

OSBP - oxysterol-binding protein

PC – phosphatidylcholine

PE – phosphatidylethanolamine

PHC – phytoceramide

PHS- phytosphingosine

PIP – phosphatidylinositol phosphate

PM – plasma membrane

PMN - piecemeal microautophagy of the nucleus

PS - phosphatidylserine

RT – room temperature

Sa – sphinganine

SD – synthetic dextrose

SMP - Synaptotagmin-like Mitochondrial lipid-binding Protein

SPOTS – Serine Palmitoyltransferase Orm Tsc10 Sac1 Complex

SPT – serine palmotoyltransferase

StART - Steroidogenic Acute Regulatory transfer

TCA - trichloroacetic acid

TLC - thin layer chromatography

TM – transmembrane

TORC2 – target of rapamycin complex 2

TPP – triphenylphosphonium

UV – ultraviolet

vCLAMPs - *v*a*c*uo*l*e *a*nd *m*itochondria *p*atch

VLCFA – very long-chain fatty acid

YPD – Yeast extract Peptone Dextrose

Paper: Mutations in sphingosine-1-phosphate lyase cause nephrosis with ichthyosis and adrenal insufficiency

Citation:

1. Lovric, S., Goncalves, S., Gee, H. Y., Oskouian, B., Srinivas, H., Choi, W.-I., Shril, S., Ashraf, S., Tan, W., Rao, J., Airik, M., Schapiro, D., Braun, D. A., Sadowski, C. E., Widmeier, E., Jobst-Schwan, T., Schmidt, J. M., Girik, V., Capitani, G., Suh, J. H., Lachaussée, N., Arrondel, C., Patat, J., Gribouval, O., Furlano, M., Boyer, O., Schmitt, A., Vuiblet, V., Hashmi, S., Wilcken, R., Bernier, F. P., Innes, A. M., Parboosingh, J. S., Lamont, R. E., Midgley, J. P., Wright, N., Majewski, J., Zenker, M., Schaefer, F., Kuss, N., Greil, J., Giese, T., Schwarz, K., Catheline, V., Schanze, D., Franke, I., Sznajer, Y., Truant, A. S., Adams, B., Désir, J., Biemann, R., Pei, Y., Ars, E., Lloberas, N., Madrid, A., Dharnidharka, V. R., Connolly, A. M., Willing, M. C., Cooper, M. A., Lifton, R. P., Simons, M., Riezman, H., Antignac, C., Saba, J. D., and Hildebrandt, F. (2017) Mutations in sphingosine-1-phosphate lyase cause nephrosis with ichthyosis and adrenal insufficiency. *J. Clin. Invest.* **127**, 912–928

Summary:

The following paper identifies and characterizes 9 different recessive mutations in the human sphingosine-1-phosphate lyase gene (*SGPL1*) associated with a rare chronic kidney disease called steroid-resistant nephrotic syndrome (SRNS). SGPL1 catalyzes the irreversible degradation of sphingosine-1-phsophate – the last step of sphingolipid catabolism. SGPL1 proteins with disease-causing mutations were characterized in cultured human cells and various model organisms: mice, *Drosophila* fruit flies, budding yeast *Saccharomyces cerevisiae*.

Contribution:

My personal contribution to the paper was to test 6 disease-causing mutant forms of SPGL1 in budding yeast (shown in Figure 2 (N,O) and Supplemental Figure 7). Yeast have an ortholog of SGPL1, Dpl1 (dihydrosphingosine phosphate lyase). Yeast lacking Dpl1 protein are viable but sensitive to high concentrations of cytotoxic phytosphingosine (PHS) being unable to degrade sphingoid bases. ORF sequences of wild-type or mutant SGPL1 genes were subcloned into a centromeric yeast vector and yeast cells were transformed with the resulting plasmids. I then tested an ability of various mutant SGPL1 proteins to rescue PHS sensitivity of *dpl1Δ* strain. The results of these experiments are shown in Figure 2 (N) and Supplemental Figure 7 (A). I also tested the ability of the same mutant SGPL1 proteins to rescue the synthetic lethal phenotype resulting from the double deletion of *LCB3* and *DPL1* genes (synthetic lethality test). For this, the *lcb3Δdpl1Δ* strain, bearing a rescue plasmid expressing *LCB3* on a centromeric plasmid was transformed with wild-type or mutant human *SGPL1* genes. Then, the rescue plasmid harboring URA3 marker was removed by the counterselection with 5-FoA (5-fluoroorotic acid) and the ability of SPGL1 proteins to complement the loss of Lcb3 was assessed by growth of 5FoA plates. The data from these experiments is shown in Figure 2 (O) and Supplemental Figure 7 (B). Furthermore, I quantified the expression of wild-type and mutant human SPGL1 proteins in yeast by western blotting. The results presented in Supplemental Figure 7 (C).

Mutations in sphingosine-1-phosphate lyase cause nephrosis with ichthyosis and adrenal insufficiency

Svjetlana Lovric,[1] Sara Goncalves,[2,3] Heon Yung Gee,[1,4] Babak Oskouian,[5] Honnappa Srinivas,[6] Won-Il Choi,[1] Shirlee Shril,[1] Shazia Ashraf,[1] Weizhen Tan,[1] Jia Rao,[1] Merlin Airik,[1] David Schapiro,[1] Daniela A. Braun,[1] Carolin E. Sadowski,[1] Eugen Widmeier,[1,7] Tilman Jobst-Schwan,[1] Johanna Magdalena Schmidt,[1] Vladimir Girik,[8] Guido Capitani,[9] Jung H. Suh,[5] Noëlle Lachaussée,[2,3] Christelle Arrondel,[2,3] Julie Patat,[2,3] Olivier Gribouval,[2,3] Monica Furlano,[2,3,10] Olivia Boyer,[2,3,11] Alain Schmitt,[12,13] Vincent Vuiblet,[14,15] Seema Hashmi,[16] Rainer Wilcken,[6] Francois P. Bernier,[17] A. Micheil Innes,[17] Jillian S. Parboosingh,[17] Ryan E. Lamont,[17] Julian P. Midgley,[18] Nicola Wright,[18] Jacek Majewski,[19] Martin Zenker,[20] Franz Schaefer,[21] Navina Kuss,[22] Johann Greil,[23] Thomas Giese,[24] Klaus Schwarz,[25] Vilain Catheline,[26] Denny Schanze,[20] Ingolf Franke,[27] Yves Sznajer,[28] Anne S. Truant,[29] Brigitte Adams,[30] Julie Désir,[26] Ronald Biemann,[31] York Pei,[32] Elisabet Ars,[33] Nuria Lloberas,[34] Alvaro Madrid,[35] Vikas R. Dharnidharka,[36] Anne M. Connolly,[37] Marcia C. Willing,[38] Megan A. Cooper,[39] Richard P. Lifton,[40,41] Matias Simons,[3,42] Howard Riezman,[8] Corinne Antignac,[2,3,43] Julie D. Saba,[5] and Friedhelm Hildebrandt[1]

[1]Division of Nephrology, Boston Children's Hospital, Harvard Medical School, Boston, Massachusetts, USA. [2]Institut National de la Santé et de la Recherche Médicale, Unité Mixte de Recherche 1163, Laboratory of Hereditary Kidney Diseases, Paris, France. [3]Université Paris Descartes, Sorbonne Paris Cité, Imagine Institute, Paris, France. [4]Department of Pharmacology, Brain Korea 21 PLUS Project for Medical Sciences, Yonsei University College of Medicine, Seoul, Republic of Korea. [5]UCSF Benioff Children's Hospital Oakland, Oakland, California, USA. [6]Novartis Institutes for BioMedical Research, Basel, Switzerland. [7]Department of Medicine, Renal Division, Medical Center – University of Freiburg, Faculty of Medicine, University of Freiburg, Freiburg, Germany. [8]National Centre of Competence in Research (NCCR) Chemical Biology and Biochemistry Department, University of Geneva, Geneva, Switzerland. [9]Laboratory of Biomolecular Research, Paul Scherrer Institute, Villigen, Switzerland. [10]Nephrology Department, Fundació Puigvert, Instituto de Investigaciones Biomédicas Sant Pau (IIB–Sant Pau), Universitat Autònoma de Barcelona, REDinREN, Instituto de Investigación Carlos III, Barcelona, Spain. [11]Department of Pediatric Nephrology, Necker Hospital, Assistance Publique – Hôpitaux de Paris, Paris, France. [12]Plateforme de Microscopie Electronique, Institut National de la Santé et de la Recherche Médicale 1016, Institut Cochin, Paris, France. [13]Centre National de la Recherche Scientifique, Unité Mixte de Recherche 81044, Paris, France. [14]Centre National pour la Recherche Scientifique, Unité Mixte de Recherche 7369, Laboratory of Matrice Extracellulaire et Dynamique Cellulaire, Reims, France. [15]Nephrology and Renal Transplantation Department and Biopathology Laboratory, Centre Hospitalier et Universitaire de Reims, Reims, France. [16]Department of Pediatric Nephrology, Sindh Institute of Urology and Transplantation, Karachi, Pakistan. [17]Department of Medical Genetics and [18]Department of Pediatrics, University of Calgary, Alberta Health Services, Calgary, Canada. [19]Department of Human Genetics, McGill University, Montréal, Quebec, Canada. [20]Institute of Human Genetics, University Hospital Magdeburg, Magdeburg, Germany. [21]Division of Pediatric Nephrology, [22]Department of Neonatology, [23]Department of Pediatric Hematology and Oncology, Center for Pediatrics and Adolescent Medicine, and [24]Institute of Immunology, University of Heidelberg, Heidelberg, Germany. [25]Institute for Transfusion Medicine, University of Ulm, and Institute of Clinical Transfusion Medicine and Immunogenetics Ulm, German Red Cross Blood Service Baden-Württemberg – Hessen, Ulm, Germany. [26]ULB Center of Human Genetics. Hôpital Erasme, Université Libre de Bruxelles (ULB), Brussels, Belgium. [27]Department of Dermatology, University Hospital Magdeburg, Magdeburg, Germany. [28]Centre de Génétique Humaine, Cliniques Universitaires Saint Luc, [29]Pediatric Neonatology, Center for Human Genetics, Université Catholique de Louvain (UCL), [30]Nephrology ped, Hôpital universitaire des enfants Reine Fabiola (HUDERF), Université Libre de Bruxelles (ULB), Brussels, Belgium. [31]Institute of Clinical Chemistry and Pathobiochemistry, University Hospital Magdeburg, Magdeburg, Germany. [32]Division of Nephrology, Department of Internal Medicine, University Health Network and University of Toronto, Ontario, Canada. [33]Molecular Biology Laboratory, Fundació Puigvert, IIB-Sant Pau, Universitat Autònoma de Barcelona, REDinREN, Instituto de Investigación Carlos III, Barcelona, Spain. [34]Nephrology Service and Laboratory of Experimental Nephrology, Hospital Universitari de Bellvitge, Catalonia, Spain. [35]Nefrología Pediátrica, Hospital Universitario Materno–Infantil Vall d' Hebron, Barcelona, Spain. [36]Department of Pediatrics, Division of Pediatric Nephrology, Washington University School of Medicine, St. Louis, Missouri, USA. [37]Department of Neurology, Neuromuscular Division, [38]Department of Pediatrics, Division of Genetics and Genomic Medicine, and [39]Department of Pediatrics, Division of Rheumatology, Washington University School of Medicine, St. Louis, Missouri, USA. [40]Department of Genetics, Yale University School of Medicine, New Haven, Connecticut, USA. [41]Howard Hughes Medical Institute, Chevy Chase, Maryland, USA. [42]Institut National de la Santé et de la Recherche Médicale, Unité Mixte de Recherche 1163, Laboratory of Epithelial Biology and Disease, Paris, France. [43]Department of Genetics, Necker Hospital, Assistance Publique – Hôpitaux de Paris, Paris, France.

Steroid-resistant nephrotic syndrome (SRNS) causes 15% of chronic kidney disease cases. A mutation in 1 of over 40 monogenic genes can be detected in approximately 30% of individuals with SRNS whose symptoms manifest before 25 years of age. However, in many patients, the genetic etiology remains unknown. Here, we have performed whole exome sequencing to identify recessive causes of SRNS. In 7 families with SRNS and facultative ichthyosis, adrenal insufficiency, immunodeficiency, and neurological defects, we identified 9 different recessive mutations in *SGPL1*, which encodes sphingosine-1-phosphate (S1P) lyase. All mutations resulted in reduced or absent SGPL1 protein and/or enzyme activity. Overexpression of cDNA representing *SGPL1* mutations resulted in subcellular mislocalization of SGPL1. Furthermore, expression of WT human SGPL1 rescued growth of SGPL1-deficient *dpl1*Δ yeast strains, whereas expression of disease-associated variants did not. Immunofluorescence revealed SGPL1 expression in mouse podocytes and mesangial cells. Knockdown of *Sgpl1* in rat mesangial cells inhibited cell migration, which was partially rescued by VPC23109, an S1P receptor antagonist. In *Drosophila*, *Sply* mutants, which lack SGPL1, displayed a phenotype reminiscent of nephrotic syndrome in nephrocytes. WT *Sply*, but not the disease-associated variants, rescued this phenotype. Together, these results indicate that *SGPL1* mutations cause a syndromic form of SRNS.

Authorship note: S. Lovric, S. Goncalves, and H.Y. Gee contributed equally to this work.

Conflict of interest: The authors have declared that no conflict of interest exists.

Submitted: July 20, 2016; **Accepted:** December 12, 2016.
Reference information: *J Clin Invest*. 2017;127(3):912–928.
https://doi.org/10.1172/JCI89626.

Introduction

Steroid-resistant nephrotic syndrome (SRNS), when also resistant to other immunosuppressive agents, leads to chronic kidney disease (CKD) within a few years of onset, requiring renal replacement therapy for survival. It causes 15% of all end-stage kidney disease that manifests by 25 years of age (1). Histologically, SRNS manifests mostly as focal segmental glomerulosclerosis (FSGS) (2).

The first insights into the pathogenesis of SRNS were gained by the discovery of monogenic causes of SRNS, revealing that the encoded proteins are essential for the function of the renal glomerular cells called podocytes (3, 4). We recently demonstrated in a worldwide cohort of 1,783 families that a monogenic cause of SRNS can be detected in 1 of 27 genes in approximately 30% of SRNS cases manifesting before age 25 years (5). Currently, more than 40 monogenic forms of SRNS have been identified (6).

Interestingly, syndromic forms of SRNS have been increasingly characterized and display variable involvement of other organs besides the kidney, in most of the cases the central nervous system, but also the genital tract, eye, muscle, bone, and the immune system. To date, mutations have been identified in transcription factors and nuclear proteins (WT1, LMX1B, SMARCAL1, NXF5, NUP93, NUP205, and XPO5), lysosomal proteins (SCARB2), basement membrane proteins (LAMB2), and proteins involved in COQ_{10} biosynthesis (COQ2, COQ6, PDSS2, and ADCK4) (6). Because genetic mapping data indicated a multitude of potential additional loci for SRNS, we here performed whole exome sequencing (WES) to identify additional monogenic SRNS genes and identified 9 different mutations in sphingosine-1-phosphate lyase (*SGPL1*) in 7 families as causing a previously unrecognized syndromic SRNS with a combination of ichthyosis/acanthosis, adrenal insufficiency, immunodeficiency, and/or neuronal dysfunction. We characterized mechanisms of molecular loss of function for the mutations detected and implicated sphingosine-1-phosphate (S1P) metabolism in the pathogenesis of SRNS. The syndromic features resulting from *SGPL1* mutations indicate the pivotal role of S1P metabolism in multiple tissues including kidney.

Results

SGPL1 mutations cause nephrotic syndrome, ichthyosis, facultative adrenal insufficiency, immunodeficiency, and neurologic defects in humans. Using WES in 7 families with a disease phenotype of SRNS, with adrenal insufficiency, ichthyosis-like acanthosis, immunodeficiency, or neurologic abnormalities (Table 1, Table 2, and Supplemental Figures 1–3; supplemental material available online with this article; https://doi.org/10.1172/JCI89626DS1), we identified recessive mutations in *SGPL1* (Figure 1, A–E). Homozygosity mapping (HM) in a Pakistani family (A280) (Supplemental Figure 1) with 3 siblings yielded a nonparametric lod score peak on chromosome 10, which did not coincide with any of the known recessive SRNS loci (Figure 1A) (7). Using WES, we detected a homozygous missense mutation (p.Arg222Gln) in a highly conserved (*Caenorhabditis elegans*) amino acid residue encoded by *SGPL1* (Table 1 and Figure 1, B–E). Notably, affected individuals from another consanguineous family (EB) showed a homozygous missense mutation involving the same amino acid residue (p. Arg222Trp), but presented with a more severe phenotype, with neonatal onset and profound immunodeficiency (Table 1 and Figure 1, B–E). A homozygous frameshift mutation of *SGPL1* (p.Ser3Lysfs*11) (Table 2 and Figure 1, B–E) was identified in affected individuals from family A5444, showing a phenotype of SRNS and cortisol deficiency. In family B46/B56, in whom 3 siblings had congenital nephrotic syndrome (NS) and severe extrarenal involvement combined with lymphopenia (Table 2 and Supplemental Figure 1), WES detected another homozygous missense mutation of *SGPL1* (p.Ser346Ile) (Table 2 and Figure 1, B–E) and in another individual with a related disease phenotype, B1245, a homozygous missense mutation, p.Tyr416Cys (Table 2 and Figure 1, B–E), with both mutations evolutionarily conserved to *S. cerevisiae*. In an individual MC with mononeuritis multiplex, SRNS, lymphopenia, and progressive contractures of extremities, WES identified compound heterozygous mutations in *SGPL1* (Table 2 and Figure 1, B–E). Both mutations are missense and affect highly conserved amino acid residues.

Patients from the nonconsanguineous family NCR61 (Table 1 and Figure 1, B–E) were found to be compound heterozygous for a frameshift mutation (p.Arg278Glyfs*17) and a missense mutation (p.Glu132Gly) not predicted to be deleterious by the PolyPhen (http://genetics.bwh.harvard.edu/pph2/) and SIFT (http://sift.jcvi.org/) prediction tools, but predicted to induce skipping of exon 5 due to the introduction of additional exon splicing silencer elements (EX-SKIP, http://ex-skip.img.cas.cz) (8). Fibroblasts of patient NCR61-1 had almost no SGPL1 protein detectable by Western blot at the predicted size (Supplemental Figure 4A). Therefore, we hypothesized that the deleterious effect of c.395A>G was indeed related to the predicted RNA splicing defect and not to the p.Glu132Gly amino acid substitution. Amplification of the patient cDNA between exons 4 and 8 by PCR revealed a light band at the expected size and an intense smaller band with a size corresponding to loss of exon 5 (Supplemental Figure 4B). Sequencing of the PCR products confirmed the absence of exon 5 for the abundant smaller fragment and showed that the normal size fragment corresponded to the frameshift allele p.Arg278Glyfs*17. Skipping of exon 5 leads to a frameshift at amino acid position 88 and a stop codon 24 amino acids downstream (p. Ile88Thrfs*25).

By high-throughput exon sequencing (5, 9) in a worldwide cohort of approximately 800 additional families with NS, we did not detect any additional families with biallelic mutations of *SGPL1*. In all 7 families with *SGPL1* mutations (Tables 1 and 2 and Figure 1, B–K), direct inspection of sequence alignments did not yield a mutation in any of the 40 known SRNS genes. Most mutations identified in this study were absent from more than 60,000 control individuals in the ExAC server (http://exac.broadinstitute.org/) (Tables 1 and 2). Two missense mutations (c.665G>A; p.Arg222Gln and c.1247A>G; p.Tyr416Cys) are reported in the ExAC server, but their allele frequencies are extremely rare and they never occur in the homozygous state (Tables 1 and 2). All mutations segregated with the disease phenotype (Supplemental Figures 1 and 2). We thereby identified recessive *SGPL1* mutations as a cause of syndromic SRNS with ichthyosis/acanthocystosis, adrenal insufficiency, immunodeficiency, or neurologic involvement. We introduced the term NPHS14 for this syndromic SRNS caused by mutations of *SGPL1*.

In the majority of cases, NS, manifested as congenital NS or in the first year of life, showed no response to steroid therapy and

Table 1. Five different mutations in *SGPL1* in 4 families with SRNS, ichtyosis, and facultative adrenal insufficiency, immunodeficiency, and neurologic defects

Family Individual	Nucleotide change	aa change	Exon (zygosity, segregation)	MT	aa conservation to species	ExAC allele frequencies	Sex	Ethnic origin	PC	Age of onset of SRNS (of ESRD)	Renal biopsy (at age)	Extrarenal manifestations
A5444	c.7dup	p.Ser3Lysfs*11	Exon 2 (HOM)	NA	NA	ND		Spanish Roma	Y			
07-306							M			4 yr	FSGS (4 yr)	Skin: ichthyosis (9 yr) Adrenal: no cortisol deficiency
MCM							M			Hematuria and proteinuria (7 mo) (transplant 5 yr); died at 8 yr	FSGS (17 mo)	Adrenal: bilateral adrenal calcifications (4 mo), AI (19 mo) Immuno: deficiency of cellular immunity (2 yr) Bones: craniotabes and rachitic rosary (5 mo) Neurol: sudden strabismus, abnormal gait (15 mo)
07-142							F			SRNS (10 mo) (first transplant, 5 yr; second, 12 yr]) relapse with massive protein-uria (15 yr)	FSGS (1 yr)	Skin: scaly lesions, hyperchromic skin (2 yr), ichthyosis vulgaris (5 yr), no skin biopsy Adrenal: glucocorticoid deficiency (11 yr) Neurol: cNMR normal (11 yr) Bones: acrosomia, asymmetric skull, moderate scoliosis
NCR61	c.395A>G	p.Glu132Gly Exon 5 skipping (p.Ile88Thrfs*25)	Exon 5 (het, p)	DC	*D. m.*	ND		France	N			
	c.832delA	p.Arg278Glyfs*17	Exon 10 (het, m)	NA	NA	ND						
1							F			2 yr (6 yr)	FSGS (2 yr)	Skin: ichthyosis Adrenal: AI (2 yr)
2							F			1 yr (4 yr)	FSGS (1 yr)	Skin: ichthyosis Adrenal: AI (2 yr)
A280	c.665G>A	p.Arg222Gln	Exon 8 (HOM)	DC	*C. e.*	2/120,744 (no homozygote)		Pakistan	Y			
21							M			19 yr	FSGS (19 yr)	Adrenal: AI (6.5 yr)
22							M			3 yr (7 yr), MHU (transplant 8 yr)	FSGS (3 yr)	Skin: calcinosis cutis Adrenal: AI (3 yr) Bones: SS Neurol: ptosis (25 yr), progressive defects, median and ulnar nerve paralysis
23							M			2 yr (2.9 yr), died at 2.9 yr	FSGS (2 yr)	Adrenal: AI (2 yr)
EB	c.664C>T	p.Arg222Trp	Exon 8 (HOM)	DC	*C. e.*	ND		Turkish	Y			
1							F			CNS (1 mo), died at 5 mo	ND	Adrenal: AI (3 mo) Immuno: immunodeficiency, lymphopenia (T and B cells) Neurol: microcephaly, hypoplasia of corpus callosum Other: anemia, failure to thrive, capillary leak syndrome
2							F			CNS, died at 2 mo	ND	Fetal hydrops
3							NA			Fetal demise	NA	ND
4							NA			Fetal demise	NA	ND

AI, adrenal insufficiency; *C. e., C. elegans;* DC, disease causing; *D. m., Drosophila melanogaster*; F, female; het, heterozygous; HOM, homozygous; immuno, immunological; MHU, microscopic hematuria; M, male; m, maternal; MT, mutationtaster; N, no; NA, not applicable; ND, no data; neurol, neurological; p, paternal; PC, parental consanguinity; SS, short stature; Y, yes.

Table 2. Four different mutations in *SGPL1* in 3 families with SRNS, ichtyosis, and facultative adrenal insufficiency, immunodeficiency, and neurologic defects

Family Individual	Nucleotide change	aa change	Exon (zygosity, segregation)	MT	aa conservation to species	ExAC allele frequencies	Sex	Ethnic origin	PC	Age of onset of SRNS (of ESRD)	Renal biopsy (at age)	Extrarenal manifestations
B56/B46	c.1037G>T	p.Ser346Ile	Exon 11 (HOM)	DC	*S. c.*	ND		Morocco	Y			
B46							F			CNS (3 mo), died at 6 mo	DMS (6 mo)	Prenatal edema/hydrops Skin: ichthyosis (at birth) Adrenal: small calcifications Neurol: microcephaly, muscular hypotonia, DD, deafness Other: hypothyroidism, intestinal malrotation, facial dysmorphism (microstomia; hypetelorism, epicanthus, dysplastic ears), hypocalcemia Immuno: lymphopenia
B56 (12M15411)							F			CNS, died at 1 mo	DMS (1 mo)	Skin: ichthyosis Neurol: microcephaly, deafness, muscular hypotonia, DD Other: fetal hydrops Immuno: lymphopenia
23							F			Fetal demise (36 wk GA)	NA	Hydrops
24							F			Fetal demise with hydrops fetalis	NA	Skin: ichthyosis
26							F			CNS (1 mo), died at 3 mo	NA	Adrenal: calcifications Neurol: microcephaly, seizures (3 mo) Immuno: lymphopenia Other: hypothyroidism, hypocalcemia
B1245	c.1247A>G	p.Tyr416Cys	Exon 12 (HOM)	DC	*S. c.*	1/121,408 (no homozygote)		Mixed European (Hutterite)	Y			
21							F			CNS (2 mo) ESRD (5 mo) PD (2 mo)	FSGS (2 mo)	Adrenal: AI (2 mo) Neurol: bilateral sensorineural hearing loss (3 yr) Immuno: T and B cell lymphopenia, anemia (2 mo) Other: failure to thrive, DD, hypothyroidism (2 mo), mild dilated cardiomyopathy, Family history of 2 related children who died at young age of suspected immunodeficiency
MC	c.605C>T c.946G>A	p.Ser202Leu p.Ala316Thr	Exon 7 Exon 11 (comp het, inherited)	DC DC	*C. e.*[A] *C. e.*	ND ND	M	Mixed European (US)	N	18 yr (18 yr)	FSGS (18 yr)	Adrenal: none Neurol: peripheral neuropathy (motor and sensory), mononeuritis multiplex Immuno: T, B, NK lymphopenia; hypogammaglobulinemia; thrombocytopenia Other: elevated TSH, amblyopia, strabismus

[A]Except Xenop has Ala. AI, adrenal insufficiency; *C. e., C. elegans;* DC, disease causing; DD, developmental delay; F, female; het, heterozygous; HOM, homozygous; GA, gestational age; immuno, immunological; M, male; m, maternal; MT, mutationtaster; N, no; NA, not applicable; ND, no data; neurol, neurological; p, paternal; PC, parental consanguinity; PD, peritoneal dialysis; *S. c., Saccharomyes cerevisiae;* Y, yes.

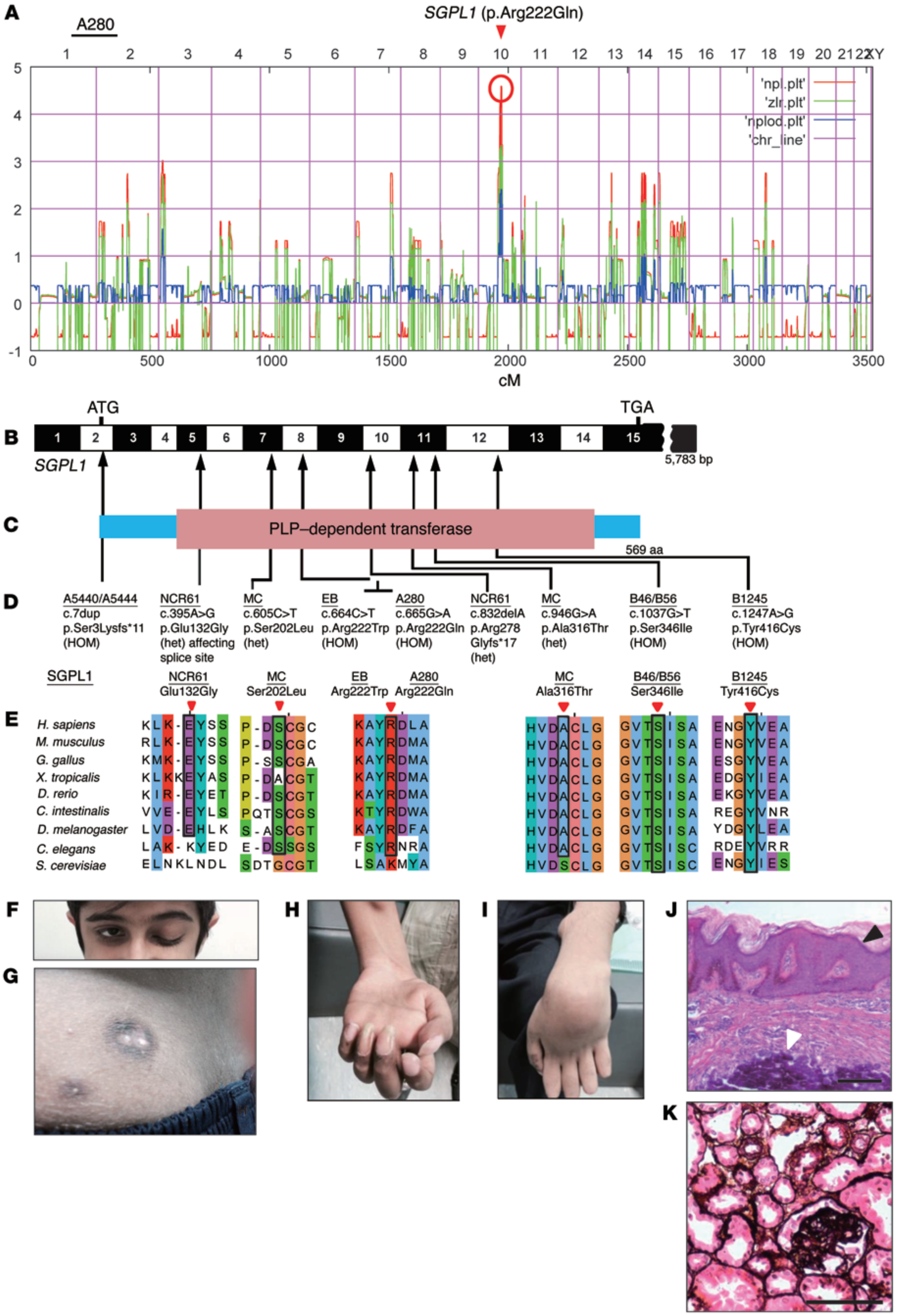
A
A280
SGPL1 (p.Arg222Gln)
1 2 3 4 5 6 7 8 9 10 11 12 13 14 15 16 17 18 19 20 21 22 XY
5
4
3
2
1
0
-1
0 500 1000 1500 2000 2500 3000 3500
cM
'npl.plt'
'zlr.plt'
'nplod.plt'
'chr_line'
ATG
TGA
B
1 2 3 4 5 6 7 8 9 10 11 12 13 14 15
SGPL1
5,783 bp
C
PLP–dependent transferase
569 aa
D
A5440/A5444 c.7dup p.Ser3Lysfs*11 (HOM)
NCR61 c.395A>G p.Glu132Gly (het) affecting splice site
MC c.605C>T p.Ser202Leu (het)
EB c.664C>T p.Arg222Trp (HOM)
A280 c.665G>A p.Arg222Gln (HOM)
NCR61 c.832delA p.Arg278 Glyfs*17 (het)
MC c.946G>A p.Ala316Thr (het)
B46/B56 c.1037G>T p.Ser346Ile (HOM)
B1245 c.1247A>G p.Tyr416Cys (HOM)
SGPL1
NCR61 Glu132Gly
MC Ser202Leu
EB Arg222Trp
A280 Arg222Gln
MC Ala316Thr
B46/B56 Ser346Ile
B1245 Tyr416Cys
E
H. sapiens KLK-EYSS P-DSCGC KAYRDLA HVDACLG GVTSISA ENGYVEA
M. musculus RLK-EYSS P-DSCGC KAYRDMA HVDACLG GVTSISA ENGYVEA
G. gallus KMK-EYSS P-SSCGA KAYRDMA HVDACLG GVTSISA ESGYVEA
X. tropicalis KLKKEYAS P-DACGT KAYRDMA HVDACLG GVTSISA EDGYIEA
D. rerio KIR-EYET P-DSCGT KAYRDMA HVDACLG GVTSISA EKGYVEA
C. intestinalis VVE-EYLS PQTSCGS KTYRDWA HVDACLG GVTSISA REGYVNR
D. melanogaster LVD-EHLK S-ASCGT KAYRDFA HVDACLG GVTSISA YDGYLEA
C. elegans LAK-KYED E-DSSGS FSYRNRA HVDACLG GVTSISC RDEYVRR
S. cerevisiae ELNKLNDL SDTGCGT LSAKMYA HVDSCLG GVTSISC ENGYIES
F
G
H
I
J
K

Figure 1. HM and WES reveal *SGPL1* mutations as causing SRNS with ichthyosis and facultative adrenal insufficiency or neurologic defects (NPHS type 14). (**A**) Nonparametric lod scores across the human genome in 3 siblings of consanguineous family A280 with SRNS, acanthosis, and ichtyosis with facultative adrenal insufficiency. The *x* axis shows single-nucleotide polymorphism positions on human chromosomes concatenated from p-ter (left) to q-ter (right). Genetic distance is given in cM. The *SGPL1* locus (arrowhead) is positioned within the maximum nonparametric lod peak on chromosome 10. (**B**) Exon structure of human *SGPL1* cDNA. *SGPL1* contains 15 exons. Positions of start codon (ATG) and of stop codon (TGA) are indicated. (**C**) Domain structure of SGPL1. The extent of the PLP-dependent transferase domain is shown. (**D**) Five homozygous (HOM) and 4 compound-heterozygous *SGPL1* mutations (het) detected in 7 families with NPHS type 14. Family numbers (underlined), mutations, and predicted translational changes are indicated (see also Tables 1 and 2). (**E**) Evolutionary conservation of altered amino acid residues of SGPL1. Note that c.395A>G also resulted in p.Ile88Thrfs*25 through exon 5 skipping. (**F**) Ptosis in individual A280-22. (**G**) Skin image from individual A280-22 showing brownish black desquamation on sebostatic skin with multiple radial papules with a blueish/black erythema and central calcinosis. (**H** and **I**) Median (**H**) and ulnar nerve (**I**) paralysis in individual A280-22. (**J**) H&E-stained epidermal section from individual A280-22 showing acanthosis/orthokeratotic hyperkeratosis (black arrowhead) and calcinosis (white arrowhead). (**K**) Renal histology (silver staining) of individual A280-22, showing FSGS. Scale bars: 100 μm.

rapidly progressed to end-stage renal disease (ESRD). Histologically, FSGS was the main finding, but diffuse mesangial sclerosis (DMS) was found in cases with congenital NS (Tables 1 and 2 and Supplemental Figure 3). Extrarenal manifestations included ichthyosis and primary adrenal insufficiency, present in almost all cases except in those patients deceased at very early ages. About half of the affected individuals had a severe immunodeficiency. Patients presented with lymphopenia and multiple bacterial infections. A more detailed immunological work-up performed in patient EB-1 revealed severe lymphopenia with markedly reduced CD4 and CD8 T lymphocytes as well as B lymphocytes. In vitro cytokine generation upon stimulation was also deficient (Supplemental Table 3). Neurological deficits were also present in half of the patients and included sensorineural deafness, microcephaly (Supplemental Figure 3), corpus callosum hypoplasia in 1 case, peripheral nerve paralysis of the median and ulnar nerves, and ptosis of the left eye (Tables 1 and 2 and Figure 1, F–I). In a few cases, dysmorphic features and bone defects were also present. Two families had a history of fetal demise and hydrops fetalis.

SGPL1 encodes S1P lyase, an intracellular enzyme responsible for the final step in sphingolipid breakdown, converting its main substrate S1P into ethanolamine phosphate and hexadecenal. S1P is a bioactive sphingolipid that acts extracellularly by binding to protein-coupled receptors of the lysophospholipid receptor family and intracellularly through S1P receptor–independent (S1PR-independent) mechanisms. Through receptor activation, S1P mediates autocrine and paracrine signals, controlling cell migration and proliferation as well as lamellipodia dynamics (10). An *Sgpl1*-deficient mouse model exhibits glomerular proteinuria, a skin phenotype of acanthosis with orthokeratotic hyperkeratosis and platelet activation (11).

Sgpl1 localizes to the endoplasmic reticulum of renal glomerular cells. All of the 40 monogenic genes that, when mutated, cause SRNS are highly expressed in podocytes. We therefore examined cell-type–specific and subcellular localization of SGPL1 in mouse kidney. To assess the specificity of an anti-SGPL1 antibody used in immunofluorescence, we first stained kidney sections of *Sgpl1*$^{-/-}$ and *Sgpl1*$^{+/+}$ mice (Figure 2, A and B). Most of the SGPL1 signal observed in kidneys of *Sgpl1*$^{+/+}$ mice was absent from kidneys of *Sgpl1*$^{-/-}$ mice (Figure 2A), demonstrating specificity of the signal. To determine cellular localization of SGPL1, immunofluorescence was performed using various cell- and organelle-specific markers (Figure 2, C–F). SGPL1 localized to podocytes, whose nuclei were marked with WT1 (Figure 2C). As shown by the colocalization of SGPL1 with the ER marker BiP, it localized to ER in podocytes, although this colocalization was more obvious in proximal tubules (Figure 2C). In addition, SGPL1 appeared to be present in other renal glomerular cell types, for example, in mesangial cells stained with α–smooth muscle actin (Figure 2E) and endothelial cells stained with CD31 (Figure 2F).

In silico modeling of SGPL1 missense mutations. To predict potential structural changes in SGPL1 protein that might arise from the mutations (p.Arg222Gln and p.Ser346Ile) detected in patients with NPHS type 14 Tables 1 and 2), we performed in silico analyses (Figure 2, G and H). SGPL1 forms a symmetric homodimer. Two subunits form a tightly intertwined dimer with both chains contributing to the catalytic cavity defined by the covalently bound cofactor pyridoxal phosphate (PLP) (Figure 2, G and H). Arg222 is located at the symmetric dimer interface and forms 2 important hydrogen bonds with the carbonyl backbone moieties of Tyr250 and Ser249, contributing to the binding affinity of the homodimer. The p.Arg222Gln mutation leads to a loss of these 2 hydrogen bonds in both chains (Figure 2G), which is reflected in the delta affinity being predicted as unfavorable by about 10 kcal/mol. In addition, the mutation seems to be destabilizing the protein, since Arg222 also forms hydrogen bonds with adjacent residues in its own symmetric dimer chain. Ser346 is not at the dimer interface, but buried within each chain (Figure 2H). Its hydroxyl group is involved in 2 hydrogen bonds, accepting one from Tyr221 and donating one onto His313 (Figure 2H). The p.Ser346Ile mutation is predicted to be considerably disfavored because it not only breaks this hydrogen-bond network, but because isoleucine is also much bulkier than serine, leading to steric clashes with its surrounding residues (Figure 2H). Hence the delta stability is predicted to be +130 kcal/mol.

Mutations alter subcellular localization of SGPL1. Because in silico analysis predicted that the p.Arg222Gln mutation may affect the interface of the SGPL1 homodimer, we examined this hypothesis by coimmunoprecipitation. We transfected HEK293T cells with plasmids with 2 alternative tags (Myc and FLAG). Compared with WT SGPL1, p.Arg222Gln and p.Ser346Ile mutant proteins exhibited reduced expression levels, whereas p.Glu132Gly had a similar expression level upon overexpression (Figure 2I and Supplemental Figure 5). Neither missense (p.Glu132Gly, p.Arg222Gln, and p.Ser346Ile) nor truncating (p.Arg278Glyfs*17) mutations abrogated dimer formation (Figure 2I and Supplemental Figure 5). However, when compared with overexpression of the SGPL1 WT construct, overexpression of p.Arg222Gln, p.Ser346Ile, and p.Arg278Glyfs*17 SGPL1 proteins in HEK293T cells led to abnormal cytoplasmic aggregates (Figure 2J). Aggregation of SGPL1 mutant proteins was confirmed upon overexpression in human podocytes (Supplemental Figure 6).

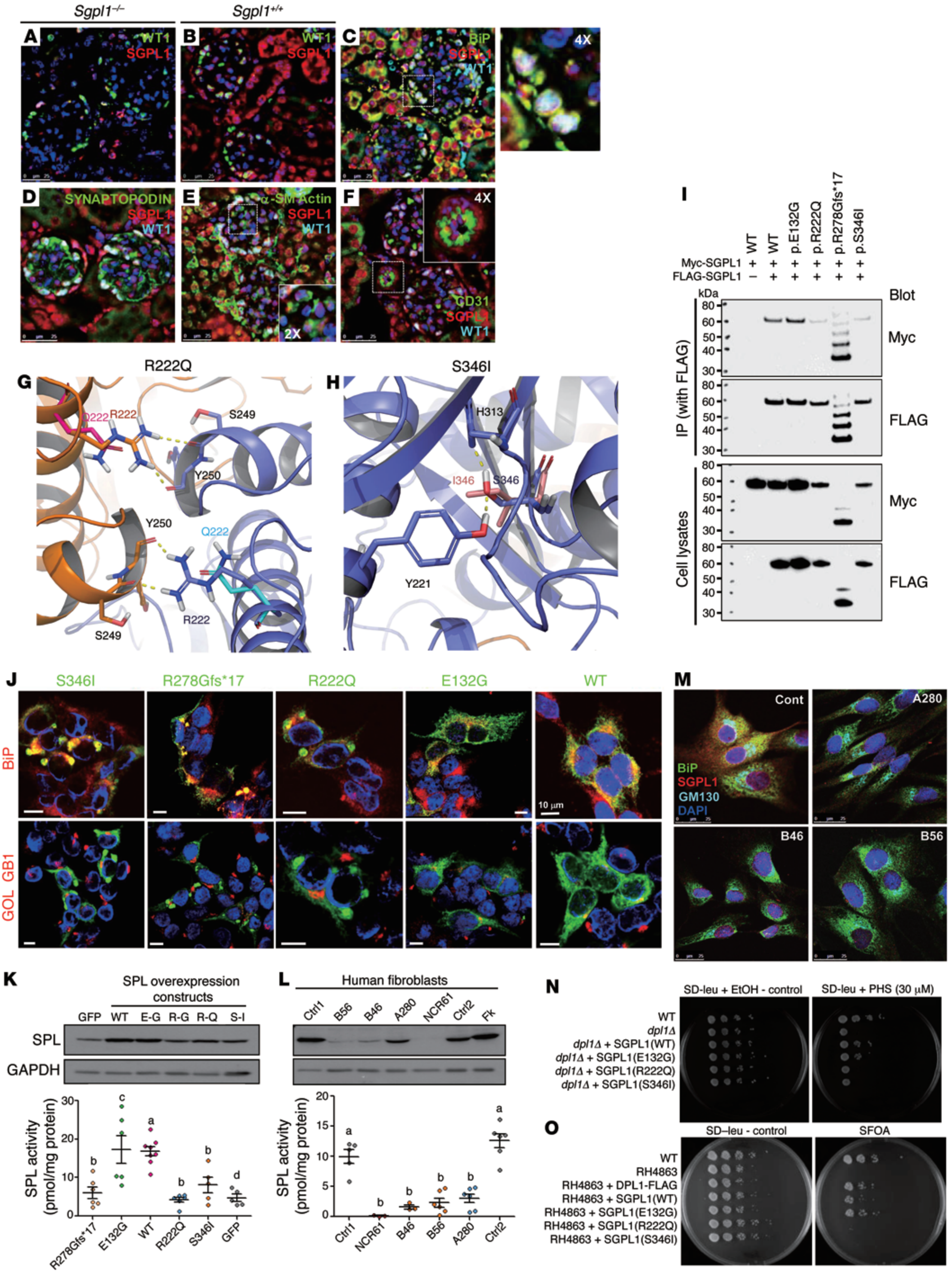
Sgpl1−/−
Sgpl1+/+
A WT1 SGPL1
B WT1 SGPL1
C BiP SGPL1 WT1
4X
D SYNAPTOPODIN SGPL1 WT1
E α-SM Actin SGPL1 WT1
2X
F CD31 SGPL1 WT1
4X
G R222Q
Q222 R222 S249 Y250 Y250 Q222 R222 S249
H S346I
H313 I346 S346 Y221
I
WT WT p.E132G p.R222Q p.R278Gfs*17 p.S346I
Myc-SGPL1 + + + + + +
FLAG-SGPL1 − + + + + +
kDa
80 60 50 40 30
Blot
Myc
FLAG
IP (with FLAG)
Cell lysates
J
S346I R278Gfs*17 R222Q E132G WT
BiP
GOL GB1
10 μm
M
Cont A280 B46 B56
BiP SGPL1 GM130 DAPI
K
SPL overexpression constructs
GFP WT E-G R-G R-Q S-I
SPL
GAPDH
SPL activity (pmol/mg protein)
30 20 10 0
R278Gfs*17 E132G WT R222Q S346I GFP
b c a b b d
L
Human fibroblasts
Ctrl1 B56 B46 A280 NCR61 Ctrl2 Fk
SPL activity (pmol/mg protein)
20 15 10 5 0
Ctrl1 NCR61 B46 B56 A280 Ctrl2
a b b b b a
N
SD-leu + EtOH - control
SD-leu + PHS (30 μM)
WT
dpl1Δ
dpl1Δ + SGPL1(WT)
dpl1Δ + SGPL1(E132G)
dpl1Δ + SGPL1(R222Q)
dpl1Δ + SGPL1(S346I)
O
SD–leu - control
SFOA
WT
RH4863
RH4863 + DPL1-FLAG
RH4863 + SGPL1(WT)
RH4863 + SGPL1(E132G)
RH4863 + SGPL1(R222Q)
RH4863 + SGPL1(S346I)

Figure 2. Biological and biochemical consequences of recessive *SGPL1* mutations. (**A**–**F**) Kidney sections of *Sgpl1*$^{-/-}$ mice (**A**) and *Sgpl1*$^{+/+}$ mice (**B**) were stained with anti-SGPL1 (red) and WT1 antibodies (green). (**B**–**F**) Coimmunofluorescence of SGPL1 with marker proteins (green) in *Sgpl1*$^{+/+}$ kidney: podocyte (**B**, WT1), ER (**C**, BiP), podocyte foot processes (**D**, synaptopodin), mesangial cells (**E**, α–smooth muscle actin), and endothelial cells (**F**, CD31). Scale bars: 25 μm. (**G** and **H**) Structural modeling of *SGPL1* mutations. The 2 monomers of the SGPL1 homodimer are shown in the drawing in blue and orange, respectively. (**G**) p.Arg222Gln; (**H**) p.Ser346Ile. (**I**) Coimmunoprecipitation to assess dimerization of WT vs. mutant SGPL1 proteins (see also Supplemental Figure 5). Coimmunoprecipitation is representative of 3 experiments. (**J**) Mislocalization of variant SGPL1 proteins upon overexpression in HEK293T cells. BiP (red), or Golgi marker GOLGB1 (red), and anti-Myc antibody (green). Scale bars: 10 μm. (**K**) SGPL1 enzyme activity levels in transformed HEK293T cells. HEK293T cells expressing a GFP indicate endogenous SGPL1 activity levels (a vs. b and a vs. d, $P < 0.0025$; c vs. d, $P = 0.013$; a vs. c, no significant difference). (**L**) SGPL1 protein expression and enzyme activity levels in fibroblasts from 2 control individuals (Ctrl 1 and 2), normal human foreskin fibroblasts (Fk), and 4 individuals with *SGPL1* mutations. (a vs. b, $P < 0.0001$.) Results are from the averages of triplicates in **K** and **L**. (**M**) Immunofluorescence of SGPL1 in fibroblasts. BiP (green), Golgi marker GM130 (blue), and anti-SGPL1 antibody (red). Scale bars: 25 μm. (**N**) PHS toxicity test. Ability to complement *dpl1Δ* deletion on medium containing PHS was tested for human SGPL1 WT and mutants. (**O**) Synthetic lethality test. Human WT and p.Glu132Gly SGPL1 expressing RH4863 survived on 5-FOA plates. However, p.Arg222Gln and p.Ser346Ile mutants did not allow for survival of *DPL1* (*SGPL1*) deficient strains.

Mutations in SGPL1 result in decreased expression and reduced lyase activity. To assess whether mutations detected in individuals with NPHS type 14 altered SGPL1 enzyme activity, we measured SGPL1 and enzyme activity levels in HEK293T cells transiently expressing either WT or mutant SGPL1 (Figure 2K). We found that overexpression of the p.Arg222Gln, p.Ser346Ile, and p.Arg278Glyfs*17 mutant alleles resulted in strongly reduced enzyme activity levels, whereas the p.Glu132Gly mutant (c.395A>G) did not, consistent with our finding that c.395A>G leads to skipping of exon 5 and protein truncation (p.Ile88Thrfs*25) (Supplemental Figure 4). We also found that protein expression levels and corresponding SGPL1 enzyme activity levels in patient dermal fibroblasts (Figure 2L) exhibited reduced SGPL1 enzyme activity for individuals B46 (p.Ser346Ile), B56 (p.Ser346Ile), NCR 61-1 (p.R278fs*17 and p.Ile88Thrfs*25), and A280-21 (p.Arg222Gln) compared with controls (Figure 2L). In addition, there was reduced expression of SGPL1 protein when examined by immunofluorescence microscopy in patient fibroblasts (Figure 2M). Taken together, these results suggest that the primary impact of the patient's mutations is on SGPL1 expression level and protein stability.

SGPL1 mutations fail to rescue growth in DPL1-deficient yeast. Functionality of human WT and mutant SGPL1 proteins were tested in an in vivo yeast complementation assay by measuring their ability to complement the deletion of the *SGPL1* yeast ortholog *DPL1* (*dpl1Δ*) on medium containing phytosphingosine (PHS) (Figure 2N and Supplemental Figure 7A). Inability to degrade toxic long-chain bases led to decreased viability and slowed growth. Human WT and p.Glu132Gly mutant SGPL1 were found to be able to partially restore *dpl1Δ*, while p.Arg222Gln, p.Ser346Ile, and p.Tyr416Cys as well as frameshift mutants p.Arg278Glyfs*17 and p.Ser3Lysfs*11 showed no improved growth compared with *dpl1Δ* (Figure 2N and Supplemental Figure 7A), consistent with our finding that the c.395A>G allele most likely conveys loss of function through its splice defect (Supplemental Figure 4B). The results were also reproduced on plates containing C17 and C18 dihydrosphingosine (DHS).

To further investigate functional consequences of *SGPL1* mutants, we carried out a synthetic lethality assay in yeast (Figure 2O and Supplemental Figure 7B) using an RH4863 strain in which *DPL1* and *LCB3* were deleted, rendering the strain synthetically lethal. Viability of the strain was maintained by expressing *LCB3* from a *URA3* plasmid. We tested functionality of *SGPL1* and corresponding mutants expressed in RH4863 by forcing them to lose *LCB3*-coding *URA3* plasmid on plates containing 5-fluoroorotic acid (5-FOA), which selects against *URA3*-expressing cells. Survival on 5-FOA plates indicates that cells have regained the ability to degrade long-chain bases and thus compensate for the loss of *LCB3*. In agreement with the PHS toxicity test, synthetic lethality assay demonstrated functional integrity of WT and p.Glu132Gly mutant SGPL1 proteins, but not p.Arg222Gln, p.Ser346Ile, p.Tyr416Cys, p.Arg278Glyfs*17, and p.Ser3Lysfs*11 (Figure 2O and Supplemental Figure 7B).

SGPL1 mutations alter ceramide composition of patient fibroblast-conditioned medium. S1P participates in regulating multiple cellular processes, and its intracellular levels are tightly regulated. Since SGPL1 controls the only exit point for sphingolipid catabolism, inactivation of the enzyme can result in accumulation of various bioactive sphingolipid intermediates, including phosphorylated and nonphosphorylated sphingoid bases and ceramides.

Conditioned medium from patient fibroblast cultures showed significantly elevated C22:0, C24:0, and C24:1 ceramides compared with control fibroblast-conditioned medium, whereas S1P levels were below the limits of detection (Supplemental Figure 8). These very long chain ceramides are produced by ceramide synthase 2 (12).

Sgpl1$^{-/-}$ *mice exhibit podocyte foot process effacement*. *Sgpl1*$^{-/-}$ mice exhibit glomerular proteinuria, a skin phenotype of acanthosis with orthokeratotic hyperkeratosis, platelet activation, and immunodeficiency (11). In order to determine the renal histology of *Sgpl1*$^{-/-}$ mice, we performed transmission electron microscopy (TEM) of kidneys harvested from *Sgpl1*$^{+/+}$ and *Sgpl1*$^{-/-}$ mice to directly examine glomerular structures upon loss of *Sgpl1*. *Sgpl1*$^{-/-}$ kidneys exhibited complete foot process effacement and absence of slit diaphragms (Supplemental Figure 9). In addition, *Sgpl1*$^{-/-}$ mice exhibited hypoalbuminemia (serum albumin KO 2.2 ± 0.6 g/dl vs. WT or heterozygote [HET] 3.7 ± 0.4 g/dl, $n = 4$ KO and $n = 6$ WT or HET) and an elevated urinary albumin/creatinine ratio (ACR) (KO 1176.4 ± 932.8 vs. WT or HET 103.5 ± 94.2, $n = 3$ KO, $n = 5$ WT or HET, P value, no significant difference).

However, when we examined apoptosis in response to S1P in cultured podocytes, we did not observe an effect in a dose range expected to be present in SGPL1-induced pathology (Supplemental Figure 10). Likewise, we did not observe any effect of *SGPL1* knockdown on podocyte migration rate, a pathogenic effect that has previously been demonstrated in many monogenic forms of SRNS (Supplemental Figure 11) (13).

Decreased mesangial cell migration rate upon SGPL1 knockdown is reversed by an S1PR inhibitor. Because we did not observe any cellular pathologic effect in cultured podocytes regarding apop-

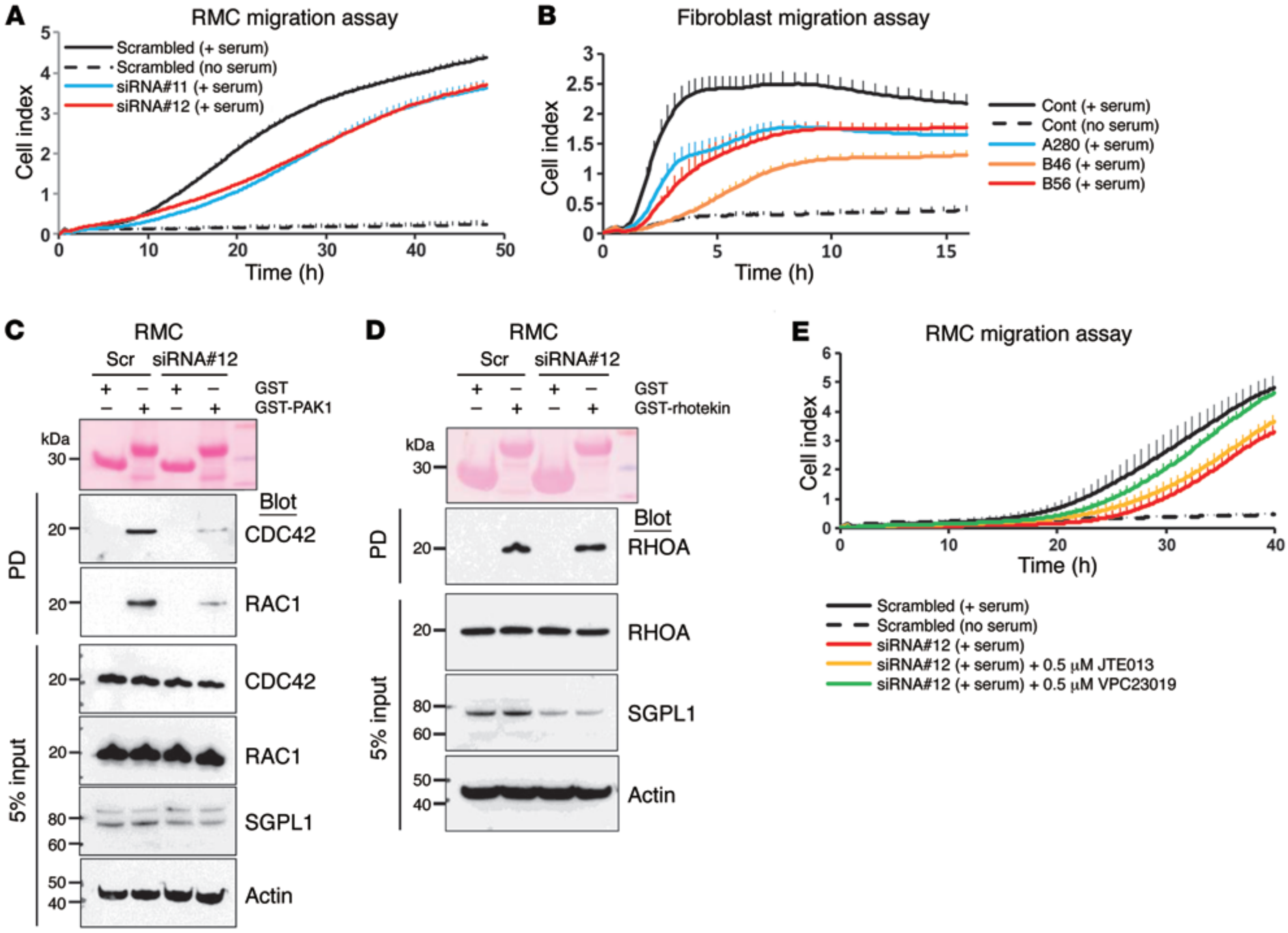

Figure 3. Effect of *Sgpl1* knockdown on RHO GTPase activity in RMCs and patient fibroblasts. (**A**) Effect of SGPL1 knockdown on rat RMCs using the xCELLigence system. RMC transfected with 2 different SGPL1 siRNAs exhibited decreased serum-induced migration rate (blue and red lines) compared with scrambled siRNA control (black line). (**B**) Diminished cell migration rate in patients with *SGPL1* mutations. Using the xCELLigence system, fibroblasts from individuals with *SGPL1* mutations (blue, red, and orange lines) showed decreased migration rate compared with control (black solid line). (**C**) Active GTP-bound RAC1 and CDC42 precipitated from RMCs transfected with scrambled (Scr) or *SGPL1* siRNA using a GST-PAK1 (CRIB) pulldown assay. Compared with control cells, RMCs transfected with SGPL1 siRNA exhibited a significant decrease in relative CDC42 and RAC1 activity. The efficiency of knockdown by siRNA was confirmed by immunoblotting with an anti-SGPL1 antibody (second to lowest panel). (**D**) Active GTP-bound RHOA precipitated from RMCs using a GST-rhotekin (RBD) pulldown assay. RMCs transfected with scrambled control siRNA versus *SGPL1* siRNA exhibited no significant differences in relative RHOA activity. **C** and **D** represent 3 experiments each. (**E**) Effect of S1PR antagonists on RMC migration rate. SGPL1 knockdown caused decreased migration rate (red line) (Supplemental Figure 3B), which was partially rescued by VPC23109 (green line), but not by JTE013 (orange line). VPC23109 is an antagonist that selectively inhibits S1PR1 and S1PR3, whereas JTE013 is an antagonist for S1PR2. Each cell index value corresponds to the average of more than triplicates and SD is in only 1 direction for clarity in **A**, **B**, and **E**.

tosis or cell migration, because SGPL1 was present in mesangial cells (Figure 2E), and because *Sgpl1*$^{-/-}$ mice exhibited reduced glomerular mesangial cell numbers (11), we examined pathogenic effects of siRNA knockdown of *Sgpl1* in mesangial cells (Figure 3).

To test whether *SGPL1* or S1P is involved in cell survival or proliferation, we investigated the effect of silencing SGPL1 on cell apoptosis and proliferation in rat mesangial cells (RMCs). Knockdown of *Sgpl1* did not affect apoptosis or proliferation in RMCs (Supplemental Figure 12). We then examined the effect of *Sgpl1* knockdown on migration of RMCs and found that migration of RMCs was reduced (Figure 3A) upon knockdown of *Sgpl1* by transfection with either of 2 siRNAs (Supplemental Figure 12). In addition, we confirmed this effect by showing that cell migration was significantly reduced in fibroblasts from individuals with *SGPL1* mutations (Figure 3B).

S1P has previously been implicated in the regulation of RHO-like small GTPases (RHOA/RAC1/CDC42), and disruption of RAC1 signaling was previously implicated in the pathogenesis of SRNS (13–15). We therefore tested whether knockdown of *SGPL1* would affect activation of the RHO-like small GTPases. When *Sgpl1* was silenced by siRNA in RMCs, we observed a decrease in active GTP forms of CDC42 and RAC1 (Figure 3C), whereas active RHOA (Figure 3D) was unchanged.

To test for specificity of the migration defect observed upon *Sgpl1* knockdown, we employed S1PR antagonists. Among 5 S1PR (S1PR1-5), S1PR1, S1PR2, and S1PR3 are expressed in kidney (16). Therefore, we chose VPC23109, which preferentially acts on S1PR1 and S1PR3, and JTE013, which is an antagonist for S1PR2. Interestingly, VPC23109 partially rescued the decreased migration conferred by *Sgpl1* knockdown in RMCs, whereas JTE013 failed to rescue the migration defect, suggesting that the S1P effect on RMC migration rate is mediated through S1PR1 and/or S1PR3 (Figure 3E).

SGPL1 is required for Drosophila nephrocyte function. *Sply* is the *SGPL1* ortholog of *Drosophila*, and a *Sply* null allele has previously been characterized and shown to decrease fly viability (17). Accordingly, *Sply* null hemizygous flies (*Sply* null/*Df*) had decreased viability (Figure 4A).

To assess whether *Sply* deficiency evoked a podocytopathy phenotype in flies, we assessed the structure and function of nephrocytes in *Sply* null hemizygous flies. Nephrocytes are thought to represent the *Drosophila* counterparts of podocytes. These cells display invaginations of plasma membrane that form analogous structures to podocyte foot processes and are connected by a slit diaphragm (18). This structure allows filtering of hemolymph and macromolecules that can then undergo endocytosis. We observed no major decrease of the slit diaphragm protein kirre (NEPH1 ortholog) by immunofluorescence (Supplemental Figure 13); however, by TEM, we identified a reduction of foot process density (Figure 4C). To assess the impact of *Sply* on nephrocyte function, we analyzed the uptake of fluorescent-coupled albumin. Albumin is filtered and endocytosed in nephrocytes under normal conditions, but not when there is disruption of foot processes (18, 19). Consistently, *Sply* null hemizygous flies had significantly reduced uptake of albumin as compared with control (Figure 5A).

Due to the known role of *Sply* on sphingolipid catabolic pathway and its indirect implication in other lipid pathways, such as the regulation of sterol regulatory element-binding protein processing in *Drosophila* (20), we also studied the effect of *Sply* KO on the lipid content of nephrocytes. *Sply* null hemizygous flies showed an almost complete absence of lipid droplets stained by Bodipy (Figure 5B) or Nile red (data not shown), suggesting a reduction of neutral lipids. Using liquid chromatography–mass spectrometry (LC/MS), we also assessed the accumulation of sphingoid bases and ceramides in *Sply* null hemizygous flies. *Drosophila* has been shown to have C14 and C16 sphingosine (21) and C14 and C16 sphingadienes (22), a sphingoid base with an extra double bond compared with sphingosine. Sphingolipid intermediates upstream of S1P, including long chain bases and ceramides, have been shown to accumulate when SGPL1 activity is inhibited, including in *Sply* mutant flies (17, 22). As expected, we observed a significant increase of C16 sphingosine, C14 sphingadiene, and C16 ceramide in *Sply* null hemizygous third instar larvae (Figure 5C and Supplemental Figure 14). Together, these data suggest that *Sply* null hemizygous flies have defects reminiscent of the podocyte disease found in humans with *SGPL1* mutations and display altered lipid metabolism due to the disruption of sphingolipid catabolic pathway.

Lack of rescue with mutant alleles in the Drosophila model. To assess the effect of *SGPL1* missense mutations in vivo, we reexpressed the HA-tagged *Sply* carrying WT or the corresponding human mutations p.Glu119Gly, p.Arg210Gln, and p.Ser335Ile (equivalent to human mutants p.Glu132Gly, p.Arg222Gln, and p.Ser346Ile, respectively). We observed that under its endogenous promoter, HA-tagged *Sply* is expressed in nephrocytes (Figure 4B). Consistent with our previous results, the expression of mutants p.Arg210Gln and p.Ser335Ile was greatly reduced at the protein level compared with WT (Figure 4B), but without any significant difference at the mRNA level (Supplemental Figure 15).

Reexpression of *Sply* WT and p.Glu119Gly transgenes rescued *Sply* mutant viability defect and nephrocyte dysfunction, which was not the case for p.Arg210Gln and p.Ser335Ile mutations (Figure 4 and Figure 5A). Regarding the neutral lipid content of nephrocytes, we observed a rescue of the *Sply* phenotype with *Sply* WT and p.Glu119Gly transgenes, but not with p.Arg210Gln or p.Ser335Ile (Figure 5B).

In whole third instar larvae, the phenotype of C16 sphingosine and C16 ceramide accumulation present in *Sply* null hemizygous flies was rescued with equal efficiency by *Sply* WT and p.Glu119G transgenes (Figure 5C). However, p.Ser335Ile mutant failed to rescue (Figure 5C). p.Arg210Gln mutant partially rescued the *Sply* null phenotype, but with significantly less efficiency than *Sply* WT (Figure 5C). This suggests that p.Arg210Gln and p.Ser335Ile, but not p.Glu119Gly, mutations affect the *Sply* enzymatic activity and result in the accumulation of upstream sphingolipids, sphingosines, and ceramides. Similar results were observed when analyzing fly sphingadienes, although complementation results for the mutants p.Arg210Gln and p.Ser335Ile did not reach a statistically significant difference from control (Supplemental Figure 14). We conclude that SGPL1 missense mutations p.Arg222Gln and p.Ser346Ile are pathogenic, impair sphingolipid metabolism, and induce nephrocyte defects reminiscent of those found in human podocytopathies. Consistent with our data on the splicing defects (Supplemental Figure 4B) induced by p.Glu132Gly mutation, we found that the corresponding amino acid change did not induce any defect in *Drosophila*.

Discussion

In this study, we identified recessive *SGPL1* mutations as a cause of syndromic SRNS. The disease phenotype entailed SRNS with facultative ichthyosis, adrenal insufficiency, neurologic involvement, and immunodeficiency. We show that *SGPL1* mutations are loss-of-function mutations that lead to reduced protein levels and enzyme activity and impaired degradation of long-chain sphingoid bases. In *Drosophila*, the missense mutations led to decreased viability and nephrocyte defects that are reminiscent of podocyte changes in human NS. WT *Sply* complemented *Sply* phenotype and sphingolipid profiles, whereas *Sply* harboring mutations did not complement.

SGPL1 is ubiquitously expressed in tissues and is an essential enzyme of the sphingolipid catabolic pathway. It is thus considered a main regulator of S1P levels and other sphingoid bases. Loss of *Sgpl1* in mouse models phenocopies the human disease. In fact, *Sgpl1*$^{-/-}$ mice fail to thrive and die soon after weaning, showing defects in the immune system, the urinary system, vasculature, and bone as well as altered lipid metabolism (11, 23–25). However, adrenal insufficiency has not been described in *Sgpl1*$^{-/-}$ mice, but to our knowledge, adrenal function was not assessed in these animals. In the immune system, changes in local S1P concentration and gradient between tissues (low S1P) and efferent lymph and blood (high S1P) affect T cell egress from lymphoid organs (26, 27), resulting in reduced levels of circulating lymphocytes with overrepresentation of T cells with a memory phenotype over naive T cells (27), as observed in the SGPL1 mutant patient in which a complete immunological work-up has been performed. Interestingly, partial deficiency of *Sgpl1* in inducible knockout models led

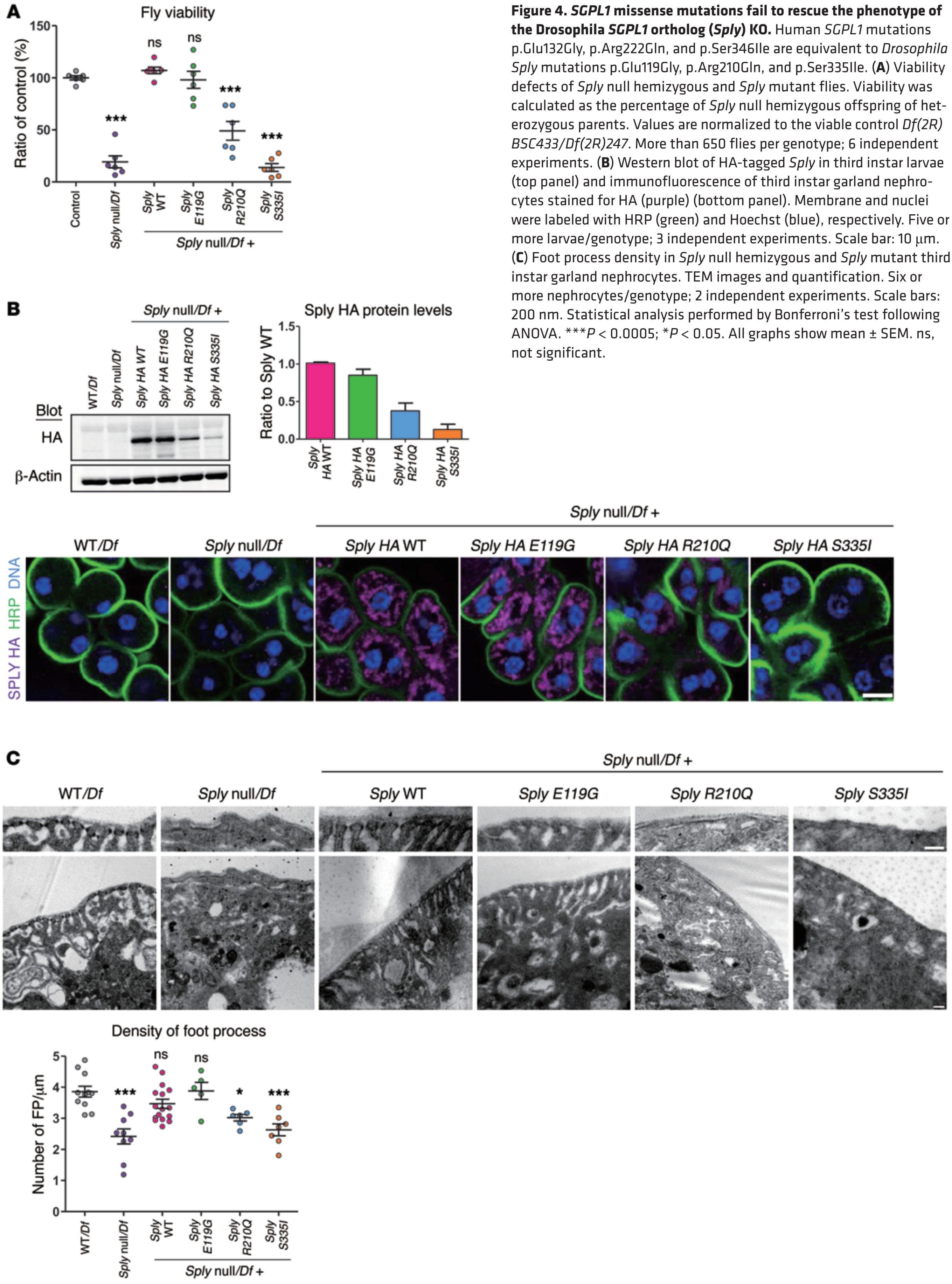

Figure 4. *SGPL1* missense mutations fail to rescue the phenotype of the Drosophila *SGPL1* ortholog (*Sply*) KO. Human *SGPL1* mutations p.Glu132Gly, p.Arg222Gln, and p.Ser346Ile are equivalent to *Drosophila Sply* mutations p.Glu119Gly, p.Arg210Gln, and p.Ser335Ile. (**A**) Viability defects of *Sply* null hemizygous and *Sply* mutant flies. Viability was calculated as the percentage of *Sply* null hemizygous offspring of heterozygous parents. Values are normalized to the viable control *Df(2R) BSC433/Df(2R)247*. More than 650 flies per genotype; 6 independent experiments. (**B**) Western blot of HA-tagged *Sply* in third instar larvae (top panel) and immunofluorescence of third instar garland nephrocytes stained for HA (purple) (bottom panel). Membrane and nuclei were labeled with HRP (green) and Hoechst (blue), respectively. Five or more larvae/genotype; 3 independent experiments. Scale bar: 10 μm. (**C**) Foot process density in *Sply* null hemizygous and *Sply* mutant third instar garland nephrocytes. TEM images and quantification. Six or more nephrocytes/genotype; 2 independent experiments. Scale bars: 200 nm. Statistical analysis performed by Bonferroni's test following ANOVA. ****P* < 0.0005; **P* < 0.05. All graphs show mean ± SEM. ns, not significant.

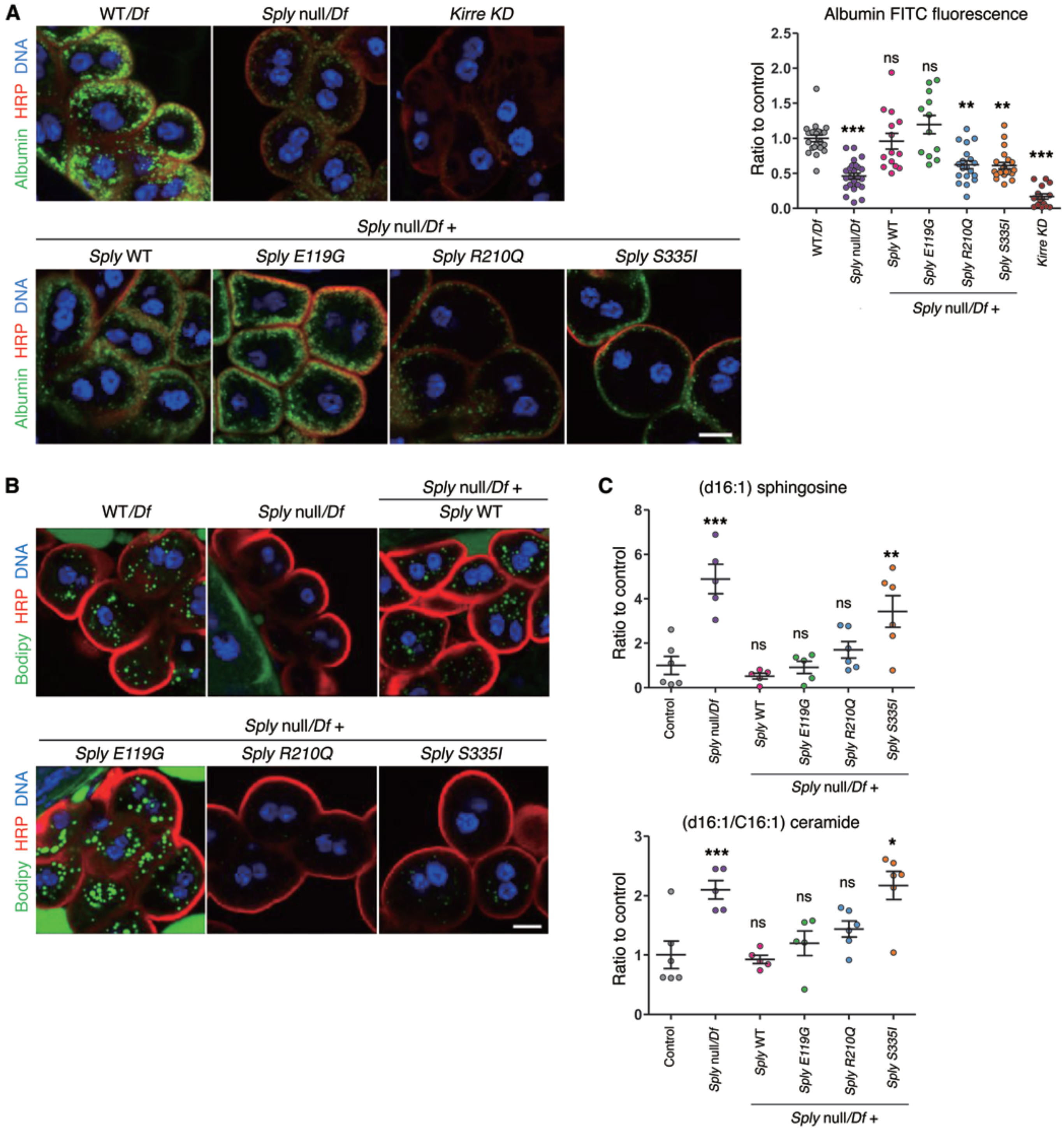

Figure 5. Defects of vesicular transport and sphingosine metabolism in the SGPL1 drosophila ortholog (*Sply*) KO. (**A**) Albumin uptake in *Sply* null hemizygous and *Sply* mutant third instar garland nephrocytes. Nephrocytes were incubated for 2.5 minutes with albumin-FITC (green), fixed and stained for the membrane marker HRP (red). Ten or more larvae/genotype; 3 independent experiments. Scale bar: 10 μm. (**B**) Lipid droplets in *Sply* null hemizygous and *Sply* mutant third instar garland nephrocytes, assessed by Bodipy staining. Six or more larvae/genotype; 2 independent experiments. Scale bar: 10 μm. (**C**) Sphingoid bases accumulation in *Sply* null hemizygous and *Sply* mutant third instar larvae assessed by LC/MS. Note that p.Arg210Gln mutant rescues with less efficiency than *Sply* WT (p.Arg210Gln vs. *Sply* WT, $P = 0.009$ for sphingosines and $P = 0.02$ for ceramides, *t* test). $n = 6$ independent experiments. For *Sply* null, *Sply* WT, and p.E119G, 1 analysis was removed due to poor quality chromatography. Control corresponds to WT larvae. Statistical analysis performed by Dunnet's (**C**) post-hoc tests following ANOVA or Dunn's post-hoc test following Kruskal-Wallis (**A**). ***$P < 0.0005$; **$P < 0.005$; *$P < 0.05$. All graphs show mean ± SEM.

to a less severe phenotype, with decreased lethality and in which prevailing manifestations involved kidney (massive proteinuria with FSGS), the immune system, platelets, and skin (28, 29). The variable organ involvement found in different *SGPL1* mutated families may be related to levels of residual functional SGPL1 conveyed by different mutations. However, the intrafamilial variability may be explained by the presence of other genetic factors that may influence the disease manifestations. For instance, variants or polymorphisms in genes involved in S1P metabolism and signaling, such as *SGPP1*, *SGPP2*, *SPHK1*, *SPHK2*, *SPNS2,* or *S1PR1-5*, may contribute to intrafamilial variability.

The phenotypic spectrum of *SGPL1* mutations is reminiscent of Schimke immunoosseous dysplasia (MIM 242900), which is caused by recessive mutations in *SMARCAL1* encoding SWI/SNF-related, matrix-associated, actin-dependent regulator of chromatin, subfamily A-like protein 1. Specifically, mutations in both *SMARCAL1* and *SGPL1* are associated with FSGS and T cell–related immunodeficiency. Whereas *SMARCAL1* is involved in reannealing stably unwound DNA, *SGPL1* has been implicated as a mediator of DNA damage response (DDR). Increased *SGPL1* expression and activity in DDR promotes apoptosis through a pathway involving p53 and caspase 2 (30). Therefore, defects in DDR may also contribute to the pathogenesis of *SGPL1* deficiency. However, it should be noted that the T cell defects in patients with *SMARCAL1* mutations are global and involve impairment of T cell proliferation, survival, and function. In contrast, *SGPL1* deficiency in mice leads to lymphopenia as a result of trafficking defects, as shown by the sequestration of mature T cells in mutant mouse thymus, whereas T cell proliferation in thymus is unaffected (J.D. Saba and colleagues, unpublished observations).

Patient fibroblasts had significantly elevated C22:0, C24:0, and C24:1 ceramides compared with control fibroblast (Supplemental Figure 8). Interestingly, total serum ceramide levels and C24:0 and C16:0 lactyosylceramides were found to be high in children with CKD, which suggests they may play a causal role in the development of FSGS in our cohort (31). Total ceramide levels and the balance of different ceramide species can influence apoptosis and autophagy, thereby contributing to the pathophysiology of many diseases.

S1P is a bioactive lipid implicated in the regulation of cell survival, apoptosis, proliferation, and migration (32, 33). It can act in a paracrine and autocrine fashion by acting on G protein–coupled S1PRs that account for activation of signaling pathways such as Akt, mTOR, and RHO/RAC/CDC42 (34). However, S1P can also act intracellularly by regulating proapoptotic effector molecules such as BAK and BAX (35), TRAF2 (36), HDAC activity, and thus, epigenetic programs in the nucleus (37). The pathogenesis of disease within the target organs could result from both an excess of intracellular S1P and an imbalance of other sphingoid bases, but also from S1P signaling through the S1PRs. Podocytes are known to exhibit S1PRs, and as components of the glomerular filtration barrier, they could exhibit increased sensitivity to circulating S1P levels, especially under conditions of reduced *SGPL1* activity, as has been shown in neuron primary cultures (38). In *Drosophila*, the phenotype we observed in nephrocytes upon constitutive *Sply* deletion is most likely to be secondary to intracellular accumulation of S1P, but also to increased interstitial S1P levels, and cannot argue against or in favor of a cell no-autonomous effect of SGPL1 deficiency. However, in our study, cultured podocytes stimulated with S1P did not show increased apoptosis at the S1P expected disease level. Additionally, *SGPL1* knockdown in podocytes also did not lead to a phenotype in cell migration or cell proliferation, although these results could be due to insufficient SGPL1 decrease, since in neurons, a 70% reduction of *SGPL1* using an RNA strategy is insufficient to induce accumulation of S1P (38). In *Drosophila*, there has still been no identification of a S1PR orthologue. However, we cannot exclude the possibility of a *Drosophila* S1PR. Accordingly, the phenotype we observed in nephrocytes upon the constitutive *Sply* knockout cannot argue against or in favor of a cell-nonautonomous effect of SGPL1 deficiency.

However, in mesangial cells, *SGPL1* knockdown induced a decrease of active RAC1 and CDC42 and a phenotype of decreased cell migration, which was partially mitigated by S1PR inhibition. Our findings in RMCs and *Drosophila* nephrocytes suggest that both cell types can be affected by SGPL1 deficiency, but it is not clear which cell type is primary in the pathogenesis. To address this, generation of transgenic mice with glomerular cell type–specific deletion of *Sgpl1* is under way.

Methods

Study participants. We obtained clinical data, blood samples, and skin biopsies from SRNS patients from worldwide sources. The diagnosis of NS was made by nephrologists based on standardized clinical and histologic criteria (39). Renal biopsies were evaluated by pathologists. Additional, clinical data were obtained using a standardized questionnaire (http://www.renalgenes.org).

WES. In consanguineous families, we combined WES with HM, as established previously (40, 41). Genetic regions of homozygosity were plotted across the genome (Figure 1A) (42, 43). Exome capture was performed with the Agilent SureSelect V5 Enrichment Capture Kit. The enriched library was sequenced on an Illumina HiSeq 4000 (100 bases paired end). Variant burden analysis was performed as previously described (44). Sequence reads were mapped against the human reference genome (NCBI build 37/hg19) using CLC Genomics Workbench (version 6.5.1) software (CLC bio). High-throughput exon resequencing was performed largely as described previously (9). For the nonconsanguineous family NCR61 and consanguineous family EB, exome sequencing was performed in 2 (NCR61-1 and NCR61-2) and 1 (EB-1) affected children. The enriched library was sequenced on an Illumina HiSeq 2500 (V4 chemistry, 2 × 125 bases). Variants were called as described (45).

RNA extraction, RT-PCR, and cDNA cloning. Human *SGPL1* full-length cDNA was obtained (clone MGC: 60255 IMAGE: 6150776) and subcloned into pRK5-N-Myc, pDEST69-N-FLAG, or BABE-puro-gateway (Addgene plasmid no. 51070). Mutations were introduced using the QuikChange II XL Site-Directed Mutagenesis Kit (Agilent Technologies).

SGPL1 enzymatic activity assay. SGPL1 activity in whole cell extracts of patient fibroblasts and HEK293T cells expressing WT and mutant SGPL1 cDNA constructs was measured by quantifying the amount of hexadecenal formed over time as described (46).

3D protein structure. The crystal structure of human SGPL1 (PDB code 4Q6R) was prepared using the protein preparation wizard in Schrödinger Maestro release 2015.1. (version 10.1). After protein preparation, the effects of mutations were computationally assessed using the Residue Scanning module in BioLuminate 1.8 (Biologics Suite 2015-1: BioLuminate, version 1.8).

Cell culture and transfection. Human podocytes were provided by M. Saleem (University of Bristol, Bristol, United Kingdom) and maintained at the permissive temperature of 33°C in RPMI + GlutaMAX-I (Gibco, Thermo Fisher Scientific) supplemented with 10% FBS, penicillin (50 IU/ml)/streptomycin (50 μg/ml), and insulin–transferrin–selenium-X. RMCs (ATCC CRL-2573) were maintained in DMEM supplemented with 15% FBS, 0.4 mg/ml G418, and penicillin/streptomycin. *SGPL1*-specific and control scrambled siRNAs were purchased from Dharmacon. siRNAs were transfected into podocytes or RMCs using Lipofectamine RNAiMAX (Invitrogen). The target sequences of siRNAs are in Supplemental Table 1. Human fibroblasts were grown in DMEM supplemented with 15% FBS, penicillin/streptomycin, and nonessential amino acids (Invitrogen). HEK239T cells were used for lentivirus production and transfected by the calcium phosphate precipitation method.

Immunoblotting, immunofluorescence, and GST pulldown assay. Experiments were performed as described previously (47). GST-PAK1 and GST-Rhotekin beads were purchased from Cytoskeleton Inc. Anti-SGPL1 (AF5535, R&D Systems), anti-BiP (ab21685), anti–β-actin (ab6276, Abcam), anti-CD31 (MA3100, Thermo), anti-RAC1 (610650), anti-CDC42 (610928), anti-GM130 (610822, BD Transduction Laboratories), anti-Myc (sc-789), anti-RHOA (sc-418), anti-WT1 (sc-7385, Santa Cruz Biotechnology Inc.), anti-GOLGB1(HPA011008), anti–α-smooth muscle actin (A2547), anti-FLAG (F3165, Sigma-Aldrich), anti-HA (11867423001, Roche), and anti-synaptopodin (20-4694, American Research Products) antibodies were purchased from commercial sources. Immunoblotting was quantified by densitometry using ImageJ software (NIH). For immunofluorescence in *Drosophila* nephrocytes, third instar garland nephrocytes were dissected and fixed for 20 minutes in 4% paraformaldehyde at room temperature. For Kirre stainings, an alternative fixation method was used: nephrocytes were heat fixed during 5 seconds at 90°C in 0.7% NaCl, 0.05% Triton X-100 solution (48). The following primary antibodies were used: anti-Kirre (gift from Karl Fischbach, University of Freiburg) anti-HA, and Alexa Fluor 488 or Cyanine Cy3–conjugated anti–horseradish peroxidase (Jackson Immunoresearch). Nile red and Bodipy 493/503 (Thermo Fisher Scientific) were used to stain lipid droplets. For albumin uptake assay, garland nephrocytes were dissected from third instar larvae in Schneider's medium (Pan-Biotech), incubated for 2.5 minutes with 0.1 mg/ml Alexa Fluor 488–conjugated albumin (Thermo Fisher Scientific) at room temperature, and fixed in 4% PFA for 20 minutes. Confocal images were obtained with a Leica TCS SP8 SMD, and ImageJ (NIH) was used for image analysis.

Migration and proliferation assay. Migration assays were performed using the xCELLigence system (ACEA Biosciences). For migration assays, 48 hours after transfection, 4×10^4 cells were plated with serum-free media in the upper chamber of CIM-plate 16. The lower chambers were filled with 10% FBS for chemoattraction or with serum-free media. For proliferation assays, 4×10^4 cells were plated in the E-plate 16. The data obtained were analyzed with RTCA software (ACEA Biosciences Inc.). Results are presented as the time versus cell index curve.

Yeast strains and plasmids. The following yeast strains were used in this study: BY4741-Euroscarf, MAT*a*, *his3Δ1, leu2Δ0, met15Δ0, ura3Δ0, dpl1Δ::KanMx,* RH4863, MATα *lcb3Δ*::KanMx *dpl1Δ*::KanMx *ura3 leu2 his4 ade2 bar1,* pLCB3::URA3 (PCR amplified genomic *LCB3* cloned into YCplac33), RH431, and MATα *ura3 leu2 his4 bar1* (49). pRS415-ADH[2] was used to overexpress human *SGPL1* in yeast. pRS415-ADH-SGPL1 was constructed by cloning *SGPL1* in the *Xma*I-*Xho*I sites of pRS415-ADH.

PHS toxicity test. Yeast *dpl1Δ* cells transformed with PRS415-ADH bearing WT or mutant human *SGPL1* coding sequences were cultured overnight in synthetic defined minus leucine medium and spotted onto synthetic defined plates containing ethanol (vehicle control) and PHS (40 μM) as previously described (50).

Synthetic lethality test. RH4863 yeast cells were transformed with plasmids overexpressing human SGPL1 (WT and mutant variants) or yeast (positive control). Cells grown in synthetic defined minus leucine medium were 10-fold serially diluted and spotted onto synthetic defined–agar without leucine, without uracil, or with 1 mg/ml 5-FOA (50).

Fly strains and generation of transgenic flies. Stocks were maintained on standard cornmeal-yeast food at 25°C. The following fly stocks were used: *Sply*^{05091}*/CyO,Act-GFP* (from BL #11393), *Df(2R)BSC433/ CyO,Act-GFP* (from BL #24937), and *Df(2R)247/CyO,Act-GFP* (BL #7155), obtained from the Bloomington Stock Center, and *Kirre* RNAi (GD #14476), obtained from the Vienna *Drosophila* RNAi Center. *Pros-GAL4* (a gift from Barry Denholm, Center for Integrative Physiology, University of Edinburgh, Edinburgh, United Kingdom) *y,w*^{1118} was used as a WT control. Due to inbreeding, homozygous *Sply*^{05091} (*Sply* null allele) were almost impossible to obtain. We therefore generated *Sply* null hemizygous flies by crossing the *Sply*^{05091}*/CyO,Act-GFP* flies with *Df(2R)BSC433/ CyO,Act-GFP* flies that carry a deletion of the *Sply* locus and 5 other contiguous genes. In the F1 generation, *Sply* null hemizygous flies were identified by the absence of the balancer chromosome (*CyO,Act-GFP*). We confirmed the absence of *Sply* mRNA in *Sply* null hemizygous flies by reverse-transcriptase PCR (RT-PCR) (Supplemental Figure 15). For *Sply* rescue constructs, the HA tag (in-frame before the stop codon) and the corresponding *SGPL1* human mutations were individually inserted by site-directed mutagenesis in the cloned 4-kb *Sply* genomic locus, including regulating sequences (–491 bp) and 3′ UTR (+1066 bp). Subsequently, the WT and mutant *Sply* rescue constructs were cloned into a *pattB* vector (Konrad Basler, Institute of Molecular Life Sciences, University of Zurich, Zurich, Switzerland) and injected into flies with an attP landing site at 76A2 by BestGene Inc. Primer sequences and cloning details are available in Supplemental Table 2. For the rescue experiments, 1 copy of the *Sply* rescue constructs was transferred by mating to the *Sply* null hemizygous background.

Viability assay. Fly crosses were allowed to lay eggs for 48 hours on standard cornmeal-yeast food. The percentage of hatching adults of the appropriate genotype was recorded. As a control, we crossed the Df(2R)BSC433/CyO,Act-GFP with Df(2R)247/CyO,Act-GFP (carrying a deletion nonoverlapping with Df[2R]BSC433), and the percentage of the normally viable Df(2R)BSC433/Df(2R)247 flies was recorded. On average, a total of 120 F1 hatching flies were counted per condition, and the experiments were repeated 6 times. Values reported were normalized to the control.

Mice. *Sgpl1*$^{-/-}$ mice were previously described (11). *Sgpl1*$^{-/-}$ mice, littermate controls, and heterozygote breeders were handled in pathogen-free conditions.

TEM. After dissection, third instar garland nephrocytes and kidneys from *Sgpl1*$^{+/+}$ and *Sgpl1*$^{-/-}$ mice were fixed in 2.5% glutaraldehyde at room temperature and processed for TEM with standard techniques.

Sphingoid bases analysis. Sphingolipid metabolites from fly larvae and patient fibroblast samples were extracted using a protocol described previously (51). Analytical systems used were composed of Agilent 1290 UPLC coupled with Agilent 6490 triple quadruple mass spectrometer. Analysis was carried out using multiple reaction monitoring (MRM) mode. The general source settings in the positive ionization modes were as follows: gas temperature, 200°C; gas flow, 16 minute^{-1}; nebulizer, 20 psi; sheath gas temperature, 250°C; sheath gas flow, 11 minute^{-1}; and capillary voltage, 3.0 kV. Specific MRM transitions for fly sphingoid bases were programmed based on the transitions described previously (52). Chromatographic separation of sphingolipids was performed with a Zorbax RRHD Eclipse Plus C18 (2.1 × 150 mm, 1.8 μm) equilibrated at 50°C. A binary gradient of mobile phase A (water containing 0.2% formic acid and 2 mM ammonium formate) and B (methanol containing 0.2% formic acid and 1 mM ammonium formate) was delivered at a constant flow rate of 1 ml/min. The total run time was 10 minutes. Initial gradient was 70% B and increased to 100% B at 8 minutes and returned to baseline at 8.5 minutes and maintained until 10 minutes. Data processing of all metabolites was performed using MassHunter software (Agilent).

RT-PCR and real-time PCR. Total RNA was isolated from fibroblasts using a QIAGEN RNA extraction kit (QIAGEN). cDNA was prepared using reverse transcriptase Superscript II (Invitrogen). PCR was performed using ReadyMix Taq PCR (Sigma-Aldrich) and the following primers: SGPL1 exon 4 forward, 5′-CTCACCAGGAAGATGCCCAT-3′ and SGPL1 exon 8 reverse, 5′-GCTTTGCAGGCCATCAGTAT-3′. The amplified PCR products were then cloned into a pGEM–T Easy Vector (Promega) and analyzed by Sanger sequencing. In *Drosophila*, relative expression levels were determined using the Absolute SYBR Green ROX Mix (ABgene) and specific primers as follows: *Sply* forward, 5′-CTGGCTCTGGACTGTGATCTG-3′ and reverse, 5′-GACGCTTGCCACGAATGTAA-3′. Expression levels were normalized to actin.

Statistics. Results are presented as mean ± SEM or SD for the indicated number of experiments. Statistical analysis of continuous data was performed with 2-tailed Student's *t* test or 1-way ANOVA, with Dunnet's, Bonferroni's, or Dunn's post hoc test, as appropriate. $P <$ 0.05 was considered statistically significant.

Study approval. Approval for human subject research was obtained from the University of Michigan (Ann Arbor, Michigan, USA) and Boston Children's Hospital institutional review boards and the Comité de Protection des Personnes Ile de France II. All subjects gave informed consent. Approval for mouse research was obtained from the University Committee on Use and Care of Animals (UCUCA) of the UCSF Benioff Children's Hospital Oakland and Boston Children's Hospital.

Supplemental appendix. For additional data, including Supplemental Tables 1–3 and Supplemental Figures 1–15, see the supplemental material, available with the full text of this article.

Author contributions

SL, SG, HYG, SS, CES, KS, RPL, OG, MF, MAC, C Antignac, and FH prepared and evaluated genetic mapping and exome sequences. SL, SG, HYG, KS, MAC, C Antignac, and FH identified mutations in the human *SGPL1* gene. SG, HYG, SL, BO, WIC, SH, MZ, VC, C Arrondel, OB, VV, JDS, C Antignac, and FH provided and evaluated critical cell lines and animal resources. JDS, BO, JHS, HYG, and WIC performed all mouse studies and analyzed mutant SGPL1 expression or enzyme activity in fibroblasts and HEK293 cells. JDS, BO, HYG, and WIC analyzed the *Sgpl1*$^{-/-}$ mouse model, critically evaluated mouse data, and wrote mouse studies. SG, N Lachaussée, MS, JP, and C Antignac performed *Drosophila* studies. AS performed TEM. JHS performed all LC/MS assays for quantification of cellular SPLY activity and SPL distribution. HR and VG performed yeast complementation experiments. SL, HYG, SG, MZ, VC, C Antignac, D Schapiro, MF, DAB, FS, NK, JG, TG, KS, VC, D Schanze, IF, YS, AST, BA, JD, RB, YP, EA, N Lloberas, AM, CES, FPB, JPM, VRD, AMC, MCW, MAC, NW, and FH recruited patients and gathered detailed clinical information for the study. JG and TG performed the immunophenotyping of patient EB-1. HS, RW, and GC performed structural molecular modeling of the SGPL1 enzyme. JDS directed studies undertaken by BO and JHS. All authors critically reviewed the paper. FH and C Antignac conceived of and directed the entire project and wrote the paper with help from SL, SG, HYG, BO, and JDS.

Acknowledgments

The authors thank the families who contributed to this study. We thank the Yale Center for Mendelian Genomics for WES analysis, U. Pannicke for help in analyzing data, and S. Braun for technical assistance. FH was supported by grants from the NIH (DK076683, DK068306). FH is the Warren E. Grupe Professor. HYG was supported by the Basic Science Research Program through the National Research Foundation of Korea, funded by the Ministry of Education (2015R1D1A1A01056685), by a Nephcure-ASN Foundation Kidney Research Grant, and by a faculty research grant of Yonsei University College of Medicine (6-2015-0175). C Antignac was supported by grants from the Agence Nationale de la Recherche (GenPod project ANR-12-BSV1-0033.01), the European Union's Seventh Framework Programme (FP7/2007-2013/no 305608-EURenOmics), the Fondation Recherche Médicale (DEQ20150331682), and the ''Investments for the Future'' program (ANR-10-IAHU-01). SG was supported by the Program Santé-Science (MD-PhD) of Imagine Institute. FS was supported by the European Union's Seventh Framework Programme (FP7/2007-2013/n°305608-EURenOmics). Immunophenotyping was supported by the German Centre for Infectious Diseases (Thematical Translation Units: Infections of the immunocompromised host). JDS was supported by the John and Edna Beck Chair in Pediatric Cancer Research, the Swim Across America Foundation, and a grant from the NIH (GM66594, NCI CA129438). KS was supported by the Center for Personalized Immunology (supported by the National Health and Medical Research Council of Australia [NHMRC]), the Australian National University, Canberra, Australia. MZ was supported by the German Ministry of Education and Research (Bundesministerium füur Bildung und Forschung, project: GeNeRARe). EW was supported by the Leopoldina Fellowship Program, German National Academy of Sciences Leopoldina (LPDS 2015-07). TJS was supported by grant Jo 1324/1-1 of Deutsche Forschungsgemeinschaft (DFG). MF was supported by grants from the Spanish Society of Nephrology and the Catalan Society of Nephrology. HR was supported by grants from the Swiss National Science Foundation, SystemsX.CH, and the NCCR Chemical Biology. This work was performed under the Care4Rare Canada Consortium funded by Genome Canada, the Canadian Institutes of Health Research, the Ontario Genomics Institute, the Ontario Research Fund, Genome Quebec, and the Children's Hospital of Eastern Ontario Research Foundation. We acknowledge the contribution of the high-throughput sequencing platform of the McGill University and Génome Québec Innovation Centre, Montréal, Canada. The names of Care4Rare Canada steering committee members appear in the Supplemental Acknowledgments.

Address correspondence to: Friedhelm Hildebrandt, Boston Children's Hospital, Enders 561, Harvard Medical School, 300 Longwood Avenue, Boston, Massachusetts 02115, USA. Phone: 617.355.6129; E-mail: friedhelm.hildebrandt@childrens.harvard.edu. Or to: Corinne Antignac, Imagine Institute, Inserm U1163, 24 Bd du Montparnasse, 75015 Paris, France. Phone: 33142754345; E-mail: corinne.antignac@inserm.fr. Or to: Julie Saba, UCSF Benioff Children's Hospital Oakland, Children's Hospital Oakland Research Institute, 5700 Martin Luther King Jr. Way, Oakland, California 94609, USA. Phone: 510.450.7690; E-mail: jsaba@chori.org.

---

1. Smith JM, Stablein DM, Munoz R, Hebert D, McDonald RA. Contributions of the Transplant Registry: The 2006 Annual Report of the North American Pediatric Renal Trials and Collaborative Studies (NAPRTCS). *Pediatr Transplant*. 2007;11(4):366–373.
2. Hildebrandt F, Heeringa SF. Specific podocin mutations determine age of onset of nephrotic syndrome all the way into adult life. *Kidney Int*. 2009;75(7):669–671.
3. Somlo S, Mundel P. Getting a foothold in nephrotic syndrome. *Nat Genet*. 2000;24(4):333–335.
4. Tryggvason K, Patrakka J, Wartiovaara J. Hereditary proteinuria syndromes and mechanisms of proteinuria. *N Engl J Med*. 2006;354(13):1387–1401.
5. Sadowski CE, et al. A single-gene cause in 29.5% of cases of steroid-resistant nephrotic syndrome. *J Am Soc Nephrol*. 2015;26(6):1279–1289.
6. Lovric S, Ashraf S, Tan W, Hildebrandt F. Genetic testing in steroid-resistant nephrotic syndrome: when and how? *Nephrol Dial Transplant*. 2016;31(11):1802–1813.
7. Lovric S, et al. Rapid detection of monogenic causes of childhood-onset steroid-resistant nephrotic syndrome. *Clin J Am Soc Nephrol*. 2014;9(6):1109–1116.
8. Raponi M, et al. Prediction of single-nucleotide substitutions that result in exon skipping: identification of a splicing silencer in BRCA1 exon 6. *Hum Mutat*. 2011;32(4):436–444.
9. Halbritter J, et al. High-throughput mutation analysis in patients with a nephronophthisis-associated ciliopathy applying multiplexed barcoded array-based PCR amplification and next-generation sequencing. *J Med Genet*. 2012;49(12):756–767.
10. Saba JD, Nara F, Bielawska A, Garrett S, Hannun YA. The BST1 gene of Saccharomyces cerevisiae is the sphingosine-1-phosphate lyase. *J Biol Chem*. 1997;272(42):26087–26090.
11. Schmahl J, Raymond CS, Soriano P. PDGF signaling specificity is mediated through multiple immediate early genes. *Nat Genet*. 2007;39(1):52–60.
12. Pewzner-Jung Y, et al. A critical role for ceramide synthase 2 in liver homeostasis: I. alterations in lipid metabolic pathways. *J Biol Chem*. 2010;285(14):10902–10910.
13. Gee HY, et al. ARHGDIA mutations cause nephrotic syndrome via defective RHO GTPase signaling. *J Clin Invest*. 2013;123(8):3243–3253.
14. Gee HY, et al. FAT1 mutations cause a glomerulotubular nephropathy. *Nat Commun*. 2016;7:10822.
15. Gee HY, et al. KANK deficiency leads to podocyte dysfunction and nephrotic syndrome. *J Clin Invest*. 2015;125(6):2375–2384.
16. Rosen H, Gonzalez-Cabrera PJ, Sanna MG, Brown S. Sphingosine 1-phosphate receptor signaling. *Annu Rev Biochem*. 2009;78:743–768.
17. Herr DR, et al. Sply regulation of sphingolipid signaling molecules is essential for Drosophila development. *Development*. 2003;130(11):2443–2453.
18. Weavers H, et al. The insect nephrocyte is a podocyte-like cell with a filtration slit diaphragm. *Nature*. 2009;457(7227):322–326.
19. Zhuang S, Shao H, Guo F, Trimble R, Pearce E, Abmayr SM. Sns and Kirre, the Drosophila orthologs of Nephrin and Neph1, direct adhesion, fusion and formation of a slit diaphragm-like structure in insect nephrocytes. *Development*. 2009;136(14):2335–2344.
20. Dobrosotskaya IY, Seegmiller AC, Brown MS, Goldstein JL, Rawson RB. Regulation of SREBP processing and membrane lipid production by phospholipids in Drosophila. *Science*. 2002;296(5569):879–883.
21. Fyrst H, Herr DR, Harris GL, Saba JD. Characterization of free endogenous C14 and C16 sphingoid bases from Drosophila melanogaster. *J Lipid Res*. 2004;45(1):54–62.
22. Fyrst H, et al. Identification and characterization by electrospray mass spectrometry of endogenous Drosophila sphingadienes. *J Lipid Res*. 2008;49(3):597–606.
23. Vogel P, et al. Incomplete inhibition of sphingosine 1-phosphate lyase modulates immune system function yet prevents early lethality and non-lymphoid lesions. *PLoS ONE*. 2009;4(1):e4112.
24. Allende ML, et al. Sphingosine-1-phosphate lyase deficiency produces a pro-inflammatory response while impairing neutrophil trafficking. *J Biol Chem*. 2011;286(9):7348–7358.
25. Bektas M, et al. Sphingosine 1-phosphate lyase deficiency disrupts lipid homeostasis in liver. *J Biol Chem*. 2010;285(14):10880–10889.
26. Schwab SR, Pereira JP, Matloubian M, Xu Y, Huang Y, Cyster JG. Lymphocyte sequestration through S1P lyase inhibition and disruption of S1P gradients. *Science*. 2005;309(5741):1735–1739.
27. Yu XQ, et al. Pharmacokinetic/pharmacodynamic modelling of 2-acetyl-4(5)-tetrahydroxybutyl imidazole-induced peripheral lymphocyte sequestration through increasing lymphoid sphingosine 1-phosphate. *Xenobiotica*. 2010;40(5):350–356.
28. Billich A, et al. Partial deficiency of sphingosine-1-phosphate lyase confers protection in experimental autoimmune encephalomyelitis. *PLoS One*. 2013;8(3):e59630.
29. Schümann J, et al. Reduced activity of sphingosine-1-phosphate lyase induces podocyte-related glomerular proteinuria, skin irritation, and platelet Activation. *Toxicol Pathol*. 2015;43(5):694–703.
30. Oskouian B, et al. Sphingosine-1-phosphate lyase potentiates apoptosis via p53- and p38-dependent pathways and is down-regulated in colon cancer. *Proc Natl Acad Sci USA*. 2006;103(46):17384–17389.
31. Mitsnefes M, et al. Ceramides and cardiac function in children with chronic kidney disease. *Pediatr Nephrol*. 2014;29(3):415–422.
32. Rosen H, Goetzl EJ. Sphingosine 1-phosphate and its receptors: an autocrine and paracrine network. *Nat Rev Immunol*. 2005;5(7):560–570.
33. Fyrst H, Saba JD. An update on sphingosine-1-phosphate and other sphingolipid mediators. *Nat Chem Biol*. 2010;6(7):489–497.
34. Blaho VA, Hla T. An update on the biology of sphingosine 1-phosphate receptors. *J Lipid Res*. 2014;55(8):1596–1608.
35. Chipuk JE, et al. Sphingolipid metabolism cooperates with BAK and BAX to promote the mitochondrial pathway of apoptosis. *Cell*. 2012;148(5):988–1000.
36. Alvarez SE, et al. Sphingosine-1-phosphate is a missing cofactor for the E3 ubiquitin ligase TRAF2. *Nature*. 2010;465(7301):1084–1088.
37. Hait NC, et al. Regulation of histone acetylation in the nucleus by sphingosine-1-phosphate. *Science*. 2009;325(5945):1254–1257.
38. Hagen N, Van Veldhoven PP, Proia RL, Park H, Merrill AH, van Echten-Deckert G. Subcellular origin of sphingosine 1-phosphate is essential for its toxic effect in lyase-deficient neurons. *J Biol Chem*. 2009;284(17):11346–11353.
39. [No authors listed]. Primary nephrotic syndrome in children: clinical significance of histopathologic variants of minimal change of diffuse mesangial hypercellularity. A Report of the International Study of Kidney Disease in Children. *Kidney Int*. 1981;20(6):765–771.
40. Hildebrandt F, et al. A systematic approach to mapping recessive disease genes in individuals from outbred populations. *PLoS Genet*. 2009;5(1):e1000353.
41. Gee HY, et al. Whole-exome resequencing distinguishes cystic kidney diseases from phenocopies in renal ciliopathies. *Kidney Int*. 2014;85(4):880–887.
42. Hildebrandt F, et al. A systematic approach to mapping recessive disease genes in individuals from outbred populations. *PLoS Genet*. 2009;5(1):e1000353.
43. Otto EA, et al. Candidate exome capture identifies mutation of SDCCAG8 as the cause of a retinal-renal ciliopathy. *Nat Genet*. 2010;42(10):840–850.
44. Boyden LM, et al. Mutations in kelch-like 3 and cullin 3 cause hypertension and electrolyte

abnormalities. *Nature*. 2012;482(7383):98–102.

45. Field MA, Cho V, Andrews TD, Goodnow CC. Reliably detecting clinically important variants requires both combined variant calls and optimized filtering strategies. *PLoS ONE*. 2015;10(11):e0143199.
46. Suh JH, Eltanawy A, Rangan A, Saba JD. A facile stable-isotope dilution method for determination of sphingosine phosphate lyase activity. *Chem Phys Lipids*. 2016;194:101–109.
47. Gee HY, Tang BL, Kim KH, Lee MG. Syntaxin 16 binds to cystic fibrosis transmembrane conductance regulator and regulates its membrane trafficking in epithelial cells. *J Biol Chem*. 2010;285(46):35519–35527.
48. Rothwell WF, Sullivan W. Fluorescent analysis of Drosophila embryos. In: Sullivan W, Ashburner RS, ed. *Drosophila Protocols*, pp. 141–158. New York, NY: Cold Spring Harbor Laboratory Press; 2000:141–158.
49. Mukhopadhyay D, Howell KS, Riezman H, Capitani G. Identifying key residues of sphinganine-1-phosphate lyase for function in vivo and in vitro. *J Biol Chem*. 2008;283(29):20159–20169.
50. Bourquin F, Riezman H, Capitani G, Grütter MG. Structure and function of sphingosine-1-phosphate lyase, a key enzyme of sphingolipid metabolism. *Structure*. 2010;18(8):1054–1065.
51. Bielawski J, Szulc ZM, Hannun YA, Bielawska A. Simultaneous quantitative analysis of bioactive sphingolipids by high-performance liquid chromatography-tandem mass spectrometry. *Methods*. 2006;39(2):82–91.
52. Guan XL, et al. Biochemical membrane lipidomics during Drosophila development. *Dev Cell*. 2013;24(1):98–111.

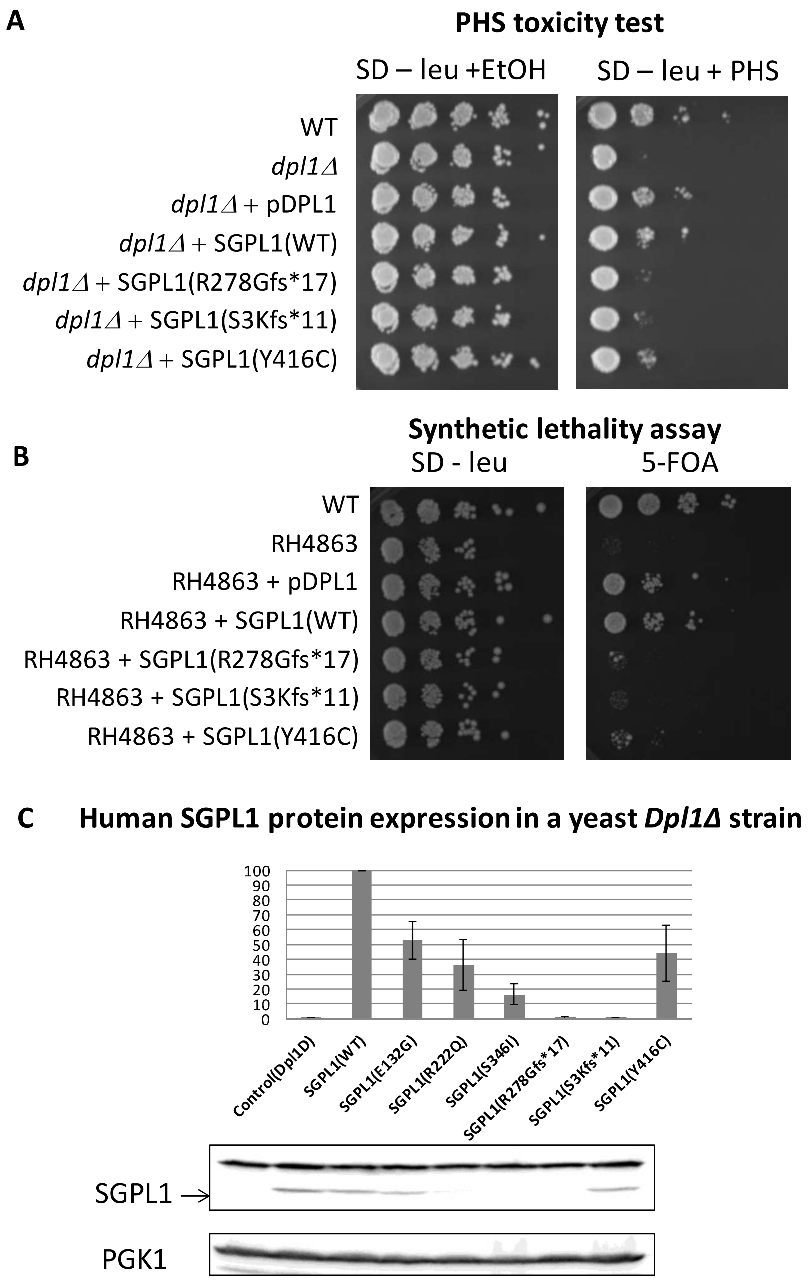

Supplemental Figure 7. Human *SGPL1* mutations fail to rescue yeast growth.

(A) Phytosphingosine toxicity test. Ability to complement *dpl1Δ* deletion on a medium containing phytosphingosine (PHS) was tested for human SGPL1 WT and the mutants Y416C, R278Gfs*17, S3Kfs*11. None of this mutants was able to restore the impaired growth of a dpl1 knockout strain.

(B) Synthetic lethality test. Synthetically lethal yeast strain RH4863, in which *DPL1* and *LCB3* were deleted, was maintained by expressing *LCB3* from a *URA3*-plasmid. Human WT SGPL1 expressing RH4863 survived on 5-FoA plates, showing to be able to compensate for the loss of *LCB3* and to degrade long-chain bases. However, overexpression of the mutants Y416C, R278Gfs*17, S3Kfs*11, observed in patients with NPHS type 14, did not allow for survival of *DPL1* (*SGPL1*) deficient strains.

(C) Human SGPL1 WT and mutants expression in a yeast *Dpl1Δ* strain. Protein expression of SGPL1 WT and mutants Glu132Gly, Arg222Gln, Ser346Ile, Arg278Glyfs*17, Ser3Lysfs*11, and Tyr416Cys in yeast Dpl1Δ strain. PGK1 was used as a loading control. Values correspond to 3 independent experiments and are shown as % to WT.